Strike-slip faulting and block rotations in the McConnell Creek area, north-central British Columbia: structural implications for the interpretation of paleomagnetic observations

by

Guowei Zhang

A thesis submitted to the Faculty of Graduate Studies and Research
in partial fulfilment of the requirements for
the degree of Doctor of Philosophy

Earth and Planetary Sciences
McGill University
Montreal, Canada
May 1994

ISBN 0-612-00149-0

A structural and paleomagnetic study in north-central British Columbia

Guowei Zhang

Earth & Planetary Sciences

(Short title of Ph.D. thesis)

ABSTRACT

Structures associated with dextral transpression on Finlay-Ingenika fault (FIF) in the McConnell Creek area, north-central British Columbia, are dominated by subvertical to vertical strike-slip faults, as indicated by a variety of kinematic indicators. Position-gradient tensors determined from strain analysis of deformed volcanic fragments in a succession of Late Triassic Takla Group rocks abutting one of the north-northwest trending faults indicate that they are dextrally transpressive, in accord with the common occurrence of subvertical intersections of the fault planes with other planar fabrics and subhorizontal stretching lineations within the fault zones. Principal directions of the magnetic susceptibility ellipsoids from Early Jurassic to Cretaceous dioritic rocks are consistent with those of the strain ellipsoids in their adjacent volcanics, suggesting that the plutonic rocks experienced the same deformation as the Late Triassic Takla Group volcanics. The age of the strike-slip faulting is unknown but was probably not earlier than mid Cretaceous as the Early Jurassic to Cretaceous dioritic rocks were involved in the faulting in many places.

Some of the major faults cut the area into discrete, fault-bounded blocks several kilometres wide. As the dextral motion on the FIF progressed, deformation was concentrated within the previously formed fault zones while the fault-bounded blocks remained weakly deformed. Stress tensors for 24 sites were inverted from the regional cleavage within the blocks, which predates the block-bounding faults.

The site-mean stress tensors indicate that the fault-bounded blocks were rotated clockwise about a subvertical axis during progressive dextral motion on the FIF. The amount of rotation varies systematically over the area with maximum value (58.7±3.3°) close to the FIF and minimum value (0.0±1.6°) about 20 kilometres away from it.

Paleomagnetic samples were collected from 13 sites in the widespread Early Jurassic to Cretaceous plutonic rocks. Interpretable magnetic components of the Late Cretaceous, isolated by both stepwise AF and thermal demagnetization from 6 sites, were used to calculate the paleopole. The observed paleopole has a low value of Fisher's precision k = 48, and is significantly different from the Late Cretaceous reference pole for cratonal North America (CNA). After corrections for the local block rotations, the observed paleopole has a high value of k = 383 and moves closer to the reference pole but is still significantly different from it. Rotation about the Eulerian pole for the best-fitting small circle to the Tintina trench and northern Rocky Mountain trench fault zone, however, brings the observed pole into coincidence with that for CNA, and requires only ~670 kilometres of dextral displacement on the fault zone. It is likely, therefore, that local structures associated with dextral strike-slip faults in the western Canadian Cordillera may account for at least part of the paleomagnetic disparity between some western parts of the Canadian Cordillera and CNA.

RÉSUMÉ

Les structures associées à la transpression dextre sur la faille Finlay-Ingenika (FIF) dans la région du McConnell Creek au centre-nord de la Colombie Britannique consistent de décrochements subverticales à verticales comme l'indique une variété d'indicateurs cinématiques. Des tenseurs à pente-positionale qui ont été déterminés utilisant l'analyse de déformation des fragments volcaniques déformés provenant d'une succession de couches de Groupe Takla du Triasique tardif en contact avec une des failles ayant une orientation nord nord-ouest, indiquent que ces fragments ont subi une transpression dextre. Ceci est en accord avec les intersections subverticales fréquentes entre les plans de failles et d'autres foliations et linéations subhorizontales à l'interieur des zones de failles. Les directions principales des ellipsoïdes de susceptibilité magnétique des roches dioritiques du début Jurassique au Crétacé sont en accord avec celles des ellipsoïdes de déformation des volcaniques adjacents, ce qui suggère que les roches plutonique ont subi la même déformation que les volcaniques du groupe Takla d'âge Triasique tardif. L'âge du décrochement n'est pas connu mais il s'est probablement produit pas plus tôt que le milieu-Crétacé car les roches dioritiques provenant du début Jurassique au Crétacé ont été impliquées dans la formation des failles à plusieurs endroits.

Quelques failles majeures coupent le territoire en blocs distincts de quelques

kilomètres de largeur. Pendant que le mouvement dextre sur la FIF continuait, la déformation a été concentrée à l'intérieur des zones de failles déja formées tandis que les blocs limités par les failles ont resté légèrement déformés. Des tenseurs de contrainte pour 24 sites à l'intérieur des blocs ont été tirés du clivage régional; le clivage s'est produit avant les failles qui délimitent les blocs. La moyenne de site des tenseurs de contrainte indique que ces blocs ont subi une rotation dans un sens horaire autour d'un axe subvertical pendant un mouvement dextre progressif sur la FIF. Le degré de rotation varie systematiquement dans cet endroit avec une valeur maximale (58.7 ± 3.3^{o}) près de la FIF et une valeur minimale (0.0 ± 1.6^{o}) à 20 kilomètres de la FIF.

Des échantillons paleomagnétiques provenant de 13 sites dans les roches plutoniques du début Jurassique au Crétacé ont été amassés. Le pôle paleomagnétique a été calculé utilisant les composantes magnétiques interprétables provenant du Crétacé tardif; les composantes ont été isolées par la démagnétisation en détail thermale et à champ alternatif de 6 sites. Le pôle paleomagnétique observé a une valeur basse de k = 48 pour la précision de Fisher, ce qui est très différent du pôle de réference pour le craton nord-américain (CNA) du Crétacé tardif. Après quelques corrections pour la rotation des blocs, le pôle paleomagnétique a une valeur plus élevée de k = 383 et il se déplace plus près du pôle de réference mais il est toutefois très différent de celui-ci. En tournant le pôle observé autour du pôle Eulerien pour le petit cercle de la fosse Tintina et de la section nord de la zone de faille du Rocky Mountain Trench, le pôle observé devient en coincidence avec celui du CNA, et il éxige ~670 kilomètres de déplacement dextre sur la zone de la faille. Il est donc probable que les structures locales associés aux décrochements dextres dans la portion ouest du Cordillère Canadien peuvent en partie justifier la disparité paleomagnétique entre des portions ouest du Cordillère et le CNA.

MANUSCRIPTS AND AUTHORSHIP

This thesis is prepared according to the "Guidelines Concerning Thesis Preparation", Faculty of Graduate Studies and Research, McGill University:

*"Candidates have the option, **subject to the approval of their Department**, of including, as part of their thesis, copies of the text of a paper(s) submitted for publication, or the clearly-duplicated text of a published paper(s), provided that these copies are bound as an integral part of the thesis.*

*-If this option is chosen, **connecting texts, providing logical bridge between the different papers, are mandatory.***

*-The thesis must still conform to all other requirements of the "Guidelines Concerning Thesis Preparation" and should be in a literary form that is more than a mere collection of manuscripts published or to be published. **The thesis must included, as separate chapters or sections:** (1) a Table of Contents, (2) a general abstract in English and French, (3) an introduction which clearly states the rationale and objectives of the study, (4) a comprehensive general review of the background literature to the subject of the thesis, when this review is appropriate, and (5) a final overall conclusion and/or summary.*

-Additional material (procedural and design data, as well as descriptions of equipment used) must be provided where appropriate and in sufficient detail

(eg. in appendices) to allow a clear and precise judgment to be made of the importance and originality of the research reported in the thesis.

-In the case of manuscripts co-authored by the candidate and others, ***the candidate is required to make an explicit statement in the thesis of who contributed to such work and to what extent;*** *supervisors must attest to the accuracy of such claims at the Ph.D. Oral Defense. Since the task of the examiners is made more difficult in these cases, it is in the candidate's interest to make perfectly clear the responsibilities of the different authors of co-authored papers."*

The following papers, which have been submitted to scientific journals for publication, are included in the thesis:

1. Fabrics and kinematic indicators associated with the local structures along Finlay-Ingenika fault, McConnell Creek area, north-central British Columbia.

    G. Zhang and A. Hynes

    Canadian Journal of Earth Sciences (in press)

2. Determination of position-gradient tensor from strain measurements and its implications for the displacement across a shear zone.

    G. Zhang and A. Hynes

Journal of Structural Geology (in review)

3. Block rotations in the McConnell Creek area, north-central British Columbia: structural implications for the interpretation of paleomagnetic observations.

G Zhang, A. hynes and E. Irving

Tectonics (submitted)

All research work presented in these papers was carried out by the first author. Dr. A. Hynes, the research supervisor and co-author, contributed significantly through instruction, consultation and editing throughout the duration of the research work. Dr. E. Irving, the co-author, donated the use of his paleomagnetic laboratory and provided valuable instruction and consultation in the paleomagnetic aspects of this thesis.

ACKNOWLEDGEMENTS

The thesis could not have been completed without support and encouragement from my supervisor, family and colleagues. I would first and foremost like to express my sincere thanks and appreciation to Andrew Hynes, my thesis supervisor, who suggested the research project and gave me the confidence to take on the challenging and interesting project while also providing the valuable, enthusiastic guidance in the field and out. His excellent supervision and constant encouragement and motivation provided me with just the right direction in the research, and his proof reading of this thesis added significantly to the quality of my writing and science.

I would like to express my heart-felt gratitude to my loving wife, Ying Luan, for her unfailing support, patience and understanding throughout the duration of my study. Expertly keeping the family in order and taking care of our kid were just part of her contribution.

I also wish to express my sincere thanks and appreciation to Eric Mountjoy and Jafar Arkani-Hamed, members of my Ph.D. advisory committee, for their valuable and constructive advice and suggestions during the four years of my study.

Many other people also contributed to the thesis. I am deeply indebted to

Ted Irving of the Geological Survey of Canada at the Pacific Geoscience Centre. Ted not only generously donated the use of his paleomagnetic laboratory for the measurements of paleomagnetic specimens, anisotropy of magnetic susceptibility and isothermal magnetization work, but also contributed his helpful and skillful guidance while I was working in the laboratory. Jane Wynne and Judith Baker of the Pacific Geoscience Centre are gratefully thanked for their constant and cheerful assistance with the laboratory work. Ron Doig of McGill University is sincerely acknowledged for generously donating the use of his laboratory for separating minerals for radiometric dating and providing valuable guidance. Gary Nassif of McGill University is appreciated for translating the English abstract into French. The thesis also benefitted from the valuable discussions on the regional geology with Kim Bellefontaine, Filippo Ferri, JoAnne Nelson of the British Columbia Ministry of Energy, Mines and Petroleum Resources and Hugh Gabrielse of the Geological Survey of Canada and discussions with Paul Budkewitsch of McGill University. They are sincerely appreciated for their discussions.

This research was supported by grants from the British Columbia Ministry of Energy, Mines and Petroleum Resources, the Geological Survey of Canada and the Natural Sciences and Engineering Research Council (NSERC) to Dr. Hynes. I am truly indebted for the awards of Davidson, McGregor (x2) and Reinhardt (x3) scholarships through the Department of Earth and Planetary Sciences, McGill University. All the support is gratefully acknowledged.

TABLE OF CONTENTS

LIST OF FIGURES

LIST OF PLATES

LIST OF TABLES

PREFACE

Since Beck and Noson's (1972) interpretation of discordant paleomagnetic directions from the mid-Cretaceous Mount Stuart batholith in the northern Cascade Range, a large body of paleomagnetic data has been reported from the western Canadian Cordillera (see Irving and Wynne (1990) for a review; see also Beck (1992) for more). Paleomagnetic directions obtained from well-bedded Early to Middle (48-53 Ma) Eocene volcanics across the western Canadian Cordillera are statistically concordant with the reference direction for cratonic North America (Irving and Wynne, 1990; Vandall and Palmer, 1990), suggesting that the Intermontane and Insular Belts (i.e. allochthonous Composite Terranes I and II, respectively, cf. Monger *et al.*, 1982; Monger, 1984) were in the same latitudinal position relative to the North American craton during the Middle Eocene as they are at present. This indicates that the allochthonous terranes had assembled and docked with North America by at least the Middle Eocene. On the other hand, paleomagnetic results from bedded, palaeontologically well-dated Early Permian to Early Jurassic rocks in the Intermontane and Insular Belts show broadly concordant inclinations, although their declinations vary greatly, indicating that apparent paleolatitudinal displacements of the terranes relative to the North American craton are negligible (Irving and Wynne, 1990). In contrast, paleomagnetic results from Cretaceous, mostly plutonic, rocks in the Intermontane and Coast Belts are largely discordant, exhibiting systematically flatter inclinations and more easterly declinations (Irving and Wynne, 1990).

For about the last two decades, many efforts have been made to understand the mechanism responsible for the discordance between the paleomagnetic directions of Cretaceous rocks in the western Canadian Cordillera and the North American reference direction. In reviewing a large body of up-to-date Cretaceous paleomagnetic results from the Cordillera, Irving and Wynne (1990) summarized the three hypotheses: (1) regional tilting to the west and southwest; (2) northward displacement and clockwise rotation about a vertical axis, which has been popularized as the "Baja British Columbia" model (Irving, 1985; Umhoefer, 1987); (3) moderate northward displacement combined with variable tilting (see also Vandall, 1993). Until now, however, no geological evidence has been found in full support of any of the above hypotheses. The regional tilting hypothesis requires en bloc tilting of the Coast Belt to the southwest by 28-33^{o} (Irving and Wynne, 1990) and en bloc tilting of the Intermontane Belt to the west and southwest by about 18-24^{o} (Wynne *et al.*, 1992), which seems unlikely in the light of regional tectonics of the western Canadian Cordillera (Oldow *et al.*, 1989; Beck, 1992) and is also inconsistent with the data from bedded volcanic rocks of the Spences Bridge and Carmacks groups of the Intermontane Belt (Irving and Wynne, 1990). The "Baja British Columbia" model, which has been widely preferred because northward displacement of the terranes could be readily explained by oblique Kula (or Farallon) plate convergence against North America during the mid Cretaceous to

Early Tertiary (e.g. Umhoefer, 1987; Irving and Wynne, 1990; 1991), requires a northward paleolatitudinal displacement of over 2000 kilometres and clockwise rotation of 9-75° (Irving and Wynne, 1990; Wynne *et al.*, 1992). The northward displacement was thought to have been accomplished by motion along the dextral strike-slip Tintina trench and northern Rocky Mountain trench fault zone as it is approximately parallel to the boundary between the western allochthonous terranes and North America (Irving and Wynne, 1990; 1991). The amount of displacement inferred from the paleomagetic results is, however, much greater than that (450-900 kilometres) required to match the offsets of geological boundaries along the fault zone (Roddick, 1967; Tempelman-Kluit, 1979; Gabrielse, 1985). While discussing hypothesis (3), Irving and Wynne (1990) indicated that the required local tilt directions vary greatly, approximately 90° apart. Similarly, Vandall (1993) demonstrated that, given a moderate northward paleolatitudinal displacement (e.g. 1000 kilometres) for the discordant paleomagnetic directions from the Coast Belt, the required tilt angles range from 7-28° and the downward tilt directions range from 209-285°. Testing of the local tilting following a moderate northward displacement (i.e. the third hypothesis), inferred from the paleomagnetic data, however, requires further geological evidence.

Recently, Brown and Burmester (1991) analysed the P-T conditions of the contact metamorphic aureole around the mid Cretaceous Spuzzum pluton of the Coast Belt, site of one of the major discordant paleomagnetic data sets upon which the "Baja British Columbia" model is based (Irving and Wynne, 1990). Their results indicate that the aberrant paleomagnetic direction of the Spuzzum pluton could be completely explained by a single postmetamorphic tilting to the southwest by about 30° as deduced from the barometry. Furthermore, recent paleomagnetic data from the mid Cretaceous Spetch Creek pluton of the Coast Belt (Vandall, 1993) exhibit inclination (73.5°) similar to those expected (75.1°), indicative of an insignificant apparent northward paleolatitudinal displacement (330±770 kilometres). This result, which is incompatible with those previously reported (Irving and Wynne, 1990), led Vandall to conclude that local post-emplacement tilting of the plutons of the Coast Belt may have been responsible for the discordant paleomagnetic data. The results of recent studies therefore severely challenge the "Baja British Columbia" model and indicate the need for careful petrological or structural studies so as to fully understand the implications of discordant paleomagnetic data.

As discussed above, paleomagnetic directions, like other linear structures, can be easily reoriented through rotations of rigid fault-bounded blocks in which they are embedded, especially in a complexly deformed region. Interpretation of aberrant paleomagnetic directions should, therefore, be made after the effects of tectonic structures have been removed. In order to investigate the effects, a systematic and detailed structural analysis within a region from which the aberrant paleomagnetic directions are observed must be carried out. One purpose of this research project is therefore to examine the deformation associated with dextrally transpressive displacement along Finlay-Ingenika fault in the McConnell Creek area, one of the prominent dextral strike-slip fault zones in north-central British Columbia (Gabrielse, 1985), from which aberrant paleomagnetic directions have been reported (Monger and Irving, 1980; Wynne *et al*, 1992). This is the subject of the first chapter or the first paper of the dissertation. In this chapter the fabrics and kinematic indicators, developed along the subvertical to vertical strike-slip faults resulting from the dextrally transpressive displacement on the Finlay-Ingenika fault, as well as magnetic fabrics in the Early Jurassic to Cretaceous dioritic rocks are documented.

With the kinematic indicators alone, shear senses of shear zones can be determined (Ramsay, 1967; Berthé *et al.*, 1979; Lister and Snoke, 1984; Passchier and Simpson, 1986), but the displacement-boundary conditions, for example the displacements along, or across, the shear zones, are indeterminate unless a mode of deformation is assumed. In order to determine the displacement-boundary conditions, the position-gradient tensor (cf. Means, 1983) must be provided. Determination of the position-gradient tensor from conventional strain data, with some simplifications about the geometry of the structures within a shear zone, is discussed in the second chapter (second paper) of the dissertation. This technique has been applied to the strain data from deformed volcanic fragments in a succession of the Late Triassic Takla Group, abutting a large north-northwest trending, subvertical shear zone in the study area. The results indicate that the shear zone is dextrally transpressive, which is in accord with other geological structures observed in the area.

Structural analysis in the area indicates that the local structures associated with dextral transpression on the Finlay-Ingenika fault are dominated by subvertical to vertical strike-slip faults and the fault-bounded blocks were rotated clockwise during progressive transpression. The questions are, have the local structures affected the observed paleomagnetic directions and if so, how are the paleomagnetic data changed by removal of these effects? This is discussed in the third chapter (third paper) of the dissertation. The third chapter also deals with the effects of anisotropy of magnetic susceptibility on the natural remanent magnetic directions and the implications of the corrected paleomagnetic directions for the regional tectonics.

The fourth chapter is a general conclusion to the dissertation. In this chapter, the contributions of the dissertation to original knowledge and suggestions for future work are described in detail. Some of our raw data are presented in the appendices.

References

Beck, M. E. and Noson, L. 1972. Anomalous palaeolatitudes in Cretaceous granitic rocks. *Nature*, 235, 11-13.

Beck, M. E. 1992. Some thermal and paleomagnetic consequences of tilting a batholith. *Tectonics*, 11, 297-302.

Beck, M. E. 1992. Tectonic significance of paleomagnetic results for the western conterminous United States, in *The Geology of North America-The Cordilleran Orogen: Conterminous U.S.*, edited by B. C. Burchfiel, P. W. Lipman and M. L. Zoback, Geological Society of America, 683-697.

Berthé, D., Choukroune, P. and Jegouzo, P. 1979. Orthogneiss, mylonite and non-coaxial deformation of granites: the example of the south Armorican shear zone. *J. Struct. Geol.* 1, 31-42.

Brown, E. H. and Burmester, R. F. 1991. Metamorphic evidence for tilt of the Spuzzum pluton: diminished basis for the "Baja British Columbia" concept. *Tectonics*, 10, 978-985.

Gabrielse, H. 1985. Major dextral transcurrent displacement along the Northern Rocky Mountain Trench and related lineaments in north-central British Columbia. *Geological Society of America Bulletin*, 96, pp. 1-14.

Irving, E. 1985. Whence British Columbia. *Nature*, 314, 673-674.

Irving, E. and Wynne, P. J. 1990. Paleomagnetic evidence bearing on the evolution of the Canadian Cordillera. *Phil. Trans. R. Soc. Lond.* 331, 487-509.

Irving, E. and Wynne, P. J. 1991. Paleomagnetic evidence for motions of parts of the Canadian Cordillera. *Tectonophysics*, 187, 259-275.

Means, W. D. 1983. Application of the Mohr-circle construction to problems of inhomogeneous deformation. *J. Struct. Geol.* 5, 279-286.

Lister, G. S. and Snoke, A. W. 1984. S-C mylonites. *J. Struct. Geol.* 6, 617-638.

Monger, J. W. H. 1984. Cordilleran tectonics: a Canadian perspective. *Bulletin Societé Géologique de France*, 7, pp. 255-278.

Monger, J. W. H. and Irving, E. 1980. Northward displacement of north-central British Columbia. *Nature*, 285, pp. 289-294.

Monger, J. W. H., Price, R. A. and Tempelman-Kluit, D. J. 1982. Tectonic accretion and the origin of the two major metamorphic and plutonic welts in the Canadian Cordillera. *Geology*, 10, 70-75.

Passchier, C. W. and Simpson, C. 1986. Porphyroclast systems as kinematic indicators. *J. Struct. Geol.* 8, 831-843.

Oldow, J. S., Bally, A. W., Avé Lallemant, H. G. and Leeman, W. P. 1989. Phanerozoic evolution of the North American Cordillera; United States and Canada. in *The Geology of North America-An overview*, edited by A. W. Bally and A. R. Palmer, Geological Society of America, 139-232.

Ramsay, J. G. 1967. Folding and fracturing of rocks. *McGraw-Hill, New York and San Francisco*, p.568.

Roddick, J. A. 1967. Tintina Trench. *Journal of Geology*, 75, 23-33.

Tempelman-Kluit, D. J. 1979. Transported cataclasite, ophiolite and granodiorite in

Yukon: evidence of arc-continent collision. *Geological Survey of Canada* Paper 79-14, 27 p.

Umhoefer, P. J. 1987. Northward translation of "Baja British Columbia" along the Late Cretaceous to Paleocene margin of western North America. *Tectonics*, 6, 377-394.

Vandall, T. A. and Palmer, H. C. 1990. Upper limit of docking time for Stikinia and Terrane I: paleomagnetic evidence from the Eocene Ootsa Lake Group, British Columbia. *Can. J. Earth Sci.* 27, 212-218.

Vandall, T. A. 1993. Cretaceous Coast Belt paleomagnetic data from the Spetch Creek pluton, British Columbia: evidence for the "tilt and moderate displacement" model. *Can. J. Earth Sci.* 30, 1037-1048.

Wynne, P. J., Irving, E. and Ferri, F. 1992. Paleomagnetism of the middle Cretaceous Germansen batholith, British Columbia (93N/9, 10). Geological Fieldwork 1991, *B.C. Ministry of Energy, Mines and Petroleum Resources*, Paper 1992-1, 119-126.

CHAPTER 1

Fabrics and Kinematic Indicators Associated with the Local Structures along Finlay-Ingenika Fault, McConnell Creek Area, North-central British Columbia

G. Zhang and A. Hynes

Earth and Planetary Sciences, McGill University, Montreal, PQ, Canada

ABSTRACT

Structures associated with dextral transpression along Finlay-Ingenika fault are characterized predominantly by subvertical to vertical faults. A variety of fabrics and kinematic indicators are developed in the deformed rocks along the faults. Intersections of the fault planes with S-C surfaces and extensional fissures as well as other planar fabrics are all subvertical, with subhorizontal predicted transport directions. This geometry, together with the common occurrence of subhorizontal slickenlines and lineations of stretched mineral grains and volcanic fragments in some strongly-deformed fault zones, indicates their strike-slip nature. Strain analysis of the deformed volcanic fragments along one of the faults shows that the principal directions of the strain ellipsoids are in accordance with those of the ellipsoids of magnetic susceptibility from the adjacent deformed plutonic rocks,

indicating that the plutonic rocks experienced the same deformation as the Late Triassic Takla Group volcanics.

Some of the major faults cut the Takla Group into fault-bounded, weakly-deformed blocks. As dextral displacement on the Finlay-Ingenika fault progressed, deformation was concentrated in the previously-formed fault zones while the fault-bounded blocks remained weakly deformed and rotated clockwise about subvertical axes. Regional cleavage within the blocks indicates that the amount of block rotation varies over the area, reaching its maximum ($58.7 \pm 3.3^{\circ}$) close to the Finlay-Ingenika fault and minimum ($0.0 \pm 1.6^{\circ}$) about 20 kilometres away from the fault.

The age of the strike-slip faulting is unknown but was probably not earlier than middle Cretaceous as Jurassic to Cretaceous dioritic rocks were involved in the faulting in many places. The mode of deformation observed in the area may characterize many parts of the Intermontane Belt and could in part explain the apparent disparities between the paleomagnetic declinations observed from the western allochthonous terranes and North America.

1.1 INTRODUCTION

The response of continental crust in strike-slip faulting has become an active area of research since the recognition of the importance of major transcurrent motion at many convergent plate margins (e.g. Atwater, 1970; Fitch, 1972; Avé Lallemant and Oldow, 1988). For the Canadian Cordillera, middle Cretaceous to early Tertiary dextral transcurrent motion on the Tintina and northern Rocky Mountain Trenches fault system is well established from geological mapping and stratigraphic correlations (Roddick, 1967; Tempelman-Kluit, 1979; Gabrielse and Dodds, 1982; Gabrielse, 1985; Gabrielse, 1991). Along the Tintina Trench, about 450 km of dextral displacement is required to explain observed offsets of Precambrian grit and intervening micaceous quartzite and schist units as well as Cretaceous rocks (Roddick, 1967; Tempelman-Kluit, 1979). Recently, Gabrielse (1985) has shown that offsets of early Paleozoic continental-shelf facies boundaries may indicate 700 to 900 km of dextral displacement along the Tintina and northern Rocky Mountain Trenches fault system, and that cumulative dextral displacement on the northern Rocky Mountain Trench and the faults west of it is probably more than 1000 km. The amount of this motion demonstrable from the geology, however, is much less than that predicted from paleomagnetic data (e.g. Beck and Noson, 1972; Monger and Irving, 1980; Armstrong *et al.*, 1985; Irving *et al.*, 1985; Umhoefer, 1987; Umhoefer *et al.*, 1989; Irving and Wynne, 1990) and its effects on the rocks in the neighbourhood of large strike-slip faults have not been studied so far in detail. It is possible that local effects, such as the rotation of discrete brittle upper crustal blocks above a more plastic lower crust (e.g. Ron and Eyal, 1985; Nelson and Jones, 1986; Nur *et al.*, 1986; Ron *et al.*, 1986; Geissman *et al.*, 1989; Ron *et al.*, 1990), may explain some of the apparent inconsistencies between paleomagnetic and geological data.

As a precursor to reconciliation of these apparent inconsistencies, we have carried out a detailed study of the local deformation along Finlay-Ingenika fault, one of the most prominent dextral strike-slip faults of north-central British Columbia (Gabrielse, 1985), through 1:50 000 geological mapping and systematic structural measurement and analysis in the McConnell Creek area. In this paper we describe a variety of deformational fabrics and kinematic indicators as well as magnetic fabrics of plutonic rocks that were developed during dextral transpression along the Finlay-Ingenika fault. The mode of local deformation in association with dextrally transpressive faulting observed in the study area may provide an important key to the understanding of the extensive dextral transcurrent motions in the eastern Intermontane Belt, and possibly part of the Omineca Belt.

1.2 REGIONAL GEOLOGY

The study area lies within the Intermontane Belt (Figs. 1.1 and 1.2), one of the five morphogeological belts of the Canadian Cordillera (Wheeler and McFeely, 1991), and straddles the Quesnellia and Stikinia tectonostratigraphic terranes (Monger, 1984; Gabrielse, 1991). North and south of the study area, Quesnellia rocks are separated from those of Stikinia to the west by the Cache Creek Terrane, a subduction-related assemblage, and bounded to the east by the Slide Mountain Terrane, a deep-water oceanic assemblage. These terranes were amalgamated by latest Triassic to earliest Jurassic time, forming a composite terrane, "Terrane I", which accreted to the ancient margin of North America in Jurassic time (Monger, 1984; Gabrielse, 1991). During the middle Cretaceous to early Tertiary, dextral strike-slip faulting took place extensively along the eastern margin of the Intermontane Belt, and possibly part of the western Omineca metamorphic belt (Gabrielse, 1985). The Finlay-Ingenika fault (Figs. 1.1 and 1.2), which lies between the Stikinia and Quesnellia Terranes in the study area, is one of the dextral strike-slip faults on which the transcurrent motion occurred.

Stikinia and Quesnellia Terranes in the study area are both underlain by volcanic, volcaniclastic and sedimentary rocks of the Late Triassic Takla Group. West of the Finlay-Ingenika fault (Stikinia) the Takla Group was subdivided into three formations during 1:250 000 mapping of the McConnell Creek map area

Fig.1.1 Generalized structural map of the Johanson Lake area. Inset, main tectonic units of the Canadian Cordillera. FTB, Fold and Thrust Belt; OB, Omineca Belt; IMB, Intermontane Belt; CPB, Coast Plutonic Belt; ISB, Insular Belt (after Monger, 1984).

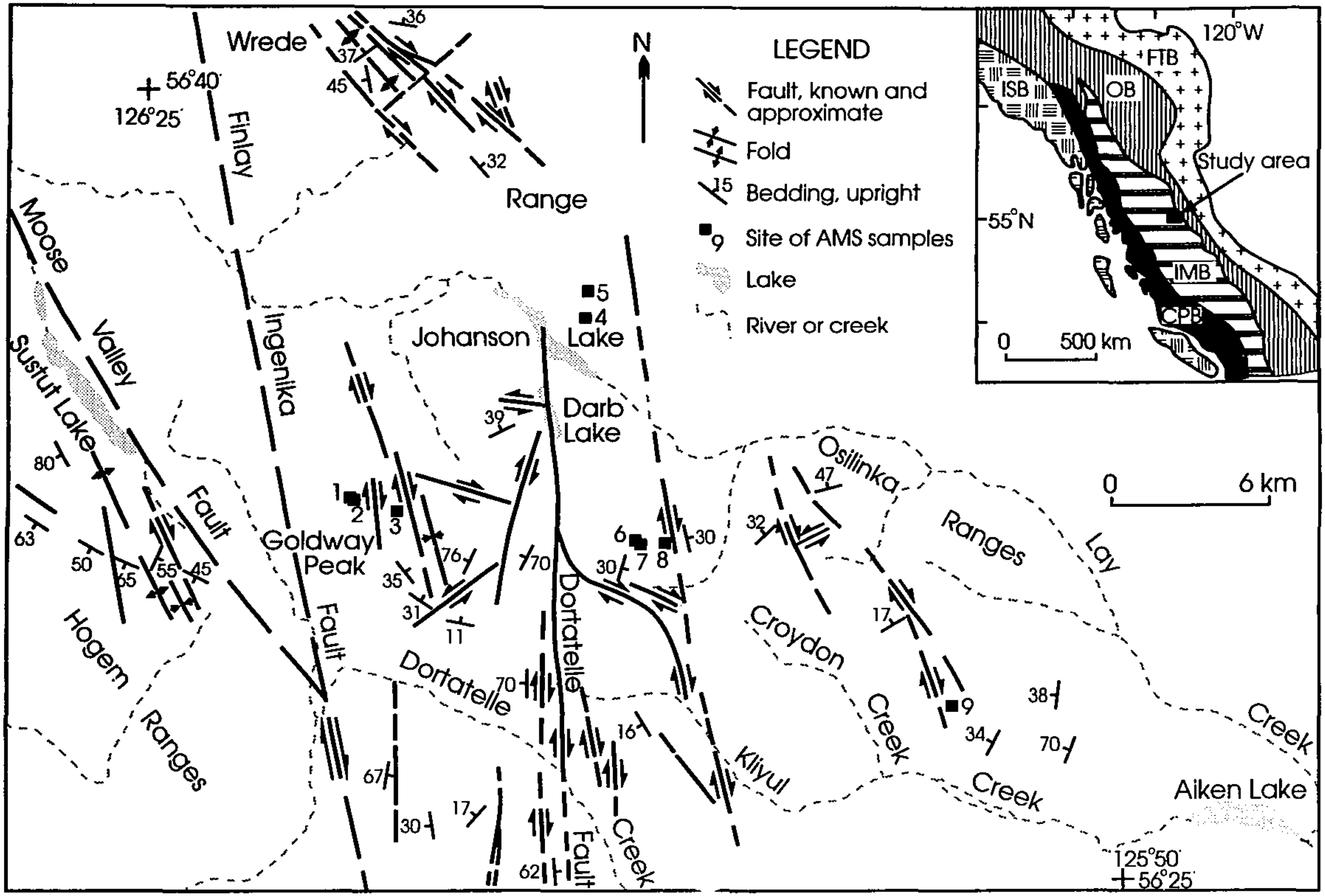
LEGEND
Fault, known and approximate
Fold
Bedding, upright
Site of AMS samples
Lake
River or creek
N
56°40'
126°25'
Wrede
Finlay
Range
Moose
Valley
Sustut Lake
Ingenika
Johanson
Lake
Darb
Lake
Fault
Goldway
Peak
Osilinka
Ranges
Lay
Hogem
Ranges
Dortatelle
Dortatelle
Fault
Creek
Croydon
Creek
Creek
Kliyul
Creek
Aiken Lake
0
6 km
125°50'
56°25'
120°W
FTB
ISB
OB
Study area
55°N
IMB
CPB
0
500 km

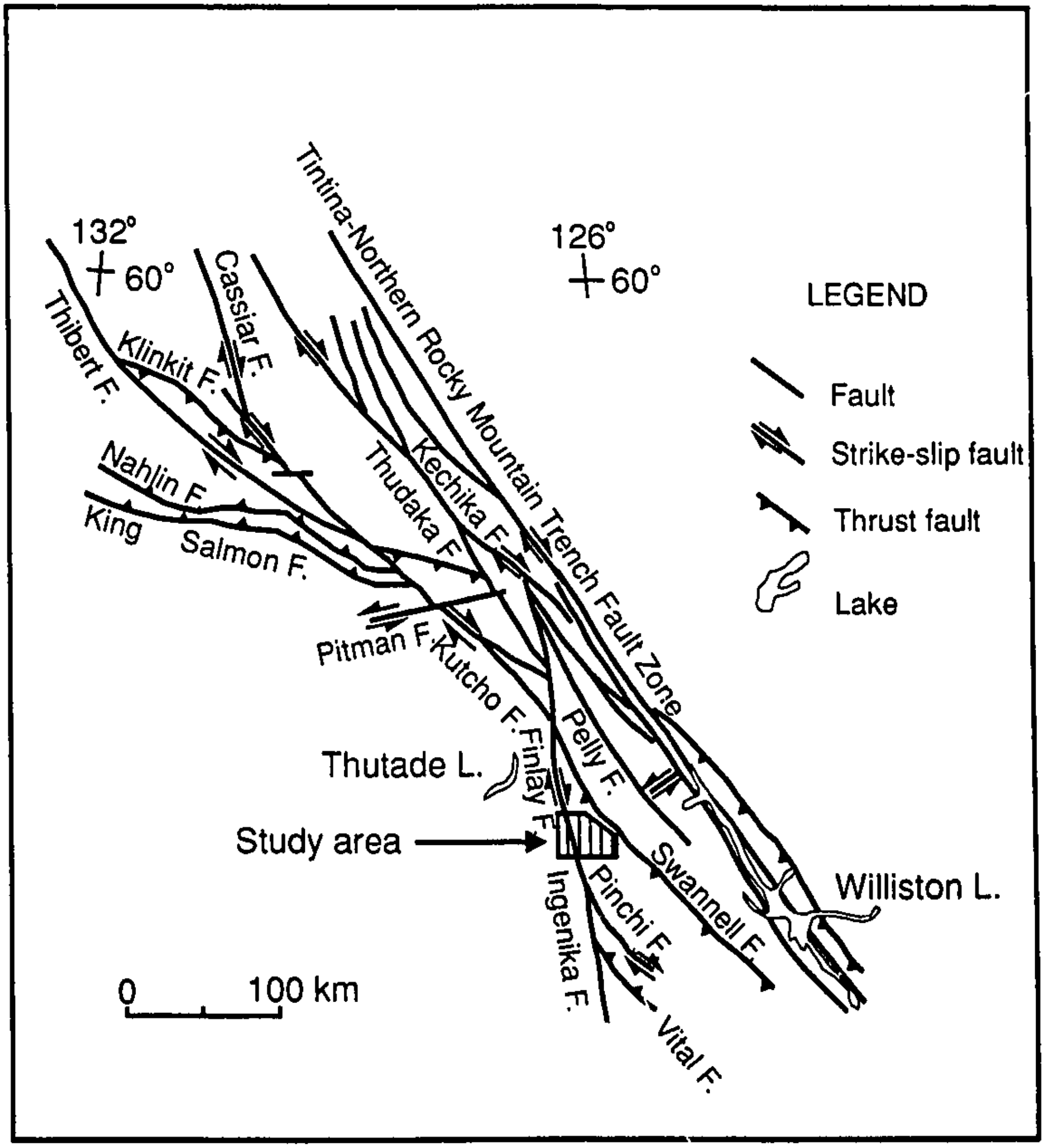

Fig.1.2 Generalized regional structural map showing location of the study area (after Gabrielse, 1985).

(Lord, 1948; Church, 1974, 1975; Richards, 1976a, b; Monger, 1977; Monger and Church, 1977). The lower Dewar Formation is characterized by reddish weathering, dark grey to black, locally graphitic and pyritic argillite with lenses of dark grey marly limestone, interbedded with pale grey volcanic sandstone and siltstone at the top. The middle Savage Mountain Formation consists of submarine, massive volcanic breccia and pillow lava with minor volcanic siltstone at the top. It contains dark grey, reddish grey and dark purple clinopyroxene and clinopyroxene-plagioclase porphyries, and locally conspicuous, coarse-grained, "bladed" feldspar porphyry. The upper Moose Valley Formation is dominated by reddish marine and nonmarine volcaniclastic rocks (Monger, 1977; Monger and Church, 1977) but is not exposed in the study area.

East of the Finlay-Ingenika fault (Quesnellia) the Takla Group remains undivided (Monger, 1977) and is predominantly volcaniclastic. Stratigraphic successions and rock assemblages, however, vary from one locality to another and are described in detail by Zhang and Hynes (1991, 1992). The stratigraphic successions east of the Finlay-Ingenika fault lithologically resemble those of the Dewar and Savage Mountain Formations west of the fault in the study area although no conclusive stratigraphic correlations have been made between the Takla Group rocks on either side of the fault. The Takla Group rocks east of the fault are extensively intruded by multi-phase, Early Jurassic to Cretaceous dioritic rocks (Woodsworth, 1976; Monger, 1977).

1.3 FOLDING

Rocks in the study area experienced deformation predominantly, and perhaps exclusively, associated with the dextral, transpression along the Finlay-Ingenika fault. This deformation is characterized by subvertical to vertical, mainly north-northwest-trending faults. There are also some large-scale, open to medium folds with axes trending northwest to north-northwest (Fig. 1.1).

Four large-scale folds, the Wrede Range anticline, Goldway Peak syncline and Sustut Lake anticline and syncline, dominate the map (Fig. 1.1). They form an approximately northwest-trending fold zone in the western part of the study area. Poles to bedding planes from the Sustut Lake anticline and syncline delineate a cylindrical fold with an axis trending 122° and plunging 41° (Fig. 1.3a). The interlimb angle estimated from the bedding planes on both limbs distant from the fold closure is about 90°. The folds are truncated by north-northwest trending faults (Fig. 1.1), and strata adjacent to the faults are steepened. In contrast, the fold axis of Wrede Range anticline trends northwesterly and plunges shallowly, as shown by the intersection of axial cleavage and bedding planes (Fig. 1.3b). In cross-section, the folds are open to medium and approximately symmetrical, having no preferred verging directions. Such a geometry implies that they were probably developed as a result of northeast-southwest shortening, perhaps accompanied by northwest-southeast extension since the fold axis is normal to

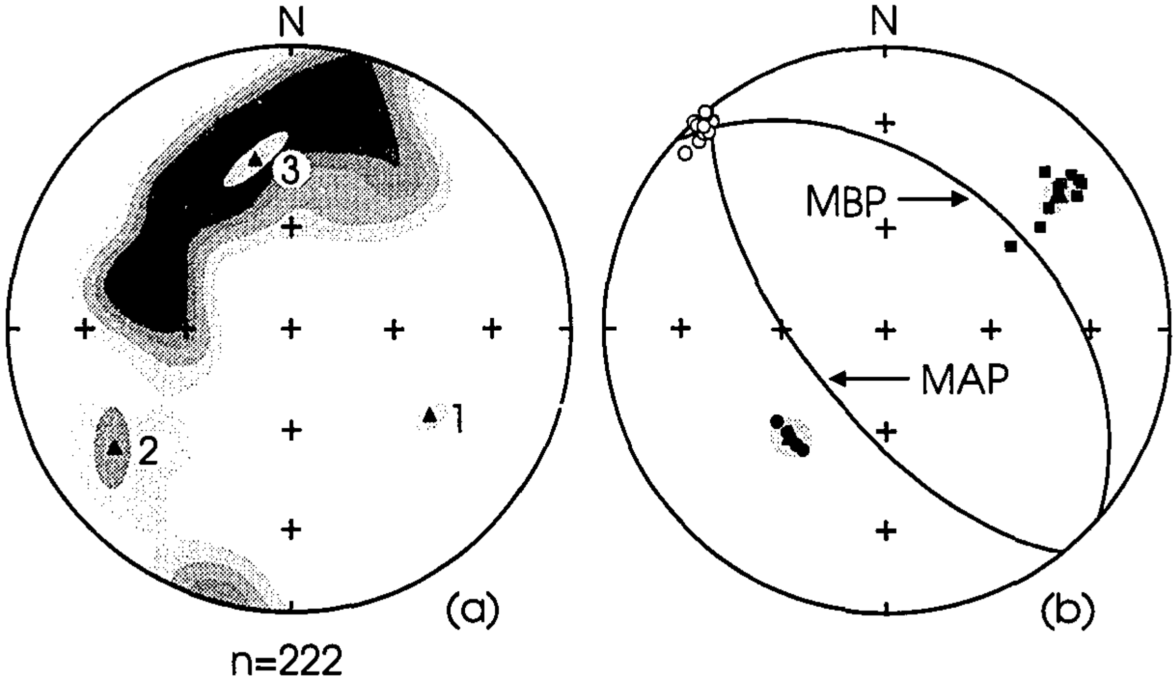

Fig. 1.3 Attitudes of major folds in the region. (a) Bedding in the Hogem Ranges. Contouring in this and all subsequent figures uses Gaussian weighting function after Robin and Jowett (1986). The lowest contour level is E=3σ, and contours are in increments of 2σ thereafter, where σ is the statistical dispersion of the data. Solid triangles are minimum (1), intermediate (2) and maximum (3) eigenvectors of poles to bedding, respectively. Fold axis was determined from the minimum eigenvector and shaded ellipses are 95% confidence ellipses. Unless otherwise noted, confidence limits were determined assuming a Bingham distribution (cf. Bingham, 1974; see Zhang *et al.*, submitted for more details). n: number of bedding measurements. (b) Poles to bedding (solid circles), poles to axial cleavage (solid squares) and poles to extensional joints (open circles) in the Wrede Ranges. Solid triangles: maximum eigenvectors; MBP: mean bedding plane; MAP: mean fold axial plane. All structural projections in this paper are lower-hemisphere, equal area projections.

extensional ('a-c') joints (Fig. 1.3b). The folds are truncated in many places by strike-slip faults (Fig. 1.1).

Outcrop-scale folds are common in the well-bedded, thin-layered units, especially in the lower thin-layered limestones interbedded with volcanic siltstone west of Kliyul Creek. Folds observed near the hinge zone of the Goldway Peak syncline show either symmetrical box-type or chevron features, and others, west of Kliyul Creek and south of Darb Lake stock and west of the Moose Valley fault (Fig. 1.1), are asymmetrical. Some folds have axial surfaces at small ($<45^{\circ}$) angles to the bedding surfaces and are probably due to bedding-parallel slip, while others, generally several tens of centimetres in wavelength and entirely included in fragments of well-bedded limestone (e.g. those west of Kliyul Creek), are presumably synsedimentary slumping folds.

Timing of formation of the folds is uncertain. They predate the faults but may well have formed in the early stages of dextral transpression (cf. Wilcox *et al.*, 1973; Sylvester, 1988).

1.4 FAULTING

Subvertical or vertical strike-slip faults are the most widespread structural features in the study area. They are abundant along and near the Finlay-Ingenika fault, and become fewer and shorter away from it. On the ridges immediately west of Aiken Lake, for example (Fig. 1.1), they are rarely seen. This spatial relationship of the strike-slip faults to the Finlay-Ingenika fault suggests that deformation in the study area was associated closely with transcurrent motion on the Finlay-Ingenika fault and was largely restricted to a narrow belt, about 30 kilometres wide, adjacent to the major fault (Fig. 1.1).

Based on the attitudes and slip senses, the faults were divided into four groups: dextral strike-slip faults trending northwest, north-northwest and north-south, and sinistral strike-slip faults trending east-northeast. All the faults can be readily interpreted as resulting from dextral motion on the Finlay-Ingenika fault (Fig. 1.4). The attitudes and slip senses of north-south and east-northeast-trending fault sets are consistent with their formation as Riedel (R) and conjugate Riedel (R') shears, respectively, related to the main motion on the Finlay-Ingenika fault (cf. Tchalenko, 1970; Keller *et al.*, 1982; Sylvester, 1988). The northwest-trending faults generally display two stages of displacement. The earlier is dip-slip with a thrust sense, and the later is horizontal, dextral. The thrusts are thought to have developed in association with the initiation of dextral

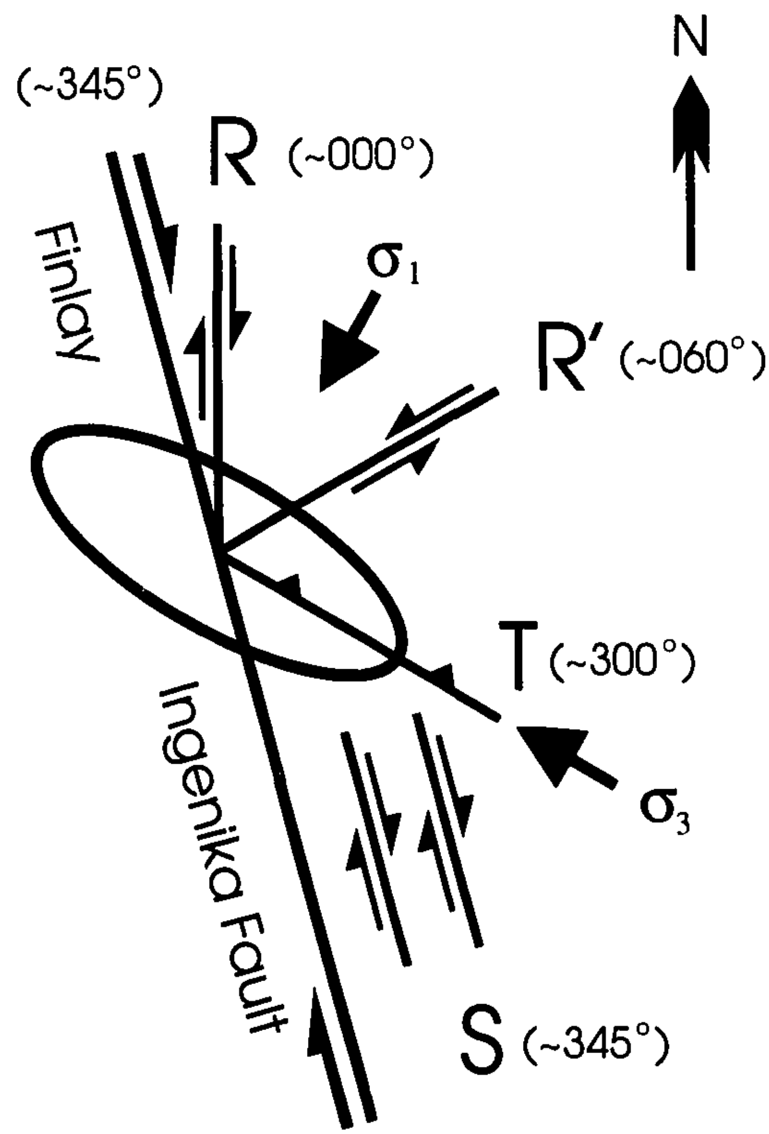

Fig. 1.4 Simplified diagram showing inferred relationship of the strike-slip faults in the study area to the stress field resulting from dextral displacement along the Finlay-Ingenika fault. Riedel (R) and conjugate Riedel (R') shears represent north-northeast trending dextral and east-northeast trending sinistral strike-slip faults, respectively; T represents northwest-trending thrust faults with superimposed dextral strike-slip; S represents north-northwest trending dextral strike-slip faults as secondary shears of the Finlay-Ingenika fault; σ_1 and σ_3 are the local principal stresses.

displacement on the Finlay-Ingenika fault (cf. Sylvester, 1988) with the dextral, strike-slip motion superimposed once the faults were fully established. Faults in the north-northwest-trending group are parallel to, and have the same slip senses as, the Finlay-Ingenika fault. They are inferred to have formed as secondary shears of the Finlay-Ingenika fault. At several localities, for example south of Darb Lake and north of Dortatelle Creek, dioritic dykes are incorporated in mylonitic zones associated with the faults (Plate 1.1), indicating that fault motions occurred after emplacement of the extensive dioritic plutons in the study area. Along the fault zones, rocks are strongly deformed and sheared into protomylonite to mylonite with a variety of kinematic indicators and fabrics, by which slip senses on the faults were determined.

1.4.1 Kinematic Indicators

S-C mylonites (Berthé *et al.*, 1979; Lister and Snoke, 1984; Shimamoto, 1989) occur in most of the faults, especially where they pass through the greenish grey clinopyroxene or clinopyroxene-plagioclase porphyries or volcanic breccias. They provide one of the most useful kinematic indicators in the study area. The C-surfaces are predominantly closely spaced displacement discontinuities or zones of relatively high shear strain, while the S-surfaces are characterized by alignment of phyllosilicate minerals such as chlorite, or bands of calcite, which replaced clinopyroxene (Plate 1.2). Intersections of the mean S- and C-surfaces are always

Plate 1.1 Deformed dioritic dike north of Dortatelle Creek. Pencil is parallel to the foliation, looking south-southwest down.

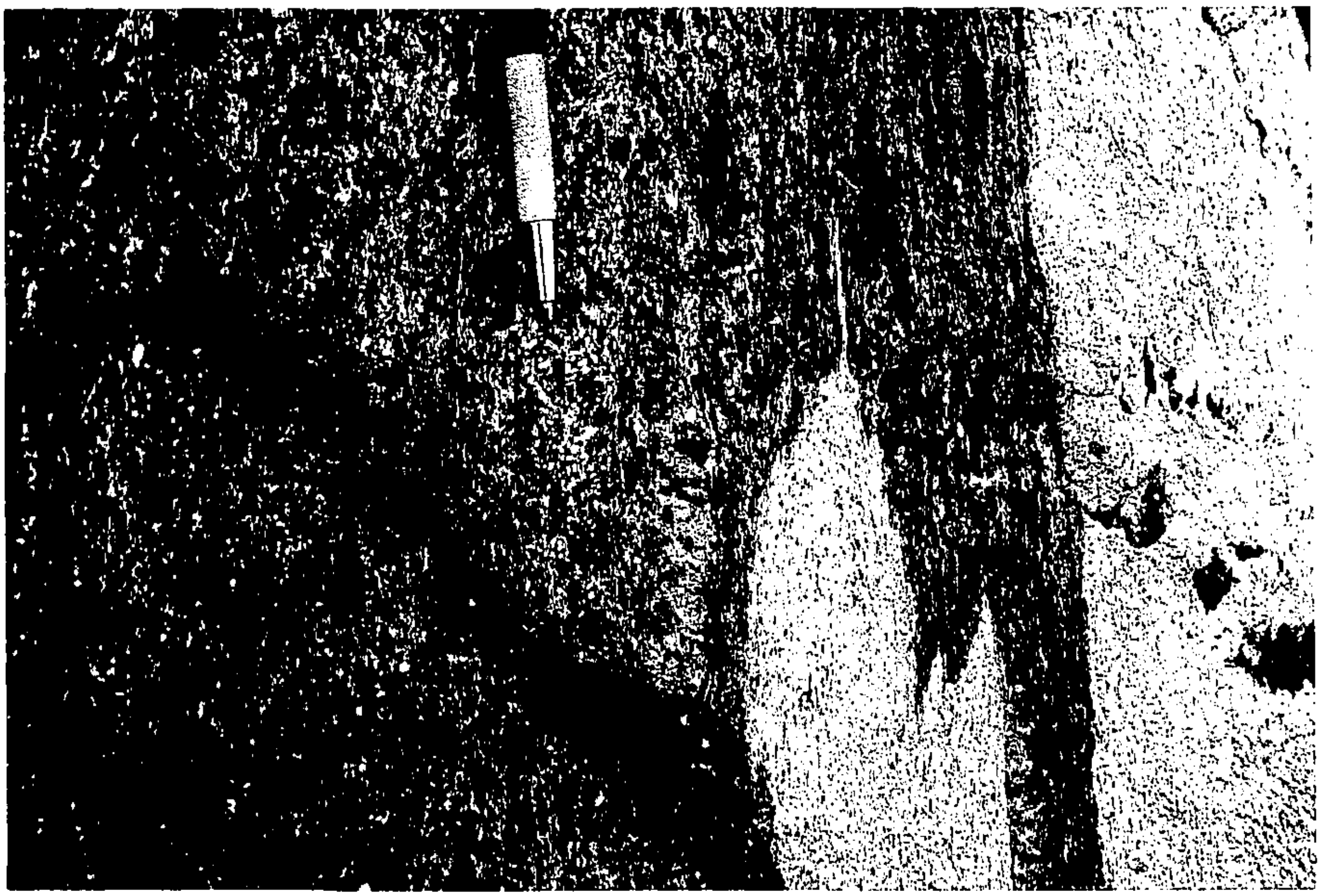

Plate 1.2 S-C fabric of the mylonitic rocks in Dortatelle fault. Pencil is parallel to the C-surface, looking south down.

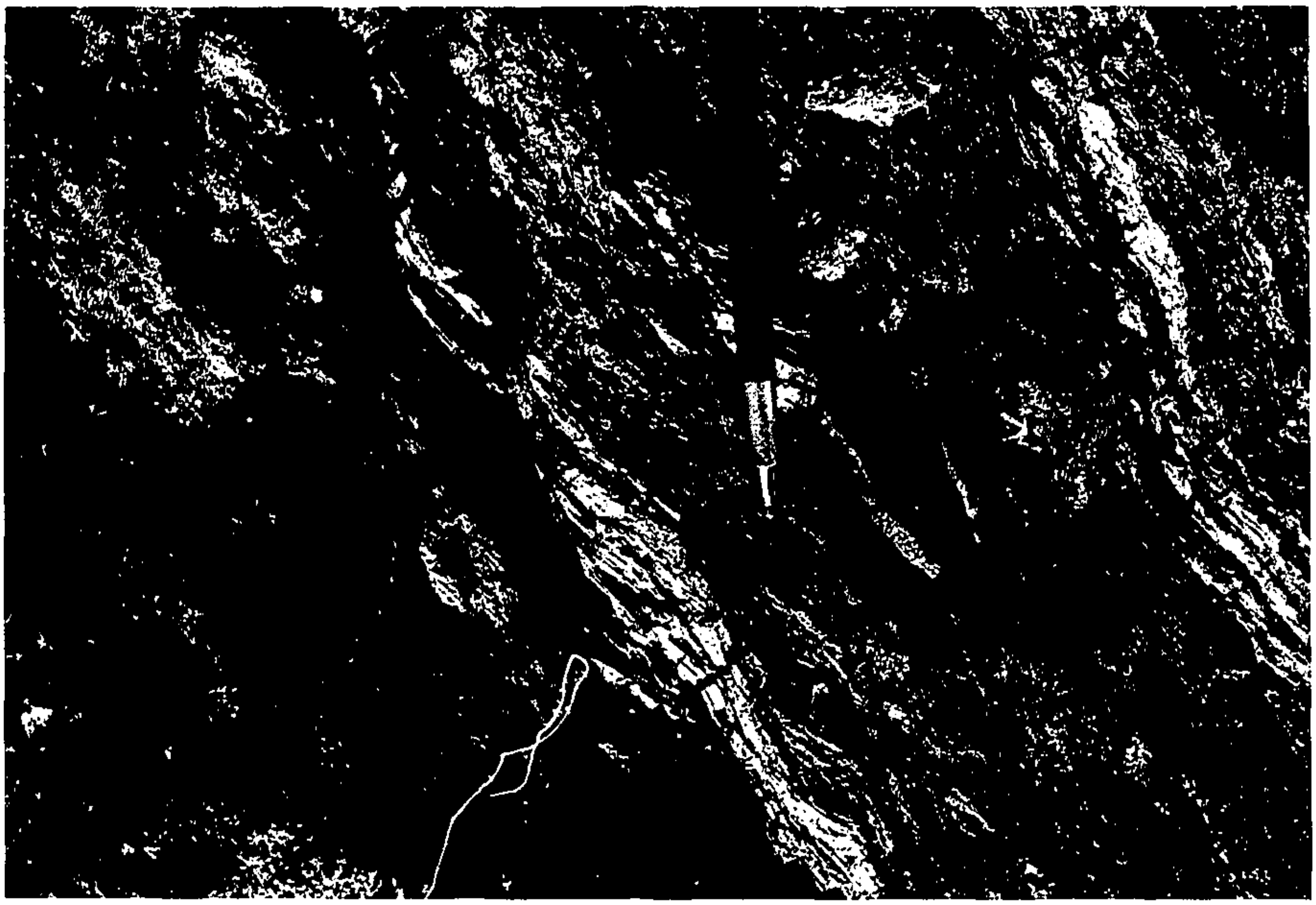

subvertical to vertical (e.g. Figs. 1.5a and b). Fault attitudes inferred from the intersections and surface traces of the faults show steep dips with shallow predicted slip directions (e.g. Figs. 1.5a and b) suggesting that dextral, strike-slip displacement was predominant along the faults. In some cases, the C-surface is parallel to the fault plane, for example in the fault east of Goldway Peak (Fig. 1.5b) whereas in others, it makes a small angle (generally less than 30°) with the fault plane; for example the angle between the C-surface and plane of Dortatelle fault (Fig. 1.1) is about 24° (Fig. 1.5a) indicating that the C-surface may have developed as a Riedel shear to the fault. Angles between S- and C-surfaces vary from about 40° (in slightly deformed domains) to 10° or less (in strongly deformed domains).

Drag folds are common features in some highly strained rocks along the strike-slip fault zones. They are small asymmetric folds which deform the mylonitic foliation (Plate 1.3), and their asymmetry confirms the sense of shear deduced from other indicators. Fold amplitude ranges from less than 1 centimetre to about half a metre with an interlimb angle generally less than 60°. Fold axial planes are generally vertical, and hinges are vertically plunging too. This geometry suggests that they may have developed from steeply dipping mylonites associated with initiation of the strike-slip faulting. Such folds in the Dortatelle fault zone, for example, are tight and asymmetrical, ranging in wavelength from less than 1 centimetre to several tens of centimetres. Mean axial plane of the folds strikes 324° and dips 89° southwest, with mean fold axis trending 318° and plunging 75°

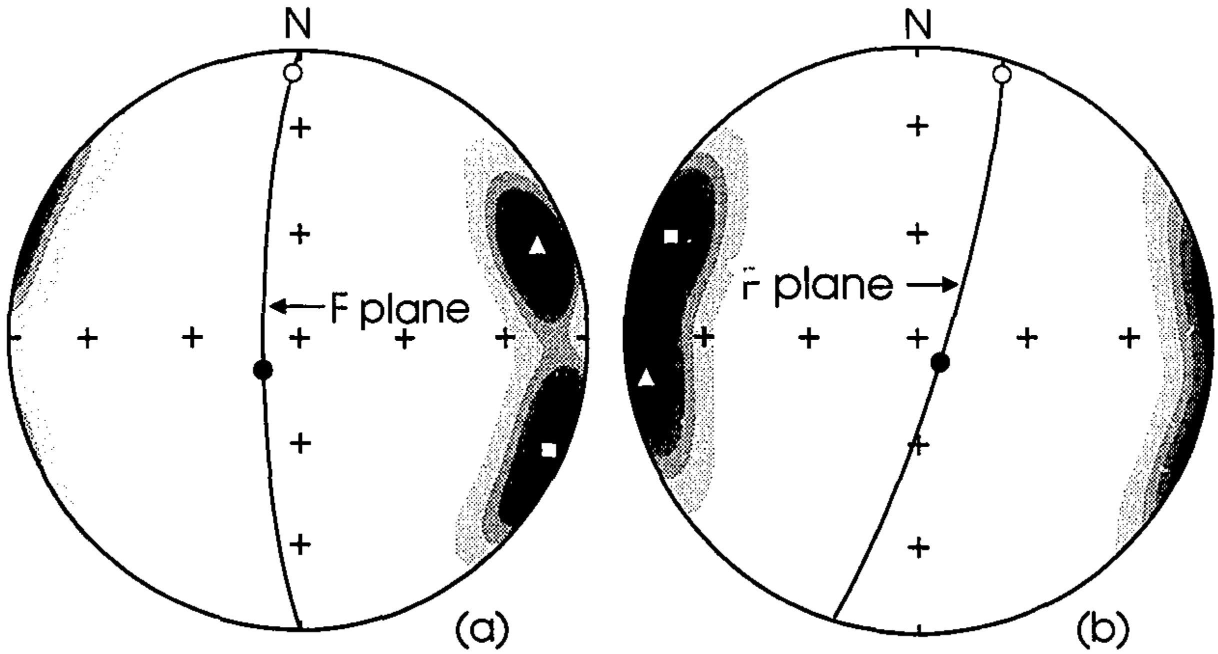

n_c=172
n_s=166

n_c=100
n_s=100

Fig. 1.5 Stereographic plot of S-C fabrics. (a) from Dortatelle fault and (b) from the fault east of Goldway Peak. Contour interval is 8σ; open square and triangle: mean poles to the C- and S-surfaces, respectively, determined by the maximum eigenvectors and with semiaxes of 95% confidence ellipses (not shown) less than 2°; solid circle: intersection of the mean C- and S-surfaces; open circle: predicted slip direction; F plane: predicted fault plane; n_c: number of C-surfaces; n_s: number of S-surfaces.

Plate 1.3 Asymmetrical drag folds developed in the mylonite of Dortatellel fault. Division of the scale bar on the left side is in centimetres, looking west down.

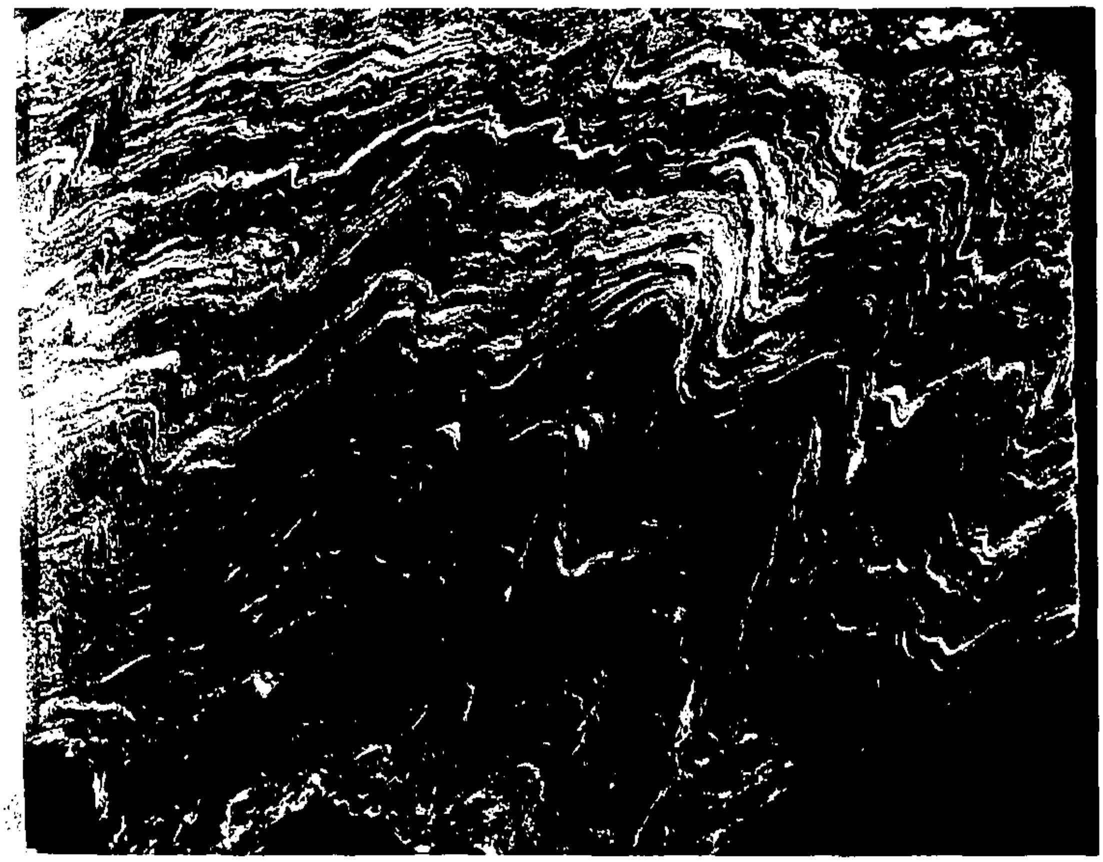

(Fig. 1.6), and has an angle of 36° to the fault plane. This geometry is consistent with that of the S-C surfaces and indicative of dextral strike-slip.

Extensional fissures are present along the strike-slip faults. They are commonly filled with fibrous tremolite or calcite that grew either perpendicular or sub-perpendicular to the walls (Plate 1.4), especially where they cut volcanic breccias or porphyries. Typical relationships are exhibited in the north-northwest trending fault on the ridge west of Aiken Lake. Here, slickenfibers marked by fibrous crystals of calcite on the fault plane display a dextral strike-slip sense, and extensional fissures filled with calcite fibers are thicker close to the fault surface and become thinner away from it. Using the attitudes of the fissures, combined with the assumptions that they developed normal to the maximum principal initial incremental strain (X) (cf. Ramsay and Huber, 1983) and that the strain reflects simple shear due to motion on the observed fault plane, it is clear (Fig. 1.7) that the intermediate principal incremental strain (Y), which is determined by the intersection of the fault plane and mean extensional fissure plane, is approximately perpendicular to the measured slickenline (the angle between them on the fault plane is 88°). The slickenlines and extensional fissures are therefore in excellent agreement with dextral strike-slip on the fault. Furthermore, the Fisher's mean (Fisher, 1953) of poles to the fissures is displaced from the maximum principal incremental strain (X), which lies in the X-Z plane and is 45° to the fault plane (Fig. 1.7), indicative of clockwise mechanical rotation of the fissures during progressive

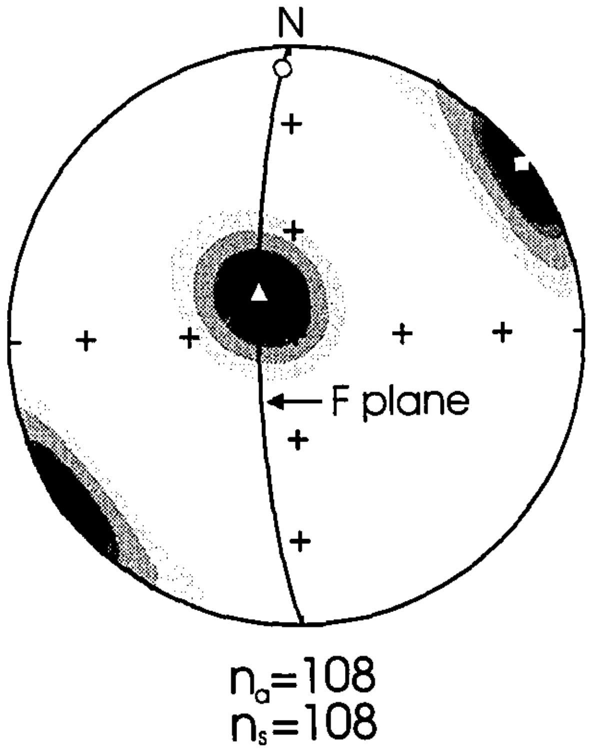

Fig. 1.6 Stereographic plot of drag folds of Dortatelle fault. Contour interval is 6σ; open triangle and square: mean fold axis and mean pole to the fold axial surfaces, respectively, determined by the maximum eigenvectors and with semiaxes of 95% confidence ellipses (not shown) less than 2.5°; open circle: predicted slip direction; F plane: predicted fault plane; n_a: number of fold axes; n_s: number of axial surfaces.

Plate 1.4 Extensional fissure filled with fibrous calcite crystals along the northwest trending fault west of Aiken Lake. Pencil is parallel to the fissure plane and fault plane is approximately parallel to the bottom edge of the photo, looking southwest down.

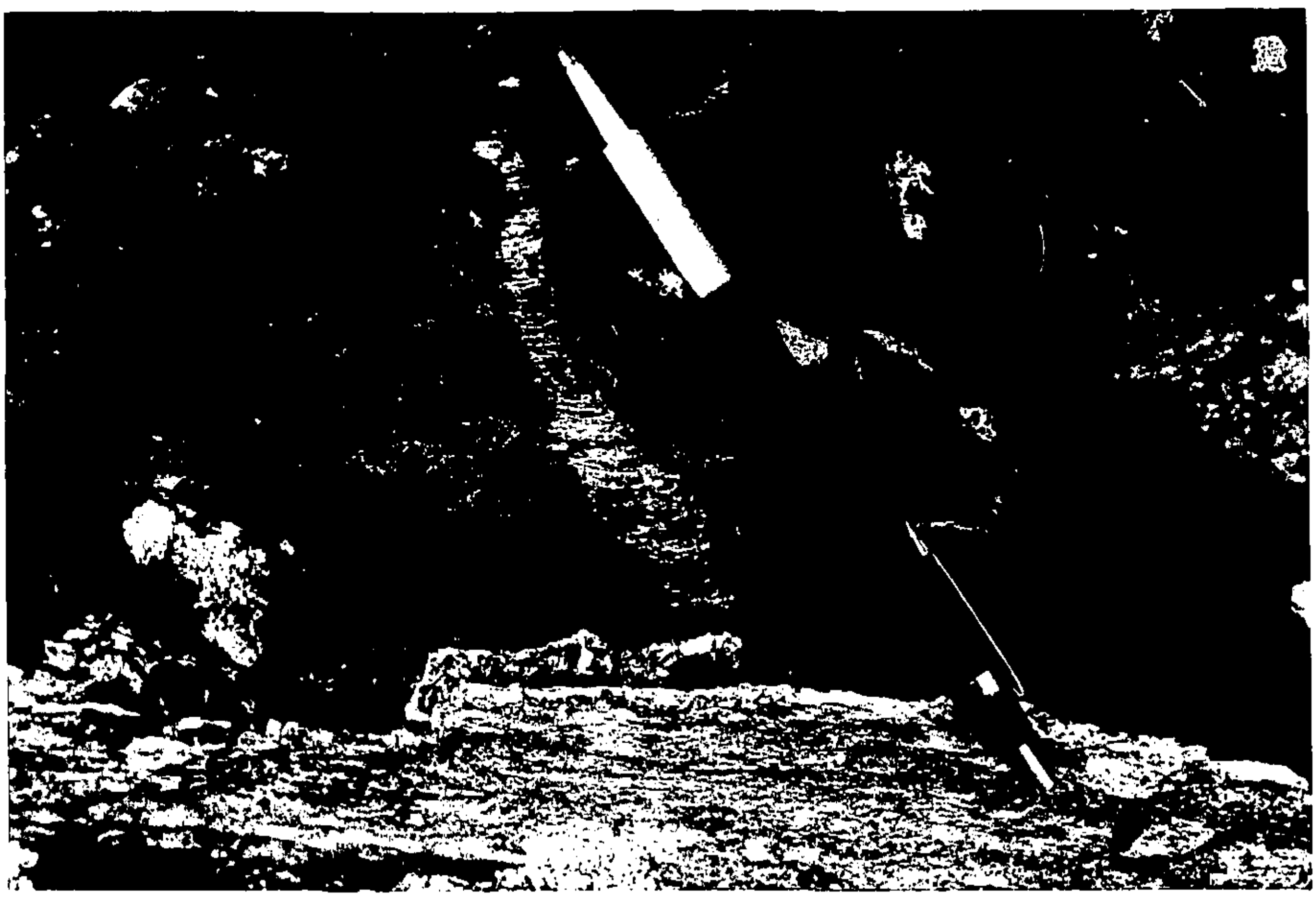

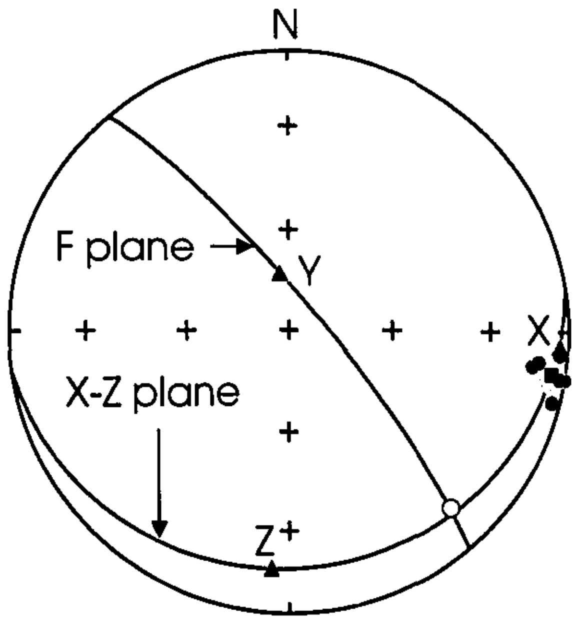

Fig. 1.7 Stereographic plot of structural data from the northwest-trending fault on the ridge west of Aiken Lake. Solid circles: poles to extensional fissure planes; solid triangles: maximum (X), intermediate (Y) and minimum (Z) initial incremental principal strains; open circle: measured slickenline; solid square: pole to the mean extensional fissure plane; shaded ellipse: 95% confidence circle (cf. Fisher, 1954); F plane: the fault plane; X-Z plane: the principal plane normal to the intermediate principal strain (Y).

straining (cf. Ramsay and Huber, 1983).

Numerous other indicators of slip sense abound in the strained rocks of the fault zones and are found from the thin-section to outcrop scale. Microscopic asymmetric buckle folds, the vorticity of rigid inclusions, local transpressive rotational structures (Zhang and Hynes, 1991) and the facing of fiber steps (roughness directions) on slickensides all provide supporting evidence for the senses and directions of motions on the faults.

1.4.2 Foliation and Lineation

Apart from the above major kinematic indicators, other fabrics such as lineations and foliations are well developed in some strongly deformed fault zones.

Here we focus only on the penetrative stretching lineations, including elongated minerals and fragments of volcanic breccia, in some strongly deformed fault zones. There are two types of mineral lineation in the study area: inferred primary and secondary. Primary mineral lineations occur only in the clinopyroxene or clinopyroxene-plagioclase porphyries, and were observed at two localities on the ridges between Dortatelle and Kliyul Creeks. They are due to the alignment of prismatic crystals of clinopyroxene and hornblende (Zhang and Hynes, 1992). No evidence of intracrystalline deformation has been found although some mineral grains are partially or entirely replaced by chlorite or epidote, which may have obscured such evidence. In its absence these lineations are tentatively attributed to primary processes. The secondary mineral lineations are characterized by stretched mineral grains, now predominantly chlorite (Plates 1.5 and 1.6) and are confined to fault zones, especially in the north-northwest trending faults on the ridges between the Dortatelle and Kliyul Creeks (Fig. 1.1). The minerals are commonly stretched subhorizontally into ribbons, up to several centimetres long (Plate 1.5), while on vertical sections they exhibit subrounded shape (Plate 1.6), defining a typical L fabric. The stretching lineations truncate the contacts between clinopyroxene-plagioclase porphyry and volcanic breccia, and minerals in different clasts of the breccia being stretched are aligned in the same direction, indicative of their deformational origin.

Lineations defined by elongated fragments of volcanic breccia are conspicuous rock fabrics in the north-northwest trending fault west of Kliyul Creek (Fig. 1.1). As for the mineral lineations, the fragments are elongated in a subhorizontal plane (Plate 1.7) and show subrounded shape in a vertical section. The orientation of the lineation was determined using Lowe's method (Lowe, 1946), in which the apparent lineation and the plane in which it is observed are combined to provide a plane in which the lineation must lie. The mean stretching lineation is subhorizontal, with azimuth 313° and plunge 13° (Fig. 1.8a). The angle between the stretching lineation and the Bingham's mean (Bingham, 1974) of

Plate 1.5 Stretching lineation of chlorite mineral grains in the north-northwest trending faults east of Dortatelle Creek. The scale bar on the left side is in centimetres, looking northwest down.

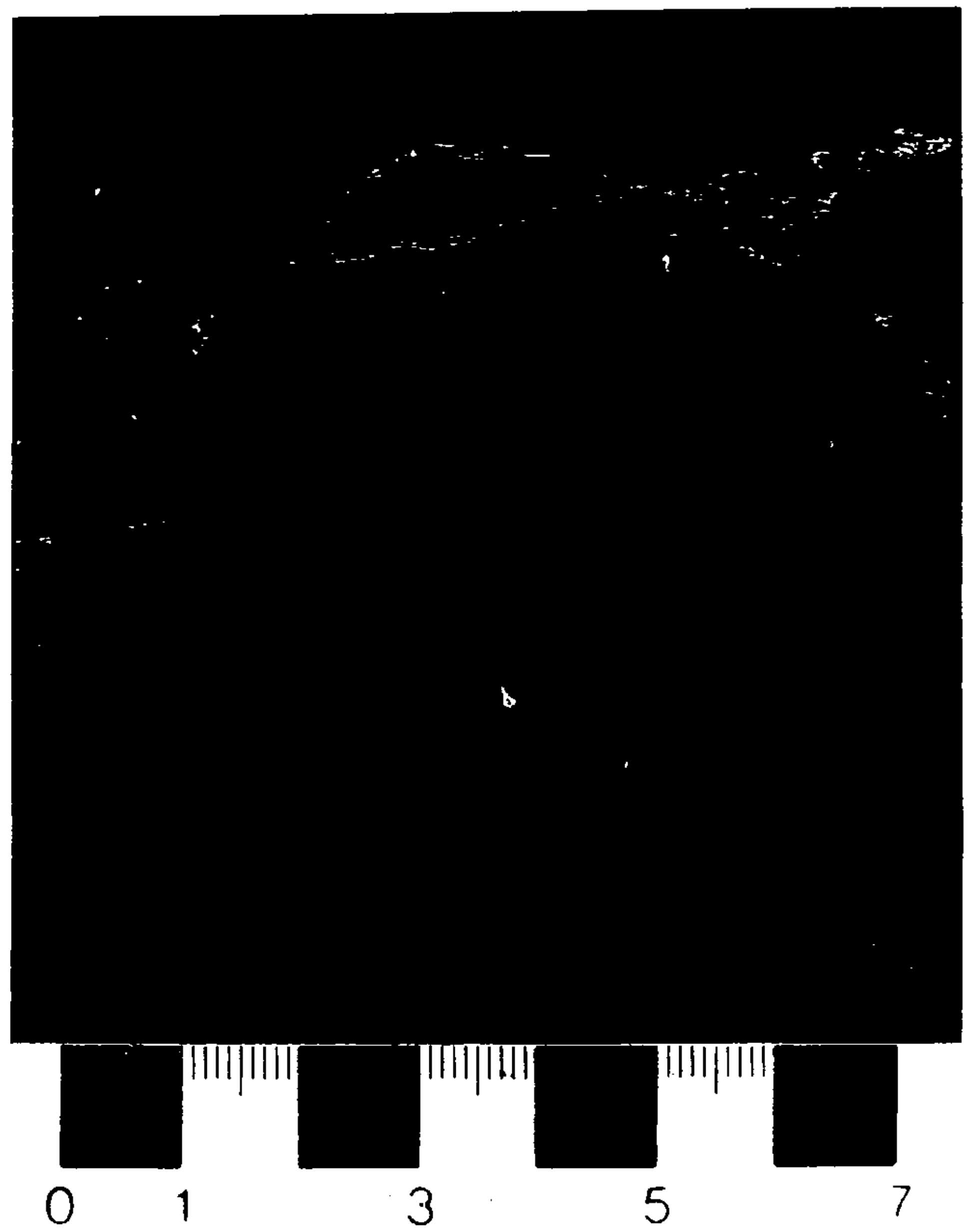
0
1
3
5
7

Plate 1.6 Cross-sectional view of the stretching lineation of Plate 1.5.

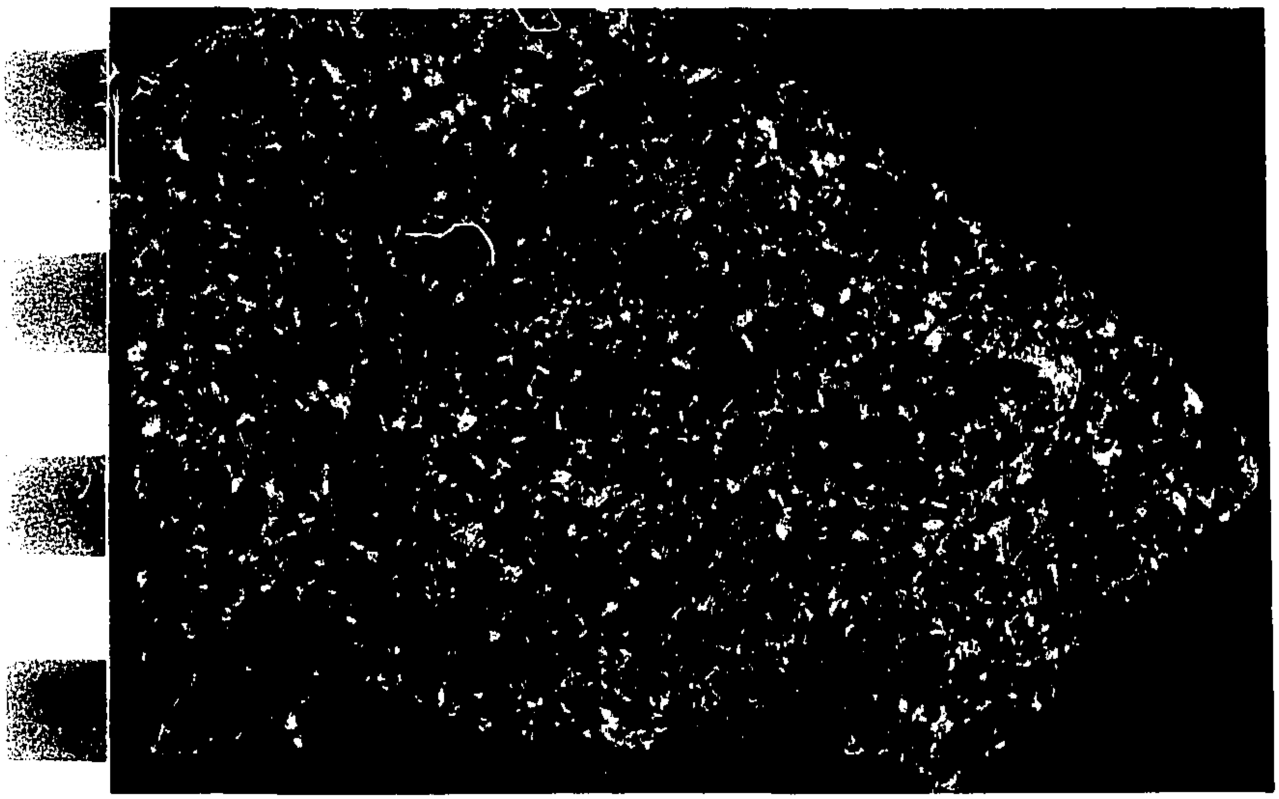

Plate 1.7 Stretching lineation of volcanic fragments in the north-northwest trending fault west of Kliyul Creek. Pencil is parallel to the lineation, looking west-southwest down.

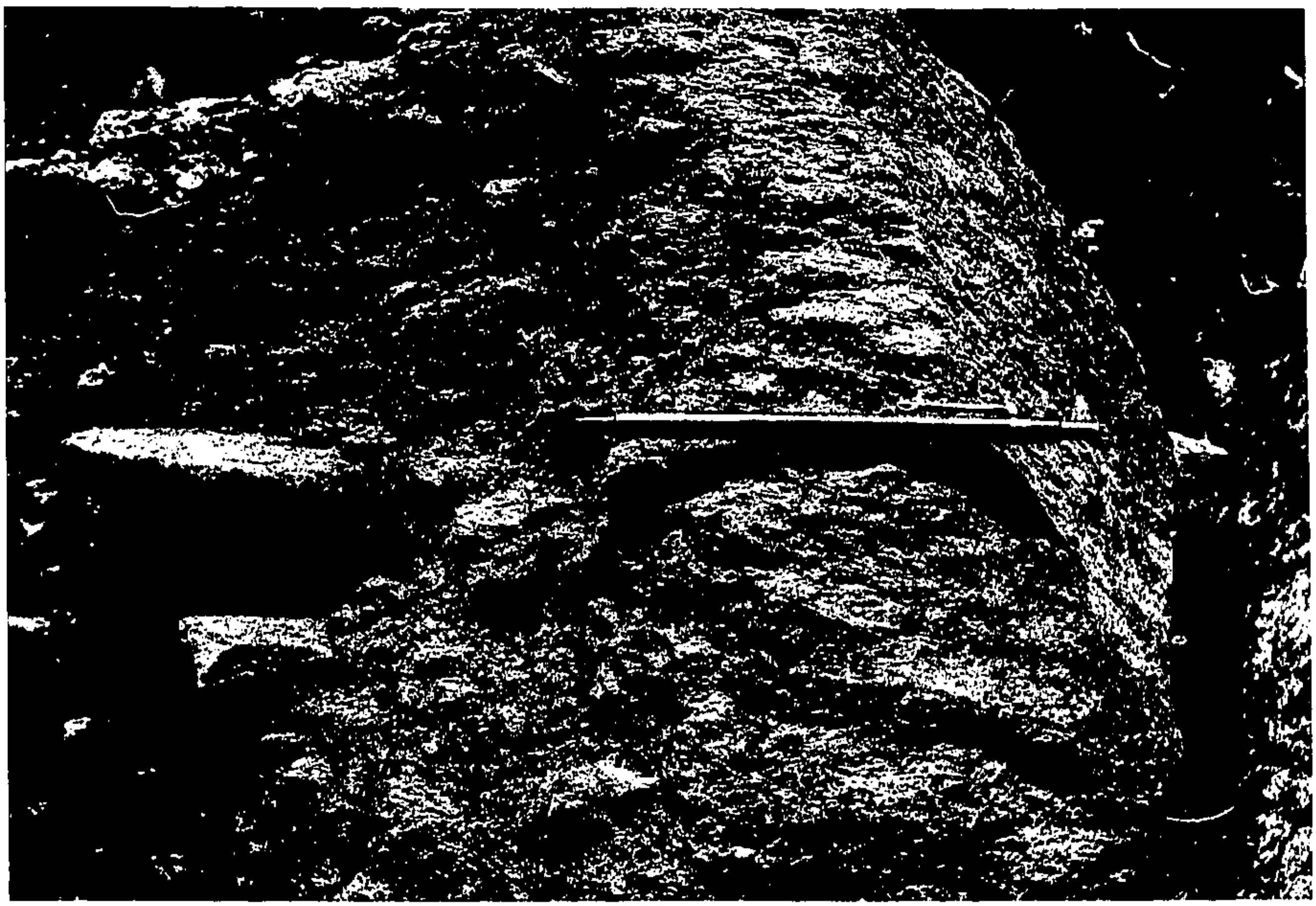

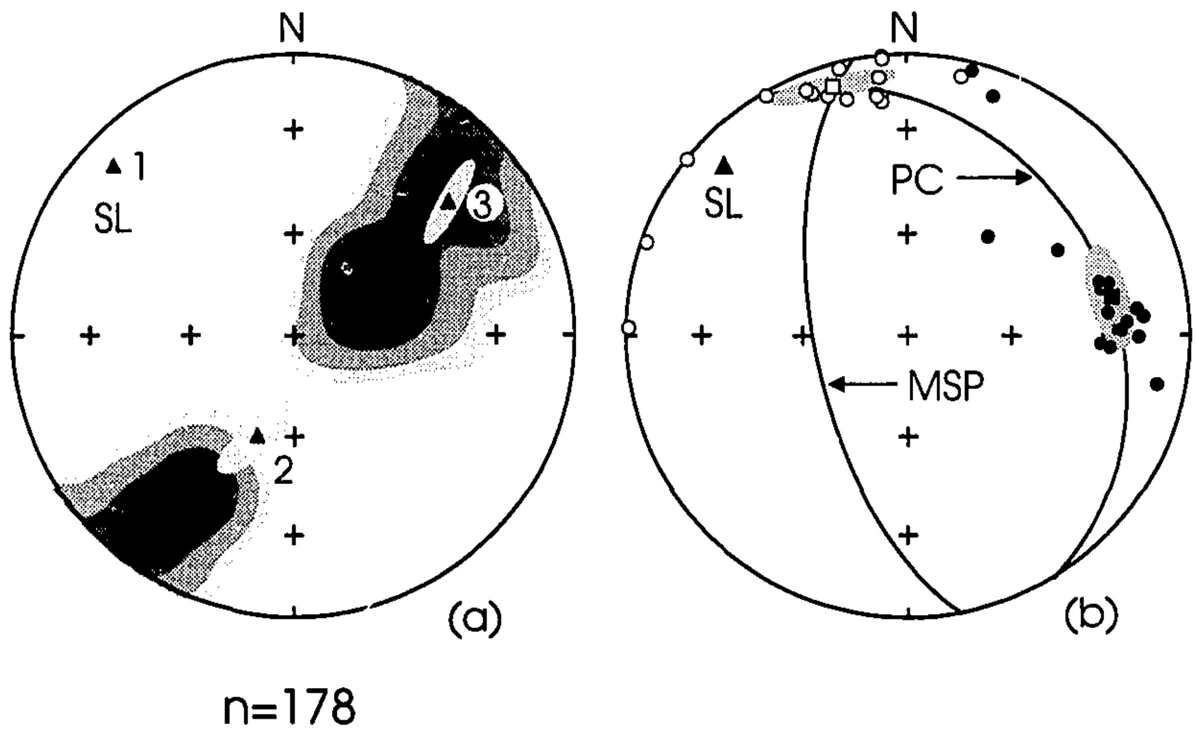

Fig. 1.8 Secondary lineation in the Kliyul Creek area. (a) Poles to the planes in which the lineation lies. Contour interval: same as in Fig. 1.3; solid triangles: minimum (1), intermediate (2) and maximum (3) eigenvectors, respectively, with their 95% confidence ellipses; SL: mean stretching lineation; n: number of planes. (b) Poles to shear planes (solid circles) and slickenlines (open circles). Solid and open squares: mean pole to the shear planes and mean slickenline determined by the maximum eigenvectors with their 95% confidence ellipses (cf. Bingham, 1974) respectively; MSP: mean shear plane; PC: plane common to mean slickenline and mean pole to the shear planes.

minor shear planes occurring within, and subparallel to, the fault zone is 21° and the geometric configuration is compatible with dextral strike-slip. The stretching lineation does not lie in the plane that is common to the mean observed slickenlines and poles to the minor shear planes (Fig. 1.8b) as would be anticipated for simple shear deformation, which presumably reflects a non-plane character to the strain associated with the shearing. Other lineations such as slickenlines and slickenfibers marked by fibers of calcite or tremolite are seen everywhere along the strike-slip faults or subvertical small-scale shear surfaces in the area. All these surficial lineations are consistently subhorizontal to horizontal (Fig. 1.9) in conformity to the interpretation that strike-slip faulting was the dominant mode of deformation in the area.

Foliations are widespread, even in the absence of C-surfaces. They presumably resulted from local shortening, perhaps accompanied by mechanical rotation, due to displacements on the strike-slip faults. They are characterized by parallel alignment of either phyllosilicate minerals (e.g. chlorite or biotite) or deformed fragments of volcanic breccia. The latter are discussed in detail in the following section. The foliations are steeply dipping with a maximum stretching direction approximately horizontal, forming an L-S fabric, and are confined to the fault zones. The foliations always make a small angle, generally less than 45°, with the fault planes. The angles between foliation and fault surfaces become progressively smaller approaching the fault surface. It is therefore likely that

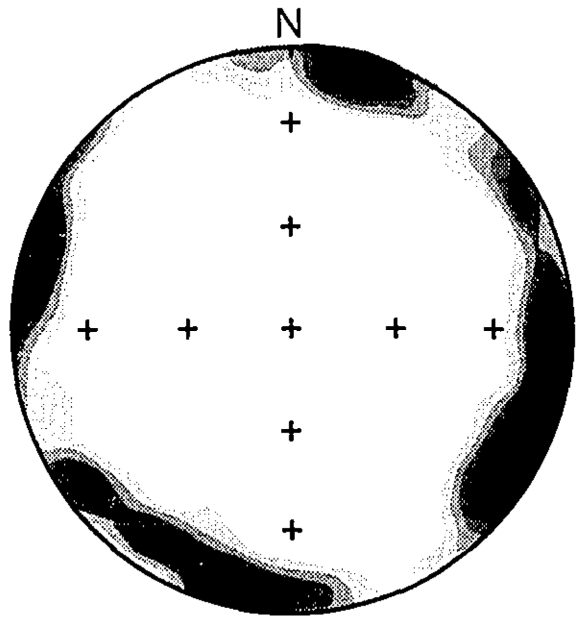

Fig. 1.9 Stereographic plot of the slickenlines from strike-slip faults and minor shear planes. Contour interval: same as in Fig. 1.3; n: number of slickenlines.

mechanical rotation of the foliations after their formation, during progessive displacement along the faults, was important.

1.4.3 Strain in Deformed Volcanic Fragments

Progressive development of foliation due to straining of volcanic breccia fragments is well exhibited in an area of about one square kilometres, bounded to the west by a dextral strike-slip fault trending approximately 350° and dipping 75° northeast, immediately north of Goldway Peak (Fig. 1.1). Strained volcanic fragments, which consist mainly of greenish grey clinopyroxene and clinopyroxene-plagioclase porphyries, commonly in a porphyritic matrix with the same composition as the fragments, are clearly displayed on a variety of sections of different orientations. The observed aspect ratios of the strained fragments on arbitrarily oriented sections are denoted by X'/Z' (where X' $\geq$ Z') since most of the sections on which the strained fragments appear may not be parallel to the principal planes of the strain ellipsoid. According to the apparent aspect ratios and degree of development of the foliations, the area has been divided into three domains in the direction normal to the strike of the north-northwest trending fault. Domain 1 is about 600 metres wide and lies in the east, about 300 metres from the fault. Domain 2 is about 200 metres wide, extending from Domain 1 to within about 100 metres of the fault, and Domain 3 is directly adjacent to and within the fault zone.

In Domain 1, fragments of clinopyroxene and clinopyroxene-plagioclase porphyry, in which phenocrysts of euhedral clinopyroxene and wispy plagioclase are relatively fresh, undeformed and randomly distributed, are only slightly strained (Plate 1.8). Passing westwards into Domain 2 the strain is demonstrably more intense, giving rise to a marked increase in the apparent aspect ratios of the strained fragments (Plate 1.9) and the local development of foliation. Other evidence which supports the tectonic straining is the deformation of a mafic dyke (Plate 1.10), which locally truncates the strained fragments. The dike is cut by conjugate shear planes, with shear senses in accord with those resulting from shortening normal to the foliation plane in the volcanic breccia. The shear planes stop at the contact of the dike and volcanic breccia, and instead foliation is developed in the breccia (Plate 1.10). The contrast of structural styles may reflect mechanical contrast of the dike and volcanic breccia. In Domain 3, within and immediately adjacent to the fault, fragments are very strongly deformed (Plate 1.11), and foliation is extensive and penetrative where the phenocrysts of euhedral clinopyroxene have been completely replaced by chlorite and calcite. The straining of the fragments is attributed to the local deformation resulting from dextral displacement along the fault to the west of Domain 3 because the apparent aspect ratios of the strained fragments increase progressively from Domain 1 to Domain 3 and the fragments show undeformed subrounded shapes east of Domain 1.

Poles to foliation planes from Domains 1, 2 and 3 have unipolar,

Plate 1.8 Deformed volcanic fragments in Domain 1 along the north-northwest trending fault north of Goldway Peak; looking northeast down.

34

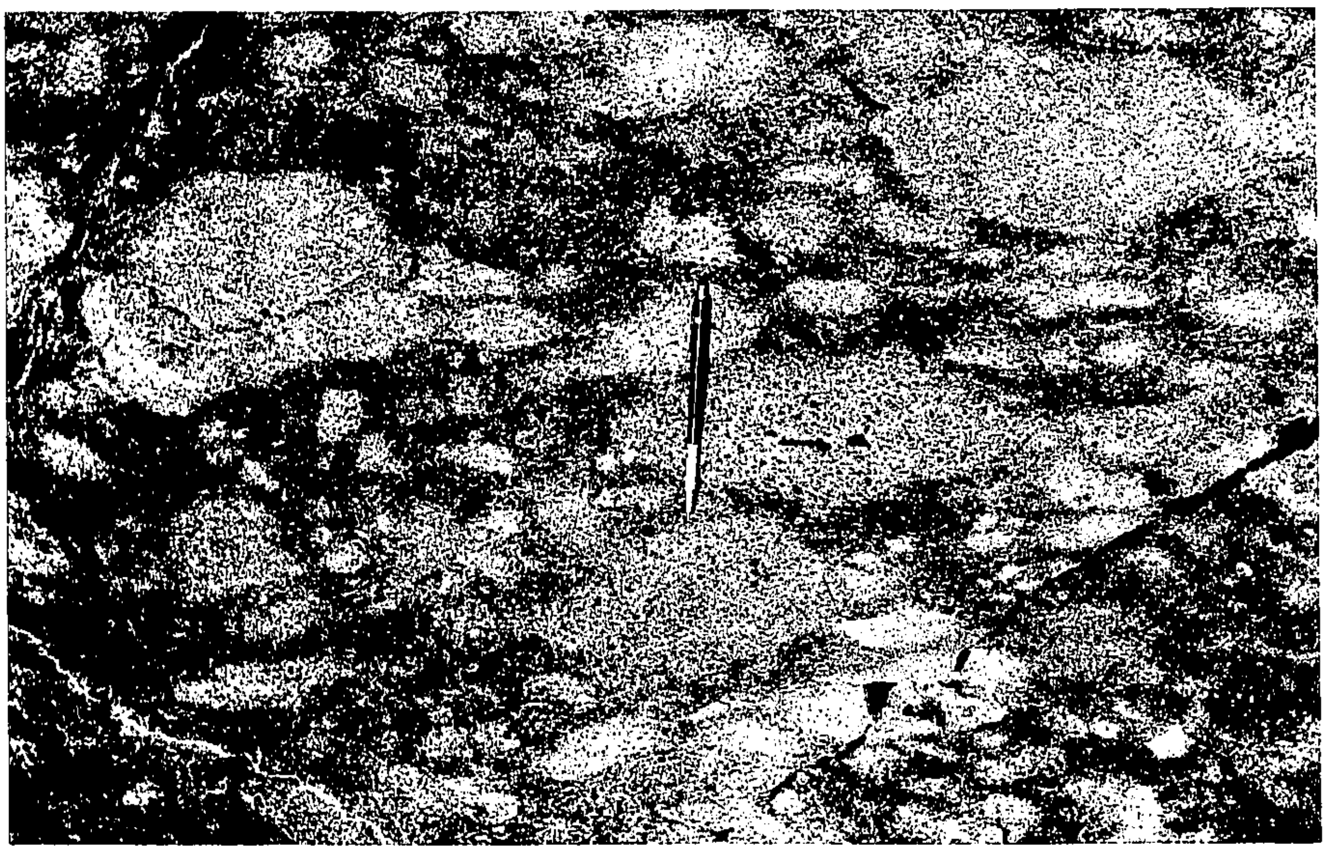

Plate 1.9 Deformed volcanic fragments in Domain 2; looking northwest down.

Plate 1.10 Deformed mafic dike in Domain 2; pencil parallel to one of the conjugate shear planes, looking northwest.

Plate 1.11 Deformed volcanic fragments in Domain 3; looking northeast down.

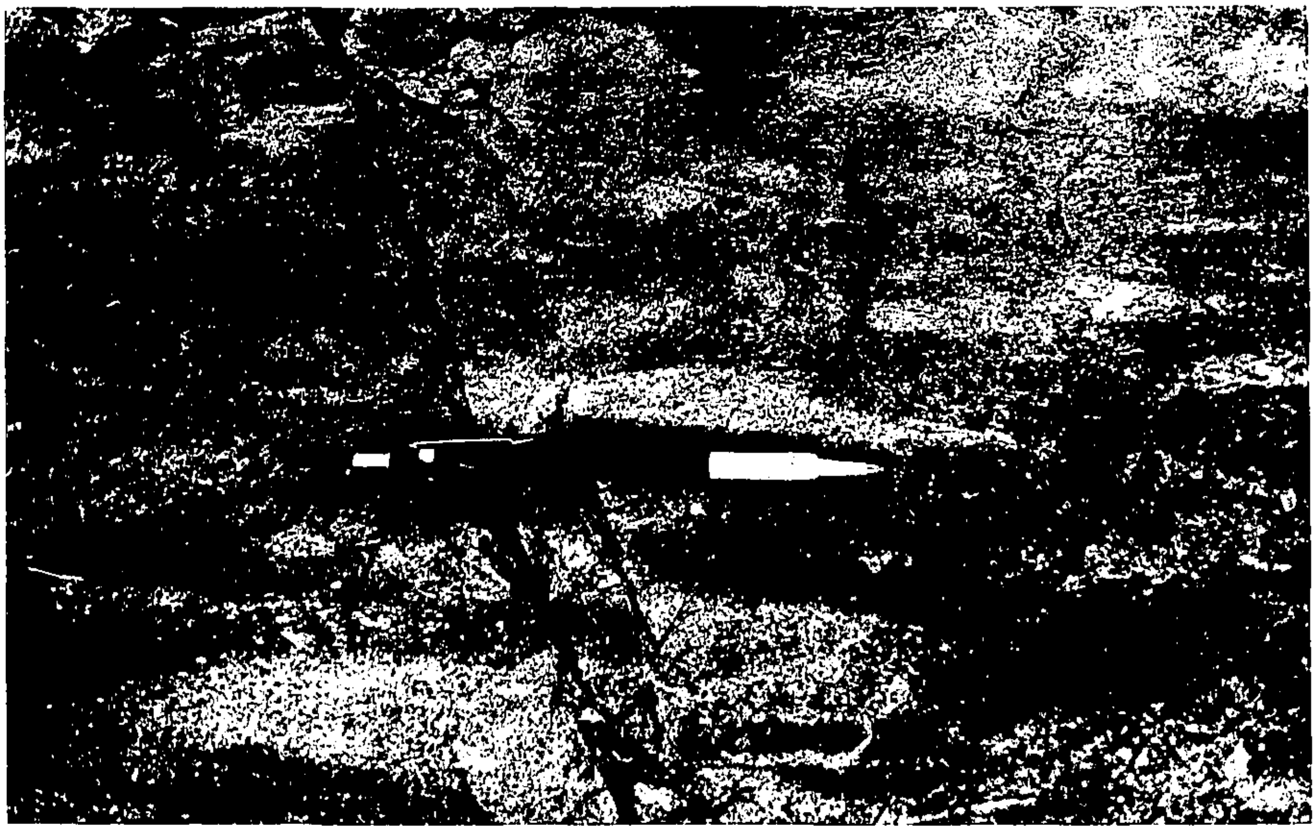

approximately axially symmetrical distributions (Figs. 1.10a, b and c); hence Fisher's statistics (Fisher, 1953) have been used to calculate the mean plane for each domain. The domain-mean directions of the foliation planes are apparently consistent (Fig. 1.10d). A multisample test for the three mean directions (Mardia, 1972) gave a result of $F = 1.59 < F_{\alpha} = 2.43$, where F and F_{α} are the observed and upper 5% values of $F_{(4,254)}$, respectively, and therefore the null hypothesis that the three samples are drawn from the same population is accepted (Mardia, 1972). In other words, statistically the domain-mean directions are not significantly different from each other. The domains-mean foliation plane strikes 335° and dips 72° northeast, making an angle of about 15° with the fault plane to the west of Domain 3.

More than 700 strained volcanic fragments have been measured on 60 sections of different attitudes in the three domains (Fig. 1.11). The apparent aspect ratios (X'/Z') vary between 1.59 and 16.70. This variation may arise from both the change from Domain 1 to 3 (Fig. 1.11) and the variation in section orientation. Because a variety of sections that cut randomly across the strain ellipsoids have been observed and measured, it is possible to determine the three-dimensional shapes of strain ellipsoids in the different domains. In order to determine the strain ratio in two dimensions, several techniques have been proposed (see Ramsay, 1967; Robin, 1977; Fry, 1979; Ramsay and Huber, 1983). In this paper, however, we use a least-squares best-fit technique to calculate the

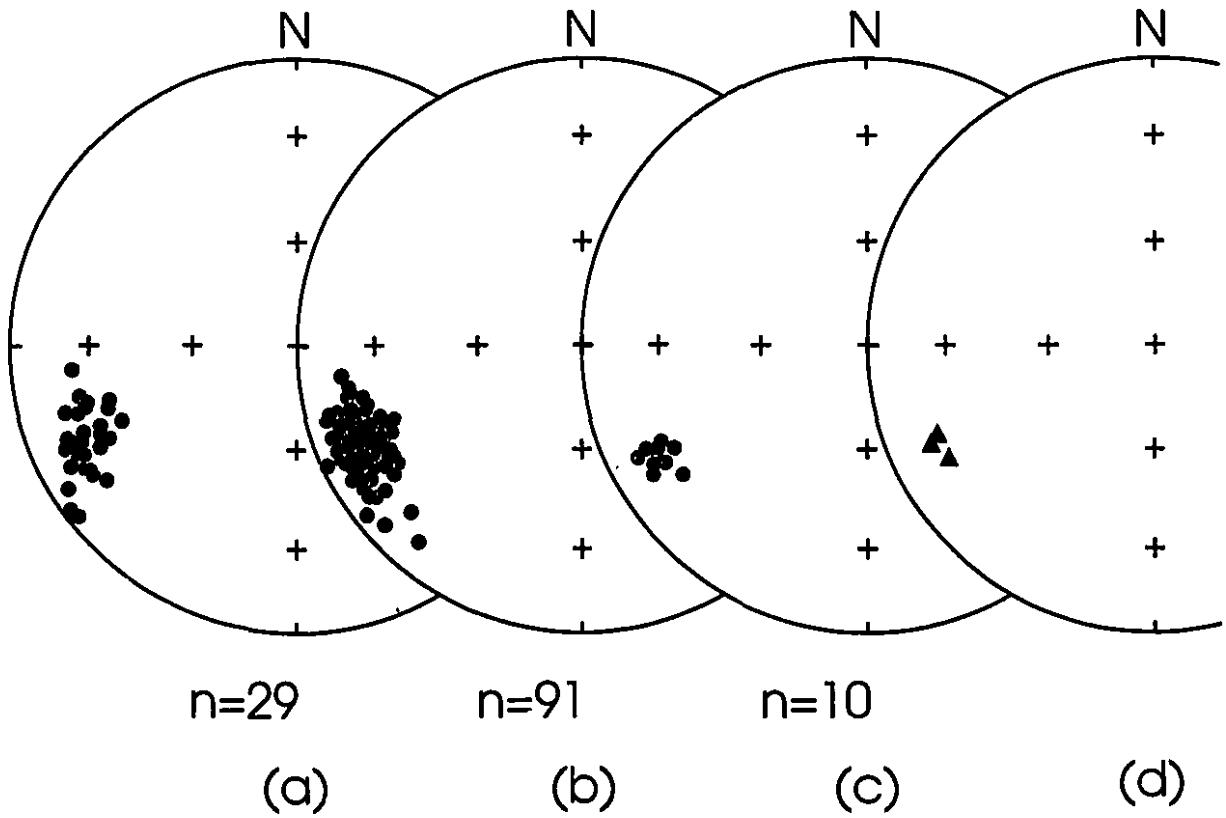

Fig. 1.10 Stereographic plot of poles to foliation planes in the deformed volcanic fragments. (a): Domain 1; (b) Domain 2; (c): Domain 3; (d): domain means; n: number of planes.

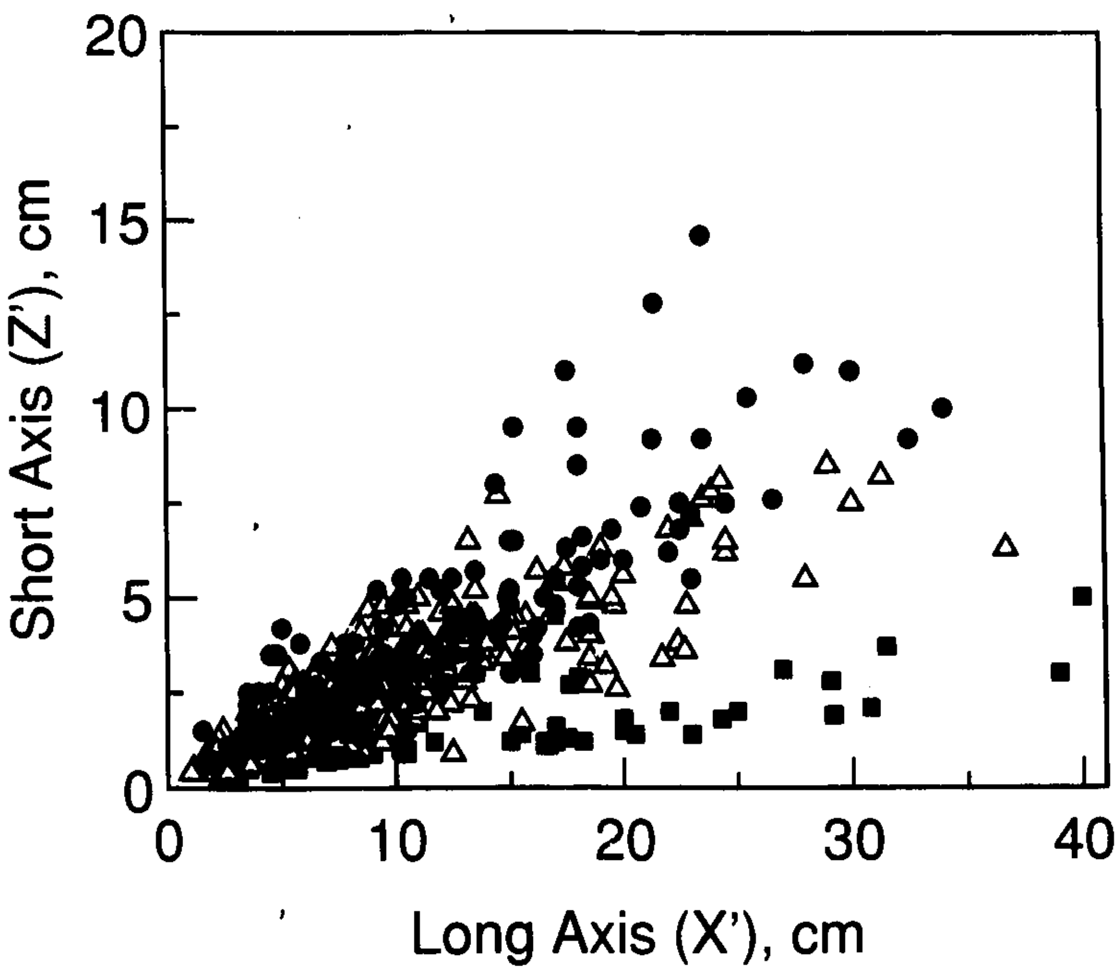

Fig. 1.11 Diagram of deformed volcanic fragments. Solid circles, open triangles and solid squares: from Domains 1, 2 and 3, respectively.

mean X'/Z' ratio for each section because typically the datum points fall approximately on straight lines through the origin of the X'-Z' plots (e.g. Fig. 1.12). The slope of the best-fit line is used to estimate the mean ratio for a specific section. All sections have high linear correlation coefficients except for one section (less than 0.5) from Domain 3 (see Appendix 1), which was not used in further analysis.

Variation of the mean X'/Z' ratios within a single domain is caused mainly by the change in section orientation, although there is also probably a continuous change in bulk strain-ratio across each domain as well. In the analysis that follows, the sections in each domain are treated as if all sampled the same bulk strain ellipsoid. Theoretically, in order to determine principal axes of the strain ellipsoid, the magnitudes and directions of principal axes of the strain ellipses in three non-parallel sections are required (Ramsay and Huber, 1983). So that we could make use of all our structural data, however, we used a least-squares best-fit ellipse technique (Erslev and Ge, 1990) in each of three mutually orthogonal sections. This technique provides statistical constraints on the orientations and eccentricity of the ellipse in each section.

First, the strain ellipses in the different sections were sequentially standardized with respect to each other by setting their radii as equal along their line of intersection. The standardized ellipses were then used to calculate

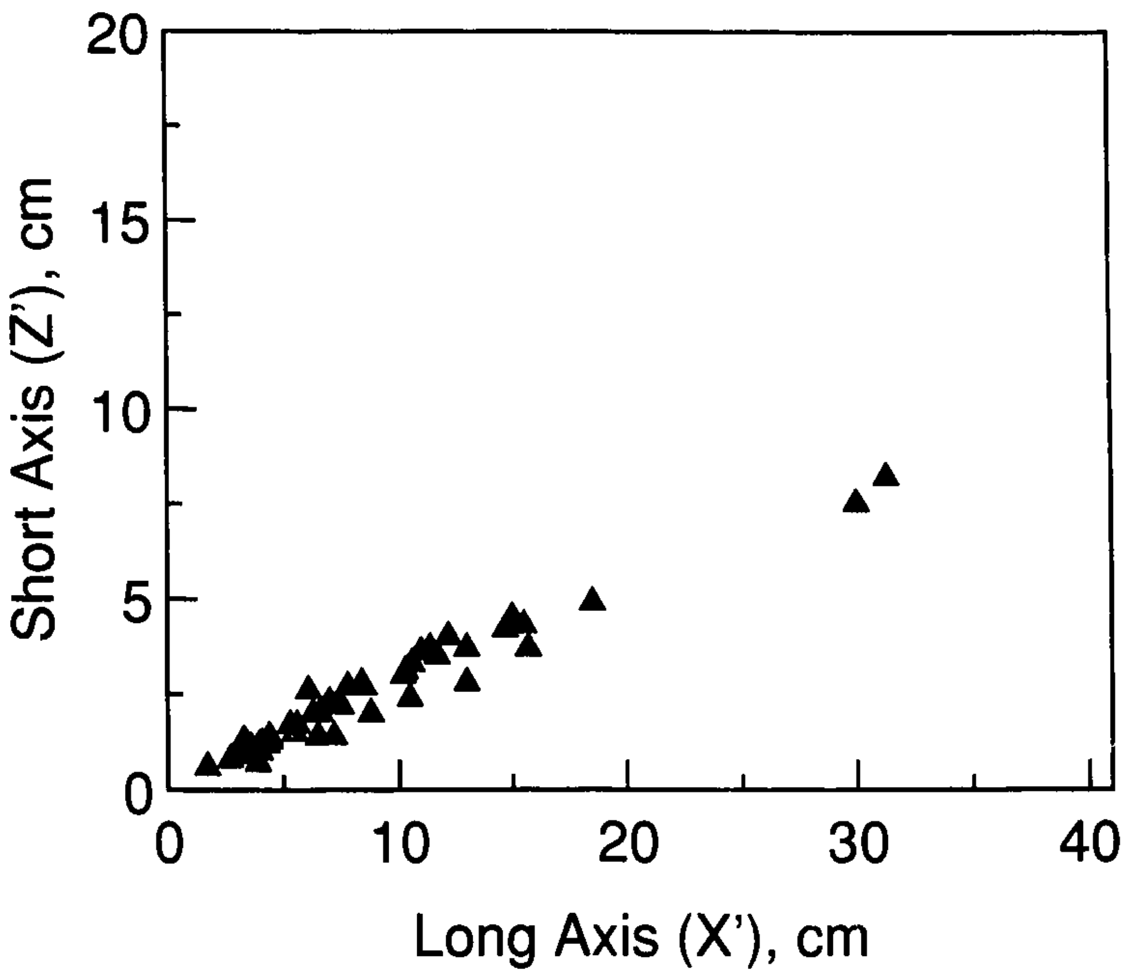

Fig. 1.12 Plot of deformed volcanic fragments from a single section in Domain 2.

longitudinal strains on horizontal, east-west vertical and north-south vertical planes. Each ellipse provides one longitudinal strain value in each plane, but is presented as two points at either end of the ellipse 'diameter' in each plane (Fig. 1.13-1.15). In the ideal case, in which all fragments in each domain had the same eccentricity, this analysis should provide three perfect ellipses in the three planes for each domain. Only two data sets, from Domains 1 and 3 (see Appendix 1), respectively, depart significantly from this condition and were not used in further analysis. Secondly, the least-squares best-fit ellipses for each of the three planes of Figures 1.13 to 1.15 were used to calculate the magnitudes and directions of principal axes of the strain ellipse. Finally, components of the deformation tensor $\mathbf{B}^{-1}$ (Malvern, 1969) in the three mutually perpendicular planes were calculated (cf. Ramsay, 1967; Ramsay and Huber, 1983) and eigenvalues and eigenvectors of the deformation tensor were used to determine the ratios and directions of the strain ellipsoid for each domain.

The maximum principal axes (X) of the strain ellipsoids from the three domains are all subhorizontal and the intermediate principal axes (Y) are subvertical (Fig. 1.16). The X-Y planes of the strain ellipsoids from the three domains are approximately parallel to the domains-mean foliation plane (Fig. 1.16). The subhorizontal maximum stretching (X) directions of the strain ellipsoids are also in accord with the field observations of stretching lineations such as stretched mineral grains and volcanic fragments (Fig. 8a).

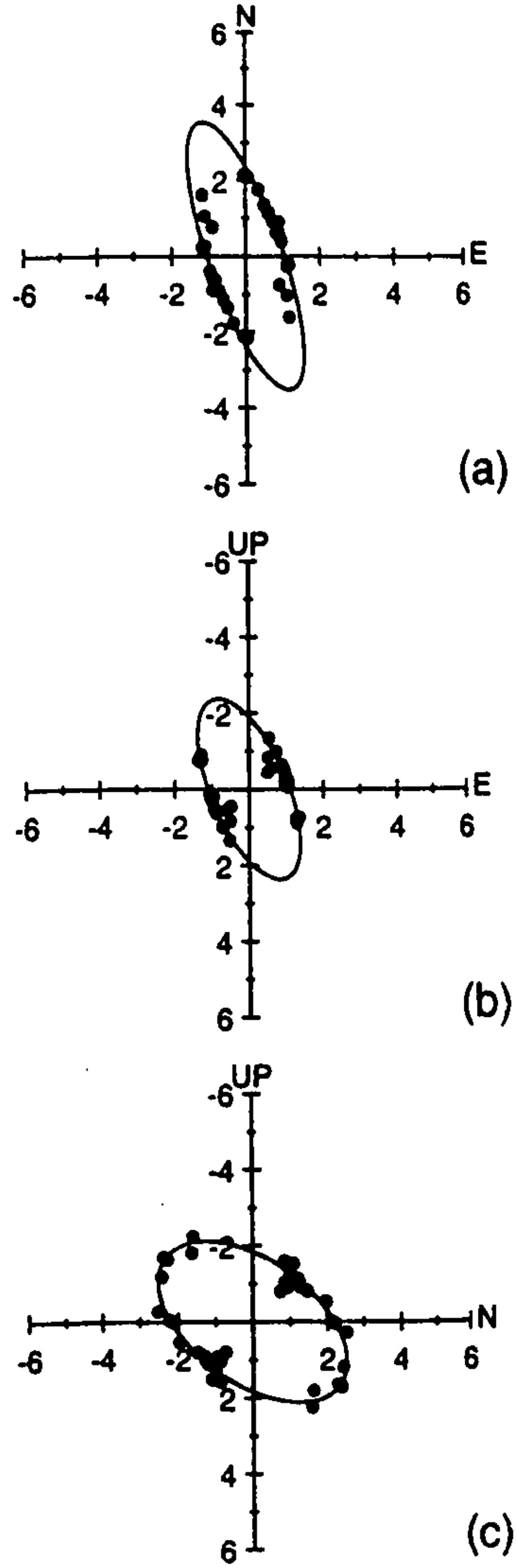

Fig. 1.13 Plots of longitudinal strain in Domain 1. (a): horizontal plane; (b): east-west vertical plane; (c): north-south vertical plane; N: north; E: east; curves: numerically best-fitted strain ellipses.

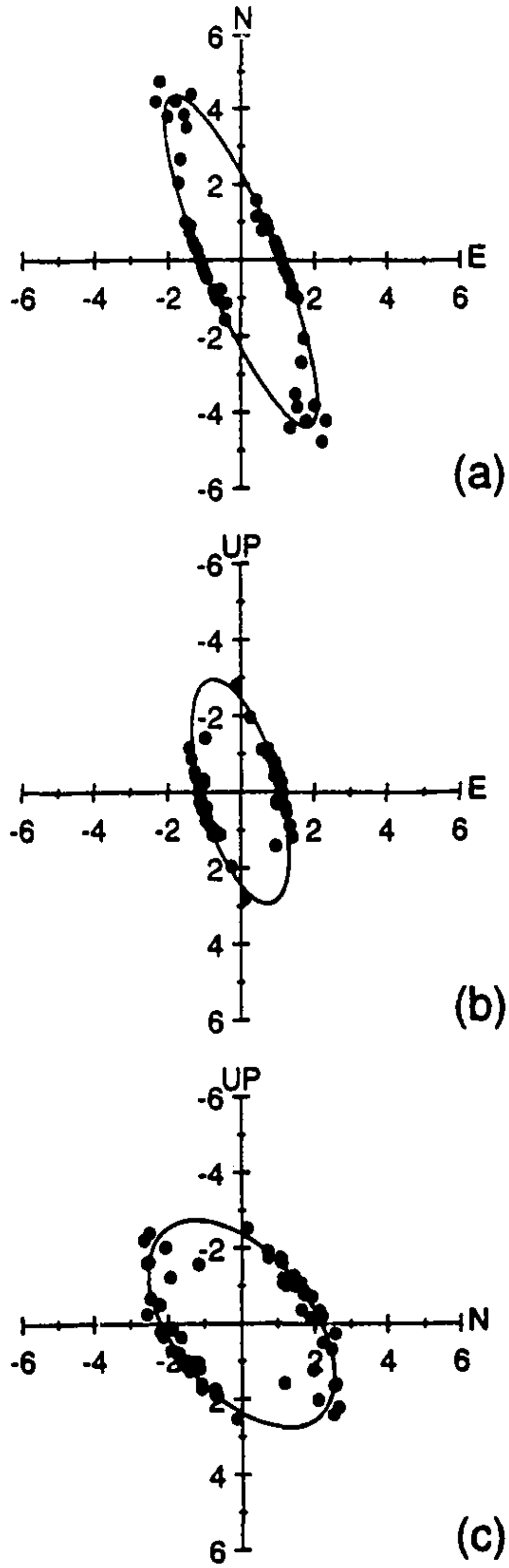

Fig. 1.14 plots of longitudinal strain in Domain 2. Labeled as in Fig. 1.13.

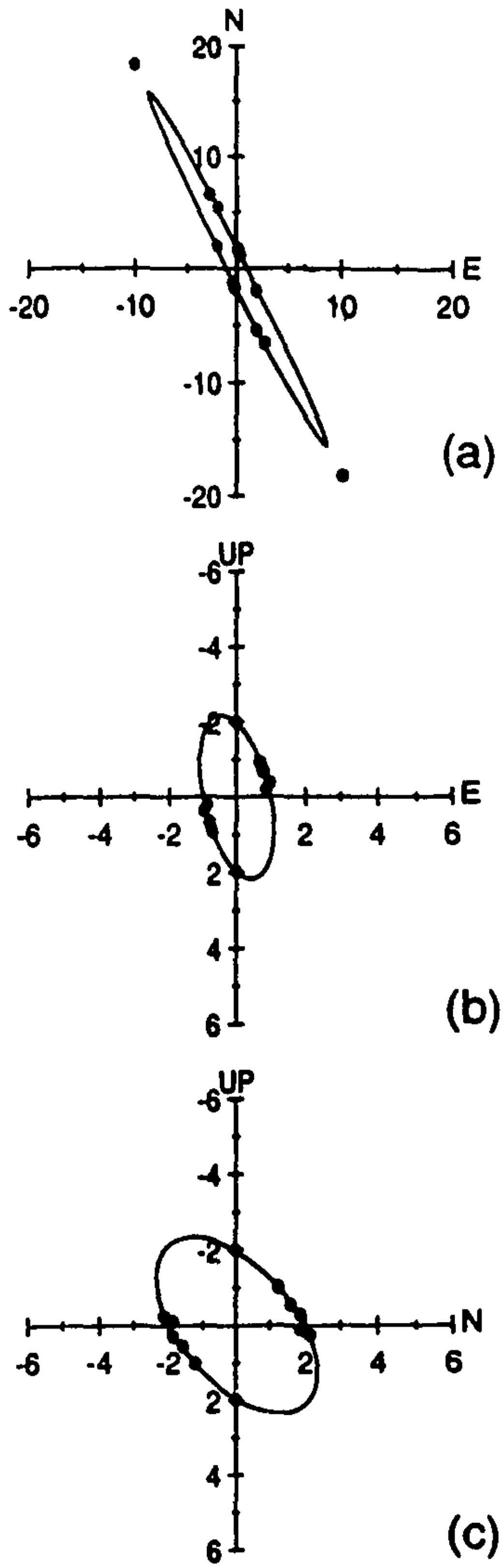

Fig. 1.15 Plots of longitudinal strain in Domain 3. Labeled as in Fig. 1.13.

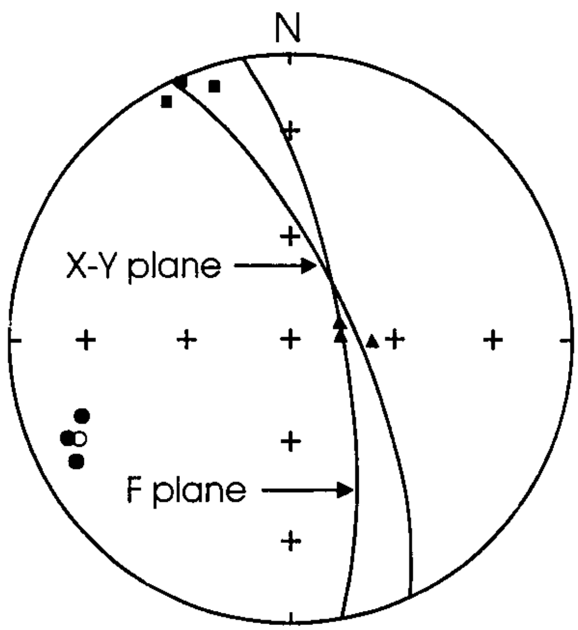

Fig. 1.16 Stereographic plot of directions of principal axes of the strain ellipsoids for the three domains. Solid squares: calculated long (X) axes; solid triangles: calculated intermediate (Y) axes; solid circles: calculated short (Z) axes; open circle: pole to domains-mean foliation plane; F plane: fault plane.

The progressive increase of aspect ratios in the strain ellipsoids (Figs. 1.13 to 1.15) without change in principal directions (Figs. 1.10 and 1.16) from Domain 1 to Domain 3 is incompatible with a progressive simple shear mode. In order to investigate the nature of the progressive strain required to explain the observed aspect ratios and their orientations, position-gradient tensors (Means, 1983) for the three domains were determined by assuming that deformation of the fragments was volume conservative and that rigid-body rotation components about the normal to the shear plane and the slickenline direction in the shear plane are both zero. These assumptions are based on the frequent observation that structures in a shear zone are symmetrical to the plane which is common to the slickenline and normal to the shear plane. The results indicate that the faulting is broadly dextrally transpressive (Zhang and Hynes, in review).

When interpreting the above results, it is important to point out several possible sources of error. First, when calculating deformation tensors for the three domains, it was assumed that the bulk strain within each domain was homogeneous, and this may contribute some error in the results as the eccentricity of the strain ellipsoid probably increased progressively approaching the fault. This error, however, is probably insignificant because the sectional data within each domain are compatible (Figs. 1.13, 1.14 and 1.15). Secondly, the strain ratios determined may underestimate the bulk strain due to the mechanical contrast between volcanic fragments and their matrix, but the error is probably not large as the fragments have the same composition as their matrix. Thirdly, because only 7 two-dimensional strain data were used in finding the shape of the strain ellipsoid in Domain 3, shape of the strain ellipsoid may not well constrained. It is unlikely, however, that these effects would alter the conclusion that the displacement along the north-northwest trending fault to the west of Domain 3 was dextrally transpressive.

1.4.4 Magnetic Fabrics of Plutonic Rocks

The Takla Group rocks east of the Finlay-Ingenika fault (Fig. 1.1) are extensively intruded by plutonic rocks occurring as stocks or dikes and ranging in composition from quartz diorite to diorite. Some of the plutonic rocks are strongly foliated, for example the quartz diorite north of Goldway Peak, while others are only slightly foliated or unfoliated. In order to investigate the nature of deformation of the plutonic rocks, oriented samples were taken from nine sites in the dioritic rocks for studies of anisotropy of magnetic susceptibility (AMS), as magnetic anisotropy has been used successfully as a tool in petrofabric and structural analysis (e.g. Graham, 1954; Kligfield, *et al.*, 1977; Kligfield, *et al.*, 1981; Hrouda, 1982; Borradaile, 1987; Hrouda, 1987; Borradaile, 1988; Borradaile and Alford, 1988; Henry, 1990; Borradaile, 1991; Borradaile *et al.*, 1992; Hrouda, 1993).

Five or six cores were drilled in the laboratory from oriented hand samples collected at each site, and each core was cut into 2 specimens. A total of 98 specimens were obtained. Magnetic susceptibility was measured with an SI-2 induction coil instrument interfaced to an IBM Personal computer (Sapphire Instruments, P.O. Box 385, Ruthven, Ont.), which is a low-field instrument with a r.m.s. field strength of 0.6 Oe operating at 750 Hz. The bulk susceptibility of each specimen, defined by $(K_1 + K_2 + K_3)/3$ where K_1, K_2 and K_3 are maximum, intermediate and minimum principal susceptibility, respectively, is 10^{-2} to 10^{-3} SI units on a volume basis (see Appendix 2). The radii of 95% confidence circles around the three principal (K_1, K_2 and K_3) axes of susceptibility were generally less than 4°, with only a few radii between 5° and 9°, and the standard deviations of the principal susceptibility were all less than 1%. Within site, the directions of principal susceptibility were well clustered (Fig. 1.17) with small 95% confidence ellipses (calculated using Hext's method (1963)). Microprobe analyses of the opaque minerals indicate that both magnetite and ilmenite occur and are the most common opaque minerals present. Ilmenite is in a small proportion and almost always occurs as exsolution lamellae within the magnetite. With these magnetic minerals present in the dioritic rocks, the magnetic anisotropy measured probably results largely from the preferred orientation of magnetite grains, which is consistent with the high values of average magnetic susceptibility observed (cf. Kligfield *et al.*, 1977; Borradaile, 1987; Rochette, 1987; Borradaile, 1988).

The observed degree of average magnetic anisotropy within site ($p = K_1/K_3$,

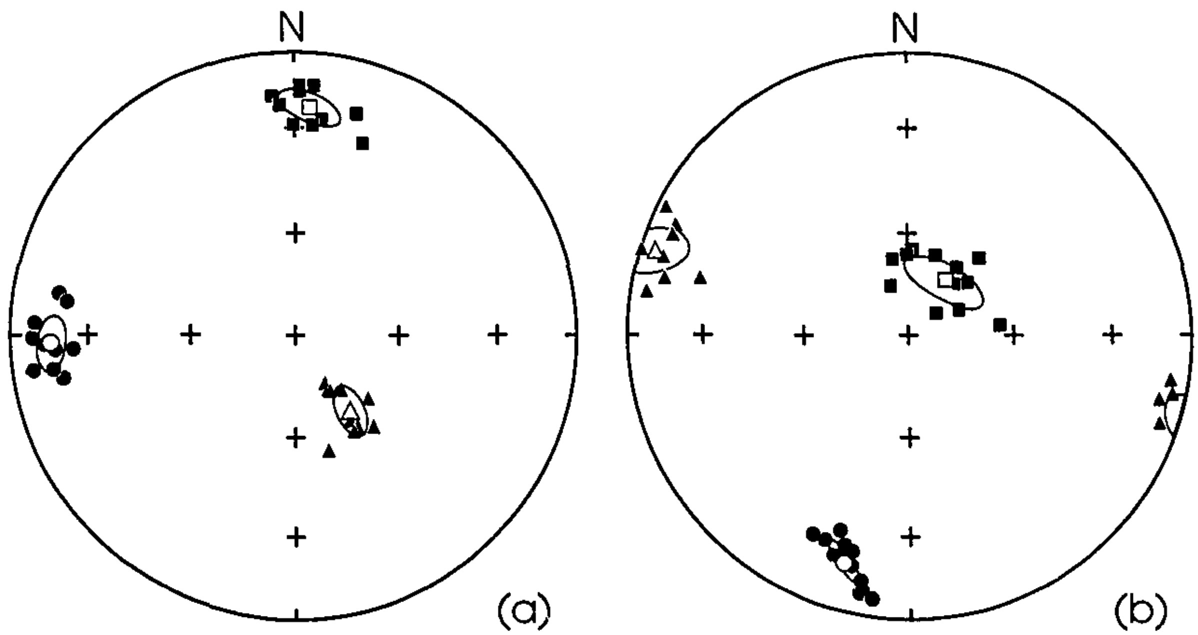

Fig. 1.17 Stereographic plot of principal magnetic susceptibility. (a) from site 1 (strongly foliated rocks) and (b) from site 7 (unfoliated rocks). Solid square, triangle and circle: maximum (K_1), intermediate (K_2) and minimum (K_3) magnetic susceptibility of individual specimen; open square, triangle and circle: site means of K_1, K_2 and K_3, respectively; ellipses: 95% confidence ellipses (cf. Hext, 1963).

cf. Ellwood *et al.*, 1988) ranges from 1.055. where rocks have no visible foliation, to 1.591, where the rocks are strongly foliated. The shape of the magnetic susceptibility ellipsoid is conveniently characterized by parameter T (cf. Jelinek, 1981; Hrouda, 1982; Ellwood *et al.*, 1988), which varies from -1 (rotational prolate ellipsoid) through 0 (neutral ellipsoid) to +1 (rotational oblate ellipsoid) and the eccentricity of the ellipsoid is then uniquely defined by P'(cf. Jelinek, 1981; Hrouda, 1982; Ellwood *et al.*, 1988), which varies from 1 (sphere) to infinite and includes some influence from all three principal magnitudes (see legend to Fig. 1.18). Specimens from sites 1 and 2 from the strongly foliated rocks north of Goldway Peak show a very high susceptibility anisotropy, as indicated by high average P' values (about 1.60), and define an L-S magnetic fabric as average T values are nearly zero (Figs. 1.18 and 1.19). In contrast, specimens from sites 3 to 8 from unfoliated rocks display low susceptibility anisotropy (the average P' values are less than 1.11) and define two dominant types of susceptibility ellipsoid, that is, L-S and S fabrics, as the average T values range from -0.04 to 0.64 (Figs. 1.18 and 1.19). Specimens from site 9 from slightly foliated rocks possess an intermediate average P' value (about 1.23) with an S fabric as the average T value is 0.65 (Figs. 1.18 and 1.19). These characteristics of the magnetic susceptibility anisotropy measured are similar to those of plutonic rocks described by Hrouda (1982, Fig. 13). Together with the evidence that the strongly foliated rocks (sites 1 and 2) possess steeply dipping magnetic foliation and gently plunging magnetic lineation (Fig. 1.17a) while the unfoliated rocks (sites 3 to 8) show varied attitudes

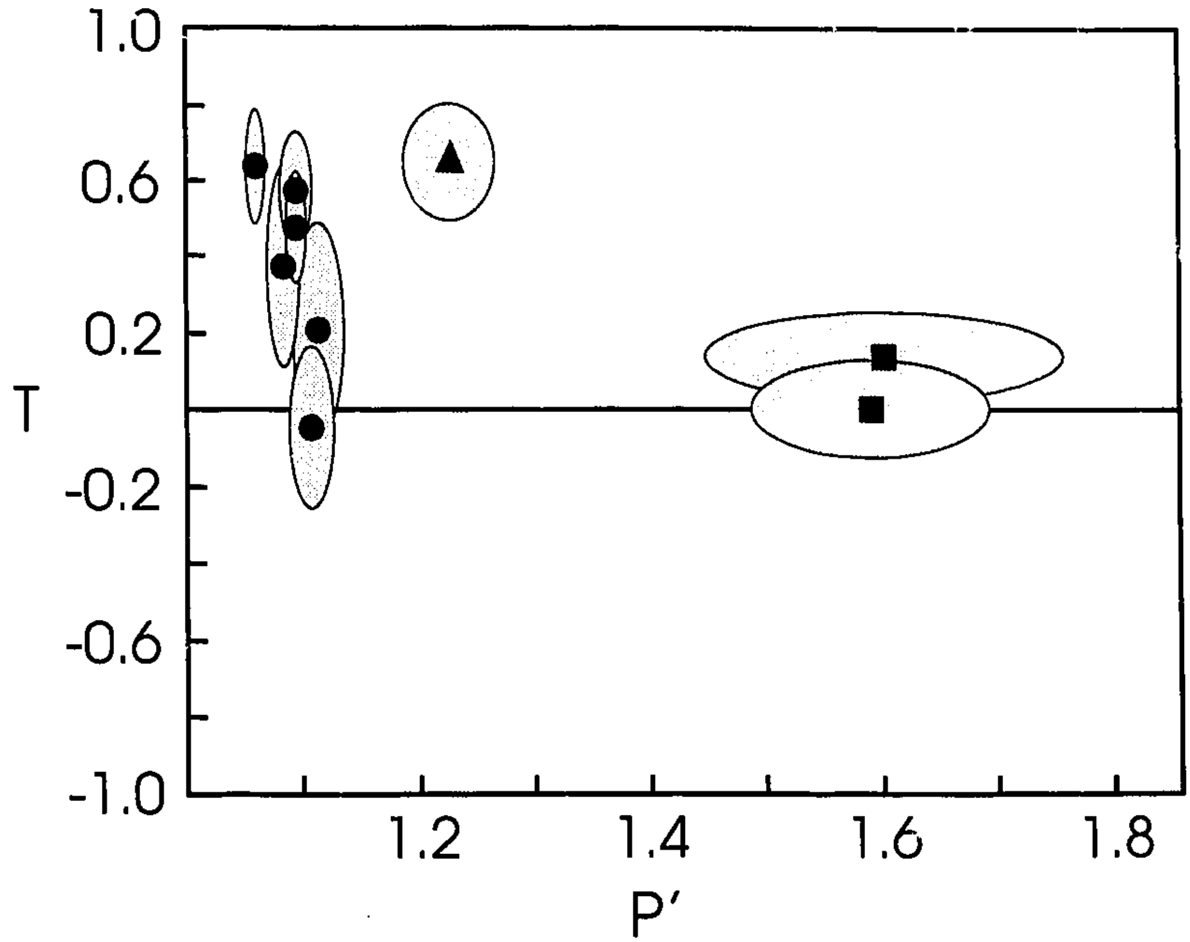

Fig. 1.18 Plot of site average magnetic anisotropy of dioritic rocks. Solid circles: rocks without foliation; solid triangle: rock with weak foliation; solid squares: rocks with strong foliation; shaded ellipses: standard deviation within site (see Appendix 2); where $T = (2K_2-K_1-K_3)/(K_1-K_3)$ and $P' = \exp[2((\ln(K_1)-LM)^2+(\ln(K_2)-LM)^2+(\ln(K_3)-LM)^2)]^{1/2}$, where $LM = (\ln(K_1)+\ln(K_2)+\ln(K_3))/3$ (after Jelinek, 1981; Hrouda, 1982; Ellwood *et al.*, 1988).

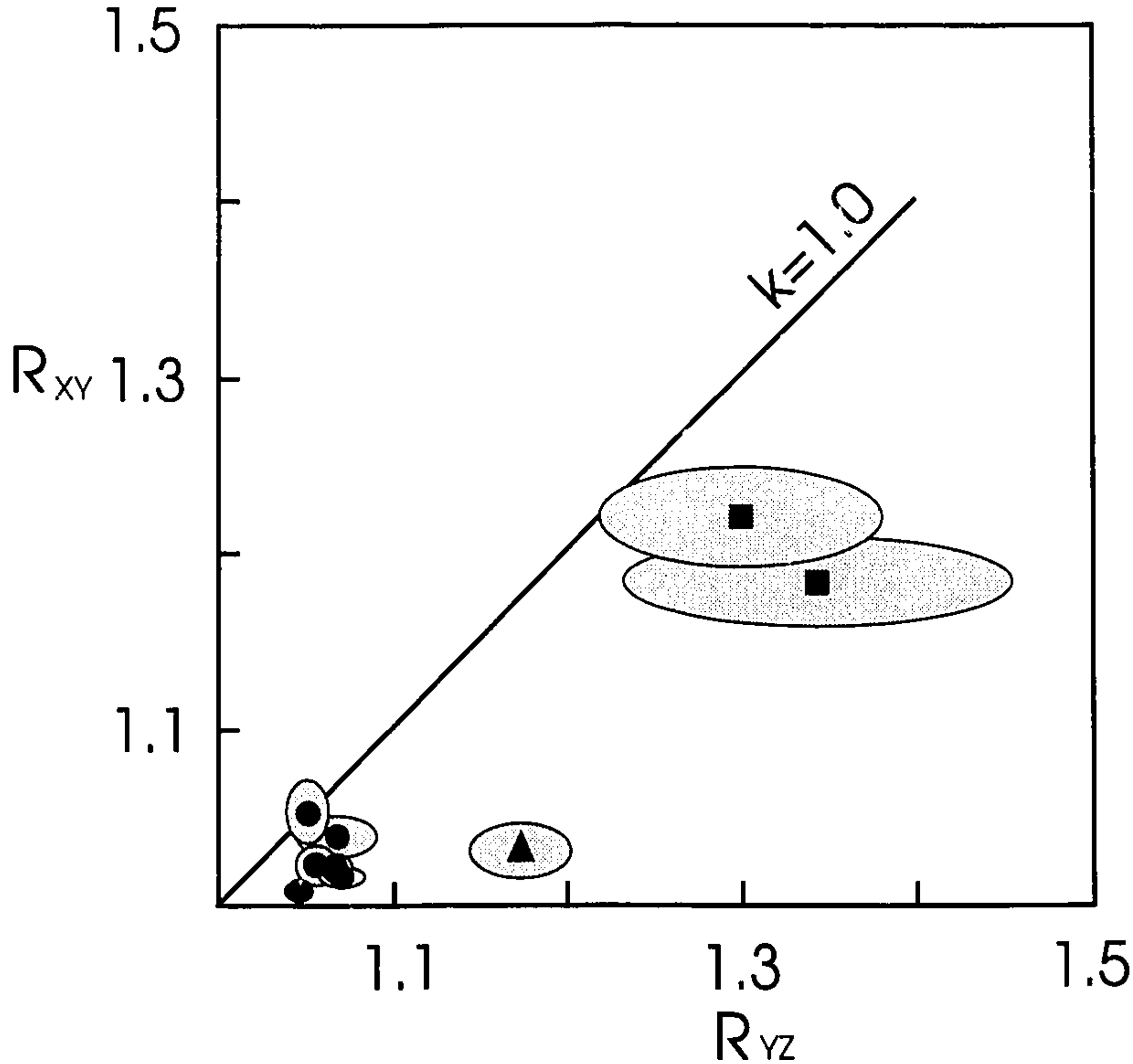

Fig. 1.19 Plot of the shapes of the site average magnetic susceptibility ellipsoids. solid circles: rocks without foliation; solid triangle: rock with weak foliation; solid squares: rocks with strong foliation; shaded ellipses: standard deviation within site (see Appendix 2); where $R_{XY} = K_1/K_2$, $R_{YZ} = K_2/K_3$ and $k = R_{XY}/R_{YZ}$.

of magnetic foliations but steeply plunging lineations (Fig. 1.17b), it may be concluded that the susceptibility anisotropy of the strongly foliated rocks probably originated from the tectonic deformation while that of the unfoliated rocks was presumably due to primary magmatic flow.

Comparing the magnetic fabrics of the strongly foliated rocks north of Goldway Peak with the deformational rock fabrics of the strained volcanic fragments, as discussed above, in the same area (Fig. 1.17a and 1.16), it is clear that the directions of the magnetic ellipsoids are consistent with those of the strain ellipsoids. This suggests that the plutons may have experienced the same deformation as the volcanics. Unfortunately, no strain markers have been observed and measured in the plutonic rocks, hence correlations of magnitudes between the magnetic ellipsoids and the strain ellipsoids were not possible.

1.5 CLEAVAGE

Some of the major faults cut the Takla Group into fault-bounded, weakly deformed blocks, ranging in size from several square kilometres to tens of square kilometres (Fig. 1.1). With progressive displacement on the Finlay-Ingenika fault, deformation was apparently concentrated in the previously formed fault zones, while the fault-bounded blocks remained only very weakly deformed and cleavage is the only visible deformation.

The cleavage within the weakly-deformed blocks is characterized by spaced shear planes and in the cleaved rocks no apparent petrofabrics have been found. The shear planes are usually steeply dipping and closely spaced, at intervals of 2 to 10 centimetres. They are commonly slickensides with subhorizontal slickenlines (Plate. 1.12) and many are characterized by fibrous crystals of tremolite and calcite or patches of chlorite and epidote. Shear senses are evident from the slickenline steps (Plate 1.12) and offset of such features as quartz veins (Plate 1.13) or the conjugate cleavage. Most cleavage is regional but some is local in its distribution. The local cleavage is commonly associated with nearby faults and can be easily distinquished from the regional by tracing away from the fault. Regionally distributed cleavage generally occurs in conjugate sets trending north to north-northeast and east-northeast to east although there is considerable variation. The regional cleavage postdated the folding since its surfaces at the

Plate 1.12 Slickenlines on a cleavage surface striking east-northeast at site 24. Pencil is parallel to the slickenlines and the slickenline steps show a sinistral shear sense, looking northwest.

Plate 1.13 Offset of a quartz vein by a cleavage plane striking north-northeast at site 18, showing a dextral shear sense. Pencil is parallel to the cleavage plane, looking north-northeast down.

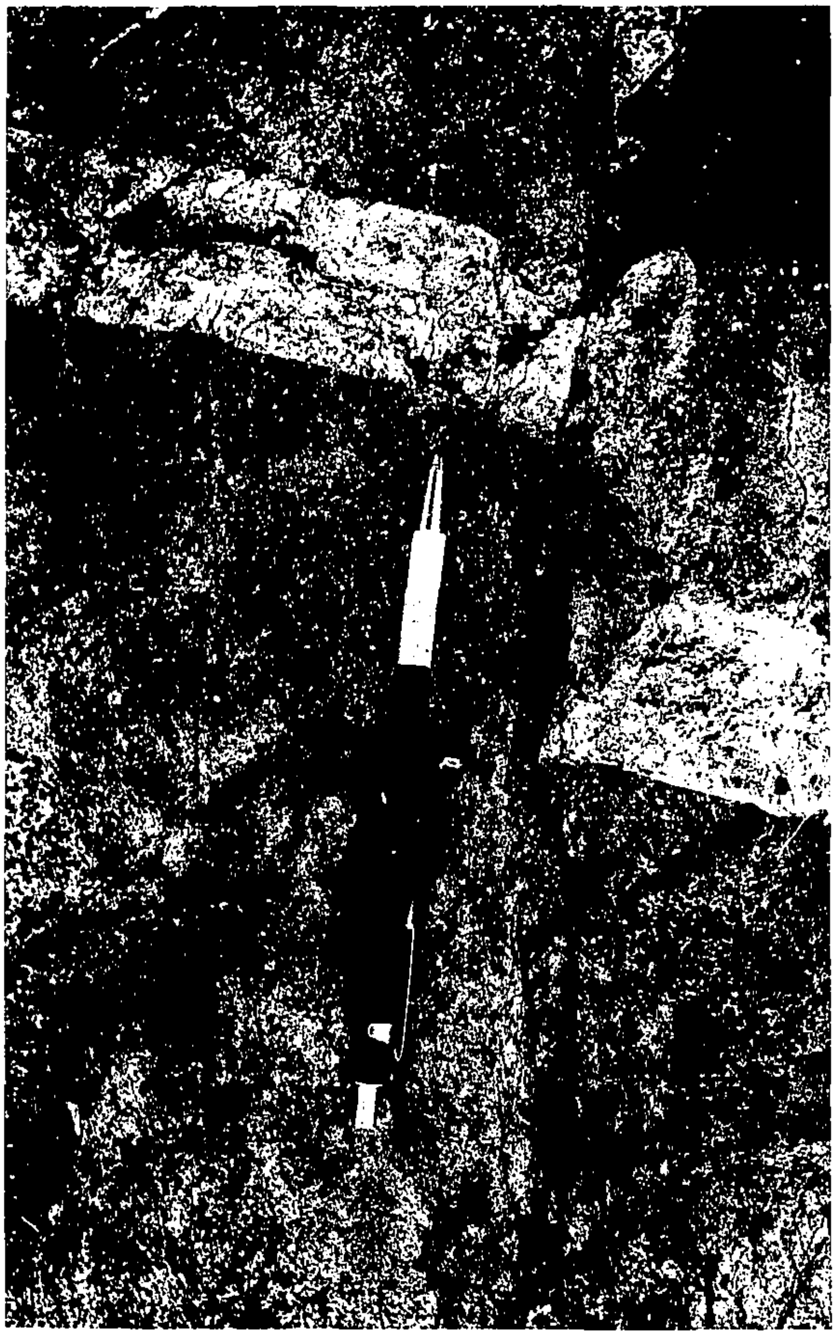

hinge zone and on the limbs are all consistently steeply dipping.

About 600 regional cleavage planes, together with slickenlines, were measured from 24 sites, one of which (site 5) is from west of McConnell Creek and outside the map sheet. Because some sites exhibit conjugate cleavage whereas others show only a single set of the cleavage, comparison of mean orientations of the cleavage between different sites cannot be made with the cleavage itself. In order that all the cleavage data might be used, the stress tensor for each site was calculated using an inversion method for fault-slip data (Hardcastle and Hills, 1991; Zhang *et al.*, submitted). This kind of inversion is considered reliable in this region because the fault-bounded blocks are weakly deformed and show no pervasive ductile deformation. Consequently, the geometrical relationship between the conjugate cleavage planes has probably remained unchanged since their formation and the orientations of cleavage planes provide a reliable indication of the stress tensor at the time of their formation. Site-mean orientations of maximum, intermediate and minimum principal stress axes (σ_1, σ_2 and σ_3) were calculated using Bingham's statistics (Bingham 1974).

Site-mean trends of σ_1 and σ_3 vary considerably across the study area while the plunges remain consistently subhorizontal. Site-mean trends of σ_2 are consistent, and all plunge steeply. Figure 1.20 shows the site-mean attitudes of σ_1. It is clear that sites 22, 23 and 24 from the ranges west of Aiken Lake,

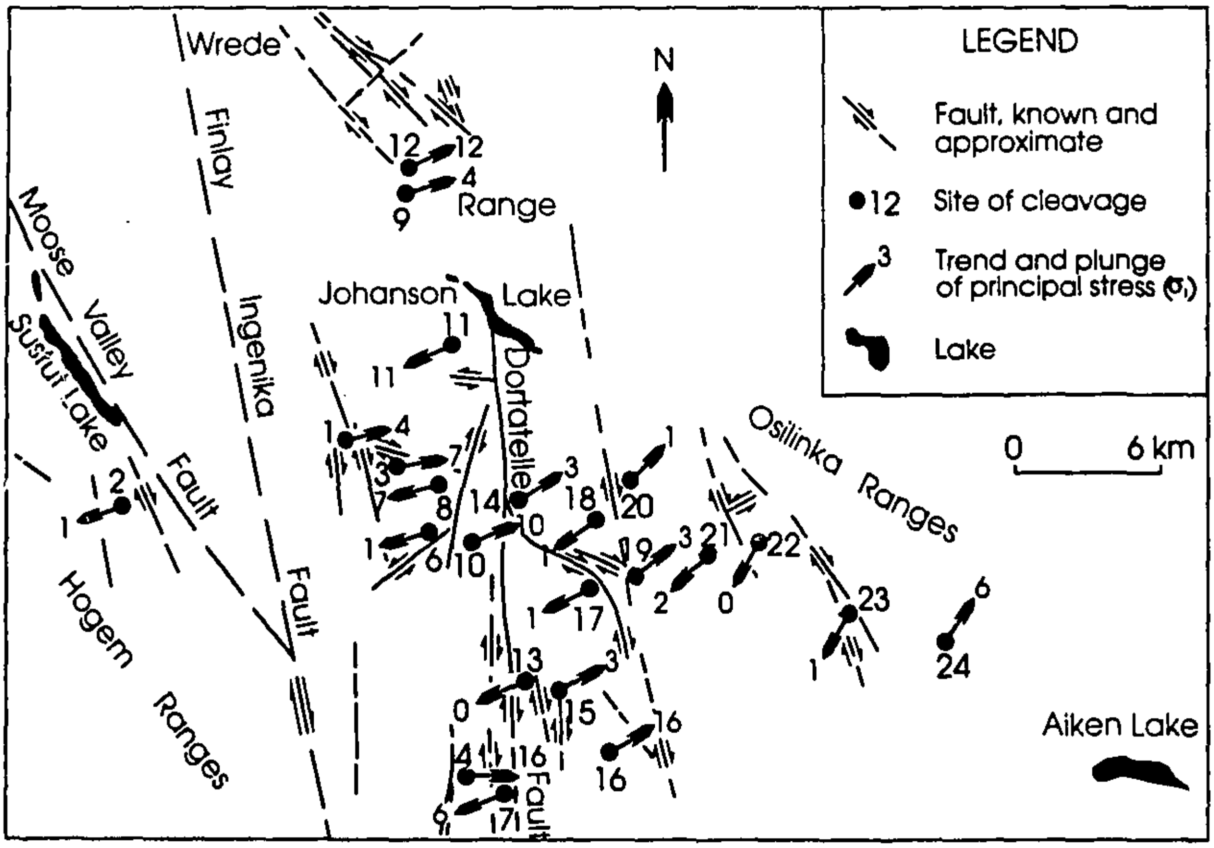

Fig. 1.20 Map showing locations of cleavage sites and site mean orientations of the principal stress σ_1 inverted from the cleavage data.

although they are from different blocks, have a similar site-mean attitude of σ_1, trending north-northeast (~33°) or south-southwest (~213°) and plunging subhorizontally (Fig. 1.20), which is consistent with that to be expected in a stress field due to the initiation of dextral transcurrent motion on the Finlay-Ingenika fault (Fig. 1.4) (cf. Tchalenko, 1970; Keller *et al.*, 1982; Sylvester, 1988). Approaching the Finlay-Ingenika fault, different sites within a single block (e.g. 14 and 18, 20 and 21, Fig. 1.20) show similar site-mean orientations of σ_1 but major changes occur between adjacent blocks. For example, the differences between sites 10 and 14, 18 and 20, 21 and 22 (Fig. 1.20) are statistically significant at 95% confidence level because their 95% confidence limits (all less than 1.5°) do not overlap. The fact that major changes in the site-mean orientations of σ_1 occur between the sites close to each other but from different blocks and that different sites far away from each other but within a single block show similar orientations is not compatible with progressive rotation of stress axes, i.e. with curved stress trajectories. We consider it for more probable that the changes in the regional cleavage attitude are due to the rotation of blocks bounded by the observed faults. This indicates that the regional cleavage probably predated the strike-slip faulting and developed in a uniform stress field associated with initiation of movement on the Finlay-Ingenika fault (see further discussion below). Other evidence supporting this assumption is the truncation and rotation of the regional cleavage by nearby strike-slip faults. One such example was observed in the volcaniclastic rocks about 300 metres west of the Dortatelle fault (Fig. 1.1). Here, one set of the regional cleavage trends north-northeast (~40°) and dips 87° to the northwest with subhorizontal slickenlines (Fig. 1.21) and dextrally offsets laminations of volcanic siltstone. It is significantly different in attitude from the Riedel shears to the fault defined by the mean C-surface (Figs. 1.5a and 1.21). Approaching the fault, the cleavage changes its attitude progressively into an east-northeast (~75°) trend and dipping 88° to the southeast, reflecting a clockwise rotation (Fig. 1.21). Poles to the cleavage planes are distributed on a great circle, and the pole to the great circle lies in the fault plane (Fig. 1.21). These features, considered together, indicate that the rotation of the cleavage probably reflects a bulk strain due to dextral displacement on the Dortatelle fault, and hence the cleavage developed prior to the Dortatelle fault.

As discussed above, the regional cleavage probably developed in a uniform stress field associated with the initiation of the Finlay-Ingenika fault prior to the strike-slip faulting in the study area. Based on this assumption, the variation in orientations of the principal stress axes inverted from the regional cleavage can be used to indicate the block rotation. The mean rotational axis was determined by averaging the best-fit cone axes to the mean principal stress axes σ_1, σ_2 and σ_3 of the 24 sites and the rotational angles were determined by comparing orientations of the principal stress axes σ_1 with that of site 22. It is again evident from Fig. 1.22 that, about 20 kilometres away from the Finlay-Ingenika fault, blocks show no rotation (e.g. sites 23 and 24, see Fig. 1.20 for site locations) and

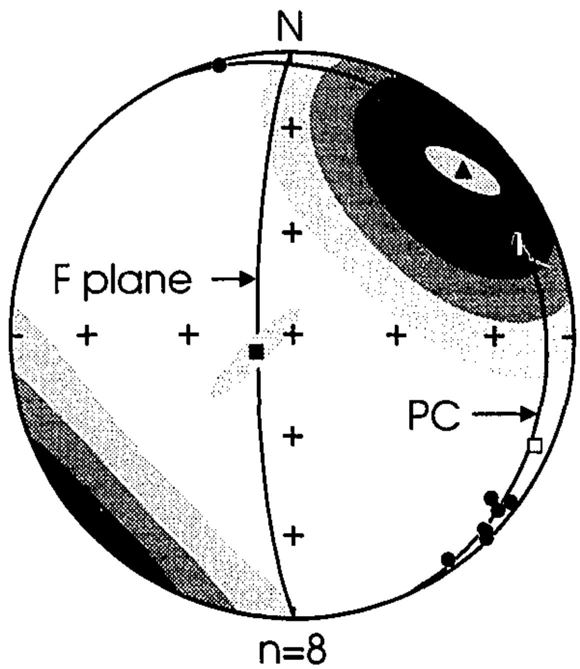

Fig. 1.21 Stereographic plot of poles to the regional cleavage planes. Contour interval: as in Fig. 1.3; solid circles: poles to the cleavage planes; open square: mean C-surface (see Fig. 1.5a); solid triangle: mean slickenline in the cleavage planes, determined by maximum eigenvector; PC: plane common to the poles to the cleavage planes; solid square: the pole to PC, determined by minimum eigenvector; F plane: Dortatelle fault plane; shaded ellipses: 95% confidence ellipses; n: number of slickenlines.

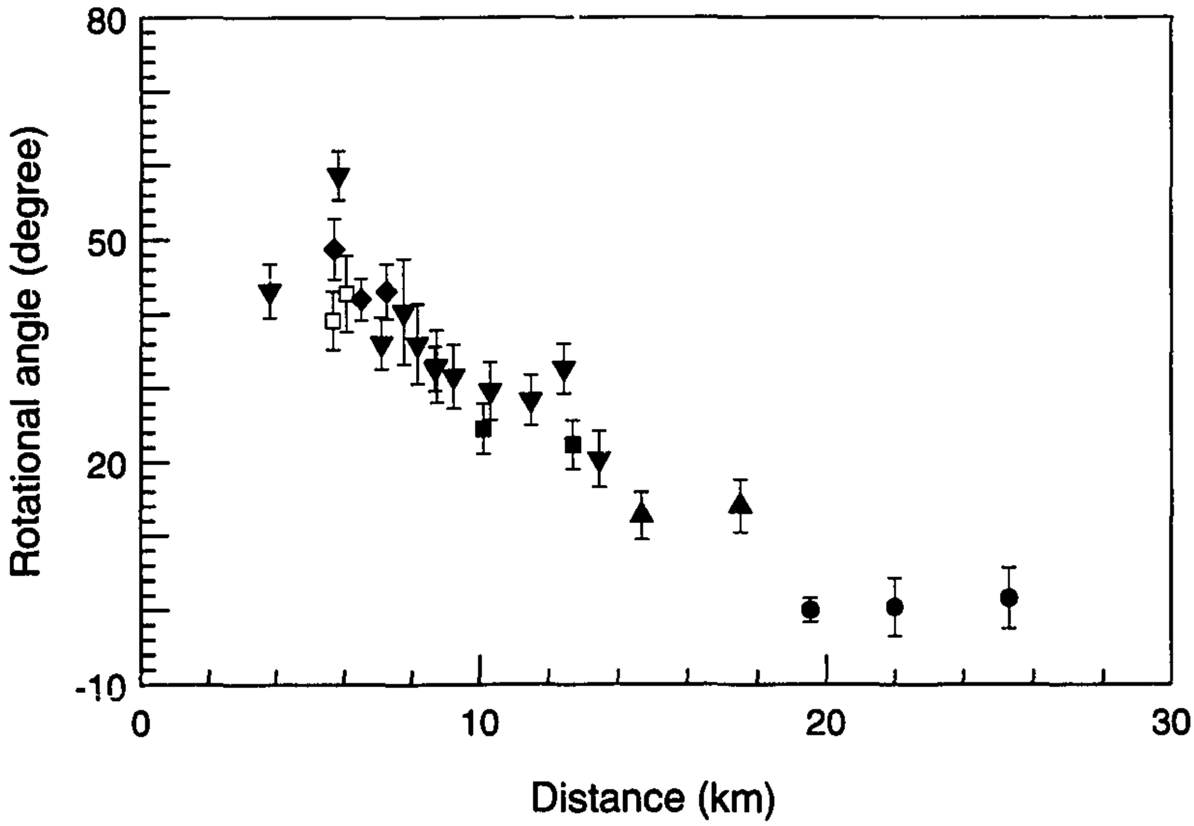

Fig. 1.22 Plot of rotational angle against distance. The abscissa represents the distance away from Finlay-Ingenika fault, and the ordinate represents the rotational angle determined from site-mean stress tensor. Solid circles: from sites 22, 23 and 24; solid triangles: from sites 20 and 21; solid squares: from sites 14 and 18; solid diamonds: from sites 3, 6 and 8; open squares: from sites 2 and 5, west of the Finlay-Ingenika fault; upside-down solid triangles: from the other sites.

approaching the fault the rotational angles obtained from different sites within an individual block are similar but increase markedly across different blocks (e.g. sites 20 and 21, sites 14 and 18, sites 3, 6 and 8, see Fig. 1.20 for site locations). It can then be concluded that the fault-bounded blocks were rotated clockwise about subvertical axes, and the amount of block rotation varies over the study area, reaching its maximum ($58.7\pm3.3^\circ$) close to the Finlay-Ingenika fault and minimum ($0.0\pm1.6^\circ$) about 20 kilometres away from the fault (Fig. 1.22).

1.6 DISCUSSION

The evolution of terrane interactions in north-central British Columbia may have started as early as the late Devonian (Gabrielse 1991). Stikinia, Cache Creek, Quesnellia and Slide Mountain terranes had been essentially amalgamated by the Early Jurassic due to the closing of the Cache Creek ocean and were subsequently juxtaposed during middle Jurassic contraction (Monger, 1984; Gabrielse, 1991). This northeast-southwest contraction continued throughout the Late Jurassic and Early Cretaceous and was followed by dextral strike-slip faulting. Two tectonic regimes were therefore present during the late stages of terrane interactions in the study area. The former may be well characterized by the northwest-trending, northeast-directed Skeena fold belt of the Bowser Basin (Evenchick, 1991) to the north of the study area although the sense of the belt is inconsistent with that of thrusting of the Cache Creek Terrane onto Stikinia (Gabrielse, 1991). However, no compelling evidence for deformation associated with this contraction has been recognized and demonstrated in the Late Triassic Takla Group volcanics in the study area. The only structures observed that might be related to this episode are the large scale, open folds. The general lack of a record could be due to several causes. First, the mechanical contrast between volcanics and thin-layered sedimentary sequences, as argued by Evenchick (1991), may produce contrasts in structural styles. In other words, the competent volcanic rocks may be more readily deformed into open folds than thrusts, or may have been transported as a rigid block during the contractional deformation. Second, strike-slip faulting along the Finlay-Ingenika fault may have been strong enough to have transformed all contractional structures into strike-slip structures. For example, the northwest-trending thrust faults produced in the northeast-southwest contractional regime could have been reused in the dextral strike-slip regime and have become dextral strike-slip faults. If this is true, some of the northwest-trending dextral strike-slip faults in the area, especially those displaying two stages of displacement, for example thrust shear sense with superimposed strike-slip, may have originated from the contractional environment. In the context of regional tectonics, the second hypothesis seems to be more realistic because the area in which the deformation was studied is immediately adjacent to the major strike-slip fault.

1.7 CONCLUSIONS

The structures observed along the Finlay-Ingenika fault are dominated by subvertical to vertical, dextral strike-slip faults trending northwest, north-northwest and north-south, and sinistral strike-slip faults trending east-northeast. The faults are distributed in a narrow belt, about 30 kilometres wide, adjacent to the Finlay-Ingenika fault. This spatial distribution, together with the attitudes and slip senses of the strike-slip faults, strongly suggests that they were local structures and developed in association with dextral, transcurrent motions on the Finlay-Ingenika fault. Along these faults, a variety of fabrics, such as S-C surfaces, drag folds, extensional fissures and stretching lineations were developed. Polarities of acute angles between the fault planes and the planar fabrics are consistent with those of slickenlines and slickenfibres, strongly supporting their strike-slip nature, and can be used as indicators for slip senses and directions of the faults. Attitudes of the strain ellipsoids obtained from strain analysis of the deformed volcanic fragments are comparable with those of magnetic susceptibility ellipsoids measured from the deformed dioritic rocks in the same area, indicating that the dioritic rocks experienced the same deformation as the volcanics. The age of the strike-slip faulting is unknown but was probably not earlier than middle Cretaceous as Jurassic to Cretaceous dioritic rocks (Woodsworth, 1976; Monger, 1977; Gabrielse, 1991) were involved in the faulting in many places.

Some of the major strike-slip faults cut the Late Triassic Takla Group rocks into a number of discrete, weakly deformed blocks with diameters ranging from a few to tens of kilometres. As dextral transcurrent displacement along the Finlay-Ingenika fault progressed, deformation was apparently concentrated in the previously-formed fault zones while the fault bounded blocks remained relatively undeformed or slightly deformed but rotated clockwise about subvertical axes in response to the transcurrent motions. Statistics of regional cleavage indicate that the amount of block rotation varies over the study area, decreasing away from the Finaly-Ingenika fault. This variable rotation of blocks is similar to that described by Nelson and Jones (1986) in the Las Vegas Range and contrasts to the uniform rotation described and modelled elsewhere (e.g. Ron *et al.*, 1986; Hudson and Geissman, 1987; Geissman *et al.*, 1989; Ron *et al.*, 1990).

The mode of deformation observed in the study area is similar to that along some well-known, large-scale strike-slip faults (cf. Wilcox *et al.*, 1973; Sylvester, 1988). Record of deformation associated with the middle Jurassic to Cretaceous contraction may have been entirely obscured by the strong local deformation resulting from dextral transcurrent displacement along the Finlay-Ingenika fault, especially in the area adjacent to it. This local deformation associated with the strike-slip faulting may characterize many parts of the Intermontane Belt and could in part explain the apparent disparities between the paleomagnetic declinations observed from the western allochthonous terranes and North America (Monger and

Irving, 1980; Irving *et al.*, 1985; Rees *et al.*, 1985; Irving and Wynne, 1990; Zhang *et al.*, submitted).

1.8 ACKNOWLEDGEMENTS

Measurement of magnetic susceptibility was conducted in the Paleomagnetism Laboratory at Pacific Geoscience Center, Geological Survey of Canada. The writers would like to thank Jane Wynne, Judy Baker and Tom Vandall for their guidance in the lab. Access to commercial software for calculation of the average principal directions of AMS and confidence ellipses was provided at the Geology Department, University of Ottawa, by Keith Benn. This research was supported by grants from the British Columbia Ministry of Energy, Mines and Petroleum Resources, Geological Survey of Canada and the Natural Sciences and Engineering Research Council and G.Z. was supported by a McGregor Scholarship during his Ph.D. study. Their support is gratefully acknowledged.

1.9 REFERENCES

Armstrong, R. L., Monger, J. W. H. and Irving, E. 1985. Age of magnetization of the Axelgold gabbro, north-central British Columbia. Canadian Journal of Earth Sciences, 22, pp. 1217-1222.

Atwater, T. 1970. Implications of plate tectonics for the Cenozoic tectonic evolution of western North America. Geological Society of America Bulletin, 81, pp. 3513-3536.

Avé Lallemant, H. G. and Oldow, J. S. 1988. Early Mesozoic southward migration of Cordillerian transpressional terranes. Tectonics, 7, pp. 1057-1075.

Beck, M. E. and Noson, L. 1972. Anomalous paleolatitudes in Cretaceous granitic rocks. Nature, 235, pp. 11-13.

Berthé, D., Choukroune, P. and Jegouzo, P. 1979. Orthogneiss, mylonite and non-coaxial deformation of granites: the example of the south Armorican shear zone. J. Struct. Geol. 1, 31-42.

Bingham, C. 1974. An antipodally symmetric distribution on the sphere. The Annals of Statistics, 2, pp. 1201-1225.

Borradaile, G. J. 1987. Anisotropy of magnetic susceptibility: rock composition versus strain. Tectonophysics, 138, pp. 327-329.

Borradaile, G. J. 1988. Magnetic susceptibility, petrofabrics and strain. Tectonophysics, 156, pp. 1-20.

Borradaile, G. J. 1991. Correlation of strain with anisotropy of magnetic susceptibility (AMS). Pure and Applied Geophysics, 135, pp. 15-29.

Borradaile, G. J. and Alford, C. 1988. Experimental shear zones and magnetic fabrics. Journal of Structural Geology, 10, pp. 895-904.

Borradaile, G. J., Puumala, M. and Stupavsky, M. 1992. Anisotropy of complex magnetic susceptibility as an indicator of strain and petrofabric in rocks bearing sulphides. Tectonophysics, 202, pp. 309-318.

Church, B. N. 1974. Geology of the Sustut area. In Geology, Exploration and Mining in British Columbia 1973, B. C. Ministry of Energy, Mines and Petroleum Resources, pp. 411-455.

Church, B. N. 1975. Geology of the Sustut area. In Geology, Exploration and Mining in British Columbia 1974, B. C. Ministry of Energy, Mines and Petroleum Resources, pp. 305-309.

Ellwood, B. B., Hrouda, F. and Wagner, J. J. 1988. Symposia on magnetic fabrics: introductory comments. Physics of the Earth and Planetary Interiors, 51, pp. 249-252.

Eslev, E. A. and Ge, H. 1990. Least-squares center-to-center and mean object ellipse fabric analysis. Journal of Structural Geology, 12, pp. 1047-1059.

Evenchick, C. A. 1991. Structural relationships of the Skeena Fold Belt west of the Bowser Basin, northwest British Columbia. Can. J. Earth Sci. 28, pp. 973-983.

Fisher, R. A. 1953. Dispersion on a sphere. Proceedings of Royal Society, 217, pp. 295-305.

Fitch, T. J. 1972. Plate convergence, transcurrent faults, and internal deformation adjacent to southeast Asia and the western Pacific. Journal of Geophysical Research, 77, pp. 4432-4459.

Flinn, D. 1962. On folding during three-dimensional progressive deformation. Quarterly Journal of the Geological Society of London, 118, pp. 385-433.

Fry, N. 1979. Random point distribution and strain measurement in rocks. Tectonophysics 60, pp. 89-105.

Gabrielse, H. 1985. Major dextral transcurrent displacement along the Northern Rocky Mountain Trench and related lineaments in north-central British Columbia. Geological Society of America Bulletin, 96, pp. 1-14.

Gabrielse, H. 1991. Late Paleozoic and Mesozoic terrane interactions in north-central British Columbia. Canadian Journal of Earth Sciences, 28, pp. 947-957.

Gabrielse, H. and Dodds, C. J. 1977. The structural significance of the northern Rocky Mountain Trench and related lineaments in north-central British Columbia. Geological Association of Canada Programs with Abstracts, 2, p. 19.

Geissman, J. W. Harlan, S. S. and Wawrzyniec, T. F. 1989. Strike-slip faulting and block rotation in the Lake Mead fault system. Geology, 17, pp. 1057-1058.

Graham, J. W. 1954. Magnetic susceptibility anisotropy, an unexploited petrofabric element. Geological Society of America Bulletin, 65, pp. 1257-1258.

programs for determination of stress tensor configurations and separation of heterogeneous populations of fault-slip data. Computers & Geosciences, 17, No. 1, pp. 23-43.

Henry, B. 1990. Magnetic fabric implications for the relationships between deformation mode and grain growth in slates from the Borrowdale Volcanic Group in the English Lake District. Tectonophysics, 178, pp. 225-230.

Hext, G. R. 1963. The estimation of second-order tensors, with related tests and designs. Biometrika, 50, pp. 353-373.

Hrouda, F. 1982. Magnetic anisotropy of rocks and its application in geology and geophysics. Geophysical Surveys, 5, pp. 37-82.

Hrouda, F. 1987. Mathematical model relationship between the paramagnetic anisotropy and strain in slates. Tectonophysics, 142, pp. 323-327.

Hrouda, F. 1993. Theoretical models of magnetic anisotropy to strain relationship revisited. Physics of the Earth and Planetary Interiors, 77, pp. 237-249.

Hudson, M. R. and Geissman, J. W. 1987. Paleomagnetic and structural evidence for middle Tertiary counterclockwise block rotation in the Dixie Valley region, west-central Nevada. Geology, 15, pp. 638-642.

Irving, E., Woodsworth, G. J., Wynne, P. J. and Morrison, A. 1985. Paleomagnetic evidence for displacement from the south of the Coast Plutonic Complex, British Columbia. Canadian Journal of Earth Sciences, 22, pp. 584-598.

Irving, E. and Wynne, P. J. 1990. Paleomagnetic evidence bearing on the evolution of the Canadian Cordillera. Philosophical Transactions of the Royal Society of London, 331, pp. 487-509.

Jelinek, V. 1981. Characterization of magnetic fabric of rocks. Tectonophysics, 79, pp. 563-567.

Keller, E. A., Bonkowski, M. S., Korsch, R. J. and Shlemon, R. J. 1982. Tectonic geomorphology of the San Andreas fault zone in the southern Indio Hills, Coachella Valley, California. Geological Society of America Bulletin, 93, pp. 46-56.

Kligfield, R., Owens, W. H. and Lowrie, W. 1981. Magnetic susceptibility, strain, and progressive deformation in Permian sediments from the Maritime Alps. Earth and Planetary Science Letters, 55, pp. 181-189.

Kligfield, R., Lowrie, W. and Dalziel, I. W. D. 1977. Magnetic susceptibility anisotropy as a strain indicator in the Sudbury Basin, Ontario. Tectonophysics, 40, pp. 287-308.

Lord, C. S. 1948. McConnell Creek Map-area, Cassiar district, British Columbia. Geological Survey of Canada, Memoir 251, 72 p.

Lowe, K. E. 1946. A graphical solution for certain problems of linear structure. American Mineralogist, 31, pp. 425-434.

Malvern, L. E. 1969. Introduction to the mechanics of a continuous medium. Prentice-Hall, New Jersey, 713 p.

Mardia, K. V. 1972. Statistics of directional data. Academic Press, London and New York, 357 p.

Means, W. D. 1983. Application of the Mohr-circle construction to problems of inhomogeneous deformation. Journal of Structural Geology, 5, pp. 279-286.

Monger, J. W. H. 1977. The Triassic Takla Group in McConnell Creek map-area, north-central British Columbia. Geological Survey of Canada, Paper 76-29, 45 p.

Monger, J. W. H. 1984. Cordilleran tectonics: a Canadian perspective. Bulletin Societé Géologique de France, 7, pp. 255-278.

Monger, J. W. H. and Church, B. N. 1977. Revised stratigraphy of the Takla Group, north-central British Columbia. Canadian Journal of Earth Sciences, 14, pp. 318-326.

Monger, J. W. H. and Irving, E. 1980. Northward displacement of north-central British Columbia. Nature, 285, pp. 289-294.

Nelson, M. R. and Jones, C. H. 1986. Paleomagnetism and crustal rotations along a shear zone, Las Vegas Range, southern Nevada. Tectonics, 6, pp. 13-33.

Nur, A., Ron, H. and Scotti, O. 1986. Fault mechanics and the kinematics of block rotations. Geology, 14, pp. 746-749.

Price, R. A. and Carmichael, D. M. 1986. Geometric test for late Cretaceous-Paleogene intracontinental transform faulting in the Canadian Cordillera. Geology, 14, pp. 468-471.

Ramsay, J. G. 1967. Folding and fracturing of rocks. McGraw-Hill, New York, 568 p.

Ramsay, J. G. and Huber, M. I. 1983. The techniques of modern structural geology. Academic Press, London and New York, v. 1, 307 p.

Richards, T. A. 1976a. McConnell Creek map area (94D/E), geology. Geological Survey of Canada, Open File 342.

Richards, T. A. 1976b. Takla Group (Reports 10-16): McConnell Creek map area (94D, East Half), British Columbia. Geological Survey of Canada, Paper 76-1a, pp. 43-50.

Robin, P.-Y. F. 1977. Determination of geologic strain using randomly oriented strain markers of any shape. Tectonophysics, 42, pp.T7-T16.

Robin, P.-Y. F. and Jowett, E. C. 1986. Computerized density contouring and statistical evaluation of orientation data using counting circles and continuous weighting functions. Tectonophysics, 121, pp. 207-223.

Rochette, P. 1987. Magnetic susceptibility of the rock matrix related to magnetic fabric studies. Journal of Structural Geology, 9, pp. 1015-1020.

Roddick, J. A. 1967. Tintina Trench. Journal of Geology, 75, pp. 23-33.

Ron, H., Aydin, A. and Nur, A. 1986. Strike-slip faulting and block rotation in the Lake Mead fault system. Geology, 14, pp. 1020-1023.

Ron, H. and Eyal, Y. 1985. Intraplate deformation by block rotation and mesostructures along the Dead Sea transform, northern Israel. Tectonics, 4, pp. 85-105.

Ron, H., Nur, A. and Eyal, Y. 1990. Multiple strike-slip fault sets: a case study from the Dead Sea transform. Tectonics, 9, pp. 1421-1431.

Shimamoto, T. 1989. The origin of S-C mylonites and a new fault-zone model. Journal of Structural Geology, 11, pp. 51-64.

Sylvester, A. G. 1988. Strike-slip faults. Geological Society of America Bulletin, 100, pp. 1666-1703.

Tchalenko, J. S. 1970. Similarities between shear zones of different magnitudes. Geological Society of America Bulletin, 81, pp. 1625-1640.

Tempelman-Kluit, D. J. 1979. Transported cataclasite, ophiolite and granodiorite in Yukon: evidence of arc-continent collision. Geological Survey of Canada Paper 79-14, 27 p.

Umhoefer, P. J. 1987. Northward translation of "Baja British Columbia" along the western margin of North America. Tectonics, 6, pp. 377-394.

Umhoefer, P. J., Dragovich, J., Cary, J. and Engebreston, D. C. 1989. Refinements of the "Baja British Columbia" plate-tectonic model for northward translation along the margin of western North America; in deep structure and past kinematics of accreted terranes. Hillhouse, J.W., Editor, Geophysical Monograph 50, IUGG v. 5, pp. 101-111.

Wheeler, J. O. and McFeely, P. (compilers). 1991. Tectonic Assemblage Map of the Canadian Cordillera and adjacent parts of the United States of America. Geological Survey of Canada, Map 1712A, scale 1:2 000 000.

Wilcox, R. E., Harding, T. P. and Seely, D. R. 1973. Basic wrench tectonics. American Association of Petroleum Geologists Bulletin, 57, pp. 74-96.

Woodsworth, G. J. 1976. Plutonic rocks of McConnell Creek (94D west half) and Aiken Lake (94C east half) map-area, British Columbia. Gelogical Survey of Canada, Paper 76-1a, pp. 26-30.

Zhang, G. and Hynes, A. 1991. Structures of the Takla Group east of the Finlay-Ingenika fault, McConnell Creek area, north-central B.C. (94D/8,9). In Geological Fieldwork 1990, B. C. Ministry of Energy, Mines and Petroleum Resources, Paper 1991-1, pp. 121-129.

Zhang, G. and Hynes, A. 1992. Structures along Finlay-Ingenika fault, McConnell Creek area, north-central British Columbia (94C/5; 94D/8,9). In Geological Fieldwork 1991, B. C. Ministry of Energy, Mines and Petroleum Resources, Paper 1992-1, pp. 147-154.

Zhang, G. and Hynes, A. (in review). Determination of position-gradient tensor from strain measurements and its implications for the displacement across a shear zone. Journal of Structural Geology.

Zhang, G., Hynes, A. and Irving, E. (submitted). Block rotations in the McConnell Creek area, north-central British Columbia: structural implications for the interpretation of paleomagnetic observations. Tectonics.

CHAPTER 2

Determination of Position-gradient Tensor from Strain Measurements and Its Implications for the Displacement across a Shear Zone

G. Zhang and A. Hynes

Earth and Planetary Sciences, McGill University, Montreal, PQ, Canada

ABSTRACT

A method is proposed for determination of the position-gradient tensor from conventional strain measurements. The position-gradient tensor can be multiplicatively decomposed into two components, left stretch and rotation tensors. The former is readily supplied by field strain-data whereas the latter is generally unknown in nature. In order to determine the position-gradient tensor using strain data, it is assumed that structures within a shear zone are symmetrical about the plane common to the transport direction and the pole to the shear zone, or alternatively, that the shear strain in the direction parallel to the pole to the shear zone on the plane normal to the transport direction in a parallel-sided shear zone is negligible. With these assumptions the position-gradient tensor is then fully determined from the attitude and principal ratios of the strain ellipsoid determined from field data. This method has been applied to the strain data from deformed

fragments in a succession of Late Triassic volcanic breccias abutting a large strike-slip shear zone in north-central B.C. The resulting position-gradient tensor is then used to constrain the displacement across the shear zone.

2.1 INTRODUCTION

A complete description of the deformation of a coherent body excluding any bulk translation is supplied by the position-gradient tensor **F** (Means 1983, p. 281, also known as the deformation-gradient tensor, Malvern 1969, p. 156, Means 1976, p. 173 and 1982, p. T2, Sanderson 1982, p. 202, or deformation tensor, De Paor 1983, p. 266, Means 1990, p. 961, Treagus 1990, p. 383, Hrouda 1992, p. 65) which includes both a rigid-body rotation and a stretch tensor. Recent descriptions of the Mohr circle for 2- and 3-D situations (De Paor 1981, as referenced by Means 1982, 1983, Allison 1984, De Paor & Means 1984, Treagus 1990, Simpson & De Paor 1993) which is derived from the **F** tensor, have demonstrated the potential of this tensor for the study of the rotation of planar and linear features during deformation.

Conventional strain data are generally used only to construct the deformation tensor ($\mathbf{B}^{-1}$ in the symbology of Malvern, 1969, and this paper) with respect to the strained state, which does not include any rigid-body rotation and forms the basis for the familiar Mohr diagram in reciprocal quadratic elongation-shear strain space. While this tensor and the associated Mohr diagram can provide information about changes in orientation between elements, they provide no information about total rotations. For these, the **F** tensor is required. With the Mohr circle representation for the **F** tensor in polar space (De Paor 1981, 1983, Treagus 1990, Simpson & De Paor 1993) deformation and rotation of lines and planes at a given point can be determined, although the operations are cumbersome for 3-D problems (Treagus 1990).

Mohr diagrams for the **F** tensor have so far not gained much importance in structural geology because of difficulties in determination of the **F** tensor in nature. In this paper we discuss the determination of the **F** tensor based on strain data obtained from deformed volcanic fragments near a shear zone. We show that, with certain simplifying assumptions that are probably valid for many shear zones, the **F** tensor may readily be determined from conventional strain data. Once the **F** tensor is known, many other features of the shear zone, and most particularly displacement across it, may be calculated.

2.2 POSITION-GRADIENT TENSOR AND ITS POLAR DECOMPOSITION

In this section we briefly review, first, the definitions of tensors, their physical meaning and application in characterising geological deformation, and secondly the polar decomposition of the position-gradient tensor.

Considering a point that moves from $x(x_1, x_2, x_3, t_0)$ in the undeformed state to $x'(x'_1, x'_2, x'_3, t)$ in the deformed state, the general relationship between x and x' may be written

$$\begin{aligned} x'_1 &= x'_1(x_1, x_2, x_3, t) \\ x'_2 &= x'_2(x_1, x_2, x_3, t) \\ x'_3 &= x'_3(x_1, x_2, x_3, t) \end{aligned} \tag{2.1}$$

where x_i and x'_i (i=1 to 3) represent the coordinates of the point in the undeformed and deformed states and t represents the time at which the strained state is achieved. If a vector $\mathbf{dx}$, with length ds, before deformation is transformed by equation (2.1) to $\mathbf{dx'}$, with length ds', after deformation, then we have

$$d\boldsymbol{x}' = \boldsymbol{F}\cdot d\boldsymbol{x} \tag{2.2a}$$

or

$$dx = F^{-1} \cdot dx' \tag{2.2b}$$

where **F** and $\mathbf{F}^{-1}$ are the position-gradient tensor and its inverse (Means 1983), where

$$F = \begin{pmatrix} \dfrac{\partial x_1'}{\partial x_1} & \dfrac{\partial x_1'}{\partial x_2} & \dfrac{\partial x_1'}{\partial x_3} \\ \dfrac{\partial x_2'}{\partial x_1} & \dfrac{\partial x_2'}{\partial x_2} & \dfrac{\partial x_2'}{\partial x_3} \\ \dfrac{\partial x_3'}{\partial x_1} & \dfrac{\partial x_3'}{\partial x_2} & \dfrac{\partial x'_3}{\partial x_3} \end{pmatrix} \tag{2.3}$$

F and $\mathbf{F}^{-1}$ are similar to the **M** and $\mathbf{M}^{-1}$ matrices of Ramsay and Graham (1970). It is evident that the elements on the leading diagonal of equation (2.3) represent stretch components along the three orthogonal coordinate axes, whereas those outside the leading diagonal are related to the shear components in the three directions. If the two elements on both sides of, and symmetric to, the leading diagonal are identical, the **F** tensor is symmetric, representing irrotational deformation. Otherwise, it is asymmetric, representing rotational deformation. As the deformation history or path of an orogenic event is generally not known in nature and what we see in the field are geological structures, the final products of a deformation, we can generally describe only the final state of the geological structures and relate them to their initial state. Consequently, the **F** tensor is reduced to the functions which are dependent only on spatial coordinates.

With the **F** tensor, it is possible to discuss the change of length of an element during deformation. The length (ds') of an element after deformation can be determined from equation (2.2),

$$(ds')^2 = (d\boldsymbol{x}')^T \cdot d\boldsymbol{x}' = (d\boldsymbol{x})^T \cdot \boldsymbol{F}^T \cdot \boldsymbol{F} \cdot d\boldsymbol{x} = (d\boldsymbol{x})^T \cdot \boldsymbol{C} \cdot d\boldsymbol{x} \qquad (2.4a)$$

where $\mathbf{F}^T$ is the transpose of **F** and $\mathbf{F}^T \cdot \mathbf{F}$ is the deformation tensor **C** (terminology of Malvern 1969) with respect to the undeformed state (d**x**). Similarly, its initial length (ds) is

$$(ds)^2 = (d\boldsymbol{x})^T \cdot d\boldsymbol{x} = (d\boldsymbol{x}')^T \cdot (\boldsymbol{F}^{-1})^T \cdot \boldsymbol{F}^{-1} \cdot d\boldsymbol{x}' = (d\boldsymbol{x}')^T \cdot \boldsymbol{B}^{-1} \cdot d\boldsymbol{x}' \qquad (2.4b)$$

where $\mathbf{F}^{-1}$ is the inverse of **F** and $(\mathbf{F}^{-1})^T \cdot \mathbf{F}^{-1}$ is the deformation tensor $\mathbf{B}^{-1}$ (terminology of Malvern 1969) with respect to the deformed state (d**x'**). It is evident from equations (2.4a) and (2.4b) that quadratic elongation of any line in the direction of d**x** and reciprocal quadratic elongation of any line in the direction of d**x'** can be expressed as

$$\lambda = \boldsymbol{n}^T \cdot \boldsymbol{C} \cdot \boldsymbol{n} \qquad (2.5a)$$

and

$$\lambda' = (\boldsymbol{n}')^{T} \cdot \boldsymbol{B}^{-1} \cdot \boldsymbol{n}' \qquad (2.5b)$$

where **n** and **n'** are unit column vectors for d**x** and d**x'**, respectively, and $\mathbf{n}^T$ and $(\mathbf{n}')^T$ are the transposes of **n** and **n'**. When **n** and **n'** in equations (2.5a) and (2.5b) are parallel to the initial and final principal directions of the strain state at a given point, the deformation tensors **C** and $\mathbf{B}^{-1}$ reach their extrema, giving the principal quadratic and reciprocal quadratic elongations. Both **C** and $\mathbf{B}^{-1}$ tensors are symmetric.

The tensor $\mathbf{B}^{-1}$ can be supplied by field strain data (see below). If we wish to determine rotation, however, it is the **F** tensor that we require. Generally, the **F** tensor can be decomposed into two components, a rigid-body rotation and a stretch tensor (Malvern 1969, De Paor 1983, Means 1983). In the case of infinitesimal strain, the symmetric and skew-symmetric matrices of the displacement-gradient tensor, which is equivalent to the position-gradient tensor, provide an additive decomposition of the displacement gradients into the sum of a pure strain and a pure rotation, because the displacement-gradient components are small compared with unity. In the case of finite strain, the symmetric and skew-symmetric matrices of the position-gradient tensor no longer provide decomposition of the position gradients. The position gradients can however be multiplicatively decomposed into the product of two tensors, one of which represents rigid-body rotation while the other represents deformation (Malvern 1969, De Paor 1983, Means 1983). The latter decomposition is frequently called the polar decomposition (Malvern 1969, De Paor 1983, Means 1983) and may be written

$$\boldsymbol{F} = \boldsymbol{R} \cdot \boldsymbol{U} = \boldsymbol{V} \cdot \boldsymbol{R} \tag{2.6}$$

where **R** is the rotation tensor, ;d **U** and **V** are symmetric right and left stretch tensors with respect to d**x** and d**x'**, respectively. Since they are the stretch tensors, **U** and **V** can be related to quadratic and reciprocal quadratic elongations as follows

$$\lambda = (\boldsymbol{P}^T \cdot \boldsymbol{U} \cdot \boldsymbol{P}) \cdot (\boldsymbol{P}^T \cdot \boldsymbol{U} \cdot \boldsymbol{P}) = \boldsymbol{P}^T \cdot \boldsymbol{U}^2 \cdot \boldsymbol{P} \tag{2.7a}$$

and

$$\lambda' = ((\boldsymbol{P}')^T \cdot \boldsymbol{V} \cdot \boldsymbol{P}')^{-1} \cdot ((\boldsymbol{P}')^T \cdot \boldsymbol{V} \cdot \boldsymbol{P}')^{-1} = (\boldsymbol{P}')^T \cdot (\boldsymbol{V}^2)^{-1} \cdot \boldsymbol{P}' \tag{2.7b}$$

where both **P** and **P'** are unit orthogonal matrices comprising column vectors for three orthogonal directions with respect to d**x** and d**x'**, respectively. Comparing equations (2.5a) with (2.7a) and (2.5b) with (2.7b), it follows that

$$\boldsymbol{C} = \boldsymbol{U}^2 \tag{2.8a}$$

and

$$\boldsymbol{B} = \boldsymbol{V}^2 \tag{2.8b}$$

The **V** tensor is the one generally determined directly by routine measurements of strain markers (e.g. oolites, concretions, reduction spots, lapilli, fossils, etc.) (Ramsay 1967, Elliott 1970, Ramsay & Huber 1983) in the field, or indirectly by measuring magnetic fabric (anisotropy of magnetic susceptibility) of strained rocks (Owens 1974, Hrouda 1987, Rochette 1988, Hrouda 1988, Borradaile & Puumala 1989, Henry 1990, Hrouda 1992, 1993). Determination of the **U** tensor in strained rocks is almost impossible because the initial directions of principal axes of the strain state are not known in nature unless the deformation was irrotational. Consequently, the right polar decomposition of the **F** tensor in equation (2.6) can rarely be applied to naturally deformed rocks and we concentrate here on the left polar decomposition. The **R** tensor, an orthogonal matrix, rotates the principal axes of **U** at **P** to the principal axes of **V** at **P'**; hence it performs rigid-body rotation of all lines and planes at a given point. The position-gradient tensor **F** can be uniquely determined if both the rotation tensor **R** and left stretch tensor **V** are known. The **R** tensor is also difficult to determine in the field, unless the initial directions of principal axes of the strain state are known (cf. Ramsay 1967, Ramsay & Graham 1970, Ramsay & Huber 1983, Hrouda 1992).

In the next sections, we discuss how to determine the **F** tensor based on strain measurements and simple assumptions concerning the geometry of structures in a shear zone.

2.3 DETERMINATION OF LEFT STRETCH TENSOR

We have determined the deformation tensor $\mathbf{B}^{-1}$ in a succession of Late Triassic volcanic breccias abutting a large strike-slip shear zone in north-central British Columbia. These volcanic breccias of the Late Triassic Takla Group are compositionally heterogeneous and dominated by sub-angular or sub-rounded fragments of greenish to dark grey clinopyroxene and clinopyroxene-plagioclase porphyries, commonly in a porphyritic matrix with the same composition as the fragments. Progressive straining of the volcanic fragments is well exhibited in an area of about one square kilometres, bounded to the west by a dextral strike-slip shear zone trending approximately 350° and dipping 75° northeast in the McConnell Creek area, north-central B. C. (Zhang & Hynes, in press). The shear zone is brittle-ductile in nature (Ramsay 1980) and displays well-defined S-C fabrics (Berthé *et al.* 1979) and horizontal slickenlines marked by tremolite and calcite fibres, from which its shear sense is inferred. The strained fragments are clearly displayed on a variety of sections with different orientations, allowing detailed strain analysis. According to the apparent aspect ratios and degree of development of foliations, the area has been divided into three domains in the direction normal to the north-northwest trending shear zone (Zhang & Hynes, in press). Domain 1 is about 600 metres wide and lies in the east, about 300 metres from the shear zone. Domain 2, about 200 metres wide, lies between Domains 1 and 3, and Domain 3 is mainly within the shear zone with a width of about 100 metres. The straining of the volcanic fragments is attributed to local deformation associated with motion along the north-northwest trending shear zone, because the aspect ratios of the strained fragments increase progressively moving from Domain 1 to Domain 3 and they show undeformed sub-rounded shapes east of Domain 1.

More than 700 strained volcanic fragments were measured on 60 sections of different orientations in the three domains, of which 20 sections are from Domain 1, 32 sections from Domain 2 and 8 sections from Domain 3 (Table 2.1). The mean sectional ellipses for all sections in each domain were then standardized with respect to each other (cf. Ramsay & Huber 1983) and used to calculate stretches along the intersections of each section with the three orthogonal planes: horizontal, east-west and north-south vertical (Zhang & Hynes, in press). In the analysis that follows, the sections in each domain are treated as if all sampled the same bulk strain ellipsoid, although there is probably a continuous change in bulk strain-ratio across each domain. In the ideal case, in which all fragments in each domain had the same eccentricity, this analysis should provide three perfect ellipses in the three planes for each domain. Only two datum sets, from Domains 1 and 3, respectively, depart significantly from this condition and were not used in further analysis. The least-squares best-fit strain ellipse (Erslev & Ge 1990) was then determined in each of the three planes (Table 2.1). Finally, components of the reciprocal quadratic deformation tensor $\mathbf{B}^{-1}$ in geographic space were

Table 2.1. Strain data from deformed volcanic fragments

Domain	plane	a	b	α (°)	$1+e_i$	trend (°)	plunge (°)	R_{12}	R_{23}	n_s	n_f
1	NE	3.73	1.00	160.6	3.785	343.3	7.6	1.552	2.589	19	170
	EW	2.54	1.03	66.8	2.438	091.3	66.6				
	NS	2.78	1.62	54.8	0.942	250.2	22.0				
2	NE	4.73	1.02	156.6	4.732	336.9	1.6	1.565	3.058	32	512
	EW	3.05	1.07	73.9	3.024	072.8	75.2				
	NS	3.24	1.86	40.6	0.989	246.5	14.7				
3	NE	17.84	0.91	151.0	35.740	332.2	6.2	15.736	2.560	7	58
	EW	2.23	0.99	75.1	2.271	087.2	75.5				
	NS	2.92	1.59	44.7	0.887	240.8	13.0				

Notes: NE, EW and NS: horizontal, east-west and north-south vertical planes; a and b: long and short axes of the least-squares best-fit strain ellipses in the above planes; α: angle between long axis of the strain ellipse and coordinate axis (eg. north, east and down in NE, EW and NS planes, respectively); $1+e_i$, where i = 1 to 3: values of long, intermediate and short axes of the strain ellipsoid; trend/plunge: direction of the corresponding axis of the strain ellipsoid; $R_{12} = (1+e_1)/(1+e_2)$; $R_{23} = (1+e_2)/(1+e_3)$; n_s: number of sections; n_f: number of fragments measured.

calculated using the strain ellipses in the three planes (cf. Ramsay 1967, Malvern 1969, Means 1976, Ramsay & Huber 1983), and eigenvalues and eigenvectors of the $\mathbf{B}^{-1}$ tensor were used to determine the axial ratios and directions of the strain ellipsoid for each domain (Table 2.1 and Fig. 2.1). Because only two-dimensional strain ratios are known, the values of the principal axes ($1+e_i$, where i = 1 to 3) of the strain ellipsoids (Table 2.1) have no physical meaning, but their ratios (R_{12} and R_{23}) can be determined. From the axial ratios R_{12} and R_{23}, it is clear that L-S fabrics are predominant in Domains 1 and 2 while L fabric characterizes Domain 3. In addition, E values (where $E=\ln[(1+e_1)/(1+e_3)]$) of Domains 1, 2 and 3 are equal to 1.39, 1.57 and 3.70, respectively and fall within the typical strain-anisotropy range of naturally deformed rocks (e.g. E is generally less than 4, cf. Pfiffner & Ramsay 1982, Hrouda 1993).

In the following analysis, it is assumed that the volcanic fragments experienced a constant volume deformation so that absolute values for the principal axes of the strain ellipsoid can be determined (Table 2.2). Here, we also define two coordinate systems, in geographic and shear spaces, respectively. In geographic space, we take axis x_g north, horizontal, y_g east horizontal and z_g pointing to the centre of Earth. In shear space, axis x_s is set parallel to the slickenlines on the shear surface of the footwall, pointing in the shear direction of the hanging wall, y_s is normal to the shear surface pointing torward the hanging wall and z_s is perpendicular to x_s and y_s, lying in the shear surface (Fig. 2.2). Both

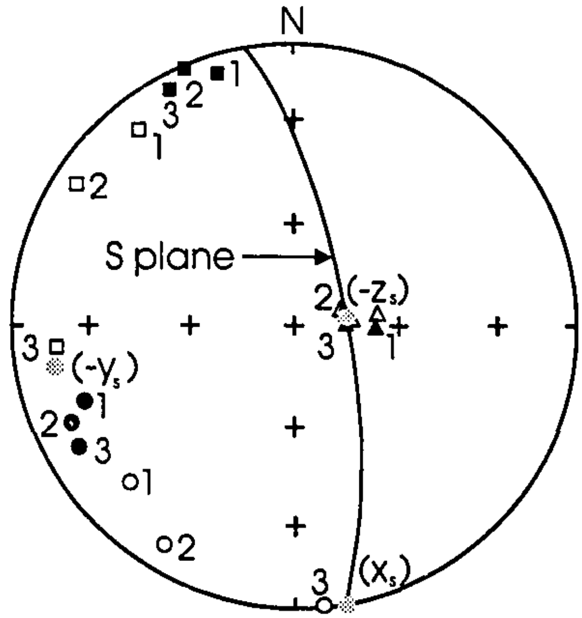

Fig. 2.1 Stereographic plot of principal directions of the strain ellipsoids from Domains 1, 2 and 3. Solid squares, triangles and circles: long, intermediate and short axes of the strain ellipsoids, respectively, in deformed state; open squares, triangles and circles: long, intermediate and short axes of the strain ellipsoids, respectively, in undeformed state (derived using the **F** tensors in Eqs. 2.20); S plane: shear plane; number: showing domain; grey circles: directions of the coordinate axes (x_s, y_s and z_s) of shear space in Fig. 2.2. All stereograms in this paper are lower-hemisphere, equal area projections.

Table 2.2. The observed and calculated strain ellipsoids

	observed			calculated				
Domain	$1+e_i$	trend (°)	plunge (°)	$1+e_i$	trend (°)	plunge (°)	d_i (%)	α_i (°)
1	1.841	343.3	7.6	1.835	341.5	2.3	0.3	5.7
	1.186	091.3	66.6	1.181	080.0	75.0	0.4	9.2
	0.458	250.2	22.0	0.470	250.9	14.8	2.5	7.2
2	1.956	336.9	1.6	1.956	337.4	3.3	0.0	1.8
	1.250	072.8	75.2	1.251	080.0	75.0	0.1	1.9
	0.409	246.5	14.7	0.409	246.5	14.6	0.0	0.1
3	8.591	332.2	6.2	8.585	331.8	4.8	0.1	1.5
	0.546	087.2	75.5	0.551	080.0	75.0	1.0	1.9
	0.213	240.8	13.0	0.213	240.6	14.2	0.1	1.2

Notes: d_i is the percentage of departure of the axis magnitude (i) of the calculated ellipsoid from that of the observed and α_i is the angle between the axes (i) of the observed and calculated strain ellipsoids, where i = 1 to 3. Other abbreviations as for Table 2.1.

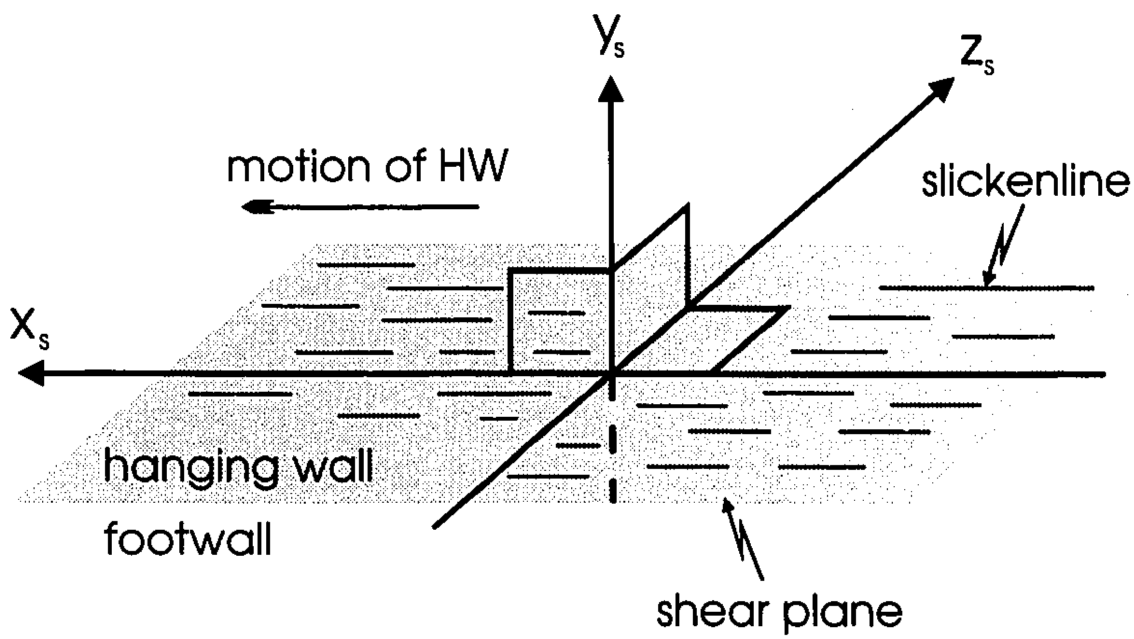

Fig. 2.2 Diagram showing the choice of coordinate system in shear space. x_s, y_s and z_s: coordinate axes in shear space; HW: hanging wall.

coordinate systems are righthanded.

As the deformation within each domain is homogeneous, the general transformations (2.1) become linear coordinate transformations and the position-gradient tensor in shear space can be written

$$\boldsymbol{F} = \begin{pmatrix} F_{xx} & F_{xy} & F_{xz} \\ F_{yx} & F_{yy} & F_{yz} \\ F_{zx} & F_{zy} & F_{zz} \end{pmatrix} \tag{2.9}$$

where $\mathbf{F}_{ij}$ are independent of position. The **F** tensor in equation (2.9) contains nine unknowns, and hence nine independent equations are required to solve for its components. From equation (2.6) it is evident that the components of the **F** tensor can be correlated to the left stretch and rigid-body rotation components of the deformation in shear space

$$\begin{pmatrix} F_{xx} & F_{xy} & F_{xz} \\ F_{yx} & F_{yy} & F_{yz} \\ F_{zx} & F_{zy} & F_{zz} \end{pmatrix} = \begin{pmatrix} V_{xx} & V_{xy} & V_{xz} \\ V_{yx} & V_{yy} & V_{yz} \\ V_{zx} & V_{zy} & V_{zz} \end{pmatrix} \begin{pmatrix} R_{xx} & R_{xy} & R_{xz} \\ R_{yx} & R_{yy} & R_{yz} \\ R_{zx} & R_{zy} & R_{zz} \end{pmatrix} \tag{2.10}$$

Furthermore, from equations (2.7b) and (2.8b), the left stretch tensor V_{ij} can be expressed as

$$\begin{pmatrix} V_{xx} & V_{xy} & V_{xz} \\ V_{yx} & V_{yy} & V_{yz} \\ V_{zx} & V_{zy} & V_{zz} \end{pmatrix} = (P'_s)^T \cdot P'_g \cdot \begin{pmatrix} 1+e_1 & 0 & 0 \\ 0 & 1+e_2 & 0 \\ 0 & 0 & 1+e_3 \end{pmatrix} \cdot (P'_g)^T \cdot P'_s \tag{2.11}$$

where $1+e_i = (1/\lambda_i)^{1/2}$, $\mathbf{P'}_g$ comprises the principal directions of the strain ellipsoid in geographic space and $\mathbf{P'}_s$ specifies the directions of the coordinate axes of shear space in geographic space. Since $\mathbf{P'}_g$ and $1+e_i$ are known from the strain analysis (Table 2.1 and Fig. 2.1) and $\mathbf{P'}_s$ is obtained from the attitudes of the slickenline and the shear zone (Fig. 2.1), the values of V_{ij} are fully specified by this equation, and determinate. The resulting **V** tensors for Domains 1, 2 and 3 are shown in equations (2.12a), (2.12b) and (2.12c).

$$\boldsymbol{V}^{(1)} = \begin{pmatrix} 1.8027 & 0.2061 & 0.0780 \\ 0.2061 & 0.5015 & -0.0803 \\ 0.0780 & -0.0803 & 1.1807 \end{pmatrix} \tag{2.12a}$$

$$V^{(2)} = \begin{pmatrix} 1.8772 & 0.3396 & -0.0218 \\ 0.3396 & 0.4873 & -0.0068 \\ -0.0218 & -0.0068 & 1.2510 \end{pmatrix} \tag{2.12b}$$

$$V^{(3)} = \begin{pmatrix} 7.7193 & 2.5497 & 0.1942 \\ 2.5497 & 1.0794 & 0.0732 \\ 0.1942 & 0.0732 & 0.5511 \end{pmatrix} \tag{2.12c}$$

2.4 DETERMINATION OF POSITION-GRADIENT TENSOR

The rotation tensor R_{ij} may be expanded, without loss of generality, into

$$\begin{pmatrix} R_{xx} & R_{xy} & R_{xz} \\ R_{yx} & R_{yy} & R_{yz} \\ R_{zx} & R_{zy} & R_{zz} \end{pmatrix} = \begin{pmatrix} \cos\omega_z & \sin\omega_z & 0 \\ -\sin\omega_z & \cos\omega_z & 0 \\ 0 & 0 & 1 \end{pmatrix} \begin{pmatrix} \cos\omega_y & 0 & \sin\omega_y \\ 0 & 1 & 0 \\ -\sin\omega_y & 0 & \cos\omega_y \end{pmatrix} \begin{pmatrix} 1 & 0 & 0 \\ 0 & \cos\omega_x & \sin\omega_x \\ 0 & -\sin\omega_x & \cos\omega_x \end{pmatrix} \quad (2.13)$$

where ω_x, ω_y and ω_z are rotational angles about coordinate axes x_s, y_s and z_s and the order of rotations is that ω_x takes place first followed sequentially by ω_y and ω_z. In order to calculate the **F** tensor, the rigid-body rotational angles (ω_x, ω_y and ω_z) and their order of rotations must be known, and it is ignorance of these that generally prevents determination of the **F** tensor.

In the region under discussion, however, the structures (e.g. the S-C fabrics) are symmetric to the plane that is common to the slickenline (x_s) and pole to the shear zone (y_s) (see Fig. 2.2), which is a common feature of shear zones (Ramsay & Graham 1970, Twiss and Gefell 1990). It follows that rotational angles ω_x and ω_y must be zero. Substituting ω_x and ω_y into equation (2.13) and then substituting equations (2.11) and (2.13) into (2.10), the relationships in equation (2.10) can be simplified to

$$\begin{pmatrix} F_{xx} & F_{xy} & F_{xz} \\ F_{yx} & F_{yy} & F_{yz} \\ F_{zx} & F_{zy} & F_{zz} \end{pmatrix} = \begin{pmatrix} V_{xx}\cos\omega_z - V_{xy}\sin\omega_z & V_{xx}\sin\omega_z + V_{xy}\cos\omega_z & V_{xz} \\ V_{yx}\cos\omega_z - V_{yy}\sin\omega_z & V_{yx}\sin\omega_z + V_{yy}\cos\omega_z & V_{yz} \\ V_{zx}\cos\omega_z - V_{zy}\sin\omega_z & V_{zx}\sin\omega_z + V_{zy}\cos\omega_z & V_{zz} \end{pmatrix} \tag{2.14}$$

The symmetry of structures within a shear zone requires not only that the rotational angles ω_x and ω_y equal zero but also that the shear components F_{xz}, F_{yz}, F_{zx} and F_{zy} in equation (2.14) be zero, as pointed out by Ramsay and Graham (1970). Consequently, equation (2.14) may be simplified to

$$\begin{pmatrix} F_{xx} & F_{xy} & 0 \\ F_{yx} & F_{yy} & 0 \\ 0 & 0 & F_{zz} \end{pmatrix} = \begin{pmatrix} V_{xx}\cos\omega_z - V_{xy}\sin\omega_z & V_{xx}\sin\omega_z + V_{xy}\cos\omega_z & 0 \\ V_{yx}\cos\omega_z - V_{yy}\sin\omega_z & V_{yx}\sin\omega_z + V_{yy}\cos\omega_z & 0 \\ 0 & 0 & V_{zz} \end{pmatrix} \tag{2.15}$$

Now we have 5 independent equations for 6 unknowns F_{xx}, F_{xy}, F_{yz}, F_{yy}, F_{zz} and ω_z, and the components F_{ij} are still indeterminate without other structural information. Below we discuss methods through which this other information may be supplied.

2.3.1 General Deformation

Provided several positions on the strain path are known, and provided the strain path results from progressive increments of strain in response to a constant stress state for constant rheology, it may be possible to determine **F** through forward modelling, searching for the incremental tensor $\mathbf{F}_i$ whose characteristics best account for the observed points along the strain path. The requirement of a successful forward model is that it reproduces the observed strain path, as illustrated on some kind of strain diagram like that of Fig. 2.3, and that the orientations of the principal axes of the modelled strain ellipsoids correspond within reasonable limits to those actually observed. With a computer such forward modelling, and the automatic searching for a viable solution, is a fairly straightforward procedure. We are able to show, however, that this procedure is unfortunately not applicable to the case we have studied.

The progressive strain path is derived by successive multipiication by the incremental F_i tensor:

$$\boldsymbol{F}_1 = \boldsymbol{F}_i \; ; \; \boldsymbol{F}_2 = \boldsymbol{F}_1 \cdot \boldsymbol{F}_i \; ; \; \boldsymbol{F}_3 = \boldsymbol{F}_2 \cdot \boldsymbol{F}_i \ldots \boldsymbol{F}_n = \boldsymbol{F}_{n-1} \cdot \boldsymbol{F}_i \tag{2.16}$$

In the following analysis, only constant volume deformation is considered.

Progressive irrotational strains for both constant and variable stress states have been discussed by a number of workers (e.g. Ramsay 1967, Ramberg 1975). The strain paths in ln R_{12}-ln R_{23} space can be expressed by the following relationships

$$(R_{12})_n = \prod_{i=1}^{n} \left(\frac{1+e_1}{1+e_2}\right)_i \tag{2.17a}$$

and

$$(R_{23})_n = \prod_{i=1}^{n} \left(\frac{1+e_2}{1+e_3}\right)_i \tag{2.17b}$$

where $1+e_i$ (i = 1 to 3) are values of the principal axes of the strain ellipsoid characterized by, and equal to the leading diagonal elements of, the incremental $\mathbf{F}_i$ tensor. For a constant stress state with constant stress-strain relationships throughout deformation, the above equations lead to

$$R_{12} = R_{23}^{K} \tag{2.18}$$

where $K = \ln[(1+e_1)/(1+e_2)]/\ln[(1+e_2)/(1+e_3)]$; hence the strain paths in ln R_{12}-ln R_{23} space are all straight lines (Ramsay 1967). In contrast, strain paths for variable stress states or variable stress-strain relationships are curved and they may move in various ways, including passing from an apparent flattening field to a field of apparent constriction (Ramsay 1967).

For progressive rotational strain it is clear from equation (2.16) that, if the strain ellipsoid described by the final position-gradient tensor $\mathbf{F}_n$ is symmetrical about the x_s-y_s plane of shear space (Figs. 2.1 and 2.2), as discussed earlier, the shear components F_{xz}, F_{zx}, F_{yz} and F_{zy} of the incremental $\mathbf{F}_i$ tensor must be zero; hence the $\mathbf{F}_i$ tensor contains only five non-zero components. All strain paths in ln R_{12}-ln R_{23} space for any $\mathbf{F}_i$ tensors are curved except those for plane strain even if the stress state and the stress-strain relationships are constant. This is because the non-zero shear components F_{xy} and F_{yx} contribute to the values of $1+e_i$, so that the simple relationships of equations (2.17) and (2.18) are no longer valid.

Figure 2.3 plots the strain paths for progressive simple shear (path 1) and simple shear combined with shortening along one axis (e.g. y_s, z_s and x_s for paths 2, 3 and 4, respectively) and equal extension along the other two axes, with extension along one axis (e.g. x_s, y_s and z_s for paths 5, 6 and 7, respectively) and equal shortening along the other two axes and with unequal extension along the three axes (e.g. paths 8 and 9). Their corresponding $\mathbf{F}_i$ tensors are:

$$\boldsymbol{F}_i^{(1)} = \begin{pmatrix} 1.0000 & 0.0600 & 0.0000 \\ 0.0000 & 1.0000 & 0.0000 \\ 0.0000 & 0.0000 & 1.0000 \end{pmatrix} \tag{2.19a}$$

$$F_i^{(2)} = \begin{pmatrix} 1.0057 & 0.0593 & 0.0000 \\ 0.0000 & 0.9887 & 0.0000 \\ 0.0000 & 0.0000 & 1.0057 \end{pmatrix} \tag{2.19b}$$

$$F_i^{(3)} = \begin{pmatrix} 1.0057 & 0.0603 & 0.0000 \\ 0.0000 & 1.0057 & 0.0000 \\ 0.0000 & 0.0000 & 0.9887 \end{pmatrix} \tag{2.19c}$$

$$F_i^{(4)} = \begin{pmatrix} 0.9887 & 0.0603 & 0.0000 \\ 0.0000 & 1.0057 & 0.0000 \\ 0.0000 & 0.0000 & 1.0057 \end{pmatrix} \tag{2.19d}$$

$$F_i^{(5)} = \begin{pmatrix} 1.0114 & 0.0597 & 0.0000 \\ 0.0000 & 0.9944 & 0.0000 \\ 0.0000 & 0.0000 & 0.9944 \end{pmatrix} \tag{2.19e}$$

$$F_i^{(6)} = \begin{pmatrix} 0.9944 & 0.0607 & 0.0000 \\ 0.0000 & 1.0114 & 0.0000 \\ 0.0000 & 0.0000 & 0.9944 \end{pmatrix} \tag{2.19f}$$

$$F_i^{(7)} = \begin{pmatrix} 0.9944 & 0.0597 & 0.0000 \\ 0.0000 & 0.9944 & 0.0000 \\ 0.0000 & 0.0000 & 1.0114 \end{pmatrix} \tag{2.19g}$$

$$F_i^{(8)} = \begin{pmatrix} 1.0070 & 0.0594 & 0.0000 \\ 0.0000 & 0.9900 & 0.0000 \\ 0.0000 & 0.0000 & 1.0030 \end{pmatrix} \tag{2.19h}$$

$$F_i^{(9)} = \begin{pmatrix} 0.9930 & 0.0606 & 0.0000 \\ 0.0000 & 1.0100 & 0.0000 \\ 0.0000 & 0.0000 & 0.9970 \end{pmatrix} \tag{2.19i}$$

where the superscripts show the path numbers. With progressive strain, strain

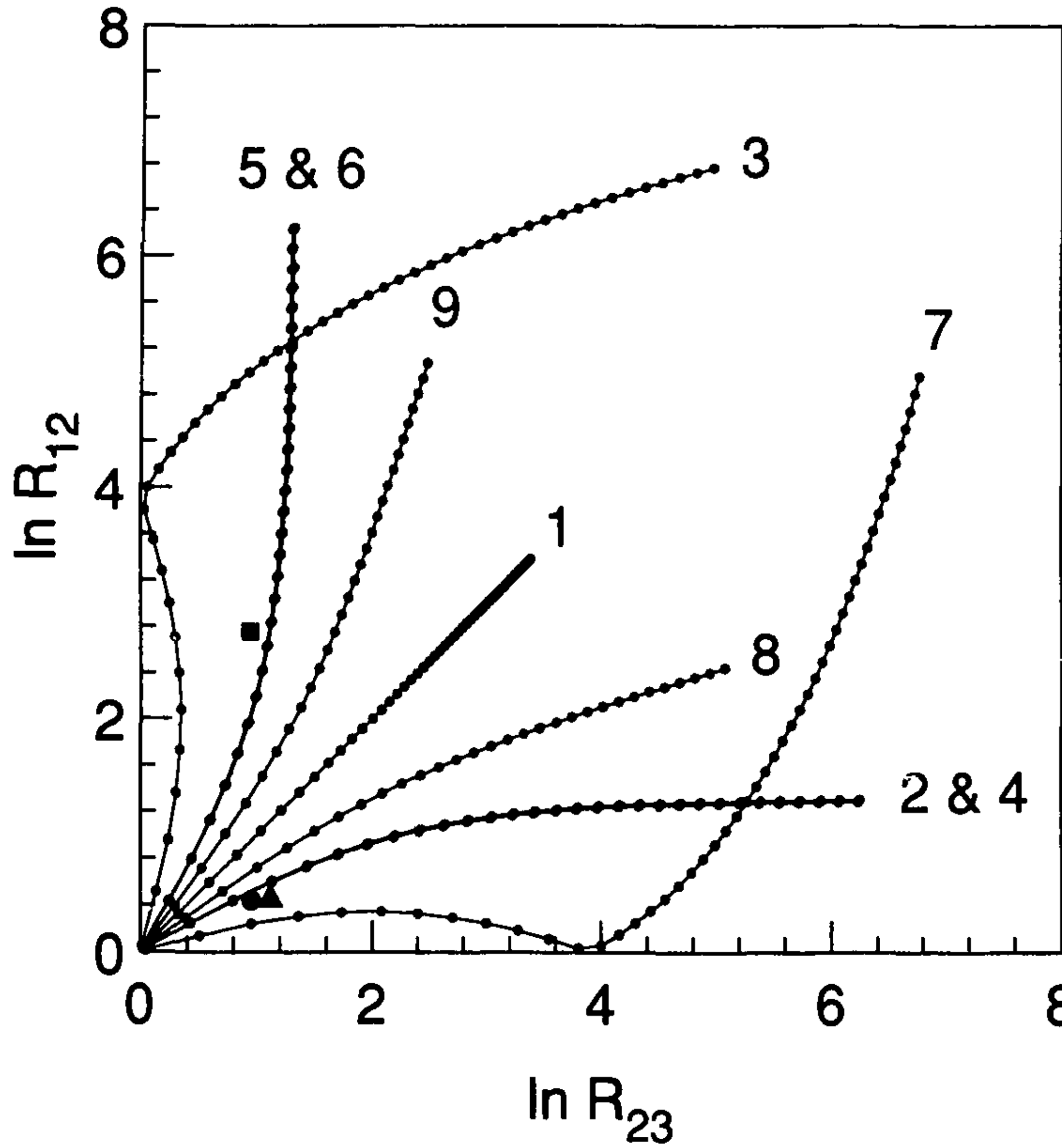

Fig. 2.3 Plot of shapes of the strain ellipsoids. R_{12} and R_{23}: as for Table 2.1; solid circle, triangle and square: the observed strain ellipsoids from Domains 1, 2 and 3, respectively; dots: the modelled strain ellipsoids. The strain ellipsoids of the first and every-tenth strain increment are plotted for each strain path; number shows the strain path. 500 increments for paths 1, 3 and 7 and 300 increments for the remaining paths.

ellipsoids starting in the apparent flattening field ($\ln R_{23} > \ln R_{12}$) change progressively toward oblate ellipsoids, giving rise to upward-convex strain paths (see paths 2, 4 and 8, Fig. 2.3), whereas those starting in the apparent constrictional field ($\ln R_{12} > \ln R_{23}$) change progressively toward prolate ellipsoids, displaying upward-concave strain paths (see paths 5, 6 and 9, Fig. 2.3). This is, however, not true for paths 3 and 7 (see below), which characterize simple shear combined with equal extension along x_s and y_s and shortening along z_s (Eq. 2.19c) and with equal shortening along x_s and y_s and extension along z_s (Eq 2.19g). The reason for this is that the shapes of the strain ellipsoids on path 3 before reaching perfect prolateness (Fig. 2.3) are governed mainly by the shear component F_{xy} (Eq. 2.19c) as indicated by the fact that the axes of $1+e_3$ lie in the x_s-y_s plane (Fig. 2.4; note that there is an abrupt change of orientation of $1+e_3$ when $\ln R_{23} = 0$), whereas subsequent ones are dominated by the stretch components F_{xx}, F_{yy} and F_{zz} (Eq. 2.19c) as the axes of $1+e_3$ are parallel to z_s (Fig. 2.4). Similarly, the shapes of strain ellipsoids on path 7 before reaching perfect oblateness (Fig. 3) are governed by F_{xy} (Eq. 2.19g), whereas subsequent ones are dominated by F_{xx}, F_{yy} and F_{zz} (Fig. 2.5).

The paths of Fig. 2.3 are representative of all the general styles of path that can be generated through progressive deformation under conditions of constant stress and rheology, although the paths can of course vary according to the values of F_{ij}. Increasing the shear component F_{yx} straightens the strain paths. For

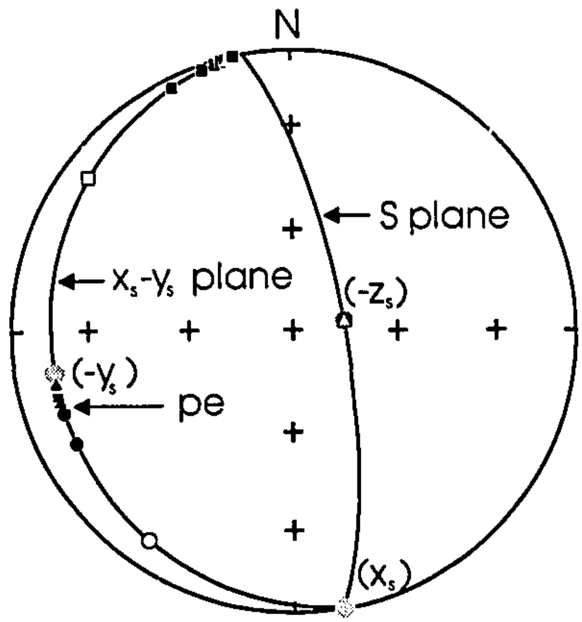

Fig. 2.4 Stereographic plot of principal axes of the strain ellipsoids for path 3 (Fig. 2.3). The strain ellipsoids of the first and every-fiftieth increment are plotted. Open square, triangle and circle: long, intermediate and short axes of the strain ellipsoid of the first incremental strain, respectively; x_s-y_s plane: plane common to x_s and y_s; pe: the prolate ellipsoid (at 114 incremental strain, Fig. 2.3); other symbols as for Fig. 2.1.

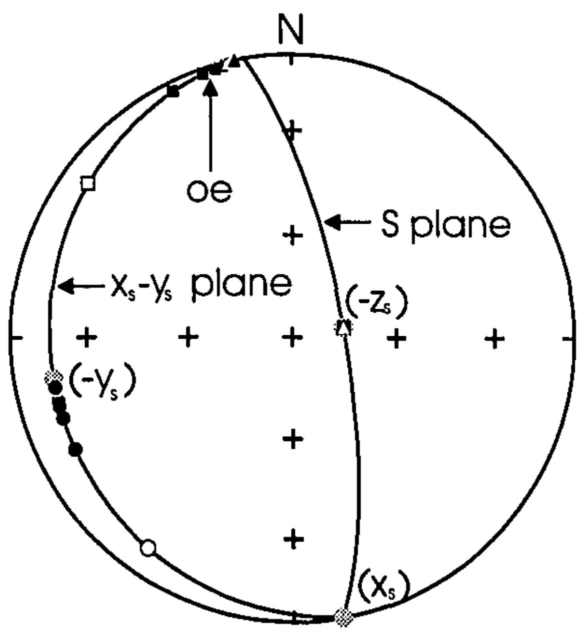

Fig. 2.5 Stereographic plot of principal axes of the strain ellipsoids for path 7 (Fig. 2.3). Oe: the oblate ellipsoid (at 114 incremental strain, Fig. 2.3); other symbols as for Fig. 2.4.

example, increasing F_{yx} from 0 to $F_{yx} = F_{xy}$, moves the resulting strain paths from 3 and 7 in Fig. 2.3 progressively to 3d and 7d of Fig. 2.6, respectively, which are the straight lines characteristic of irrotational strain. Increasing F_{xx}/F_{zz} moves path 3 in Fig. 3 to paths 3a and 3b of Fig 2.7. Decreasing the ratio changes path 3 in Fig. 2.3 to paths 3c and 3d of Fig. 2.7. Similarly, if the ratio of F_{zz}/F_{xx} increases, path 7 in Fig. 2.3 will change to paths 7a and 7b (Fig. 2.7); if the ratio decreases, path 7 will change to paths 7c and 7d (Fig. 2.7).

None of the progressive strain paths illustrated on Figs. 2.3 to 2.7 crosses the plane strain path (path 1, Figs. 2.3, 2.6 and 2.7), from the flattening to the constrictional field or vice versa, for low values of either ln R_{12} or ln R_{23}, a requirement that would be necessary for a strain path for our strain data. It appears, therefore, that our strain data cannot be explained through a progressive shear model like those presented here. The reason for this is probably that the rocks within the shear zone were involved in a progressive strain of variable stress state, or were associated with variable viscosity during the deformation. We have not pursued forward modelling further, because we have no means by which to choose among these various possibilities.

2.3.2 Simple Shear Combined with Extension Parallel to the Coordinate Axes

An alternative approach to this problem is based on the mode of

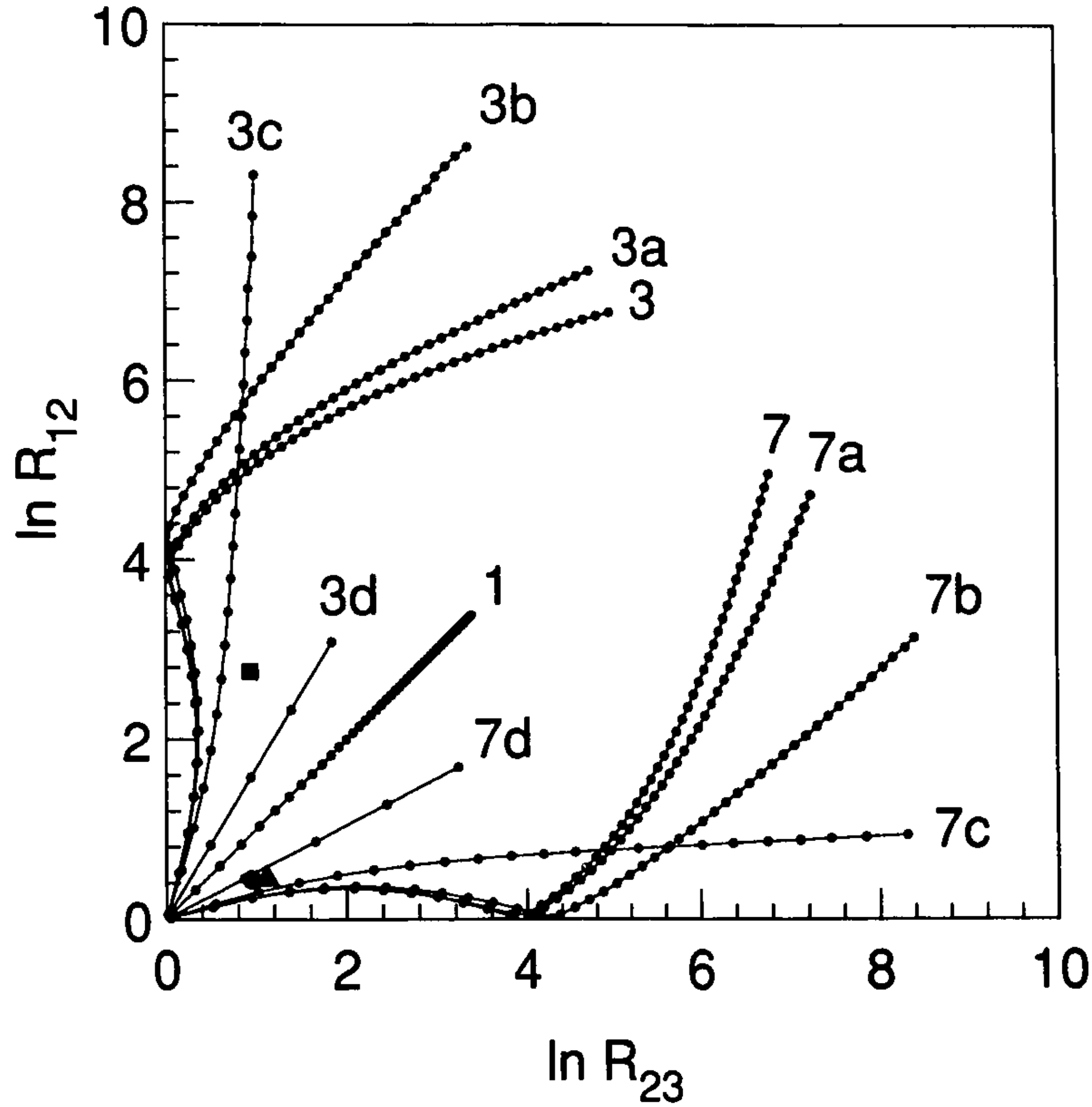

Fig. 2.6 Ln R_{12} vs ln R_{23} plot of strain paths showing the effect of the shear component F_{yx} of the $\mathbf{F}_i$ tensor on the shapes of the paths. Paths 3 and 7 are same as those in Fig. 2.3. F_{yx} = 0.0001, 0.0006, 0.0060 and 0.0604 for (a), (b), (c) and (d), respectively; values of other components of the $\mathbf{F}_i$ tensors are same as those in equations (2.19c) and (2.19g) for paths 3 and 7, respectively.

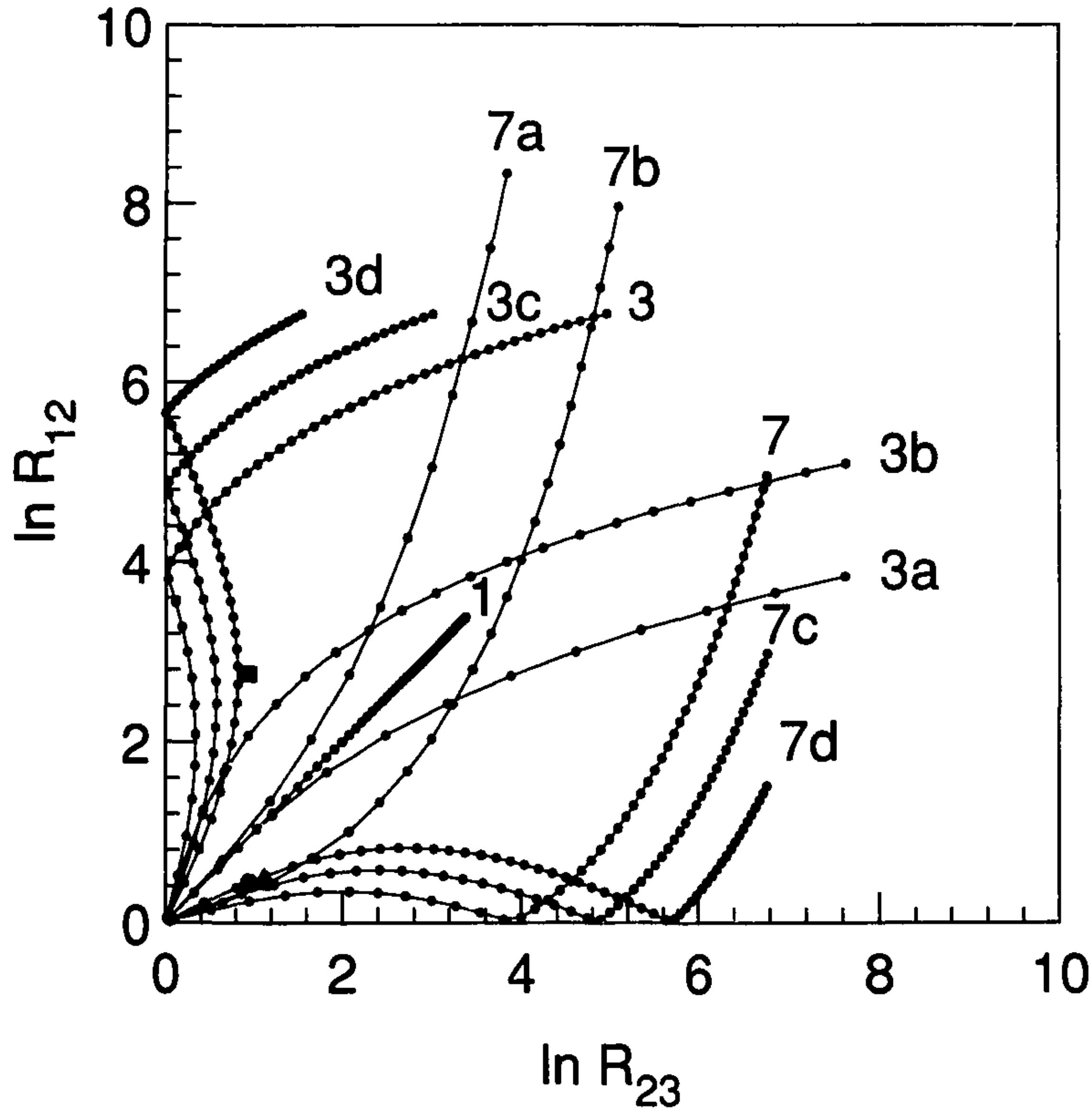

Fig. 2.7 Ln R_{12} vs ln R_{23} plot of strain paths showing the effect of ratios of F_{xx}/F_{zz} and F_{zz}/F_{xx} of the $\mathbf{F}_i$ tensor on the shapes of the paths. Paths 3 and 7 are same as those in Fig. 2.3. For paths 3a, 3b, 3, 3c and 3d the ratios of F_{xx}/F_{zz} are 1.090, 1.049, 1.017, 1.013 and 1.010, respectively; F_{xy} and F_{yx} are same as Eq. (2.19c). For paths 7a, 7b, 7, 7c and 7d the ratios of F_{zz}/F_{xx} are 1.097, 1.051, 1.017, 1.013 and 1.010, respectively; F_{xy} and F_{yx} are same as Eq. (2.19g).

deformation, which is frequently observed from field studies (Ramsay & Graham 1970, Ramsay 1980, Sanderson 1982). Since displacement along the slickenline direction is predominant in shear zones bounded by parallel planes of relatively large extent, shear strain (γ_{yx}) along y_s in the plane normal to x_s is small compared with unity (Ramsay & Graham 1970, Ramsay 1980, Sanderson 1982), and, to a first approximation, it can be neglected (i.e. $F_{yx} = 0$, cf. Ramsay 1967). The rigid-body rotational angle ω_z can then be calculated by putting $\tan \omega_z = V_{yx}/V_{yy}$. Substituting ω_z into equation (2.15), the **F** tensor can be determined by the left stretch tensor **V** alone. **F** and **R** tensors for each domain were calculated in this way and they are shown in equations (2.20) and (2.21),

$$\boldsymbol{F}^{(1)} = \begin{pmatrix} 1.5891 & 0.8758 & 0.0000 \\ 0.0000 & 0.5422 & 0.0000 \\ 0.0000 & 0.0000 & 1.1807 \end{pmatrix} \tag{2.20a}$$

$$\boldsymbol{F}^{(2)} = \begin{pmatrix} 1.3460 & 1.3518 & 0.0000 \\ 0.0000 & 0.5940 & 0.0000 \\ 0.0000 & 0.0000 & 1.2510 \end{pmatrix} \tag{2.20b}$$

$$F^{(3)} = \begin{pmatrix} 0.6616 & 8.1025 & 0.0000 \\ 0.0000 & 2.7687 & 0.0000 \\ 0.0000 & 0.0000 & 0.5511 \end{pmatrix} \tag{2.20c}$$

and

$$R^{(1)} = \begin{pmatrix} 0.9250 & 0.3801 & 0.0000 \\ -0.3801 & 0.9250 & 0.0000 \\ 0.0000 & 0.0000 & 1.0000 \end{pmatrix} \tag{2.21a}$$

$$R^{(2)} = \begin{pmatrix} 0.8205 & 0.5717 & 0.0000 \\ -0.5717 & 0.8205 & 0.0000 \\ 0.0000 & 0.0000 & 1.0000 \end{pmatrix} \tag{2.21b}$$

$$R^{(3)} = \begin{pmatrix} 0.3899 & 0.9209 & 0.0000 \\ -0.9209 & 0.3899 & 0.0000 \\ 0.0000 & 0.0000 & 1.0000 \end{pmatrix} \tag{2.21c}$$

where the superscripts show the domain numbers.

The strain ellipsoids for the three domains were calculated based on the **F** tensors in equations (2.20) (see Table 2.2 and Fig. 2.8). Errors in values of the corresponding principal axes of the observed and calculated strain ellipsoids are all less than 3 % (Table 2.2) and angles between the corresponding principal axes are less than 10° in Domain 1 and 2° in Domains 2 and 3 (Table 2.2 and Fig. 2.8). This indicates that the errors from the assumption that components F_{xz}, F_{zx}, F_{yz} and F_{zy} equal zero are not significant. The strongest support for the validity of the assumption comes from the values of V_{xz}, V_{zx}, V_{yz} and V_{zy} (Eqs. 2.12) calculated from the strain data. Since these values are all very much less than unity, and since they are the sole contributors to the values of F_{xz}, F_{zx}, F_{yz} and F_{zy} (Eq. 2.14), these **F** components could not be large.

Two-dimensional polar Mohr circles of the **F** tensors for Domains 1 (Eq. 2.20a), 2 (Eq. 2.20b) and 3 (Eq. 2.20c) are plotted in Figs. 2.9, 2.10 and 2.11, respectively. It can be seen from Figs. 2.9 to 2.11 that the deformation in the shear zone is predominantly in the x_s-y_s plane. Passing from Domain 1 to Domain 2 there is a slight increase in the deviatoric character of the strain in x_s-y_s and in the rigid-body rotational angle ω_z (see also Fig. 2.1 and Eq. 2.21, where $R_{xy} = \sin \omega_z$). Passing from Domain 2 to Domain 3 there is, however, a very large increase in both. In the y_s-z_s plane there is only minor deviatoric strain and in the z_s-x_s

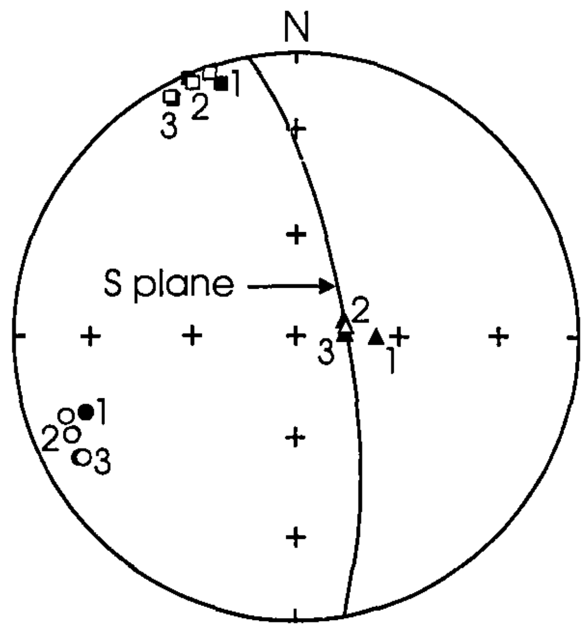

Fig. 2.8 Stereographic plot of principal axes of the strain ellipsoids from Domains 1, 2 and 3. Solid squares, triangles and circles: long, intermediate and short axes of the observed strain ellipsoids; open squares, triangles and circles: long, intermediate and short axes of the calculated strain ellipsoids (derived using the **F** tensors in Eqs. 2.20).

Fig. 2.9 Polar Mohr circles for Domain 1 in (a) x_s-y_s, (b) y_s-z_s and (c) z_s-x_s planes in shear space. In each of the Mohr diagrams, the reference axis is parallel to the undeformed pole to the shear zone and the baseline is parallel to the slickenline (x_s) in the shear plane in (a), or parallel to one of the coordinate axes (x_s, y_s and z_s) of shear space in (b) and (c). Each line in the plane represented plots as a point on the Mohr circle, determined by stretch along the line and the angle through which the line has rotated (eg. point P on Fig. 2.9b represents a line that has rotated through α and experienced stretch S_β, defined by the distance from the origin (0,0) to the point on the Mohr circle). The two lines that have experienced no rotation during the strain (the eigenvectors) plot as points on the reference axis (solid circles). Each Mohr circle has an anchor point (solid square) representing the deformed pole to the shear zone in both Mohr space and shear space. Given a point (S_β, α) on the Mohr circle (see Fig. 2.9a), the angle β' between the line and the baseline after strain is constructed by taking a line through (S_β, α) and the origin (0,0) and pivoting about its second intersection point on the Mohr circle (open circle) until it passes through the anchor point; the angle β between it and the baseline before strain is obtained by taking a line through (S_β, α) and parallel to the reference axis and pivoting about its second intersection point on the Mohr circle (open triangle) until it passes through the anchor point. S_1 and S_2 are maximum and minimum principal stretches, respectively, in the plane, and ω_z, ω_x and ω_y are rigid-body rotational angles about axes z_s, x_s and y_s, respectively. As for the conventional Mohr circle, greater degrees of deviatoric strain are reflected in larger-diameter circles. The degree of rigid-body rotation is reflected in the orientation of the diametric section of the Mohr circle whose projection passes through the origin (ω_z in Fig. 2.9a, ω_x and ω_y in Figs. 2.9b and 2.9c). Deformation of a unit square with base parallel to the baseline is sketched as a shaded parallelogram. (see Simpson & De Paor, 1993, for more detailed description of the polar Mohr circle).

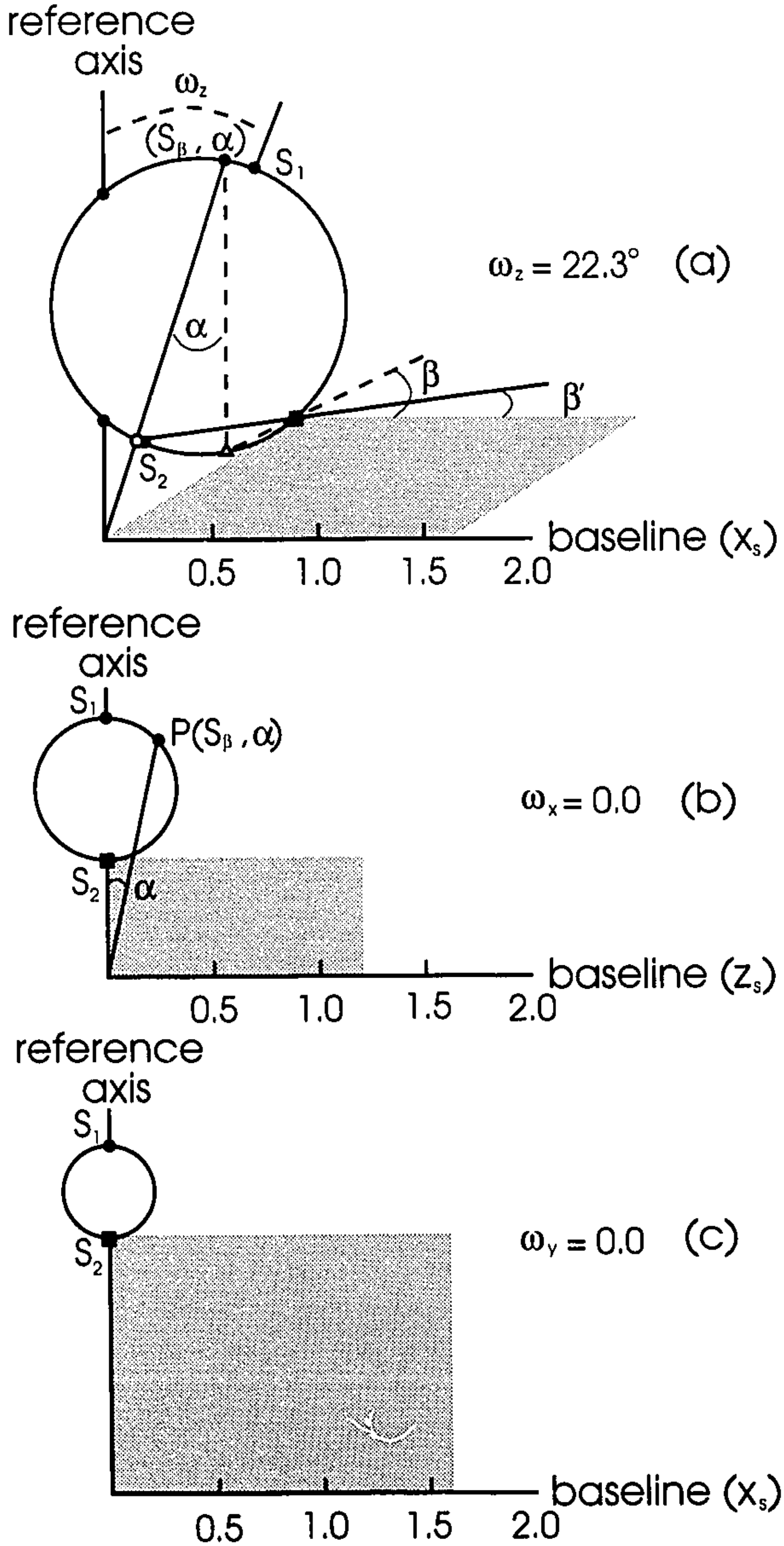

reference axis
ωz
(Sβ , α)
S1
α
β
β'
S2
ωz = 22.3°
(a)
baseline (xs)
0.5
1.0
1.5
2.0
reference axis
S1
P(Sβ , α)
S2
α
ωx = 0.0
(b)
baseline (zs)
0.5
1.0
1.5
2.0
reference axis
S1
S2
ωy = 0.0
(c)
baseline (xs)
0.5
1.0
1.5
2.0

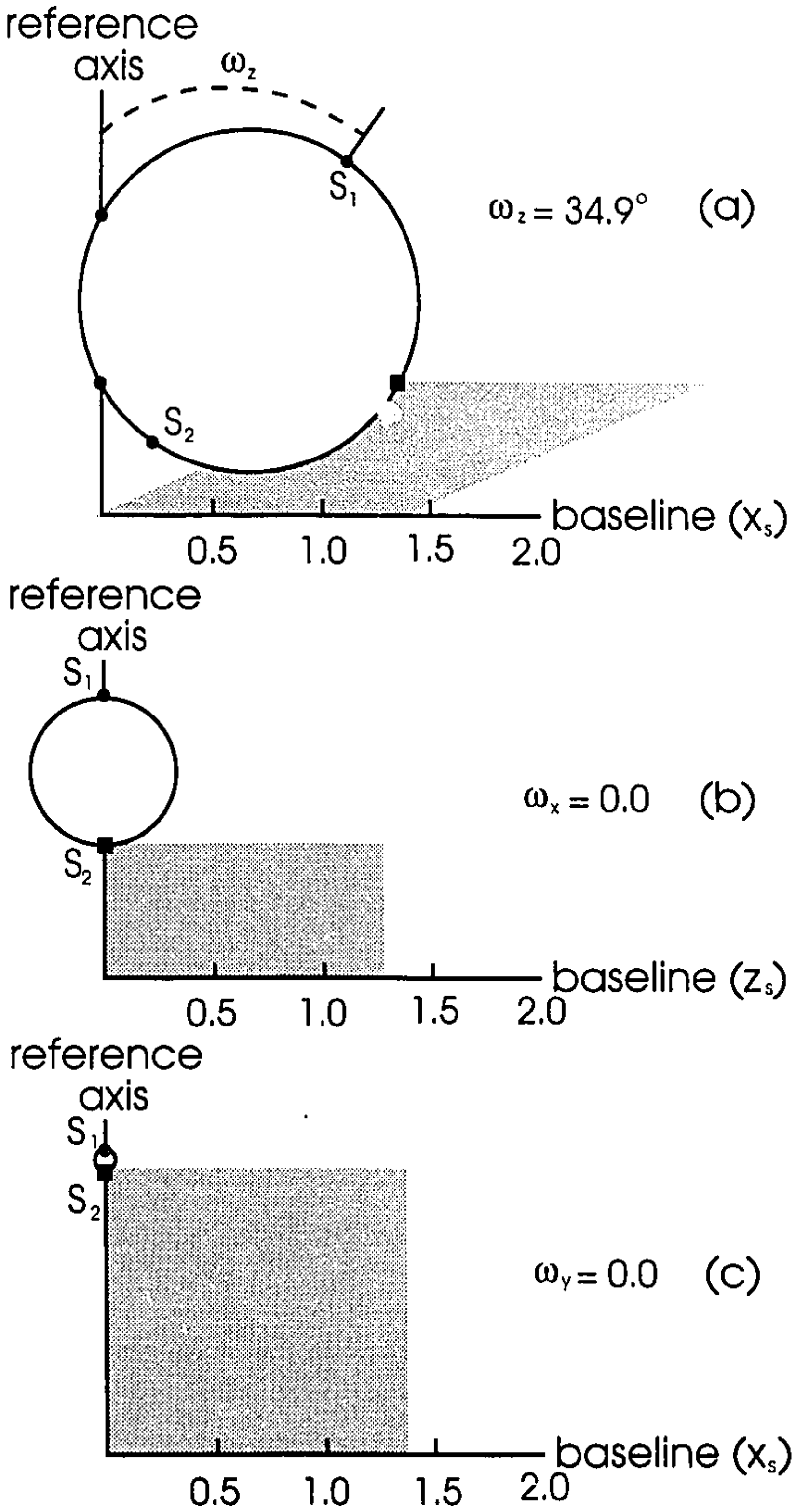

Fig. 2.10 Polar Mohr circles for Domain 2 in (a) x_s-y_s, (b) y_s-z_s and (c) z_s-x_s planes in shear space. Legend as for Fig. 2.9.

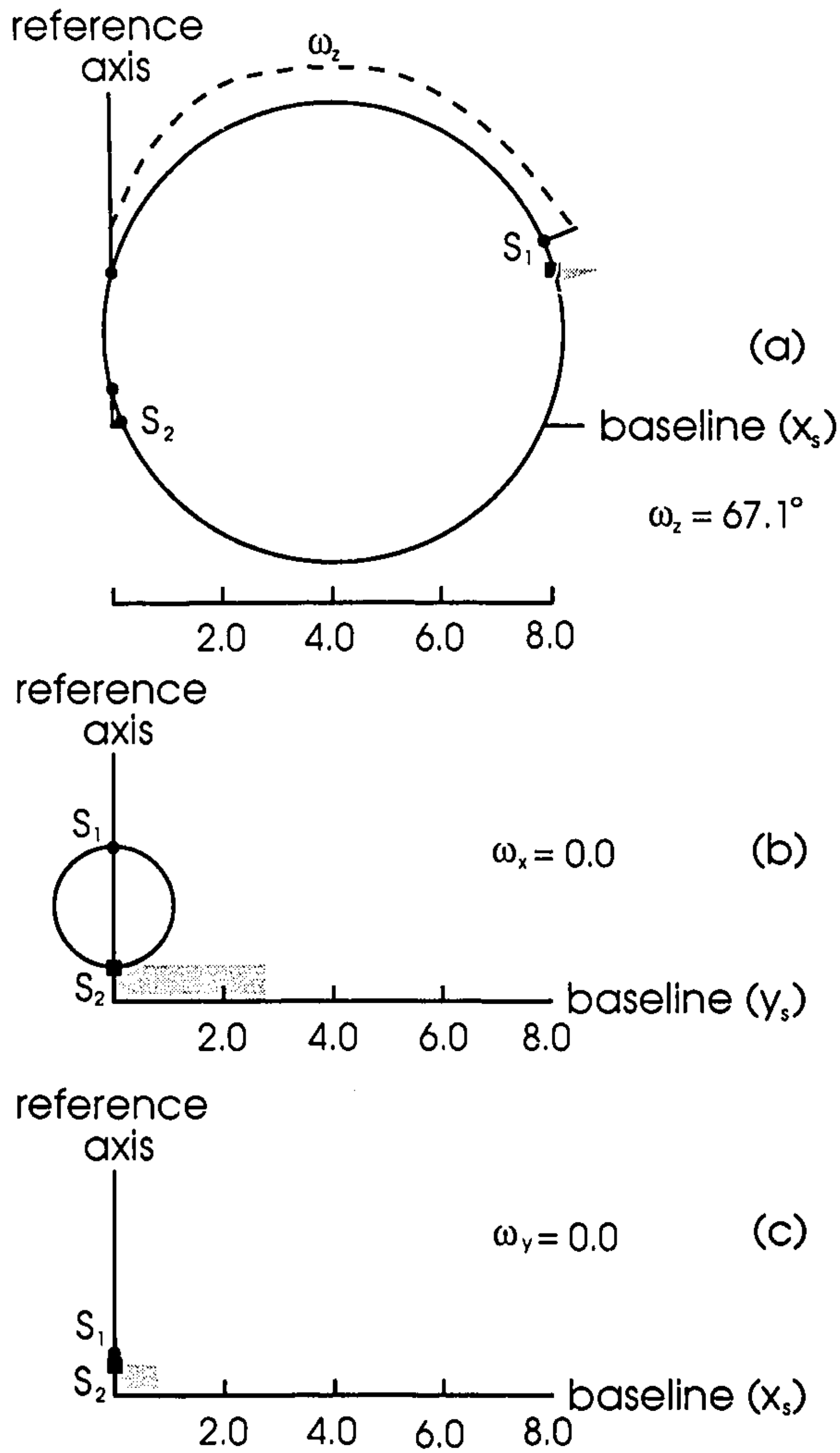

Fig. 2.11 Polar Mohr circles for Domain 3 in (a) x_s-y_s, (b) y_s-z_s and (c) z_s-x_s planes in shear space. Legend as for Fig. 2.9.

plane almost none. These characteristics are similar to those of progressive simple shear, but in true simple shear there is only one set of lines (parallel to the shear zone) that does not rotate, so that the eigenvectors (with unity eigenvalues) in the x_s-y_s plane coincide and the Mohr circle is tangential to the reference axis. This condition is not satisfied for any of the domains (see Figs. 2.9 to 2.11); their Mohr circles in x_s-y_s cut the reference axis, indicating that there was a component of flattening onto the shear plane in this region and that the shear zone is then broadly-speaking transpressional. The dextral, transpressive character of the shear zone is consistent with other geological structures observed in the region (Zhang & Hynes, in press).

2.5 IMPLICATIONS FOR DISPLACEMENT ACROSS THE SHEAR ZONE

F tensors for the three domains were derived by assuming there had been no shear strain in the direction parallel to the pole to the shear zone on the plane normal to the slickenline ($F_{yx} = 0$). The coordinate axes of shear space after deformation $x'(F_{xx}, F_{yx}, F_{zx})$ and $z'(F_{xz}, F_{yz}, F_{zz})$ are parallel to their corresponding initial axes x(1, 0, 0) and z(0, 0, 1). The **F** tensor therefore provides direct estimates of the strain on planes that were approximately parallel to the boundaries of the domains throughout the deformation, and the magnitudes of the diagonal terms correspond approximately to the longitudinal strains $(1+e_i)$ in planes parallel to these boundaries. Thus, it can be seen (Eq. 2.20) that in Domains 1 and 2 there was considerable stretching parallel to the boundaries (F_{xx}, $F_{zz} > 1$) and shortening perpendicular to them, but the opposite is true in Domain 3. While this difference may be accentuated by an overestimate of the eccentricity of the strain ellipsoid in Domain 3, its existence is not in doubt, since it is required from the strain differences and would be true for any reasonable assumptions about the rotational character of the strain. It is clear that such a marked strain discontinuity requires that the stress state changed across the boundary between Domains 2 and 3 during the progressive deformation and that the boundary was not coherent on the scale of tens of metres. This observation is consistent with the brittle-ductile character of the shear zone, although no unusual concentration of brittle features was actually observed in the boundary zone between Domains 2 and 3.

The total amount of shortening normal to the boundaries across Domains 1 and 2 is about 507 and 137 metres, respectively (the shortening across a domain is equal to $(1/F_{yy}-1)$ times the final width of the domain; for the values of F_{yy} see Eqs. 2.20a and 2.20b), and the total extension normal to the shear plane across Domain 3 is about 64 metres (the extension across a domain is equal to $(1-1/F_{yy})$ times the final width of the domain; for the value of F_{yy} see Eq. 2.20c). Total shortening normal to the shear zone is therefore 580 metres over 1480 metres, about 39 percent shortening. Cumulative dextral displacement along the shear zone is about 1700 metres (969 m in Domain 1, 455 m in Domain 2 and 293 m in Domain 3, the displacement across a domain is equal to (F_{xy}/F_{yy}) times the final width of the domain; for the values of F_{xy} and F_{yy} see Eqs. 2.20a, 2.20b and 2.20c), which represents a lower limit for the displacement since there may have been some rigid-body translation between Domains 2 and 3, and the amount of translation within the shear zone to the west of Domain 3 is at present indeterminate.

2.6 DISCUSSION AND CONCLUSIONS

Because fabrics in many natural shear zones are approximately symmetrical about the plane common to the slickenline or stretching lineation and the pole to the shear plane, shear strains γ_{xz}, γ_{zx}, γ_{yz} and γ_{zy} are probably commonly negligible. This geometrical condition requires that the components F_{xz}, F_{zx}, F_{yz} and F_{zy} of the position-gradient tensor must be zero. Strain analysis of deformed volcanic fragments from a shear zone in north-central British Columbia demonstrated that the errors arising from this assumption are negligible. Consequently, the position-gradient tensor is simplified to one that contains only five non-zero components.

Analysis of progressive strain may be used to determine the position-gradient tensor, provided deformation progresses under a constant stress regime with constant rheology, conditions that characterize many natural shear zones. The strain ellipsoids calculated in our study area are incompatible with these conditions, presumably reflecting a change in the stress state across the boundary between Domains 2 and 3.

An alternative method for determination of the position-gradient tensor from conventional strain data is based on the assumption that F_{yx} is negligible. This is valid for parallel-sided shear zones for which the stress regime is dominated by that for simple shear or simple shear combined with extension along the coordinate axes of shear space. It is clearly violated in "general shear", in the sense of De Paor (1983) and Simpson & De Paor (1993), where the shearing falls into either the sub- or super-simple shear field. The assumption $F_{yx} = 0$ overestimates the rotational angle ω_z for sub-simple shear and underestimates the angle ω_z for super-simple shear. It should therefore be used cautiously in regions in which such a regime is suspected.

As discussed above, the assumptions that F_{xz}, F_{zx}, F_{yz} and F_{zy} are negligible are probably valid for many shear zones in nature. With these assumptions the position-gradient tensor **F** can be uniquely determined from the left stretch tensor **V**, which can be obtained by conventional strain-analysis techniques. The deformation and rotation of lines and planes can then be readily studied either by tensor operations or by polar Mohr circle representations. As illustrated in this paper, once the **F** tensor is known, other features of the deformation, such as displacement on the boundaries or cumulative displacements across deformed zones, are then readily determinate.

2.7 ACKNOWLEDGEMENTS

This research was made possible by grants from the British Columbia Ministry of Energy, Mines and Petroleum Resources, the Geological Survey of Canada and the Natural Sciences and Engineering Research Council. G.Z. was supported by a McGregor Scholarship during his doctoral research. Their support is gratefully acknowledged.

2.8 REFERENCES

Allison, I. 1984. The pole of the Mohr diagram. *J. Struct. Geol.* 5, 331-333.

Berthé, D., Choukroune, P. and Jegouzo, P. 1979. Orthogneiss, mylonite and non-coaxial deformation of granites: the example of the south Armorican shear zone. *J. Struct. Geol.* 1, 31-42.

Borradaile, G. J. and Puumala, M. A. 1989. Synthetic magnetic fabrics in a plasticene medium. *Tectonophysics.* 164, 73-78.

De Paor, D. G. 1983. Orthographic analysis of geological structures--I. Deformation theory. *J. Struct. Geol.* 5, 255-277.

De Paor, D. G. and Means, W. D. 1984. Mohr circles of the first and second kind and their use to represent tensor operations. *J. Struct. Geol.* 6, 693-701.

Elliott, D. 1970. Determination of finite strain and initial shape from deformed elliptical objects. *Bull. geol. Soc. Am. 81*, 2221-2235.

Erslev, E. A. and Ge, H. 1990. Least-squares center-to-center and mean object ellipse fabric analysis. *J. Struct. Geol.* 12, 1047-1059.

Henry, B. 1990. Magnetic fabric implications for the relationship between deformation mode and grain growth in slates from the Borrowdale Volcanic Group in the English Lake District. *Tectonophysics.* 178, 225-230.

Hrouda, F. 1987. Mathematical model relationship between the paramagnetic anisotropy and strain in slates-reply. *Tectonophysics.* 142, 323-327.

Hrouda, F. 1988. Mathematical model relationship between the paramagnetic anisotropy and strain in slates-reply. *Tectonophysics.* 156, 315.

Hrouda, F. 1992. Separation of a component of tectonic deformation from a complex magnetic fabric. *J. Struct. Geol.* 14, 65-71.

Hrouda, F. 1993. Theoretical models of magnetic anisotropy to strain relationship revisited. *Physics of the Earth and Planetary Interios.* 77, 237-249.

Malvern, L. E. 1969. Introduction to the mechanics of a continuous medium. *Prentice-Hall, New Jersey.*

Means, W. D. 1976. Stress and strain. Basic concepts of continuum mechanics for geologists. *Springer, New York.*

Means, W. D. 1982. An unfamiliar Mohr circle construction for finite strain. *Tectonophysics* 89, T1-T6.

Means, W. D. 1983. Application of the Mohr-circle construction to problems of inhomogeneous deformation. *J. Struct. Geol.* 5, 279-286.

Means, W. D. 1990. Kinematics, stress, deformation and material behavior. *J. Struct. Geol.* 12, 953-971.

Owens, W. H. 1974. Mathematical model studies on factors affecting the magnetic anisotropy of deformed rocks. *Tectonophysics.* 24, 115-131.

Pfiffner, O. A. and Ramsay, J. G. 1982. Constraints on geological strain rates: arguments from finite strain states of naturally deformed rocks. *J. Geophys. Res.*, 87, 311-321.

Ramberg, H. 1975. Particle path, displacement and progressive strain applicable to rocks. *Tectonophysics* 28, 1-37.

Ramsay, J. G. 1967. Folding and fracturing of rocks. McGraw-Hill, New York and San Francisco.

Ramsay, J. G. 1980. Shear zone geometry: a review. *J. Struct. Geol.* 2, 83-99.

Ramsay, J. G. and Graham, R. H. 1970. Strain variation in shear belts. *Can. J. Earth Sci.* 7, 786-813.

Ramsay, J. G. and Huber, M. 1983. The techniques of modern structural geology. *Academic Press, London and New York*, v. 1.

Rochette, P. 1988. Mathematical model relationship between the paramagnetic anisotropy and stran in slates-discussion. *Tectonophysics.* 156, 313-314.

Sanderson, D. J. 1982. Models of strain variation in nappes and thrust sheets: a review. *Tectonophysics.* 88, 201-233.

Simpson, C. and De Paor, D. G. 1993. Strain and kinematic analysis in general shear zones. *J. Struct. Geol.* 15, 1-20.

Treagus, S. H. 1990. The Mohr diagram for three-dimensional reciprocal stretch vs rotation. *J. Struct. Geol.* 12, 383-395.

Twiss, R. J. and Gefell, M. J. 1990. Curved slickenfibers: a new brittle shear sense indicator with application to a sheared serpentinite. *J. Struct. Geol.* 12, 471-481.

Zhang, G. and Hynes, A. (in press). Fabrics and kinematic indicators associated with the local structures along Finlay-Ingenika fault, McConnell Creek area, north-central British Columbia. *Can. J. Earth Sci.*

CHAPTER 3

Block Rotations in the McConnell Creek Area, North-central British Columbia: Structural Implications for the Interpretation of Paleomagnetic Observations

G. Zhang[1], A. Hynes[1] and E. Irving[2]

[1]Earth and Planetary Sciences, McGill University, Montreal, PQ, Canada

[2]Pacific Geoscience Centre, Geological Survey of Canada, Sidney, B.C., Canada

ABSTRACT

Structures developed in association with transpressive motions on the dextral, strike-slip Finlay-Ingenika fault (FIF) in the McConnell Creek area are dominated by subvertical to vertical strike-slip faults. These faults cut the area into discrete, fault-bounded blocks several kilometres wide. Stress tensors for 24 sites were inverted from the regional cleavage which predates the block-bounding faults. The site-mean stress tensors indicate that the fault-bounded blocks were rotated clockwise about a subvertical axis during progressive dextral motion on the FIF. The amount of rotation varies systematically over the area with maximum values

(58.7 ± 3.3^o) close to the FIF and minimum values (0.0 ± 1.6^o) about 20 kilometres away from it. Paleomagnetic samples were collected from 13 sites in the widespread Early Jurassic to Cretaceous plutonic rocks. Interpretable magnetic components of the Late Cretaceous, isolated by both stepwise AF and thermal demagnetization from 6 sites, were used to calculate the paleopole. The observed paleopole has a low value of Fisher's precision $k = 48$, and is significantly different from the late Cretaceous reference pole for cratonal North America (CNA). After corrections for the local block rotations, the observed paleopole has a high value of $k = 383$ and moves closer to the reference pole but is still significantly different from it. Rotation about the Eulerian pole for the best-fitting small circle to the Tintina trench and northern Rocky Mountain trench fault zone, however, brings the observed pole into coincidence with that for CNA, and requires only ~670 kilometres of dextral displacement on the fault zone. It is likely, therefore, that local structures associated with dextral strike-slip faults in the western Canadian Cordillera may account for at least part of the paleomagnetic disparity between some western parts of the Canadian Cordillera and CNA.

3.1 INTRODUCTION

Since the 1970's, aberrant Cretaceous paleomagnetic data have been reported frequently from the western Canadian Cordillera (e.g. Beck and Noson, 1972; Irving, 1979; Monger and Irving, 1980; Beck *et al.*, 1981; Irving *et al.*, 1985; Rees, *et al.*, 1985; Marquis and Globerman, 1988; Butler *et al.*, 1988; Irving and Wynne, 1990; Irving and Thorkelson, 1990; Irving and Wynne, 1991; Wynne *et al.*, 1992). Three hypotheses have been suggested to explain them. The tilting hypothesis (cf. Beck and Noson, 1972; Beck *et al.*, 1981; Butler *et al.*, 1989; 1990; Irving and Wynne, 1990; Wynne et al., 1992) requires regional tilting to the south and southwest by 18 to 33°. The northward transport and clockwise rotation hypothesis (cf. Beck and Noson, 1972; Monger and Irving, 1980; Beck *et al.*, 1981; Irving *et al.*, 1985; Umhoefer, 1987; Irving and Wynne, 1990; Umhoefer *et al.*, 1990; Irving and Wynne, 1991) requires a northward displacement of 2000 to 3000 kilometres combined with clockwise rotation of 9-75°. The combined hypothesis of tilting and northward transport (cf. Irving and Wynne, 1990; Umhoefer *et al.*, 1990) requires a northward displacement of about 1500 kilometres but variable tilt to the south and southwest.

Both tilting and clockwise rotation should give rise to structural features observed in the field unless the entire western Canadian Cordillera experienced them as one block, which seems unlikely (cf. Beck, 1992). The purpose of this work was to conduct a detailed structural analysis of one region of the Canadian Cordillera from which aberrant paleomagnetic poles had been reported, and to use the resulting structural features to constrain the causes of the paleomagnetic disparity.

We have carried out a detailed structural analysis of part of the eastern Intermontane Belt of north-central British Columbia adjacent to the dextral strike-slip Finlay-Ingenika fault (FIF) (Gabrielse, 1985). In this paper, we first review the structural characteristics of the region. Secondly, we describe the paleomagnetism of the plutonic rocks there. Finally, we discuss correction of the observed aberrant paleomagnetic directions based on the results of the structural analysis.

3.2 TECTONIC SETTING AND MAJOR STRUCTURES

The study area lies within the Intermontane Belt in north-central British Columbia (Fig. 3.1) and straddles the boundary between the Quesnellia and Stikinia tectonostratigraphic terranes (Monger *et al.*, 1982; Monger, 1984; Gabrielse, 1991). Terrane interactions in north-central B.C. may have started as early as the Late Devonian (Gabrielse, 1991). Stikinia, Cache Creek, Quesnellia and Slide Mountain terranes had been essentially amalgamated by the Early Jurassic due to the closing of the Cache Creek ocean, forming the composite Terrane I, and were subsequently accreted to the ancient margin of North America during middle Jurassic contraction (Monger *et al.*, 1982; Monger, 1984; Gabrielse, 1991). This northeast-southwest contraction continued throughout the Late Jurassic and Early Cretaceous and was followed by dextral strike-slip faulting. The contraction regime is represented in the northwest-trending, northeast-vergent Skeena fold belt of the Bowser Basin (Evenchick, 1991) to the north of the study area, whereas the strike-slip faulting regime is represented by transpressive motion on the FIF, one of the prominent dextral strike-slip fault zones in north-central B.C., along which Gabrielse (1985) has shown that about 110 kilometres of dextral displacement is required for the restoration of Kutcho fault in the north with Pinchi fault in the south.

The area is underlain by Late Triassic Takla Group volcaniclastic and minor

Fig. 3.1 Generalized structural map of the Johanson Lake area (after Zhang and Hynes, in press). Note that site 5 is from west of McConnell Creek and outside the map sheet. Insert, main tectonic units of the Canadian Cordillera. FTB, Fold and Thrust Belt; OB, Omineca Belt; IMB, Intermontane Belt; CPB, Coast Plutonic Belt; ISB, Insular Belt (after Monger, 1984).

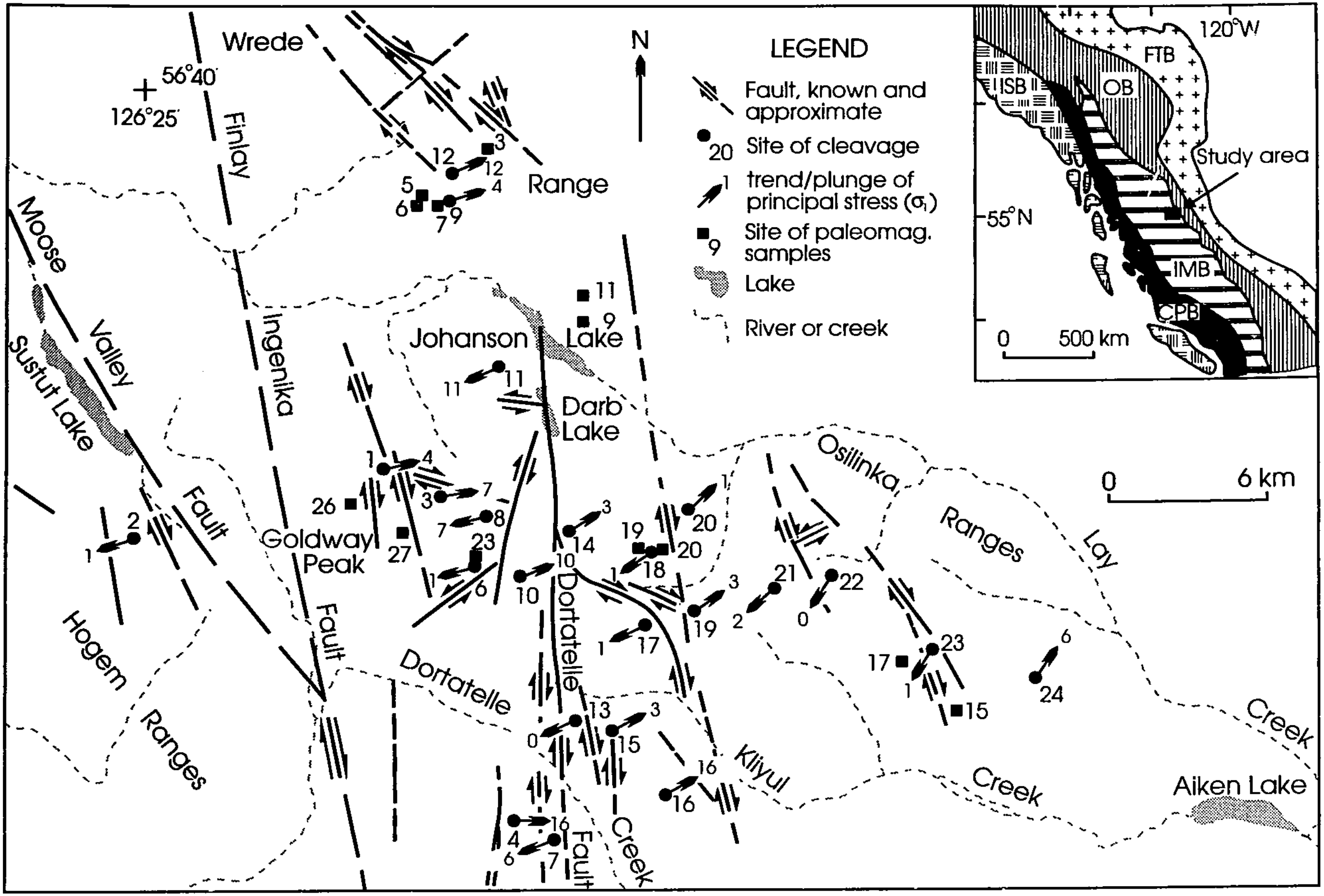

Wrede
Range
56°40'
126°25'
N
LEGEND
Fault, known and approximate
Site of cleavage
trend/plunge of principal stress (σ1)
Site of paleomag. samples
Lake
River or creek
Finlay
Ingenika
Fault
Moose
Valley
Sustut Lake
Fault
Johanson
Lake
Darb
Lake
Goldway
Peak
Hogem
Ranges
Dortatelle
Dortatelle
Fault
Creek
Osilinka
Ranges
Lay
Creek
Kliyul
Creek
Aiken Lake
0
6 km
120°W
FTB
OB
ISB
Study area
55°N
IMB
CPB
0
500 km

sedimentary rocks (Monger, 1977; Monger and Church, 1977), which are extensively intruded by Early Jurassic to Cretaceous plutonic rocks (Lord, 1948; Roots, 1954; Richards, 1976a, b; Woodsworth, 1976). Detailed geological mapping and structural analysis (Zhang and Hynes, in press) indicate that the structures resulting from dextral transpressive displacement on the FIF are dominated by subvertical to vertical, dextral strike-slip faults trending northwest, north-northwest and north-south, and sinistral strike-slip faults trending east-northeast as well as some large-scale northwest to north-northwest trending folds (Fig. 3.1). All these features can be related to the stress field associated with movement on the FIF (Zhang and Hynes, in press). Strain analysis of the deformed volcanic fragments along one of the north-northwest trending, dextral strike-slip faults shows that the principal orientations of the strain ellipsoids are in accordance with those of the magnetic susceptibility ellipsoids from the adjacent deformed dioritic rocks (Zhang and Hynes, in press), indicating that the plutonic rocks experienced the same deformation as the Late Triassic Takla Group volcanics.

The age of the strike-slip faulting is unknown but was probably not earlier than middle Cretaceous as Early Jurassic to Cretaceous dioritic rocks were involved in the faulting in many places. No compelling evidence for deformation associated with the Late Jurassic to Early Cretaceous contraction has been recognized in the Late Triassic Takla Group volcanics in this area. This is presumably because the local deformation associated with dextral transpressive displacement on the FIF was so strong that all contractional structures were transformed into strike-slip structures, as the stress state for the local deformation is similar to that for the regional contraction. For example, northwest-trending thrust faults produced in the northeast-southwest contractional regime could be readily reused in the dextral strike-slip regime (Zhang and Hynes, in press).

Some of the major strike-slip faults cut the Late Triassic Takla Group rocks into a number of discrete, weakly deformed blocks with diameters ranging from a few to tens of kilometres. As dextral transpressive displacement on the FIF progressed, deformation was apparently concentrated in the previously-formed fault zones while the fault-bounded blocks remained relatively undeformed. Within the fault-bounded blocks the only visible deformation is a spaced cleavage. This cleavage has permitted us to track the relative motions of adjacent fault blocks.

3.3 STATISTICS OF REGIONAL CLEAVAGE

The cleavage within the fault-bounded blocks has been classified into local and regional cleavage (see Zhang and Hynes, in press for details). The locally distributed cleavage is produced by displacement on the block-bounding strike-slip faults and is restricted to their vicinity. The regionally distributed cleavage is locally truncated and rotated by nearby block-bounding faults (Zhang & Hynes, in press) and hence predates the extensive strike-slip faulting. On the other hand, since the regional cleavage surfaces show consistently steep dips throughout the study area (Fig. 3.2a), they postdate the folding. The regional cleavage sometimes occurs in conjugate sets and has slickenlines on its surfaces.

About 600 regional cleavage surfaces, together with slickenlines, were measured from 24 sites (Fig. 3.1). Subhorizontal slickenlines on the cleavage surfaces (Fig. 3.2b), together with steeply plunging cleavage-surface intersections, indicate that the cleavage was produced by a stress state with subvertical intermediate principal stress (σ_2). Strikes of the cleavage surfaces, however, vary greatly over the area (Fig. 3.2a). This variation is particularly evident from conjugate cleavages. For example, close to the FIF, conjugate cleavage sets strike northeast and east-southeast (Fig. 3.3a), about 12 kilometres from the fault they have changed their strikes to north-northeast and east-west (Fig. 3.3b) and about 18 kilometres they are approximately north-south and east-northeast (Figs.

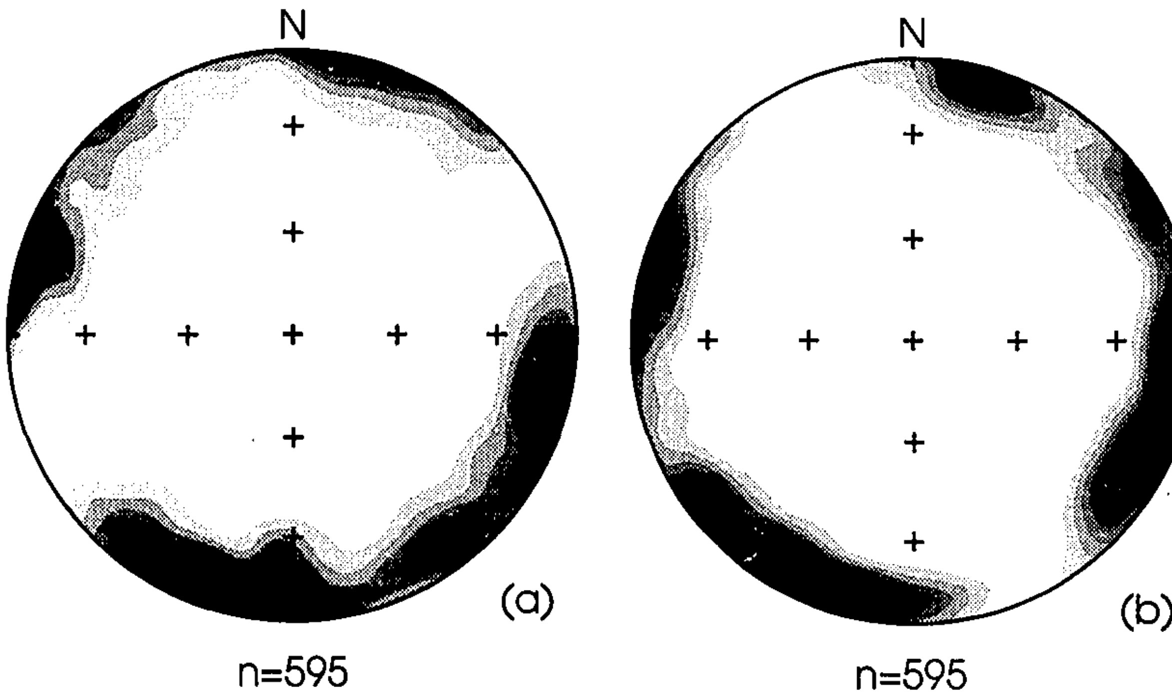

Fig. 3.2 Stereographic plots of poles to cleavage surfaces (a) and slickenlines (b). Contouring in this and subsequent figures uses Gaussian weighting function after Robin and Jowett (1986). The lowest contour level is E = 3σ, and unless otherwise noted, contours are in increments of 2σ thereafter, where σ is the statistical dispersion of the data. n: number of measurements. All stereograms in this paper are lower-hemisphere, equal-area projections except those for paleopoles which are upper-hemisphere, equal-area projections.

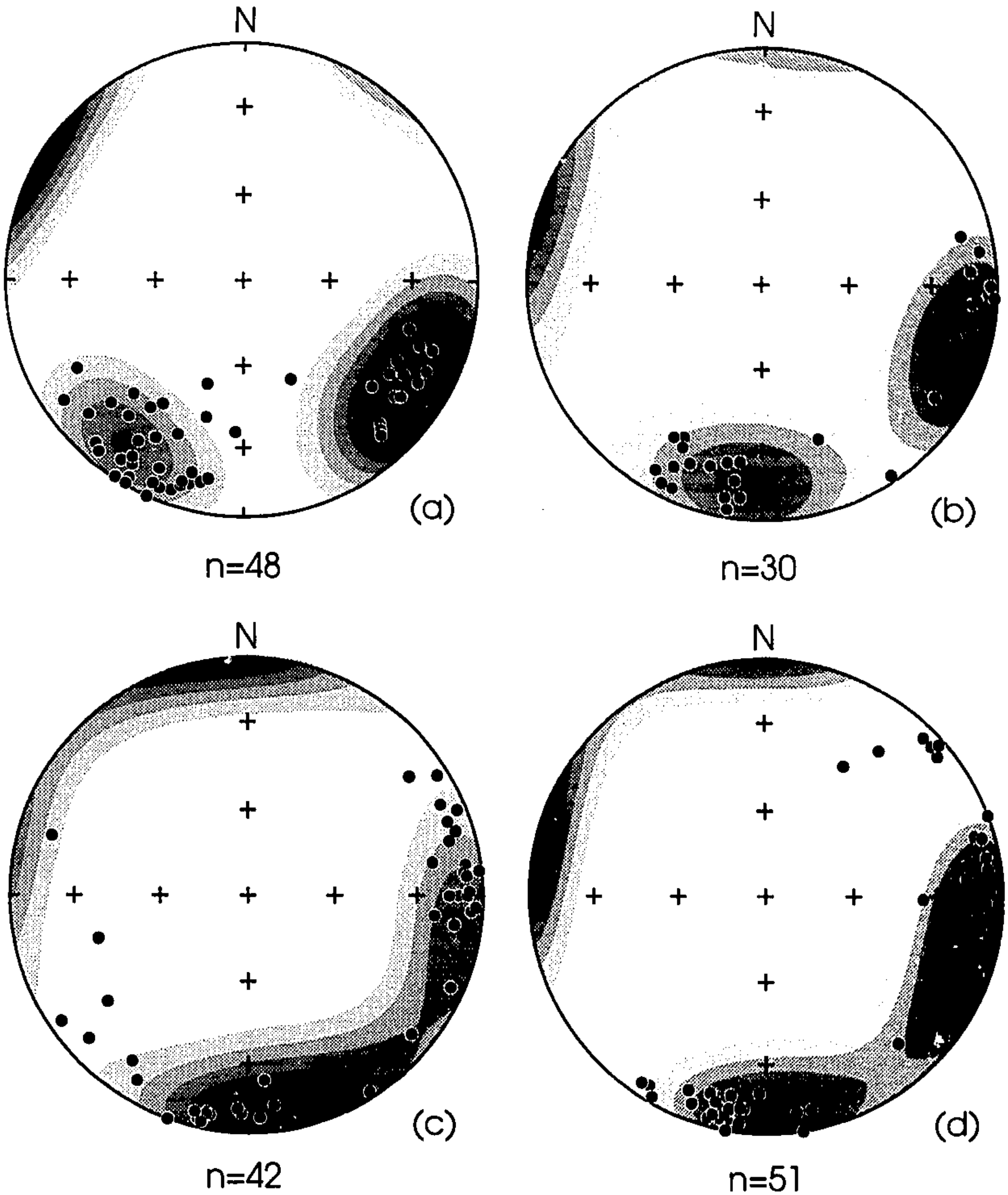

Fig. 3.3. Contours of poles to conjugate cleavage surfaces from sties 1 (a), 18 (b), 20 (c) and 21 (d) (see Fig. 3.1 for locations of sites). Contour increment: 2σ; solid circles: slickenlines; n: number of measurements.

3.3c and d).

Since the conjugate cleavages within a single fault-bounded block show the same attitude (e.g. Figs. 3.3c and d), the variation in strikes of the cleavage surfaces is probably due to differential block rotation rather than gradual change in the trajectories of cleavage through the area. On this assumption the bisector of, for example, the acute dihedral angle between conjugate cleavage sets could be used as a monitor of the rotation between blocks. There are, however, several blocks for which both cleavage sets are not well developed; instead there is just one clear orientation for the cleavage, with associated slickenlines. In order to use all our cleavage data, we have inverted the cleavage and slickenline data to determine possible configurations of the stress tensor for each site and have then used the statistical distributions of possible stress tensors to monitor changes between blocks. We emphasize that the overall character of our conclusions is not affected by the use of inverted stress results, rather than the strain data themselves, but the precision is markedly improved, because we have so many more data to use. Furthermore, with this increased precision we are able to strengthen the evidence for our inference that cleavage attitudes are consistent within blocks but change markedly between them (see below).

3.3.1 Inversion of Stress Tensors from Fault-slip Data

The principle of inversion of the stress tensor from fault-slip data is straightforward (Angelier, 1984; Michael, 1984; Reches, 1987; Angelier, 1989; Hardcastle, 1989; Hardcastle and Hills, 1991). In terms of classical solid mechanics, given a stress state **S** (stress tensor), the total stress $\overline{p}$ on any given plane can be calculated based on the force-balance equations,

$$\overline{p} = \begin{pmatrix} \sigma_{xx} & \tau_{yx} & \tau_{zx} \\ \tau_{xy} & \sigma_{yy} & \tau_{zy} \\ \tau_{xz} & \tau_{yz} & \sigma_{zz} \end{pmatrix} \begin{pmatrix} l \\ m \\ n \end{pmatrix} = \boldsymbol{S} \cdot \overline{n} \tag{3.1}$$

where **S** is symmetric and $\overline{n}$ is a unit vector normal to the plane. The resolved normal and shear stresses on the plane are

$$\overline{\sigma} = \overline{n}^T \cdot \boldsymbol{S} \cdot \overline{n} \cdot \overline{n} \tag{3.2a}$$

and

$$\overline{\tau} = \overline{p} - \overline{\sigma} = \boldsymbol{S} \cdot \overline{n} - \overline{n}^T \cdot \boldsymbol{S} \cdot \overline{n} \cdot \overline{n} \tag{3.2b}$$

respectively, where $\overline{n}^T$ is the transpose of $\overline{n}$. In our analysis, a stress tensor is considered a candidate for the one producing the observed cleavage and slickenline at a sample site if

(1) the resolved shear stress satisfies the Mohr-Coloumb yield condition $\tau \geq C+\mu\sigma$, where $\tau = |\overline{\tau}|$, $\sigma = |\overline{\sigma}|$ (see Eqs. 3.2a and b for $\overline{\sigma}$ and $\overline{\tau}$), and C and μ are the cohesion and coefficient of friction of the rock mass under study, respectively.

(2) the angle between the resolved shear stress ($\overline{\tau}$) in equation (3.2b) and the slickenline observed in the field is less than 25°.

(3) more than 80% of the faults collected from the site satisfy conditions (1) and (2).

This inversion technique assumes that the stress state is uniform, and that the rock mechanical properties (i.e. C and μ) are homogeneous and isotropic, within the area of data collection (Angelier, 1984; Michael, 1984; Reches, 1987; Angelier, 1989; Hardcastle, 1989; Hardcastle and Hills, 1991). The choice of μ is based on both experimental and field observations. In rock mechanical experiments, Byerlee (1978) demonstrated that $\mu \approx 0.85$ at intermediate pressures.

In the presence of clay minerals, however, faults yield low values of μ (Radney and Byerlee, 1988). On the other hand, natural faults often show very low strength; for example, some faults in the San Andreas fault system exhibit shear strength a factor of 2 to 3 lower than predicted by frictional theory (Zoback *et al.*, 1987). One of the reasons for this is probably that the faults possess low values of μ due to the presence of clay minerals, which is in accord with other field observations of low values of μ (e.g. $\mu < 0.1$ to $\mu = 0.8$, cf. Reches, 1987). Since the slickensides observed in our study area are almost all composed of hydrous minerals such as chlorite, epidote and tremolite, we selected a value of $\mu = 0.3$, which is consistent with that suggested by Hardcastle and Hills (1991). Because the observed slickenlines recorded the motions on the fault surfaces after their rupture, we chose $C = 0.0$ (cf. Hardcastle, 1989; Hardcastle and Hills, 1991). This simplification affects only the size of the deviatoric stress not principal directions of the stress tensor and has, therefore, no influence on our conclusions.

Stress tensors with principal axes at intervals of 10° in space were tested against the data from each site using the program BRUTE3 (Hardcastle and Hills, 1991). A few hundred to thousands of possible stress tensors were obtained for each site, although most had very similar attitudes.

3.3.2 Determination of Mean Directions of Stress Tensors and Their 95% Confidence Limits

The stress tensors obtained using this inversion technique show widely variable distributions. The maximum and minimum principal axes (σ_1 and σ_3) of the stress tensors for a single site possess distributions ranging from axial symmetry (Fig. 3.4a), through skewed axial symmetry (Fig. 3.4b), to girdle (Fig. 3.4c) whereas the intermediate axes (σ_2) all exhibit a "cross" distribution (Fig. 3.4d). Despite the range in distributions of possible stress tensors, however, they generally exhibit strongly defined maxima for each of the principal axes (Fig. 3.4) which are probability distributions for the attitudes of the principal axes at each site. To compare adjacent sites we require statistical characterizations of these probability distributions and, in light of the generally non-axial character of the distributions we have used Bingham's statistics (Bingham, 1974) rather than the common Fisher's statistics (Fisher, 1953) to calculate site means and their 95% confidence ellipses. The use of Bingham's statistics is described in the Appendix. The site-mean directions for σ_1, σ_2 and σ_3 based on Bingham's statistics are given in figures 3.1 and 3.5a (see also Appendix 3).

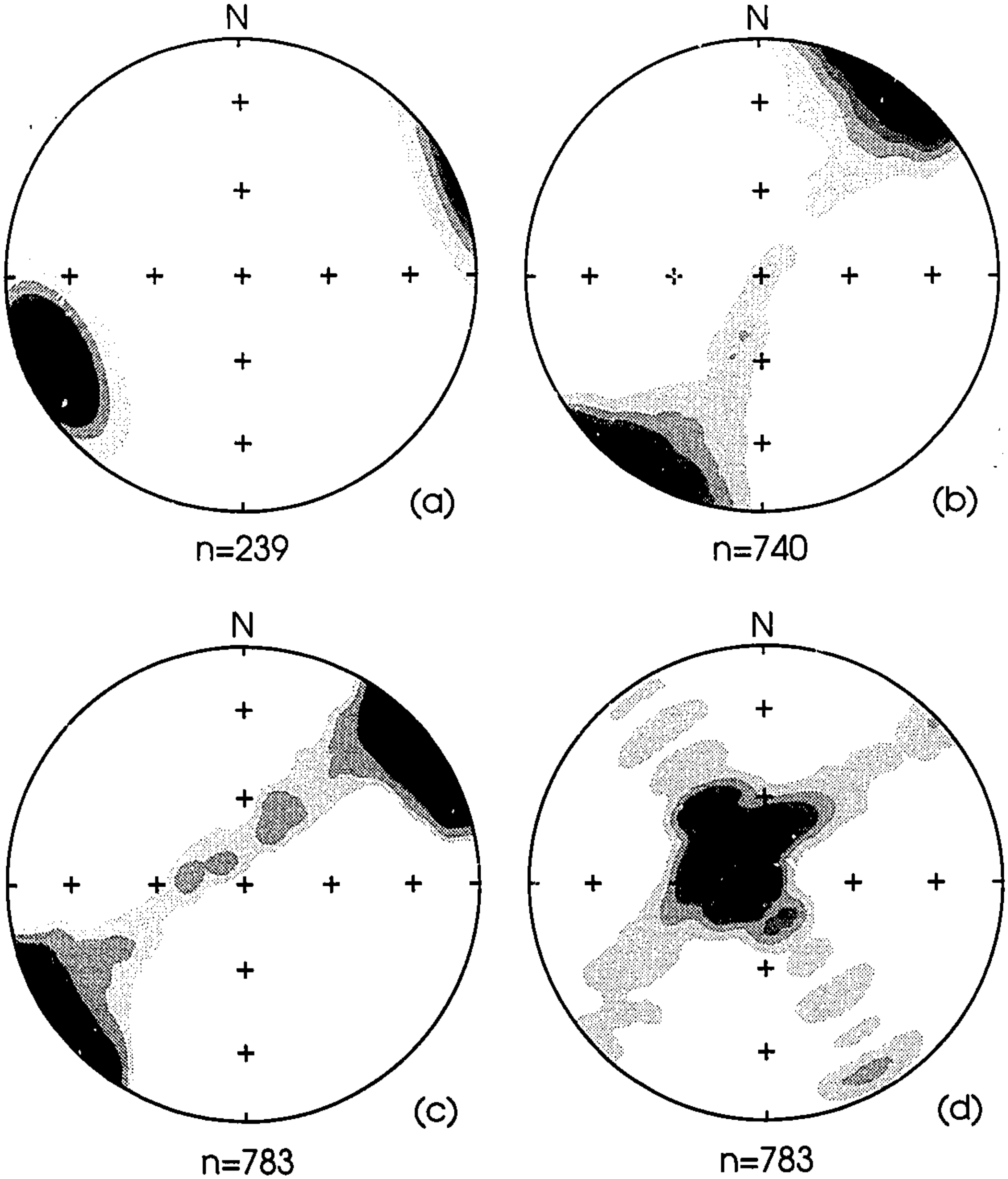

Fig. 3.4 Contours of axes of principal stresses. (a): σ_1 axes, from site 11, contour increment is 10σ; (b): σ_1 axes, from site 23, contour increment is 6σ; (c): σ_1 axes, from site 19, contour increment is 6σ; (d): σ_2 axes, from site 19, contour increment is 4σ; n: number of principal stresses.

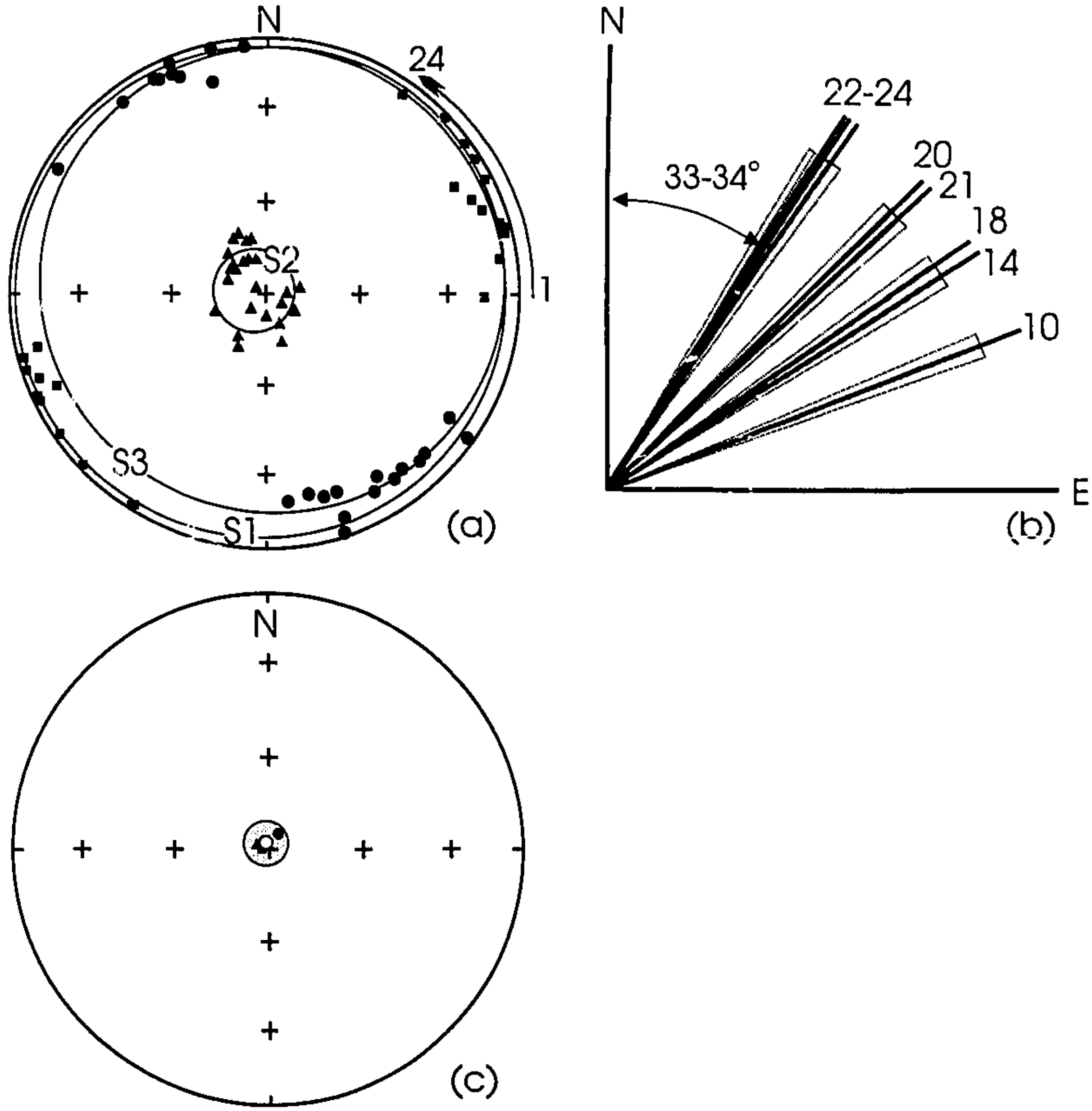

Fig. 3.5 (a) Stereographic plot of site-mean principal stress axes; solid squares, triangles and circles: maximum (σ_1), intermediate (σ_2) and minimum (σ_3) principal stress axes; lines (S1, S2 and S3): best-fitting small circles to σ_1, σ_2 and σ_3, respectively. (b) Plot of trends of σ_1 axes for some sites; shaded areas are 95% confidence limits of the corresponding axes determined by projecting their 95% confidence ellipses, calculated using equation (A8) (see Appendix), onto the horizontal plane; numbers show the sites. (c) Plot of cone axes; solid square, triangle and circle: cone axes of S1, S2 and S3 in (a), respectively; open circle: mean rotational axis; shaded circle: 95% confidence circle (unless otherwise noted, the 95% confidence circle is determined using Fisher's statistics, cf. Fisher, 1953).

3.3.3 Determination of Rotational Axis and Angle

The site-mean directions of the σ_1 and σ_3 axes are all subhorizontal whereas those of the σ_2 axes are subvertical (Fig. 3.5a). Far from the FIF, different blocks (e.g. sites 22, 23 and 24) exhibit similar site-mean directions of principal stresses (N~33°E, Figs. 3.1 and 3.5b), which are consistent with those expected in a stress field associated with the initiation of dextral transpressive displacement on the FIF. Approaching the fault, different sites within a single block (e.g. 14 and 18, 20 and 21, Figs. 3.1 and 3.5b) show similar site-mean directions of principal stresses but major changes occur between adjacent blocks. For example, the differences between sites 10 and 14, 18 and 20, 21 and 22 are statistically significant at 95% confidence level because their 95% confidence limits do not overlap (Fig. 3.5b). These major changes in the principal directions at the sites from near each other but from different blocks provide strong support for our assumption that the ranges of cleavage attitude reflect relative clockwise rotations between blocks rather than progressive variation in the cleavage attitudes.

In order to calculate the rotational axis relating the blocks to one another, the best-fit cone technique of Ramsay (1967) was applied to the site-mean σ_1, σ_2 and σ_3 axes (Fig. 3.5a), resulting in three cone axes (Fig. 3.5c). The Fisher's mean (Fisher, 1953) of the cone axes was taken as the rotational axis. It plunges at 87.7° with azimuth 336.5° (Fig. 3.5c). Using this rotational axis we calculated the rotational angle for each site with respect to the site-mean principal directions of site 22, which is one of the farthest sites from the FIF, by calculating the dihedral angle between the plane common to the rotational axis and one of the site-mean principal axes of site 22 and the plane common to the rotational axis and the corresponding site-mean principal axis of the other site.

The resulting rotational angles show systematic but large variation over the area (Fig. 3.6), reaching maximum values ($58.7\pm3.3^{\circ}$) near the FIF and decreasing away from the fault (e.g. $0.0\pm1.6^{\circ}$, about 20 kilometres distant). In keeping with the observations from the site means themselves, different sites within a single block yield similar rotational angles (e.g. sites 14 and 18, 20 and 21, Figs. 3.1 and 3.6) but there is a significant difference between the rotations inferred for some sites from close to each other but from different blocks (e.g. sites 10 and 14, 18 and 20, 21 and 22, Figs. 3.1 and 3.6). The mode of block rotations inferred in this area is similar to that described by Nelson and Jones in the Las Vegas Range (1986) and in contrast to the uniform rotation described and modelled elsewhere (Geissman *et al.*, 1989; Ron *et al.*, 1990). The local block rotations may in part explain the apparent disparities between the paleomagnetic directions observed from the study area and North America. In the next section, we describe the paleomagnetic data from the area and discuss the effects of the block rotations on them.

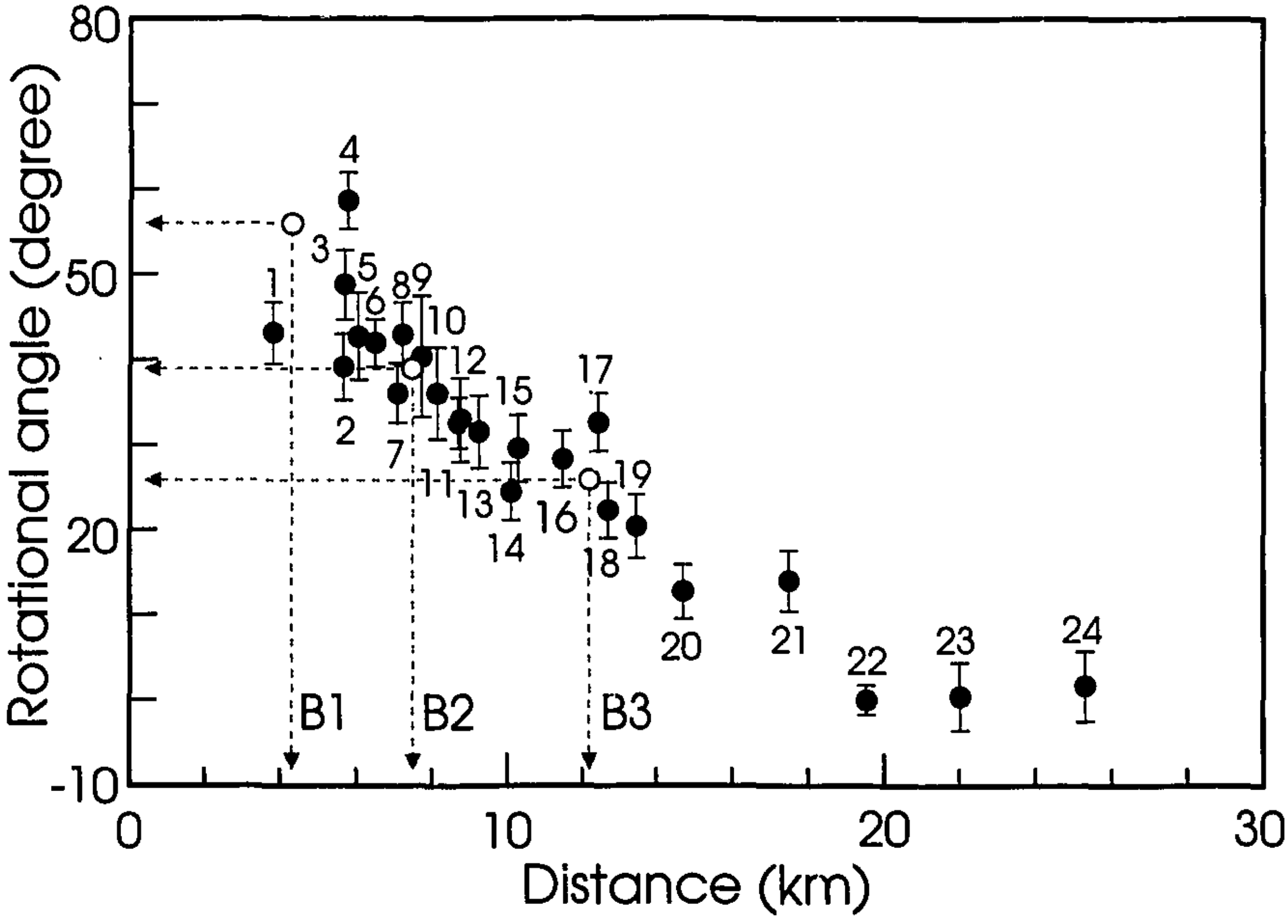

Fig. 3.6 Plot of rotational angle vs distance (after Zhang and Hynes, in press). The abscissa represents the distance from the FIF, and the ordinate represents the rotational angles. Bars: 95% confidence limits determined using the sum of long axes of the 95% confidence ellipses, calculated using equation (A8), for site 22 and the corresponding site; open circles (B1, B2 and B3): rotational angles for Blocks 1, 2 and 3, respectively (see text).

3.4 PALEOMAGNETISM OF THE PLUTONIC ROCKS

The simplest procedure for study of the effect of deformation on paleomagnetic data would have been to sample the abundant volcaniclastics of the Takla Group, since the paleohorizontal is readily determined in these rocks. Pilot studies revealed, however, that their magnetization was not stable. We concentrated instead, therefore, on plutonic rocks, although these lacked any indication of paleohorizontal.

3.4.1 Sampling and Laboratory Procedure

The Early Jurassic to Cretaceous plutonic rocks (Lord, 1948; Roots, 1954; Richards, 1976a, b; Woodsworth, 1976) in the study area occur as dikes and stocks and are inhomogeneous in composition, ranging from fine-grained biotite granodiorite to coarse-grained quartz diorite. Samples were collected from 13 sites in the intrusive rocks. Among them sites 3, 5, 6 and 7 are in the Cretaceous Johanson Creek stock (Lord, 1948; Richards, 1976a, b) in the Wrede Range (Fig. 3.1) composed of fine-grained biotite granodiorite. Sites 9, 11, 19 and 20 are in the Early Jurassic Johanson Lake and Darb Lake stocks (Lord, 1948; Richards, 1976a, b) of coarse-grained quartz diorite (Fig. 3.1). Sites 15 and 17 are in the Cretaceous leuco-granodiorite of Kliyul Creek body (Fig. 3.1, cf. Lord, 1948; Richards, 1976a, b; Woodsworth, 1976). Sites 23, 26 and 27 are in the small dioritic dikes at Goldway Peak (Fig. 3.1), which are probably coeval with the Cretaceous Johanson Lake stock to the north. At each site, two to three hand samples were collected, and the samples were oriented in-situ by magnetic compass and checked by sun compass when possible. Samples were taken as far away as possible from the block-bounding faults. At sites 5 and 6, foliation defined by alignment of biotite is visible and attributed to the emplacement of the stock, as it is parallel to, and only occurs within a certain distance from, the contact.

In the laboratory, two to three cores were taken from each hand sample and two specimens were cut from each core. A total of 77 cores (153 specimens) were obtained from the intrusive rocks. Measurements were made on automated Schonstedt (SSM-1 amd SSM-2) spinner magnetometers controlled by a microcomputer, from which four independent determinations of magnetic moment vector were obtained. These measurements permit the determination of within-specimen homogeneity by calculating specimen Fisher's (1953) precision k_s. The values of k_s were generally of the order of 10^2 to 10^3. After natural remanent magnetization (NRM) of the specimens was measured, two specimens were chosen from each site for detailed stepwise demagnetization. One specimen was subjected to alternating field (AF) demagnetization using a Schonstedt GSD-5 tumbling demagnetizer, the other was thermally demagnetized in a Schonstedt TSD-1 furnace. According to the response of the two pilot specimens from each site to the thermal (up to 700 °C) and AF (up to 100 mT) demagnetization, four or more steps of either thermal or AF cleaning treatment were applied to the rest, depending on how rapidly the precision (k_s) dropped and whether an end point was achieved.

3.4.2 Description of Magnetization

Magnetization of the plutonic rocks varies and hence is grouped into scattered magnetization, ill-defined magnetization and well-clustered magnetization. Samples from sites 3, 9, 17 and 20 exhibit scattered magnetic directions, showing the typical characteristics of lightning-induced magnetization. Within a single site different samples, several metres apart, show scattered NRM directions and unusually high NRM intensities (up to 38 A/m) and no coherent directions among the samples were obtained after either thermal or AF cleaning. During AF demagnetization by about 20 mT, the intensities of the specimens dropped to less than 10 % of their NRM intensities; hence the magnetizations of the specimens are composed mainly of low coercivity components. They were not included in the subsequent analysis.

Sites 15, 23 and 26 are characterized by ill-defined magnetization, in which most specimens have low values of k_s (ranging from 1 to 100). During both thermal and AF cleaning, the magnetic directions of individual specimens changed rapidly and randomly, indicative of unstable magnetization, and after cleaning no consistent magnetic directions within site were found. The magnetization at these sites is probably carried by coarse-grained magnetite as indicated by low coercivity (generally less than 20 mT). These sites were also excluded from the analysis.

Well-clustered magnetization was observed at sites 5, 6, 7 and 27. The NRM intensity at these sites ranges from 2.0 x 10^{-2} to 1.0 A/m (Figs. 7-12). Thermal demagnetization revealed that sites 5 and 6 have high unblocking temperatures (570-600°) and at the cleaning step of 600° the intensity of the specimens dropped to less than 15% of their NRM intensity, forming a characteristic magnetite "shoulder" (Figs. 3.7 and 3.8). AF demagnetization showed that a medium to high coercivity component (greater than 30 mT) is predominant and after 10 mT the intensity decayed linearly according to the increase of demagnetization steps, forming a straight line on orthogonal plots (Figs. 3.9 and 3.10). The magnetic directions between the cleaning steps of 200-570° and 20-80 mT are well-grouped, indicative of a stable magnetic component. In addition, microprobe analysis of the opaque minerals of the plutonic rocks indicates that they are mainly pure magnetite with minor ilmenite as exsolution lamellae within the magnetite, which is consistent with the observed unblocking temperature and coercivity. Therefore, the main carriers of magnetization at these sites are probably fine-grained, single-domain (< 0.1 µm, cf. Butler, 1992) magnetite grains. The magnetization at site 7, however, is carried by both

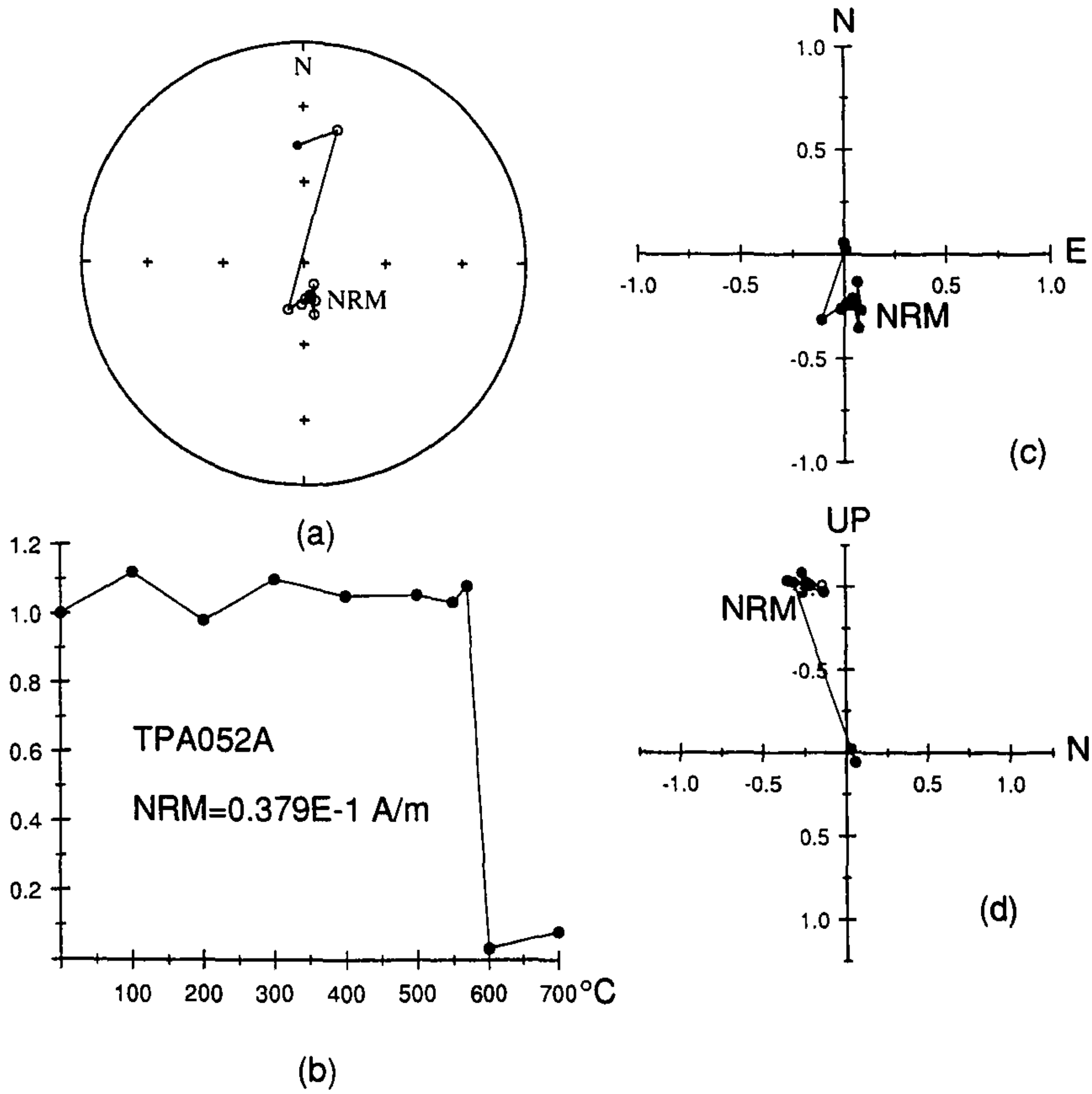

Fig. 3.7 Thermal demagnetization for a representative specimen from site 5, showing changes in orientation of the magnetic vector (a), decay of the normalized magnetic intensity (b) and decay of the normalized magnetic intensity on orthogonal plots (c) and (d), according to cleaning increments.

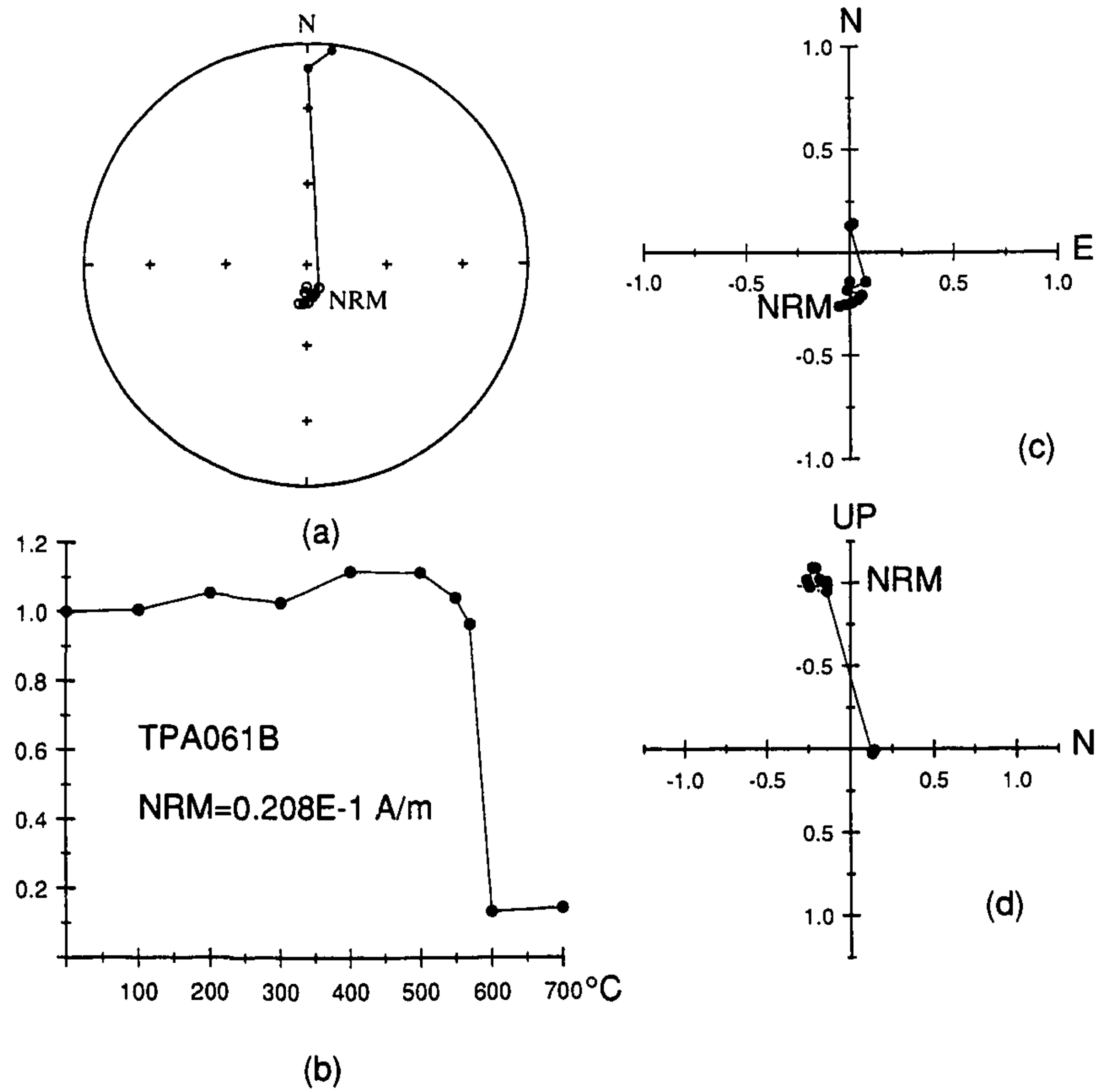

Fig. 3.8 Thermal demagnetization for a representative specimen from site 6. See legend for Fig. 3.7.

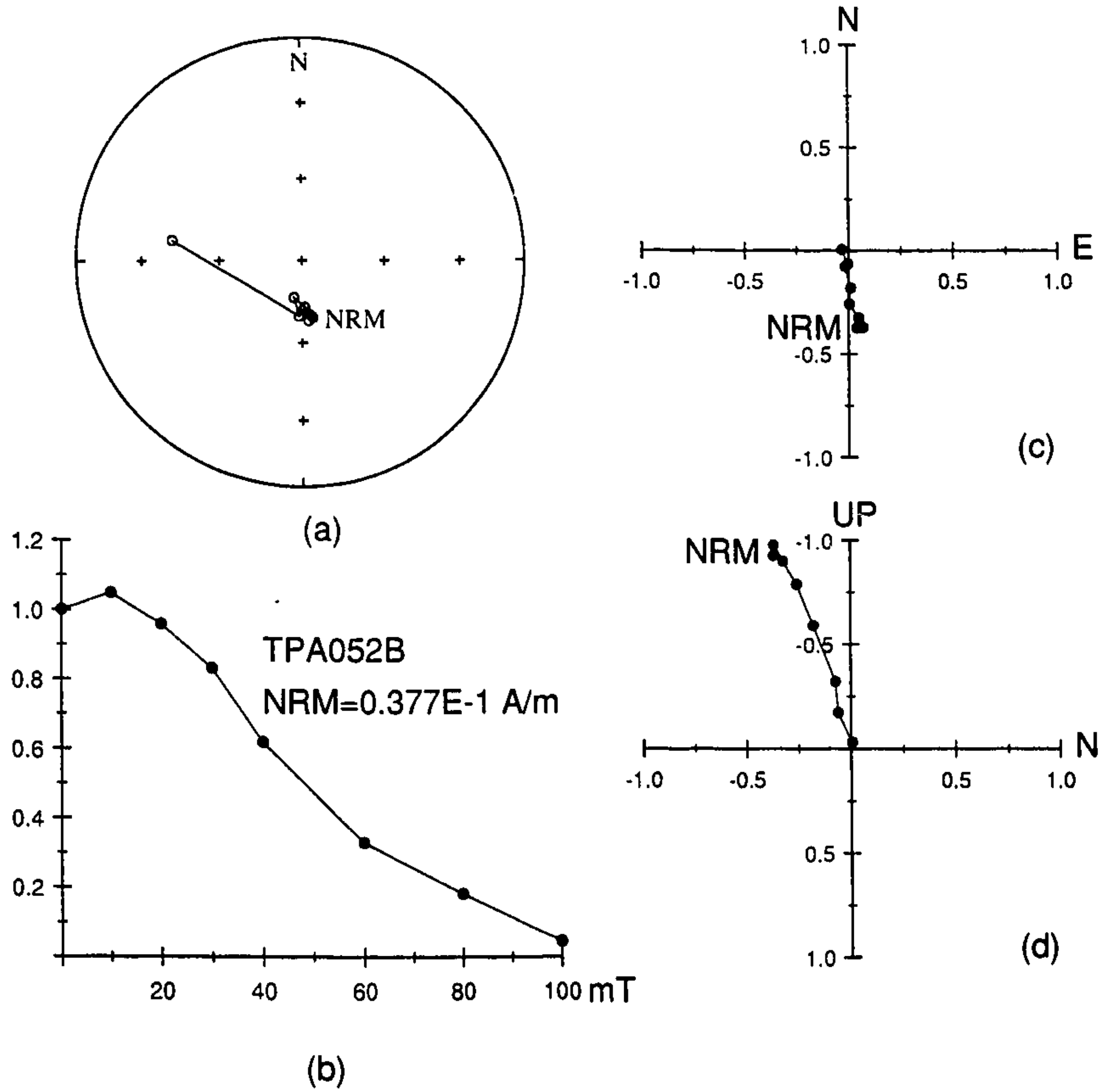

Fig. 3.9 AF demagnetization for a representative specimen from site 5. See legend for Fig. 3.7.

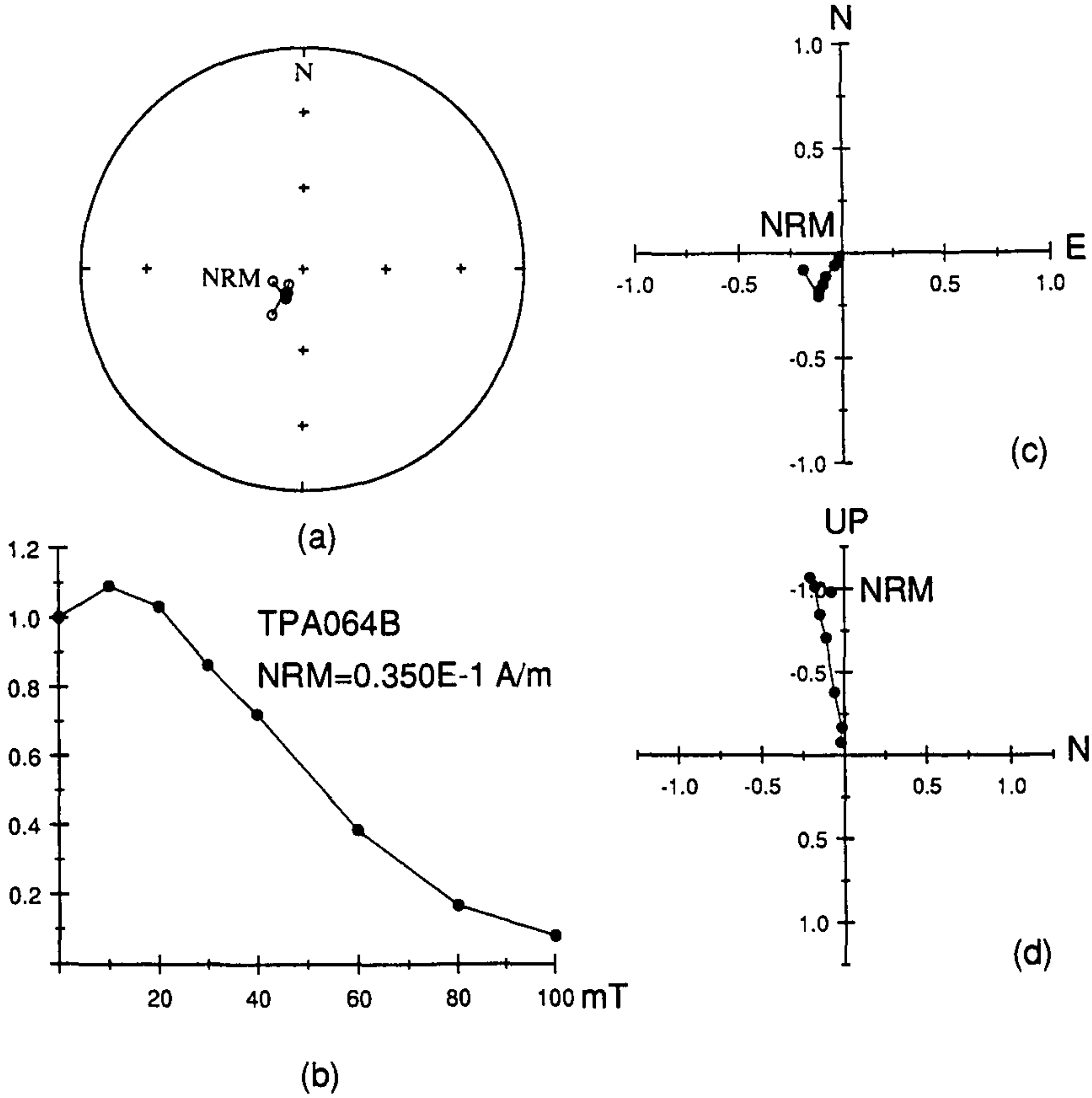

Fig. 3.10 AF demagnetization for a representative specimen from site 6. See legend for Fig. 3.7.

magnetite and hematite as indicated by a higher unblocking temperature and coercivity (greater than 600° and 100 mT, Figs. 3.11 and 3.12). Since the hematite and magnetite have similar magnetic directions (e.g. the directions at 500-600°, and 80-100 mT, Figs. 3.11 and 3.12), they were both probably magnetized during the cooling of the magma. Since the specimen demagnetization trajectories were essentially linear on orthogonal intensity plots (e.g. Figs. 3.9-3.12) the mean direction was determined by least-squares line-fitting (LINEFIT) to the directions of removed components over the cleaning steps (e.g. 30-80 mT). All specimens from these sites show stable magnetization and reversed polarity (Figs. 3.7-3.12) and are used in our analysis (Table 3.1).

An intermediate component was obtained using the removed magnetic vectors between 20-40 mT (Fig. 3.13) from sites 11 and 19, the Early Jurassic Johanson Lake and Darb Lake stocks (Lord, 1948; Richards, 1976a, b) from which two hornblendes yield K-Ar ages of 174±5 and 171±5 Ma, respectively. Because the inclinations of the magnetic directions (~70°, Fig. 3.13) are much steeper than those observed from the adjacent Early Jurassic Hazelton Group rocks (47-56°) (cf. Monger and Irving, 1980; Vandall and Palmer, 1990), we interprete magnetization of the intermediate component as a post-Jurassic overprint. The NRM directions of the specimens are scattered and centred about both present Earth's field (PEF) and the geocentric axial dipole field (GAD) (Fig. 3.13). After cleaning, the removed magnetic directions become well-clustered and the PEF and

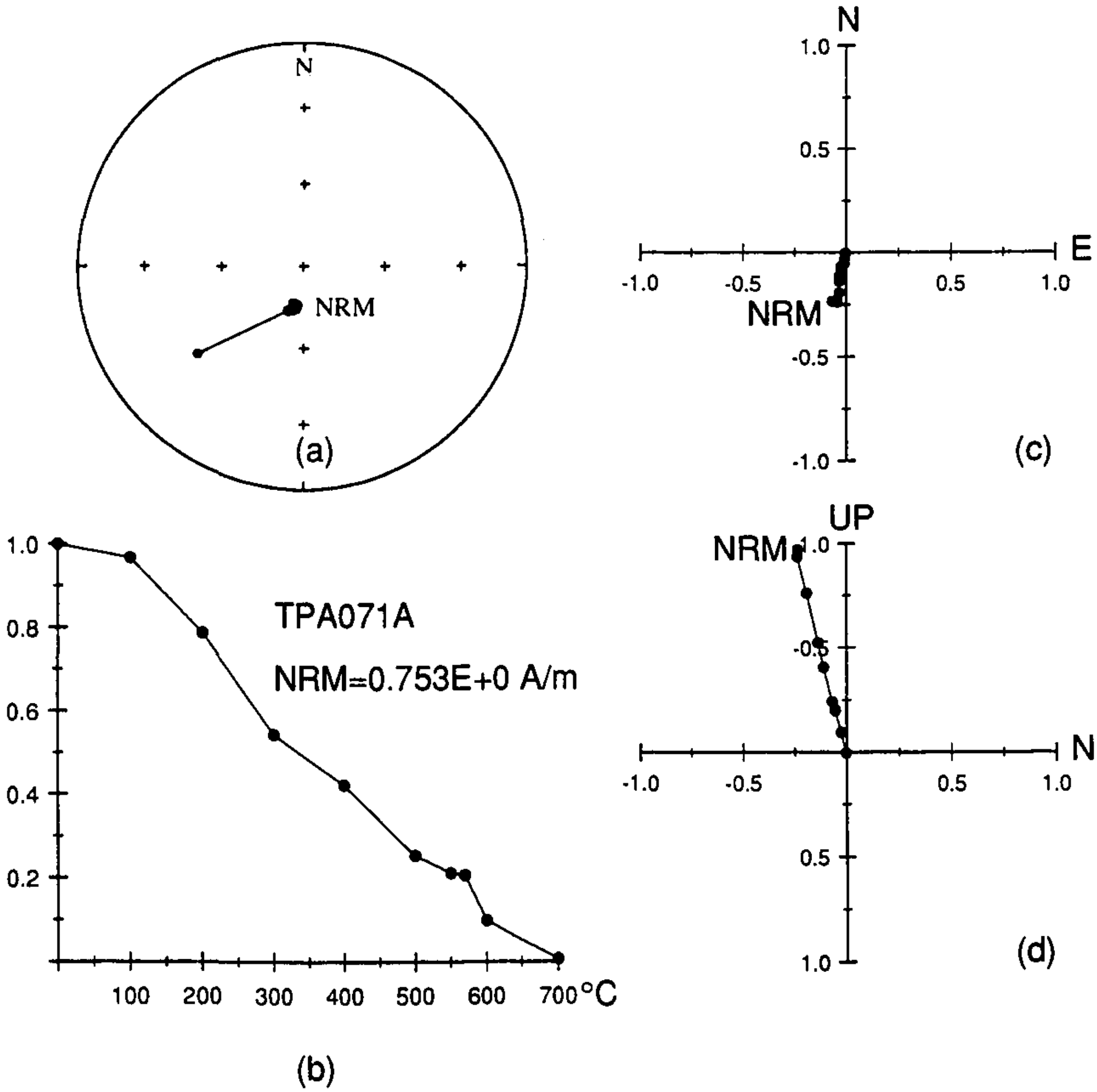

Fig. 3.11 Thermal demagnetization for a representative specimen from site 7. See legend for Fig. 3.7.

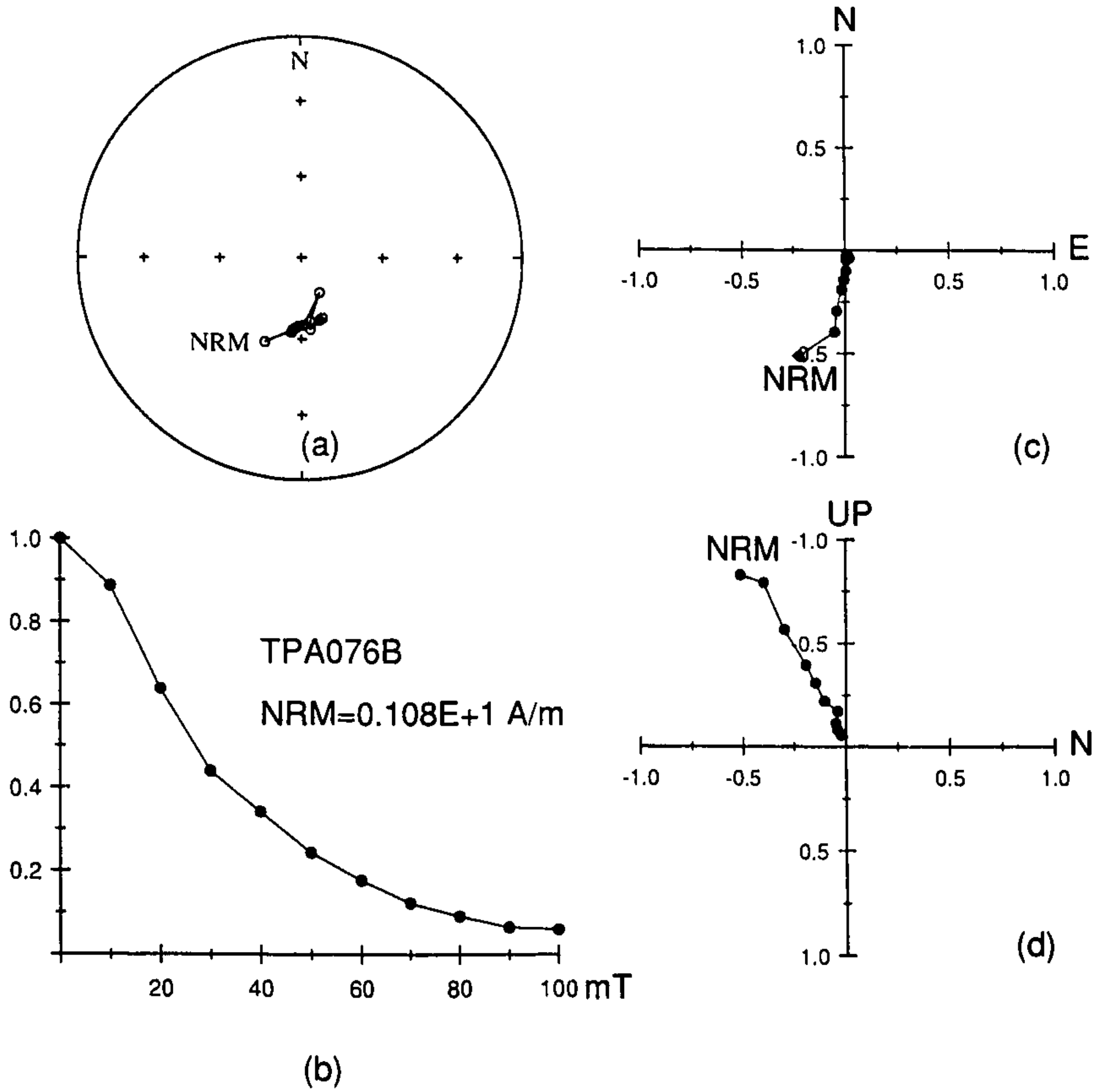

Fig. 3.12 AF demagnetization for a representative specimen from site 7. See legend for Fig. 3.7.

Table 3.1. Paleomagnetic data for plutonic rocks

Block	site	lat. °N, long. °E	n, s	D, I (°), (°)	k	α_{95} (°)	pole lat. °N, long. °E	k	A_{95} (°)
1	TPA27	56.53, 233.75	6, 8	216, -71	394	3			
	BM	56.53, 233.75		216, -71			69.3, 312.2		
2	TPA05	56.63, 233.72	5, 10	186, -73	139	4			
	TPA06	56.63, 233.72	6, 12	196, -77	89	5			
	TPA07	56.63, 233.73	6, 11	190, -60	30	9			
	BM	56.63, 233.72		190, -70	83	14	83.9, 339.2		
3	TPA11	56.62, 233.85	6, 10	009, 68	120	4			
	TPA19	56.52, 233.85	6, 10	350, 67	70	4			
	BM	56.57, 233.85		359, 67			83.7, 059.7		
BSM				194, -70	139	11	81.5, 334.9	48	18
BSMC				158, -69	1009	4	76.6, 134.0	383	6
K_{exp}				339, 76		4	77.7, 185.8	255	8

Notes: lat. °N and long. °E: latitude north and longitude east; n: number of cores; s: number of specimens used for calculation of site mean; D and I: declination and inclination of the mean direction with respect to present horizontal; k: Fisher's precision; α_{95}: half-angle of 95% confidence circle of the mean direction; A_{95}: half-angle of 95% confidence circle of blocks mean paleopole; BM: block mean; BSM: blocks mean; BSMC: blocks mean after corrections for the local block rotations; K_{exp}: Late Cretaceous reference paleomagnetic direction or pole for cratonic North America (CNA) (cf. Marquis and Globerman, 1988; Irving and Wynne, 1990).

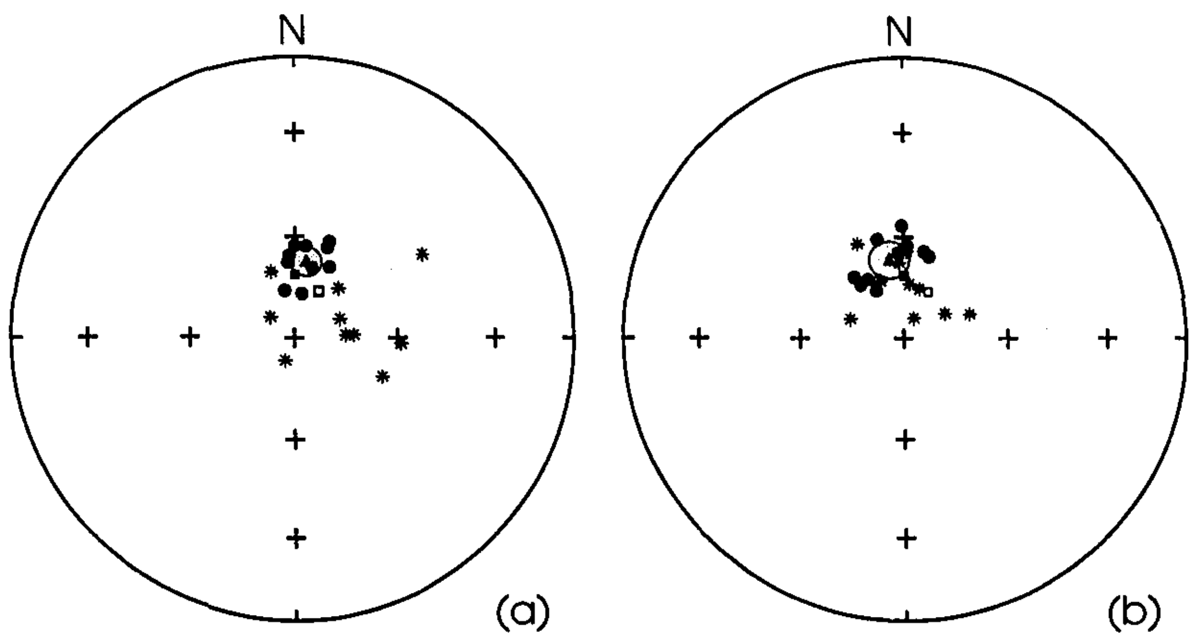

Fig. 3.13 Stereographic plots of magnetic directions of sites 11 (a) and 19 (b). Stars: NRM directions; solid circles: magnetic directions removed at 20-40 mT; open square: present Earth field; solid square: geocentric axial dipole field; solid triangle: site mean of the removed directions; shaded circle: 95% confidence circle.

GAD fields both lie outside the site mean's 95% confidence circles (Fig. 3.13). Therefore, the magnetization is probably neither Bruhnes nor present Earth field overprint. Since the polarity and directions of the magnetization are similar to those observed from the nearby mid-Cretaceous Axelgold (Monger and Irving, 1980) and Germansen (Wynne et al., 1992) intrusives, it was probably acquired during the mid to Late Cretaceous. This is also supported by the frequent observations of magnetic overprint resulting from the mid Cretaceous plutonism near the study area (Rees et al. 1985; Butler, et al., 1988). The upper limit of the overprinting temperature was probably between 350 and 525°, since biotite K-Ar ages of Early Jurassic or older intrusives were reset to the mid to Late Cretaceous (Rees et al., 1985; and references therein) while hornblende K-Ar ages like those we report, for which the unblocking temperature for Ar is ~525° (Butler, 1992), were not. The magnetic directions of the intermediate components from sites 11 and 19 are included in our subsequent analysis (Table 3.1).

We were unable to separate the tiny biotite grains from our specimens of the Cretaceous Johanson Creek stock (sites 5, 6 and 7) and so obtained no radiometric date for it. Based on the polarity and magnetic directions, however, we believe the magnetization was acquired during the Late Cretaceous, after the Cretaceous Normal Superchron (83-124 Ma, cf. Harland *et al.*, 1989) because it is dominated by reversed polarity and shows inclinations (~70°) comparable with those from the Late Cretaceous volcanics (Marquis and Globerman, 1988) to the north of the study area. We have therefore used the Late Cretaceous paleopole for cratonal North America (CNA) as a reference paleopole in our analysis (Table 3.1).

3.4.3 Experiment of Isothermal Remanent Magnetization (IRM)

In order to investigate the effects of the visible foliation on the NRM directions, anisotropy of magnetic susceptibility (AMS) of specimens from site 5 was measured with an SI-2 magnetic susceptibility and anisotropy instrument (Sapphire Instruments, P.O. Box 385, Ruthven, Ont.) interfaced to an IBM Personal computer. The results indicate that an AMS exists in the rocks, with $P = K_1/K_3 = 1.45$, $L = K_2/K_3 = 1.07$ and $F = K_2/K_3 = 1.37$ (where K_1, K_2 and K_3 are maximum, intermediate and minimum magnetic susceptibility and P, L and F are the degree of magnetic anisotropy, magnetic lineation and foliation, respectively, cf. Hrouda, 1982; Ellwood et al., 1988). The observed AMS of the rocks defines a magnetic foliation because $F > L$, and it has an orientation similar to that of the rock foliation (Figs. 3.14a and b). Since the observed bulk susceptibility ($K_m = (K_1+K_2+K_3)/3 = 1.35 \times 10^{-3}$) and degree of anisotropy ($P = 1.45$) are not much greater than 10^{-3} and 1.35, respectively, the AMS is probably contributed by both ferromagnetic minerals (e.g. magnetite in our case) and rock matrix (e.g. biotite in our case) (cf. Rochette, 1987; Borradaile, 1988). The question is whether the AMS would affect the NRM directions of the specimens.

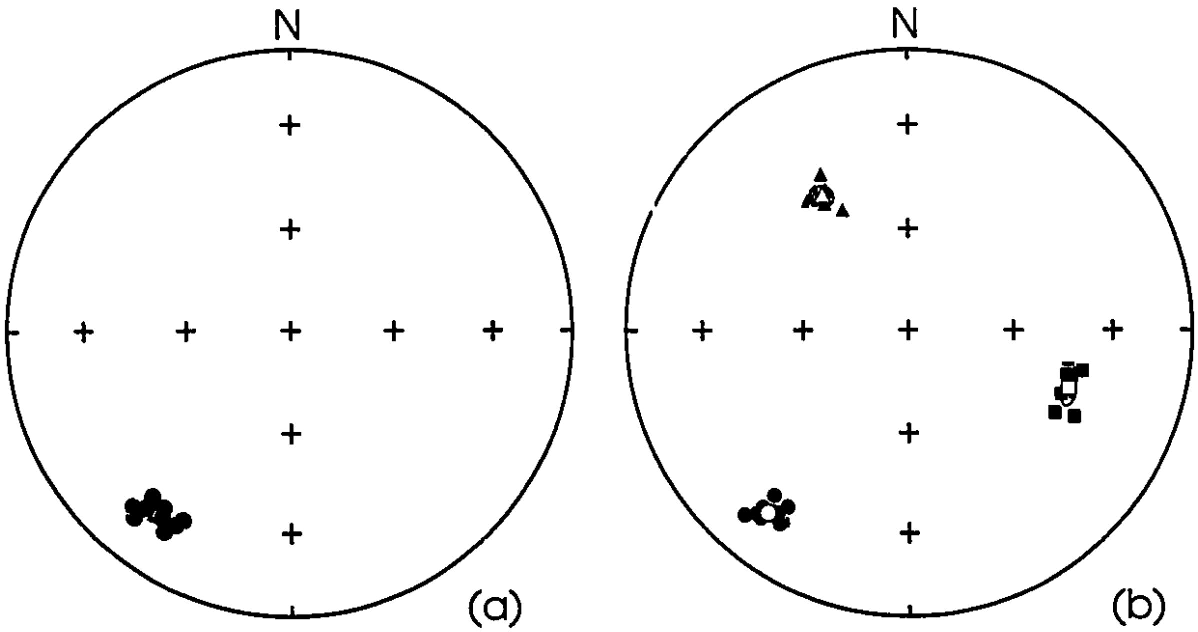

Fig. 3.14 Stereographic plots of poles to the foliation (a) and principal magnetic susceptibility (b) from site 5. Solid squares, triangles and circles: maximum (K_1), intermediate (K_2) and minimum (K_3) magnetic susceptibility; open square, triangle and circle: site mean of K_1, K_2 and K_3; ellipses: 95% confidence ellipses (cf. Hext, 1963).

Because the characteristics of AF demagnetization of high field (≥120 mT) IRM are similar to those of low field (~5 mT) TRM for fine-grained single-domain (0.1 μm) magnetite dispersion, as demonstrated implicitly by Lowrie and Fuller (1971), we used a high field IRM experiment to model the acquisition of low field TRM which is probably the case for site 5. Two specimens (TPA052B and TPA054B) were selected and magnetized in a DC field of 180 mT with a Sapphire Instrument SI-4 AF Demagnetizer after being demagnetized at 180 mT with the same instrument. Then each specimen was progressively cleaned by increments of 10 mT, up to 100 mT, using a Schonstedt GSD-5 tumbling demagnetizer. By repeating the above procedure, each specimen was magnetized three times in orthogonal directions (i.e. X, Y and Z, see Figs. 3.15a and b).

Several features are remarkable from the results in Table 3.2 and Figure 3.15. First, the IRM directions depart significantly from those of the ambient field (Figs. 3.15a and b) but are close to those theoretically predicted (i.e. directions calculated by the linear relationship $\overline{m} = \boldsymbol{K} \cdot \overline{h}$, where **K** is the second-rank tensor of magnetic susceptibility and $\overline{h}$ is a column vector specifying the ambient field direction), indicative of the effect of AMS on the IRM directions (see Figs. 3.15a and b). Secondly, during AF cleaning the magnetic directions moved toward the ambient field directions (Figs. 3.15a and b), and after 20 or 30 mT the

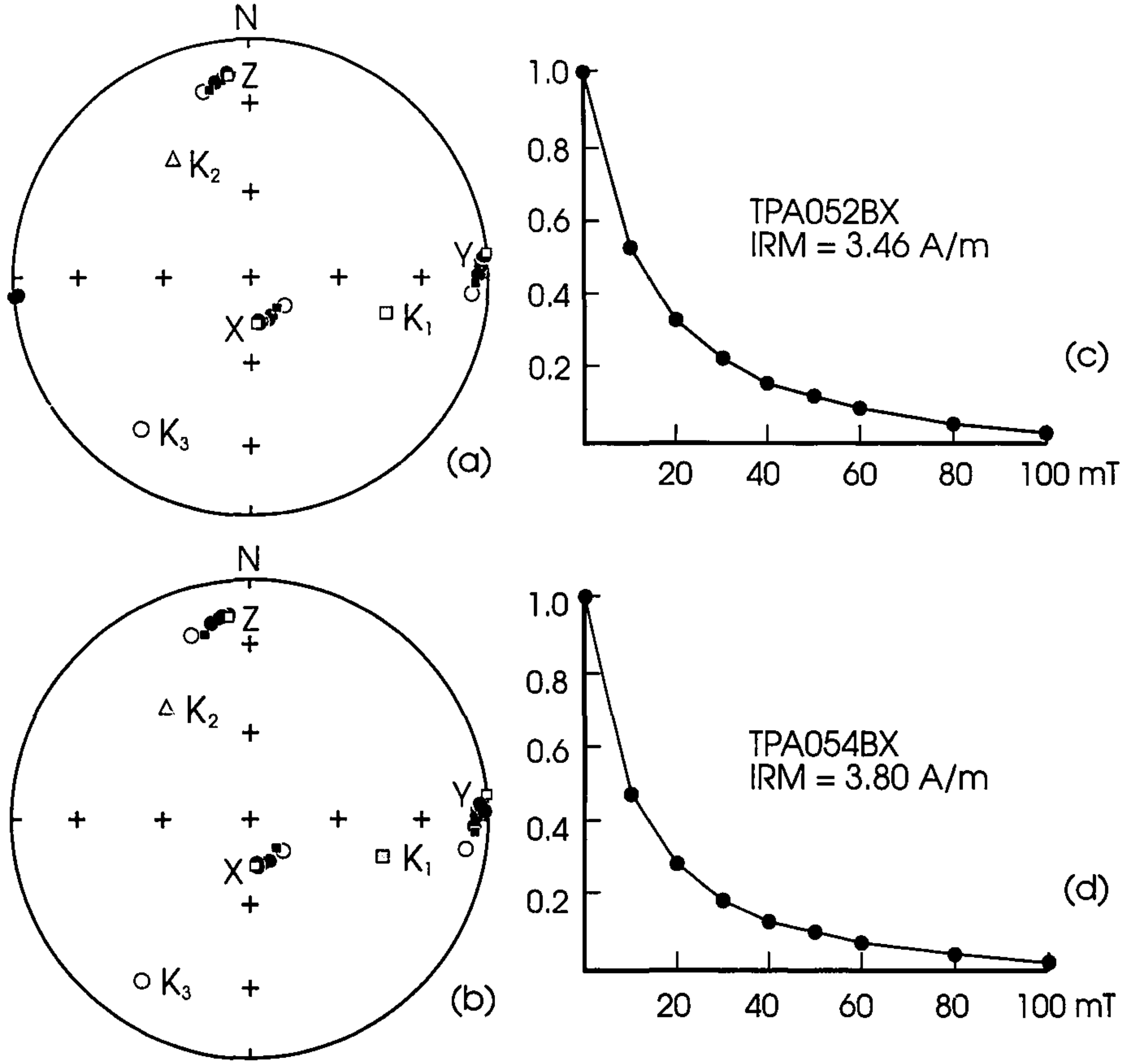

Fig. 3.15 Plots of IRM experiment data. (a) and (b) showing the changes of IRM directions of specimens TPA052B and TPA054B, respectively, during AF cleaning; gray square, triangle and circle: K_1, K_2 and K_3 (same as for Fig. 3.14b); solid squares: predicted directions (see text); open squares: ambient field directions; open circles: IRM directions; solid circles: magnetic directions at 10-100 mT. (c) and (d) showing the decrease of normalized IRM intensity (ordinate) with progressive AF demagnetization (abscissa).

Table 3.2. Results of IRM experiments

Specimen	direction	D (°)	I (°)	k	α_{95} (°)	def (°)
TPA052BX	PD	140.9	76.4			
	IRM	131.2	75.3			
	field	174.0	74.0			
	30-100 mT	169.0	74.4	16009	0.53	1.4
TPA052BY	PD	091.5	5.7			
	IRM	094.1	7.2			
	field	084.0	0.0			
	30-100 mT	085.1	0.8	2255	1.41	1.4
TPA052BZ	PD	347.9	20.6			
	IRM	345.9	20.6			
	field	354.0	16.0			
	20-100 mT	353.8	15.4	9046	0.63	0.6
TPA054BX	PD	137.4	76.8			
	IRM	133.6	74.5			
	field	174.0	74.0			
	30-100 mT	170.0	73.9	14423	0.56	1.1
TPA054BY	PD	093.0	5.8			
	IRM	097.7	9.2			
	field	084.0	0.0			
	30-100 mT	086.8	3.4	3901	1.07	4.4
TPA054BZ	PD	346.2	21.6			
	IRM	342.3	20.5			
	field	354.0	16.0			
	20-100 mT	353.1	15.4	5627	0.80	1.1

Notes: PD: predicted direction (see text); IRM: direction before cleaning; field: ambient field direction; 30-100 mT: Fisher's (1953) mean of the directions between 30-100mT; D and I: declination and inclination; k: Fisher's precision; α_{95}: half-angle of 95% confidence circle; def: angle between ambient field and high coercivity component directions.

magnetic directions were well-clustered and essentially parallel to those of the ambient field (Figs. 15a and b). The departures of mean directions (Fisher, 1953) at 20, or 30, to 100 mT from the ambient field directions were all within the range of 0.6 to 1.4° except for TPA054BY (Table 3.2 and Fig. 3.15b), which is 4.4° and may reflect an error in orienting the specimen during IRM acquisition. This indicates that AMS has little or no effect on the direction of high coercivity ($\geq$30 mT) stable components, which is consistent with the results for well-foliated gneissic rocks (cf. Irving and Park, 1973) and for laminated volcanic rocks (cf. Marquis and Globerman, 1988) and compatible with the experimental results of Pozzi and Aïfa (1989; and references therein). The reason for this is presumably that the AMS is caused mainly by the alignment of coarse-grained, multidomain magnetite grains during magmatic flow whereas the remanent magnetization is carried by fine-grained, cubic magnetite that remains dispersed in the rocks. AMS, however, does affect remanent magnetic directions in the cases of monocrystals, massive ores and rocks having coarse-grained ferromagnetic minerals (Hrouda, 1982; and references therein) or ferromagnetic minerals, with grain aspect ratios greater than 1.3, which may behave like passive markers during ductile deformation (Borradaile, 1991; Borradaile and Mothersill, 1991; Borradaile, 1992). Nevertheless, no corrections for the remanent magnetic directions are needed in our case because only the high coercivity components from these sites were used in the analysis.

3.5 STRUCTURAL INTERPRETATION OF PALEOMAGNETIC DATA

The interpretable magnetic data (6 sites) are from different fault-bounded blocks (Fig. 3.1) and hence they are grouped into three blocks, namely Block 1 (site 27), Block 2 (sites 5, 6 and 7) and Block 3 (sites 11 and 19) (see Table 3.1 and Fig. 3.1). The paleopole for each block was obtained using the block-mean magnetic direction (Table 3.1). The observed paleopoles from the three blocks are scattered (Fig. 3.16a), with a value of Fisher's precision $k = 48$ (Table 3.1), but the blocks-mean paleopole (K_{obs}) is significantly different at 95% confidence level from the Late Cretaceous expected paleopole (K_{exp}) for CNA, as indicated by an F test (where $F_{(2,8)} = 7.2 > F_{\alpha(2,8)}|_{\alpha = 0.05} = 4.46$, cf. Mardia, 1972; Upton and Fingleton, 1989), although their 95% confidence circles overlap (Fig. 3.16a). Disparity between these two paleopoles shows an apparent northward paleolatitudinal displacement of $9\pm17^{\circ}$ (Fig. 3.17) and a clockwise rotation of $35\pm32^{\circ}$ (Fig. 3.18), which is compatible with other Cretaceous paleomagnetic data from the Intermontane Belt (Figs. 3.17 and 3.18).

The results of structural analysis indicate that we should remove the effects of block rotations before attempting to explain the paleomagnetic data in the McConnell Creek region. We designated a rotational angle of 56° for Block 1, 39° for Block 2 and 26° for Block 3, according to the angles determined from the nearby cleavage data (Fig. 3.6). After unrotation about the axis of figure 5c

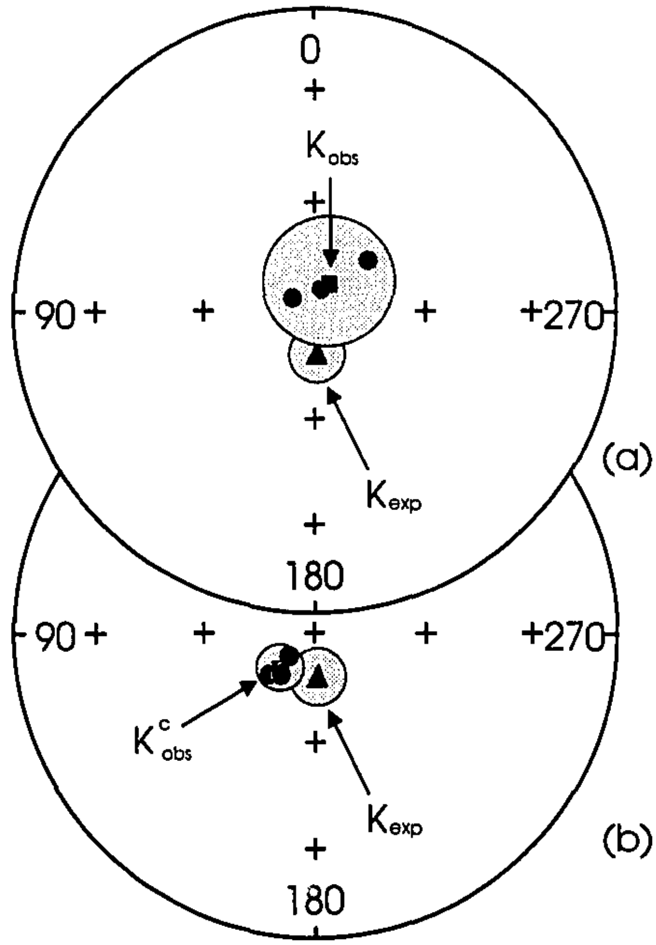

Fig. 3.16 Stereographic plots of paleomagnetic poles. (a) and (b) showing observed paleopoles before and after corrections for the local block rotations, respectively. Solid triangle (K_{exp}): expected Late Cretaceous paleopole for CNA (Table 3.1); solid circles: observed paleopoles from three fault-bounded blocks; solid square: blocks mean (K_{obs} and K^{c}_{obs} are the paleopoles before and after the corrections, respectively); shaded circles: 95% confidence circles.

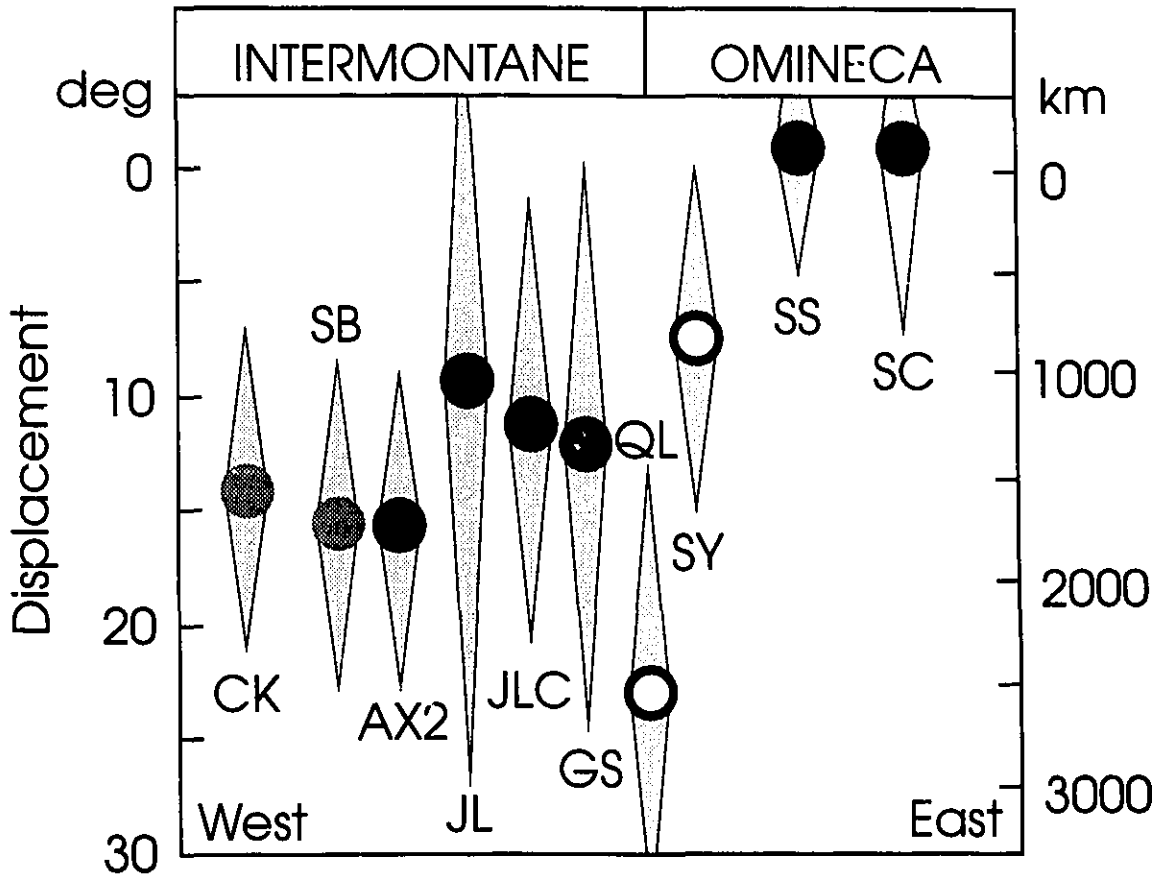

Fig. 3.17 Plot of Cretaceous paleomagnetic data observed from the Intermontane and Omineca Belts showing apparent northward displacements (after *Wynne et al.*, 1992). Solid circles: intrusives; gray circles: bedded rocks; open circle: overprint; shaded areas: 95% confidence limits. References: SC and SS, Irving and Archibald, 1990; SY, Butler, *et al.*, 1988; QL, Rees, *et al.*, 1985; GS, *Wynne et al.*, 1992; AX2, Monger and Irving, 1980; SB, Irving and Thorkelson, 1990; CK, Marquis and Globerman, 1988; JL and JLC, this study (before and after corrections for the local block rotations, respectively).

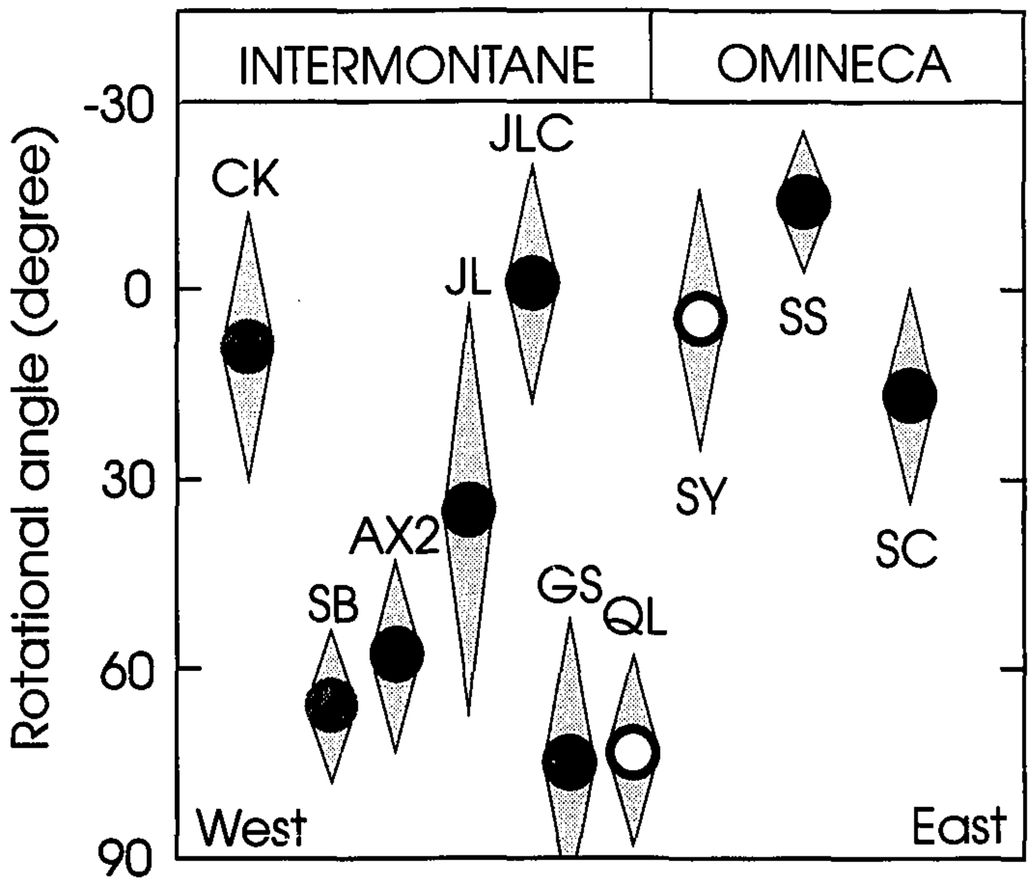

Fig. 3.18 Plot of Cretaceous paleomagnetic data observed from the Intermontane and Omineca Belts showing apparent clockwise (positive) rotations. See legend for Fig. 3.17.

through these angles, the block-mean magnetic directions from the three blocks became well clustered and the value of Fisher's precision k increased markedly (from k = 139 to 1009, Table 3.1). Similarly, block-mean paleopoles moved closer to each other (Fig. 3.16b), with a high value of Fisher's precision k =383 (» k = 48 before corrections for the local block rotations, Table 3.1). The observed blocks-mean paleopole (K^{c}_{obs}) also moved closer to the expected paleopole (K_{exp}) (Fig. 3.16b) but was still significantly different from it ($F_{(2,8)} = 6.0 > F_{\alpha(2,8)} \mid_{\alpha = 0.05} = 4.46$). Disparity between these two paleopoles shows an apparent paleolatitudinal displacement of 11±9° (Fig. 3.17) and essentially no rotation (-1±19°, where negative denotes anticlockwise rotation, Fig. 3.18). Thus, after the structural corrections, the 95% confidence limit of the observed paleopole has decreased significantly, the clockwise rotation apparent in the raw data has essentially vanished, but the amount of latitudinal displacement remains almost the same as before because of the steep plunge of the rotational axis. The local block rotations can therefore account almost entirely for the anomalous magnetic declinations of the McConnell Creek region but not for the anomalous inclinations.

Geometrically, two hypotheses, tilting and northward transport, could explain the residual disparity between the expected and corrected paleopoles (Fig. 3.16b). Tilting of ~7° to the north-northwest (N~339°W) about a horizontal axis trending N~069°E (see Table 1 for the expected and corrected magnetic directions) would remove the disparity. The required tilting axis is essentially perpendicular to the main trend of the structures in the area (Fig. 3.1) and could not be achieved even if there were substantial dip-slip motion on many of the north-northwest striking faults within the region. There is no structural evidence for such a process. We therefore favour a process of northward transport. Northward transport of the region could have been accomplished by dextral transpressive motions on the Tintina trench and northern Rocky Mountain trench (TT-NRMT) fault zone (Roddick, 1967; Tempelman-Kluit, 1979; Gabrielse and Dodds, 1982; Gabrielse, 1985; Price and Carmichael, 1986; Gabrielse, 1991). This process may be clearly illustrated by rotation about the Eulerian pole for the best-fitting small circle to the TT-NRMT fault zone (Price and Carmichael, 1986), which is located at latitude 35.4° N, longitude 201.3° E with an apical half angle of 31.2° (Fig. 3.19a). Clockwise rotation about the Eulerian pole through 11.5° moves the corrected paleopole (K^c_{obs} in Figs. 3.19a and b) closer to the expected (K_{exp} in Figs. 3.19a and b). The corrected paleopole K^r_{obs} after rotation about the Eulerian pole is not significantly different from the expected ($F_{(2,8)} = 2.0 < F_{\alpha(2,8)} |_{\alpha = 0.05} = 4.46$). The resulting rotational angle of 11.5° along the small circle represents a dextral displacement of ~670 kilometres along the TT-NRMT fault zone , which is in good agreement with the estimates ranging from 450 to 900 kilometres based on the offsets of geological boundaries (Roddick, 1967; Tempelman-Kluit, 1979; Gabrielse, 1985).

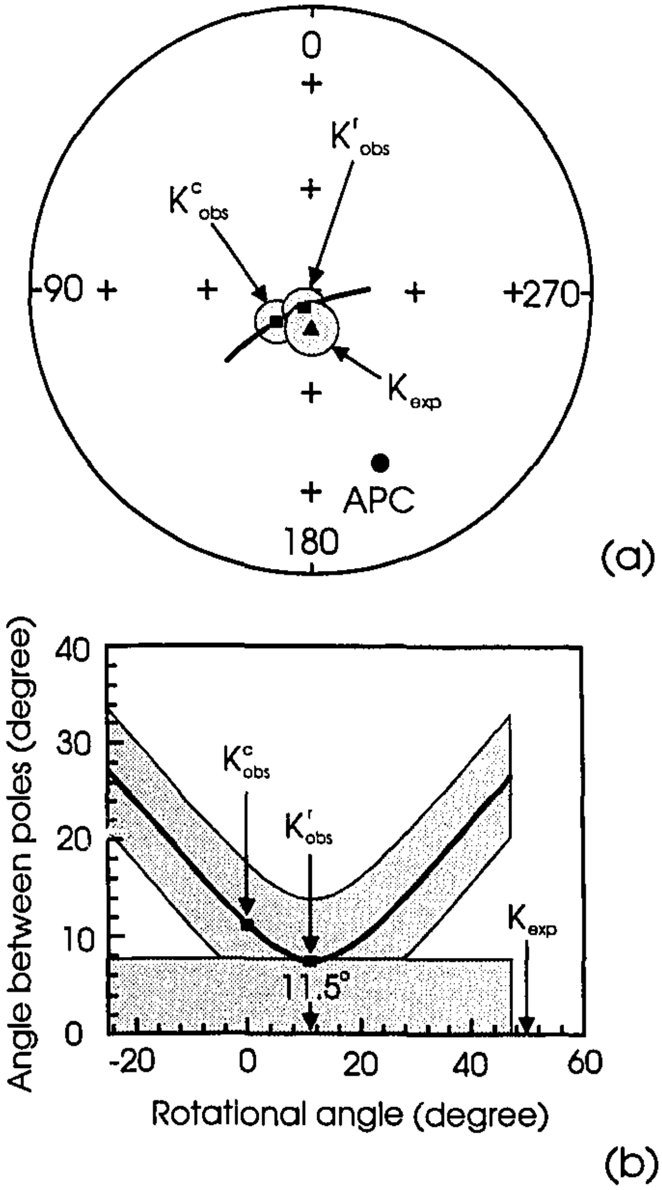

Fig. 3.19 Plots showing clockwise rotation of the observed paleopole (K^c_{obs}) about the Eulerian pole of Price and Carmichael (1986). Solid circle (APC): the Eulerian pole; K^r_{obs}: paleopole after rotation about the Eulerian pole; other symbols: as for Fig. 3.17.

3.6 DISCUSSION AND CONCLUSIONS

Several possible sources of error exist in the above results. First, the number of sampling sites within individual blocks may not be enough to remove the paleomagnetic secular variation, especially for Blocks 1 and 2. Secondly, uncertainty in the age of magnetization contributes some error, although it is small because the positions of the mid to Late Cretaceous reference poles for CNA are very similar (Irving, 1979; Irving and Irving, 1982). Thirdly, errors may arise from the assumption that the present horizontal surfaces in the plutons are parallel to their paleohorizontal, although the structural analysis provides no suggestion of any significant amount of tilting. Finally, uncertainty in the estimate of the Eulerian pole for the best-fitting small circle to the TT-NRMT fault zone may cause some error, as well. All these potential errors, together with those from the determination of rotational axis and angles, may contribute to the difference between the expected and final observed (K_{exp} and K^{r}_{obs} in Figs. 3.19a and b) paleopoles.

Other Cretaceous paleomagnetic data from the Intermontane Belt show apparent northward paleolatitudinal displacement of about 15° (Fig. 3.17) and clockwise rotations ranging from 9 to 75° (Fig. 3.18). Without data on the structures within the areas sampled, assessment of the effects of local structure on the observed magnetic directions is impossible. Some speculations about the causes of the aberrant magnetic directions may be made, however, because strike-slip faults are common in these areas (Roddick, 1967; Tempelman-Kluit, 1979; Gabrielse and Dodds, 1982; Gabrielse, 1985; Price and Carmichael, 1986; Gabrielse, 1991). We have shown that much, if not all, of the disparity in paleomagnetic declination could be explained by local block rotations associated with strike-slip fault motion. Furthermore, although it was not true in the case of our study, it is possible that such rotations could occur about axes less steeply inclined in the northeast quadrant of figure 3.5c, in which case some of the disparity in inclination may also be due to such rotations, thereby decreasing the apparent paleolatitudinal displacements in figure 3.17. Our results indicate, therefore, that it is unwise to draw firm conclusions about the transport of terranes based on paleomagnetic data from complexly deformed orogenic regions unless the collection of paleomagnetic data is accompanied by systematic structural analysis.

3.7 ACKNOWLEDGEMENTS

We would like to thank Jane Wynne and Judith Baker for their cheerful assistance in the Paleomagnetism Lab at Pacific Geoscience Centre, Geological Survey of Canada. Access to commercial software for calculation of the average principal directions of AMS and confidence ellipses was provided at the Geology Department, University of Ottawa, by Keith Benn. This study was supported by grants from the British Columbia Ministry of Energy, Mines and Petroleum Resources, Geological Survey of Canada and the Natural Sciences and Engineering Research Council, and G.Z. was supported by a McGregor Scholarship during his doctoral study. Their support is gratefully acknowledged.

3.8 REFERENCES

Angelier, J. 1984. Tectonic analysis of fault slip data sets. *J. Geophys. Res.* 89, 5835-5848.

Angelier, J. 1989. From orientation to magnitudes in paleostress determination using fault slip data. *J. Struct. Geol.* 11, 37-50.

Beck, M. E. 1992. Some thermal and paleomagnetic consequences of tilting a batholith. *Tectonics*, 11, 297-302.

Beck, M. E., Jr., Burmester, R. F. and Schoonover, R. 1981. Paleomagnetism and tectonics of the Cretaceous Mt. Stuart batholith of Washington: translation or tilt? *Earth Plan. Sci. Lett.* 56, 336-342.

Beck, M. E. and Noson, L. 1972. Anomalous palaeolatitudes in Cretaceous granitic rocks. *Nature*, 235, 11-13.

Bingham, C. 1974. An antipodally symmetric distribution on the sphere. *Ann. Statist.* 2, 1201-1225.

Borradaile, G. J. 1988. Magnetic susceptibility, petrofabrics and strain. *Tectonophysics*, 156, 1-20.

Borradaile, G. J. 1991. Remanent magnetism and ductile deformation in an experimentally deformed magnetite-bearing limestone. *Phys. Earth Planet. Int.* 67, 362-373.

Borradaile, G. J. 1992. Deformation of remanent magnetism in a synthetic aggregate with hematite. *Tectonophysics*. 206, 203-218.

Borradaile, G. J. and Mothersill, J. S. 1991. Experimental strain of isothermal remanent magnetization in ductile sandstone. *Phys. Earth Planet. Int.* 65, 308-218.

Butler, R. F. 1992. Paleomagnetism. *Blackwell Scientific Publications*, Oxford, London and Edinburgh, 319 p.

Butler, R. F., Gehrels, G. E., McClelland, W. C., May, S. R. and Klepacki, D. 1989. Discordant paleomagnetic poles from the Canadian Coast Plutonic Complex: regional tilt rather than large-scale displacement? *Geology*, 17, 691-684.

Butler, R. F., Gehrels, G. E., McClelland, W. C., May, S. R. and Klepacki, D. 1990. Reply on "Discordant paleomagnetic poles from the Canadian Coast Plutonic Complex: regional tilt rather than large-scale displacement?" *Geology*, 18, 801-802.

Butler, R. F., Harms, T. A. and Gabrielse, H. 1988. Cretaceous remagnetization in the Sylvester Allochthon: limits to post-105 Ma northward displacement of north-central British Columbia. *Can. J. Earth Sci.* 25, 1316-1322.

Byerlee, J. 1978. Friction of rocks. *Pure App. Geophys.* 116, 615-626.

Ellwood, B. B., Hrouda, F. and Wagner, J. J. 1988. Symposia on magnetic fabrics: introductory comments. *Physics of the Earth and Planetary Interiors*, 51, 249-252.

Evenchick, C. A. 1991. Structural relationships of the Skeena Fold Belt west of the Bowser Basin, northwest British Columbia. *Can. J. Earth Sci.* 28, 973-983.

Fisher, S. R. 1953. Dispersion on a sphere. *Proc. Roy. Soc. Lond.* 217, 295-305.

Fletcher, R. and Powell, M. J. D. 1963. A rapidly convergent descent method for minimization. *Computer J.* v 6, 163-168.

Gabrielse, H. 1985. Major dextral transcurrent displacements along the Northern Rocky Mountain Trench and related lineaments in north-central British Columbia. *Geol. Soc. Amer. Bull.* 96, 1-14.

Gabrielse, H. 1991. Late Paleozoic and Mesozoic terrane interactions in north-central British Columbia. *Can. J. Earth Sci.* 28, 947-957.

Gabrielse, H. and Dodds, C. J. 1977. The structural significance of the northern Rocky Mountain Trench and related lineaments in north-central British Columbia. *Geol. Assoc. Canada Prog. with Abst.* 2, 19.

Geissman, J. W., Harlan, S. S. and Wawrzyniec, T. F. 1989. Strike-slip faulting and block rotation in the Lake Mead fault system. *Geology,* 17, 1057-1058.

Hardcastle, K. C. 1989. Possible paleostress tensor configurations derived from fault-slip data in eastern Vermont and Western New Hampshire. *Tectonics,* 8, 265-284.

Hardcastle, K. C. and Hills, L. S. 1991. BRUTE3 and SELECT: QUICKBASIC 4 programs for determination of stress tensor configurations and separation of heterogeneous populations of fault-slip data. *Computers & Geosci.* 17, 23-43.

Harland, W. B., Armstrong, R. L., Cox, A. V., Craig, L. E., Smith, A. G. and Smith, D. G. 1989. A geologic time scale. *Cambridge University Press,* Cambridge, 263 p.

Hext, G. R. 1963. The estimation of second-order tensors, with related tests and designs. Biometrika, 50, 353-373.

Hrouda, F. 1982. Magnetic anisotropy of rocks and its application in geology and geophysics. *Geophy. Surv.* 5, 37-82.

Irving, E. 1979. Paleopoles and paleolatitudes of North America and speculations about displaced terrains. *Can. J. Earth. Sci.* 16, 669-694.

Irving, E. and Archibald, D. A. 1990. Bathozonal tilt corrections to paleomagnetic data from mid-Cretaceous plutonic rocks: examples from the Omineca Belt, British Columbia. *J. Geophys. Res.* 95, 4579-4585.

Irving, E. and Irving, G. A. 1982. Apparent polar wander paths Carboniferous through Cenozoic and the assembly of Gondwana. *Geophys. Sur.* [illegible], 141-188.

Irving, E. and Park, J. R. 1973. Palaeomagnetism of metamorphic rocks: errors owing to intrinsic anisotropy. *Geophys. J. R. Astr. Soc.* 34, 489-493.

Irving, E. and Thorkelson, D. J. 1990. On determining paleohorizontal and latitudinal shifts: paleomagnetism of Spences Bridge Group, British Columbia. *J. Geophys. Res.* 95, 19213-19234.

Irving, E., Woodsworth, G. J., Wynne, P. J. and Morrison, A. 1985. Paleomagnetic evidence for displacement from the south of the Coast Plutonic Complex, British Columbia. *Can. J. Earth Sci.* 22, 584-598.

Irving, E. and Wynne, P. J. 1990. Paleomagnetic evidence bearing on the evolution of the Canadian Cordillera. *Phil. Trans. R. Soc. Lond.* 331, 487-509.

Irving, E. and Wynne, P. J. 1991. Paleomagnetic evidence for motions of parts of the Canadian Codillera. *Tectonophysics*, 187, 259-275.

Lord, C. S. 1948. McConnell Creek map-area, Cassiar district, British Columbia. *Geol. Surv. Canada*, Mem. 251, 72 p.

Lowrie, W. and Fuller, M. 1971. On the alternating field demagnetization characteristics of multidomain thermal remanent magnetization in magnetite. *J. Geophys. Res.* 76, 6339-6349.

Mardia, K. V. 1972. Statistics of directional data. *Academic Press*, London and New York, 357 p.

Marquis, G. and Globerman, B. R. 1988. Northward motion of the Whitehorse Trough: paleomagnetic evidence from the Upper Cretaceous Carmacks Group. *Can. J. Earth Sci.* 25, 2005-2016.

Michael, A. 1984. Determination of stress from slip data: faults and folds. *J. Geophys. Res.* 89, 11517-11526.

Monger, J. W. H. 1977. The Triassic Takla Group in McConnell Creek map-area, north-central British Columbia. *Geol. Surv. Canada*, Paper 76-29, 45 p.

Monger, J. W. H. 1984. Cordilleran tectonics: a Canadian perspective. *Bull. Soc. Geol. France*, 26, 255-278.

Monger, J. W. H. and Church, B. N. 1977. Revised stratigraphy of the Takla Group, north-central British Columbia. *Can. J. Earth Sci.* 15, 318-326.

Monger, J. W. H. and Irving, E. 1980. Northward displacement of north-central British Columbia. *Nature,* 285, 289-294.

Monger, J. W. H., Price, R. A. and Tempelman-Kluit, D. J. 1982. Tectonic accretion and the origin of the two major metamorphic and plutonic welts in the Canadian Cordillera. *Geology,* 10, 70-75.

Nelson, M. R. and Jones, C. H. 1986. Paleomagnetism and crustal rotations along a shear zone, Las Vegas Range, southern Nevada. *Tectonics,* 6, 13-33.

Pozzi, J. P. and Aïfa, T. 1989. Effects of experimental deformation on the remanent magnetization of sediments. *Phys. Earth Planet. Int.* 58, 255-266.

Price, R. A. and Carmichael, D. M. 1986. Geometric test for Late Cretaceous-Paleogene intracontinental transform faulting in the Canadian Cordillera. *Geology,* 14, 468-471.

Radney, B. and Byerlee, J. 1988. Laboratory studies of the shear strength of montmorillonite and illite under crustal conditions. *EOS Trans. Am. Geophys. Union,* v. 69, no. 41, p. 1463.

Ramsay, J. G. 1967. Folding and fracturing of rocks. *McGraw-Hill Book Company,* London and Sydney, 568 p.

Reches, Z. 1987. Determination of the tectonic stress tensor from slip along faults that obey the Coulomb yield condition. *Tectonocs,* 6, 849-861.

Rees, C. J., Irving, E. and Brown, R. L. 1985. Secondary magnetization of Triassic-Jurassic volcaniclastic rocks of the Quesnel terrane, Quesnel Lake, B.C. *Geophys. Res. Lett.* 12, 498-501.

Rice, J. A. 1988. Mathematical statistics and data analysis. *Wadsworth & Brooks*, Pacific Grove, California, 595 p.

Richards, T. A. 1976a. McConnell Creek map area (94D/E), Geology. *Geol. Surv. Canada*, Open File 342.

Richards, T. A. 1976b. Takla Group (Reports 10-16): McConnell Creek map area (94D, east half), British Columbia. *Geol. Surv. Canada*, Paper 76-1a, 43-50.

Robin, P. -Y. F. and Jowett, E. C. 1986. Computerized density contouring and statistical evaluation of orientation data using counting circles and continuous weighting functions. *Tectonophysics*, 121, 207-223.

Rochette, P. 1987. Magnetic susceptibility of the rock matrix related to magnetic fabric studies. *J. Struct. Geol.* 9, 1015-1020.

Roddick, J. A. 1967. Tintina Trench. *J. Geol.* 75, 23-33.

Ron, H., Nur, A. and Eyal, Y. 1990. Multiple strike-slip fault sets: a case study from the Dead Sea transform. *Tectonics*, 9, 1421-1431.

Roots, E. F. 1954. Geology and mineral deposits of Aiken Lake map-area, British Columbia. *Geol. Surv. Canada*, Mem. 274, 229 p.

Tempelman-Kluit, D. J. 1979. Transported cataclasite, ophiolite and granodiorite in Yukon: evidence of arc-continent collision. *Geol. Surv. Canada*, Paper 79-14, 27p.

Umhoefer, P. J. 1987. Northward translation of "Baja British Columbia" along the Late Cretaceous to Paleocene margin of western North America. *Tectonics*, 6, 377-394.

Umhoefer, P. J. and Magloughlin, J. F. 1990. Comment on "Discordant paleomagnetic poles from the Canadian Coast Plutonic Complex: regional tilt rather than large-scale displacement?". *Geology*, 18, 800-801.

Upton, G. J. G. and Fingleton, B. 1989. Spatial data analysis by examples: categorical and directional data. Volume 2, *John Wiley & Sons*, New York, 416 p.

Vandall, T. A. and Palmer, H. C. 1990. Canadian Cordillera displacement: paleomagnetic results from the Early Jurassic Hazelton Group, Terrane I, British Columbia, Canada. *Geophys. J. Int.* 103, 609-619.

Woodsworth, G. J. 1976. Plutonic rocks of McConnell Creek (94D west half) and Aiken Lake (94C east half) map-areas, British Columbia. *Geol. Surv. Canada*, Paper 76-1A, 26-30.

Wynne, P. J., Irving, E. and Ferri, F. 1992. Paleomagnetism of the middle Cretaceous Germansen batholith, British Columbia (93N/9, 10). Geological Fieldwork 1991, *B.C. Ministry of Energy, Mines and Petroleum Resources*, Paper 1992-1, 119-126.

Zhang, G. and Hynes, A. (in press). Fabrics and kinematic indicators associated with the local structures along Finlay-Ingenika fault, McConnell Creek area, north-central British Columbia. *Can. J. Earth Sci.*

Zoback, M. D., Zoback, M. L., Mount, V. S., Suppe, J., Eaton, J. P., Healy, J. H., Oppenheimer, D., Reasenberg, P., Jones, L., Raleigh, C. B., Wong, I. G., Scotti, O. and Wentworth, C. 1987. New evidence on the state of stress of the San Andreas fault system. *Science*, v. 238, no. 4830, 1105-1111.

3.9 APPENDIX

Bingham's statistics (Bingham, 1974) describe an antipodally symmetric distribution of directional data on a unit sphere. Given $\mathbf{L}_1$, $\mathbf{L}_2, \ldots, \mathbf{L}_n$ ($\mathbf{L}_i = (l_i, m_i, n_i)^T$, unit column vectors representing the directions of axial data), a random sample from a population with a Bingham's distribution, its probability density function may be written

$$f(\boldsymbol{L}, \boldsymbol{k}, \boldsymbol{u}) = \frac{1}{4\pi d(\boldsymbol{k})}\exp[tr(\boldsymbol{k}\boldsymbol{u}^T\boldsymbol{L}\boldsymbol{L}^T\boldsymbol{u})]$$

$$= \frac{1}{4\pi d(\boldsymbol{k})}\exp[k_1(\boldsymbol{u}_1{}^T\boldsymbol{L})^2 + k_2(\boldsymbol{u}_2{}^T\boldsymbol{L})^2 + k_3(\boldsymbol{u}_3{}^T\boldsymbol{L})^2] \qquad \text{(A1)}$$

where $\mathbf{u} = (\mathbf{u}_1, \mathbf{u}_2, \mathbf{u}_3)$ is an orthogonal matrix specifying three true orthogonal (normalized) directions, $\mathbf{k} = \mathrm{diag}(k_1, k_2, k_3)$ is a diagonal matrix of precision coefficients for the distribution, $d(\mathbf{k})$ is a constant given by $\frac{1}{4\pi}\int_0^{2\pi}\int_0^{\pi}\exp(k_1\cos^2\phi\ \sin^2\theta + k_2\sin^2\phi\ \sin^2\theta + k_3\cos^2\theta)\sin\theta\ d\theta d\phi$ (where $\sin\theta\cos\phi$

$= \mathbf{u}_1{}^T\mathbf{L}$, $\sin\theta\sin\phi = \mathbf{u}_2{}^T\mathbf{L}$ and $\cos\theta = \mathbf{u}_3{}^T\mathbf{L}$), tr() represents the sum of the diagonal elements of matrix inside the parentheses and superscript (T) represents the transpose of its corresponding matrix or vector (Bingham, 1964 as referenced by himself in 1974; Mardia, 1972; Upton and Fingleton, 1989).

In terms of classical statistics, the three mean orthogonal directions ($\hat{\mathbf{u}}$) of an observed sample can be obtained from the maximum likelihood estimate (m.l.e.) of **u** (Rice, 1988). The likelihood function (Rice, 1988) of **k** and **u** in equation (A1) is found to be

$$L(\boldsymbol{L}_1,\boldsymbol{L}_2,\ldots,\boldsymbol{L}_n,\boldsymbol{k},\boldsymbol{u}) = \prod_{i=1}^{n} \frac{1}{4\pi d(\boldsymbol{k})}\exp[tr(\boldsymbol{k}\boldsymbol{u}^T\boldsymbol{L}_i\boldsymbol{L}_i^T\boldsymbol{u})]$$

$$= \left(\frac{1}{4\pi d(\boldsymbol{k})}\right)^n \exp[tr(\boldsymbol{k}\boldsymbol{u}^T\boldsymbol{T}\boldsymbol{u})] \qquad \text{(A2)}$$

where $\boldsymbol{T} = \begin{pmatrix} \sum_{i=1}^{n} l_i^2 & \sum_{i=1}^{n} l_i m_i & \sum_{i=1}^{n} l_i n_i \\ & \sum_{i=1}^{n} m_i^2 & \sum_{i=1}^{n} m_i n_i \\ & & \sum_{i=1}^{n} n_i^2 \end{pmatrix}$ is a symmetric matrix. Its logarithm may be written

$$\ln(L) = -n\ln(4\pi)-n\ln(d(\boldsymbol{k}))+tr(\boldsymbol{k}\boldsymbol{u}^T\boldsymbol{T}\boldsymbol{u})+tr(\boldsymbol{A}(\boldsymbol{I}-\boldsymbol{u}^T\boldsymbol{u})) \qquad \text{(A3)}$$

where $\mathbf{u}^T\mathbf{u} = \mathbf{I}$, because $\mathbf{u}$ is an orthogonal matrix (Eq. A1) and $\mathbf{A}$ is a symmetric matrix of Lagrangian multipliers (Mardia, 1972). Based on statistical estimate theory, the sample $\hat{\mathbf{u}}$ directions can be obtained when ln(L) of equation (A3) achieves maximum value (Rice, 1988). Thus

$$\frac{\partial(\ln(L))}{\partial \boldsymbol{u}} = tr(\boldsymbol{k}\boldsymbol{u}^T\boldsymbol{T})+tr(-\boldsymbol{A}\boldsymbol{u}^T) = 0 \qquad \text{(A4)}$$

By rewriting equation (A4) we have

$$\boldsymbol{k}^{-1}\boldsymbol{A} = \boldsymbol{k}^{-1}\boldsymbol{k}\hat{\boldsymbol{u}}^T\boldsymbol{T}\hat{\boldsymbol{u}} = \hat{\boldsymbol{u}}^T\boldsymbol{T}\hat{\boldsymbol{u}} \qquad \text{(A5)}$$

where $\mathbf{k}^{-1}$ is the inverse of $\mathbf{k}$ and $\mathbf{A}$ is a diagonal matrix as required by the right side of the equation. It is evident from equation (A5) that when equation (A4) reaches its maxima, $\mathbf{k}^{-1}\mathbf{A} = \text{diag}(\tau_1, \tau_2, \tau_3)$ and $\hat{\mathbf{u}} = (\mathbf{t}_1, \mathbf{t}_2, \mathbf{t}_3)$, where (τ_1, τ_2, τ_3) and $(\mathbf{t}_1, \mathbf{t}_2, \mathbf{t}_3)$ are the minimum, intermediate and maximum eigenvalues and eigenvectors of matrix $\mathbf{T}$, respectively. Therefore, the m.l.e. of $\mathbf{u}$ is the eigenvectors of $\mathbf{T}$.

The geometrical significance of the eigenvalues could be clearly illustrated by the analysis of moment of inertia (i.e. the sum of squares of the perpendicular distances of the observed sample (l_i, m_i, n_i) from the directions $\hat{\mathbf{u}}$, cf. Mardia, 1972). For example, when $\tau_1 \approx \tau_2 \approx \tau_3$, the distribution is uniform; when $\tau_1 \approx \tau_2 < \tau_3$, it is axially symmetric (either unipolar or bipolar) about $\mathbf{t}_3$ and when $\tau_1 < \tau_2 \approx \tau_3$, it is a symmetric girdle distribution in the plane normal to the axis $\mathbf{t}_1$, etc.

The sample precision coefficients $\hat{\boldsymbol{k}}$ can similarly be obtained from the m.l.e of $\mathbf{k}$. The sum of k_i (i = 1 to 3) of equation (A1) is arbitrary, so that k_3 may be set to zero (cf. Mardia, 1972; Bingham, 1974). Substituting $\hat{\mathbf{u}}$ into equation (A3) leads to

$$\ln(L) = -n\ln(4\pi)-n\ln(d(\boldsymbol{k}))+k_1\tau_1+k_2\tau_2 \tag{A6}$$

Maximization of ln(L) in equation (A6) as a function of k_1 and k_2 yields two nonlinear simultaneous equations, from which $\hat{\boldsymbol{k}}$ could be calculated. $\hat{\boldsymbol{k}}$ may also be solved, however, by calculating the maxima of equation (A6) by changing the values of k_1 and k_2, so that

$$\ln(L) = -n\ln(4\pi)-n\ln(d(k_1,\ k_2))+k_1\tau_1+k_2\tau_2 = \ln(L)_{\max}|_{k_1 = \hat{k}_1,\ k_2 = \hat{k}_2} \tag{A7}$$

Equation (A7) may be solved numerically by the method of Fletcher and Powell (1963). This is the procedure we adopted. Finally, based on a chi-square test, estimates of the axes of the 95% confidence ellipses about the $\hat{\mathbf{u}} = (\mathbf{t}_1,\ \mathbf{t}_2,\ \mathbf{t}_3)$

directions are found to be

$$\hat{\alpha}_{ij} = \left(\frac{\chi^2_{1-\alpha}(2)}{2(\tau_i-\tau_j)(\hat{k}_i-\hat{k}_j)}\right)^{1/2} \tag{A8}$$

in the directions of $\mathbf{t}_i$-$\mathbf{t}_j$ on a unit sphere (cf. Bingham, 1974), where i, j = 1, 3 and $i \neq j$.

The maximum eigenvectors ($\mathbf{t}_3$) were taken as site-mean directions for the principal axes (σ_1, σ_2 and σ_3) of the stress tensors, with 95% confidence limits of $\hat{\alpha}_{31}$ and $\hat{\alpha}_{32}$. A Fortran program, available on request, was used to calculate the eigenvectors t_1, t_2 and t_3 (Eq. A5), precision coefficients k_1 and k_2 (Eq. A7) and 95% confidence limits $\hat{\alpha}_{ij}$ (Eq. A8) of the stress tensors.

CHAPTER 4

General Conclusions

4.1 CONTRIBUTION TO ORIGINAL WORK

Major contributions from this research to original knowledge are as follows:

(1) The comprehensive analysis of deformational and magnetic fabrics and kinematic data and systematic statistics of cleavage data associated with the local deformation along the dextrally transpressive Finlay-Ingenika fault, all of which added significantly to our understanding of the strike-slip structures in north-central British Columbia. The mode of local deformation associated with transpression along a large-scale strike-slip fault, as documented in this research, may have characterized many parts of the western Canadian Cordillera, such as the eastern Intermontane and western Coast Belts of north-central British Columbia, and could be relevant to other regions with similar tectonic circumstances.

(2) The demonstration of the application of Bingham's statistics in structural geology, which enabled us to characterize various directional structural data quantitatively. Bingham's statistics describe distributions ranging from axially symmetric to girdle which characterize the sample probability distributions of most directional structural data such as foliations, lineations and bedding planes. This

statistical technique can therefore provide a quantitative analysis of directional structural data in structural geology, which is a prerequisite for tectonic studies.

(3) The development of a technique for determination of the position-gradient tensor from conventional strain data which provides a means to determine the displacement-boundary conditions of a shear zone. It is a straightforward technique and independent of assumptions of deformation modes. Unlike the conventional technique, which depends strongly on the assumption of deformation modes, this technique enables us to determine the position-gradient tensor through forward computer-modelling of progressive deformation. It is of particular importance in the kinematic analysis of ductile shear zones, since there are no rigid-body translations along the shear zones and the displacements calculated from the position-gradient tensor represent true displacements on the shear zones. Furthermore, in the absence of the strain markers that can be used for strain measurement, the position-gradient tensor may be determined indirectly by measuring anisotropy of magnetic susceptibility (AMS) of the strained rocks across a shear zone through the relationship between AMS and strain. The technique is, therefore, an efficient and widely applicable quantitative tool in the strain and kinematic analysis of rocks deformed in orogenic belts.

(4) The demonstration of the contribution of deformation to the production of aberrant paleomagnetic directions. The local block rotations inferred from

structural analysis can account fully for the aberrance of the observed magnetic declinations, and the paleopole after corrections for the local block rotations can be brought into coincidence with the reference pole for North America, with an amount of northward displacement in accord with that demonstrable from geological evidence. This is the first study in the western Canadian Cordillera that has reconciled aberrant paleomagnetic data with geological evidence.

4.2 SUGGESTIONS FOR FUTURE WORK

As an extension of this research, some suggestions for future studies in the following domains are proposed.

4.2.1 Relationship between AMS and Strain

In the kinematic analysis of shear zones, as discussed in the second chapter, data concerning the strain states have to be provided. Since determination of the strain state in deformed rocks using conventional techniques is tedious and time-consuming, and limited to the few cases in which the strain markers are present, AMS of deformed rocks should be used as strain indicators. The application of AMS, however, depends upon a clear understanding of AMS-to-strain relationships. Therefore, a study of relationship between AMS and strain is urgently needed.

Although various theoretical strain-response models were used to simulate the AMS-to-strain relationship, the modelling has so far been limited to problems involving simple flow geometries and magnetic particles with very simple shapes approximated by lines and planes, or by uniaxial ellipsoids. It is therefore herein suggested to revise the fluid-mechanics based on the strain-response model of Jeffrey, in order to investigate the behaviour of both spheroidal and triaxial ellipsoidal magnetic particles in more general flow systems. This could provide a theoretical model of the evolution of AMS with strain by which a quantitative relationship between AMS and strain could be determined through numerical modelling. With this relationship, AMS can be used as a rapid physical technique of strain analysis that could be applied in widely varying geological environments, especially where strain markers are absent.

4.2.2 Regarding the Implications of Discordant Paleomagnetic Directions

Further studies are required before the enigma of Cretaceous discordant paleomagnetic directions in the western Canadian Cordillera is solved. As noted, one of the key factors in paleomagnetic studies is the determination of paleohorizontals, especially in the Coast Belt since all the discordant paleomagnetic directions observed there are from plutonic rocks. Barometric analysis of the contact metamorphic assemblage around a pluton could provide an estimate of post-emplacement tilting (rotation about a horizontal axis) of the paleohorizontal, whereas structural analysis could constrain rotations of the paleohorizontal about either horizontal or vertical axes, as demonstrated from this study. This is also true for bedded volcanic rocks since the present strikes of their bedding planes are not necessarily perpendicular to their paleoslopes as commonly assumed. It would therefore be extremely beneficial if detailed petrological and structural studies could be carried out in regions in which discordant paleomagnetic directions have previously been reported or could accompany future paleomagnetic studies in the western Canadian Cordillera.

Appendix 1. Raw data on deformed volcanic fragments

Domain 1

Sec. no.	strike (°)	dip (°)	trend (°)	plunge (°)	n	X'/Z'	r_{XZ}
DOM101	101	36	147	28	9	2.13	0.86
DOM102	065	55	130	52	6	2.27	0.98
DOM103	045	38	142	38	6	1.59	0.99
DOM104	237	53	001	48	5	2.44	0.96
DOM105*	038	82	061	70	6	4.00	0.84
DOM106	133	53	150	21	13	2.94	0.96
DOM107	235	41	353	37	11	3.03	0.98
DOM108	200	55	352	34	12	2.86	0.86
DOM109	191	29	343	15	6	4.17	0.90
DOM110	100	62	135	47	9	3.03	0.94
DOM111	144	64	152	16	10	2.50	0.96
DOM112	208	57	355	40	9	2.78	0.96
DOM113	152	30	157	03	9	4.00	0.94
DOM114	182	27	341	10	6	3.33	0.98
DOM115	103	40	146	30	15	3.45	0.89
DOM116	053	49	134	49	9	2.70	0.93
DOM117	130	55	149	24	12	3.45	0.79
DOM118	209	71	004	51	9	2.56	0.96
DOM119	068	56	130	53	4	4.00	0.58
DOM120	179	13	339	04	10	3.03	0.98

Notes: strike/dip: section attitude; trend/plunge: stretching direction; n: number of fragments; X'/Z': apparent aspect ratio; r_{XZ}: coefficient of linear correlation; section with star (*) is not used in the strain analysis.

Appendix 1. Continued

Domain 2

Sec. no.	strike (°)	dip (°)	trend (°)	plunge (°)	n	X'/Z'	r_{XZ}
DOM201	110	27	151	18	45	3.85	0.98
DOM202	148	44	154	06	12	2.94	0.99
DOM203	082	40	144	36	15	2.17	0.91
DOM204	123	38	150	20	12	3.57	0.89
DOM205	140	35	153	09	15	3.45	0.96
DOM206	163	83	341	16	15	3.23	0.90
DOM207	195	21	340	12	9	6.67	0.94
DOM208	158	50	337	02	18	3.57	0.91
DOM209	123	40	150	21	39	4.17	0.92
DOM210	223	63	359	54	12	1.92	0.89
DOM211	248	42	351	41	5	3.70	1.00
DOM212	117	28	151	17	18	2.86	0.91
DOM213	255	45	353	45	15	2.86	0.87
DOM214	152	66	154	06	42	3.70	0.84
DOM215	102	43	145	33	6	1.92	1.00
DOM216	214	22	341	18	13	3.13	0.99
DOM217	036	21	150	19	15	4.35	0.98
DOM218	106	70	134	52	12	2.70	0.98
DOM219	243	36	348	35	21	3.45	0.92
DOM220	036	88	042	73	9	3.23	0.96
DOM221	096	27	149	23	6	3.70	0.97
DOM222	071	43	142	41	23	4.00	0.95
DOM223	272	32	346	31	24	3.23	0.92
DOM224	155	21	156	00	27	5.26	0.86
DOM225	063	61	128	59	21	4.17	0.94
DOM226	337	35	156	01	6	2.50	0.91
DOM227	074	57	134	53	24	3.57	0.94
DOM228	151	11	156	01	6	5.26	0.88
DOM229	123	24	152	12	9	5.88	0.99
DOM230	020	14	153	10	6	6.25	1.00
DOM231	212	61	354	48	9	3.45	0.99
DOM232	337	58	155	03	3	2.78	1.00

Notes: same as for Domain 1.

Appendix 1. Continued

Domain 3

Sec. no.	strike (°)	dip (°)	trend (°)	plunge (°)	n	X'/Z'	r_{XZ}
DOM301	160	45	334	06	3	12.50	1.00
DOM302	194	13	334	08	12	16.70	0.89
DOM303	157	22	332	02	8	10.00	1.00
DOM304	134	49	147	14	9	5.56	0.97
DOM305	185	50	341	26	9	9.09	0.98
DOM306	331	90	151	02	9	11.11	0.64
DOM307	185	52	341	27	8	14.30	0.98
DOM308*	048	81	075	71	7	100.00	0.15

Notes: same as for Domain 1.

Appendix 2. Raw data on magnetic susceptibility from plutonic rocks

Site 1

SPEC. NO.	KM	L	F	P	P'	T
2-2	4503.9	1.236	1.289	1.592	1.593	-0.026
3-1	6616.0	1.179	1.477	1.741	1.768	0.287
3-2	5231.5	1.158	1.254	1.452	1.456	0.124
4-1	10285.2	1.198	1.483	1.776	1.800	0.245
4-2	11618.4	1.207	1.445	1.744	1.761	0.196
5-1	7260.0	1.186	1.387	1.646	1.659	0.199
5-2	9887.8	1.183	1.480	1.752	1.778	0.278
6-1	5228.0	1.197	1.201	1.438	1.438	-0.082
1-1	5222.9	1.159	1.257	1.457	1.461	0.124
1-2	5215.0	1.161	1.251	1.452	1.456	0.110
2-1	5218.8	1.159	1.254	1.453	1.457	0.120
AVERAGE	6935.2	1.184	1.343	1.591	1.602	0.143
STD DEV	2502.9	0.025	0.111	0.144	0.154	0.117

Notes: KM: bulk susceptibility (i.e. KM = $(K_1+K_2+K_3)/3$, in 10^{-6} SI units, where K_1, K_2 and K_3 are maximum, intermediate and minimum principal susceptibility); L: magnetic lineation (K_1/K_2); F: magnetic foliation (K_2/K_3); P: degree of magnetic anisotropy (K_1/K_3); $P' = \exp[2((\ln(K_1)-LM)^2+(\ln(K_2)-LM)^2+(\ln(K_3)-LM)^2)]^{½}$, where LM $= (\ln(K_1)+\ln(K_2)+\ln(K_3))/3$; $T = (2K_2-K_1-K_3)/(K_1-K_3)$.

Appendix 2. Continued

Site 2

SPEC. NO.	KM	L	F	P	P'	T
1-1	5090.0	1.222	1.197	1.462	1.462	-0.149
1-2	4881.6	1.188	1.198	1.423	1.423	-0.063
2-1	7146.5	1.237	1.245	1.540	1.540	-0.092
2-2	5927.2	1.204	1.368	1.647	1.656	0.137
3-1	9846.5	1.207	1.408	1.699	1.711	0.167
3-2	5794.1	1.216	1.244	1.513	1.513	-0.049
4-1	3903.7	1.215	1.217	1.478	1.478	-0.092
4-2	6062.6	1.256	1.296	1.627	1.628	-0.056
5-1	7191.7	1.271	1.350	1.715	1.717	-0.022
5-2	5242.1	1.237	1.301	1.609	1.611	-0.011
6-1	7197.4	1.165	1.436	1.673	1.697	0.295
6-2	7220.9	1.235	1.330	1.642	1.645	0.027
AVERAGE	6292.0	1.221	1.299	1.586	1.590	0.008
STD DEV	1553.0	0.029	0.081	0.099	0.103	0.129

Appendix 2. Continued

Site 3

SPEC. NO.	KM	L	F	P	P'	T
1-2	15939.8	1.005	1.038	1.043	1.047	0.743
2-1	19648.1	1.011	1.051	1.063	1.067	0.630
3-1	16223.7	1.014	1.050	1.065	1.068	0.545
3-2	13885.6	1.010	1.045	1.055	1.059	0.621
4-1	16641.4	1.006	1.051	1.057	1.063	0.780
4-2	14735.5	1.013	1.030	1.044	1.045	0.373
5-1	18042.8	1.009	1.040	1.049	1.053	0.636
5-2	13802.4	1.011	1.045	1.057	1.060	0.596
6-1	18655.0	1.013	1.048	1.062	1.065	0.546
6-2	17444.1	1.002	1.057	1.059	1.067	0.934
AVERAGE	16501.8	1.009	1.045	1.055	1.059	0.640
STD DEV	1985.0	0.004	0.008	0.008	0.008	0.152

Appendix 2. Continued

Site 4

SPEC. NO.	KM	L	F	P	P'	T
1-1	44890.2	1.047	1.058	1.108	1.108	0.072
1-2	45215.2	1.020	1.070	1.091	1.096	0.533
3-2	35914.3	1.019	1.036	1.056	1.057	0.290
4-1	41689.5	1.008	1.066	1.075	1.082	0.774
5-1	44586.0	1.021	1.052	1.074	1.077	0.412
5-2	42727.7	1.024	1.059	1.084	1.087	0.391
6-1	35553.3	1.032	1.038	1.071	1.071	0.063
6-2	34344.8	1.035	1.049	1.085	1.086	0.143
4-2	42903.0	1.010	1.068	1.079	1.086	0.719
AVERAGE	40869.3	1.024	1.055	1.080	1.083	0.377
STD DEV	4366.2	0.012	0.012	0.014	0.014	0.263

Appendix 2. Continued

Site 5

SPEC. NO.	KM	L	F	P	P'	T
1-2	40224.2	1.049	1.047	1.099	1.099	-0.044
2-1	33924.0	1.056	1.035	1.094	1.094	-0.247
2-2	36593.8	1.040	1.039	1.081	1.081	-0.036
4-1	41967.7	1.064	1.053	1.121	1.121	-0.121
4-2	42926.4	1.055	1.038	1.094	1.095	-0.205
1-1	44136.5	1.091	1.040	1.134	1.138	-0.409
3-1	38532.0	1.055	1.061	1.119	1.119	0.019
3-2	41181.5	1.067	1.052	1.122	1.122	-0.155
5-1	38624.5	1.058	1.073	1.135	1.135	0.080
5-2	41468.9	1.050	1.056	1.109	1.109	0.030
6-1	34474.4	1.032	1.046	1.080	1.081	0.154
6-2	33546.0	1.026	1.065	1.092	1.095	0.406
AVERAGE	38966.7	1.054	1.050	1.107	1.107	-0.044
STD DEV	3631.8	0.017	0.012	0.019	0.019	0.210

Appendix 2. Continued

Site 6

SPEC. NO.	KM	L	F	P	P'	T
1-1	16381.5	1.007	1.084	1.092	1.103	0.841
1-2	16996.6	1.020	1.077	1.098	1.104	0.565
2-1	16520.6	1.013	1.079	1.093	1.101	0.701
3-1	17344.1	1.019	1.067	1.087	1.092	0.529
4-1	18595.3	1.026	1.081	1.109	1.114	0.490
5-1	18295.0	1.024	1.046	1.071	1.072	0.303
6-1	16981.6	1.020	1.077	1.098	1.104	0.570
2-2	16503.8	1.013	1.079	1.093	1.101	0.706
3-2	16803.9	1.018	1.054	1.073	1.076	0.471
5-2	17639.1	1.013	1.059	1.073	1.078	0.611
AVERAGE	17206.1	1.017	1.070	1.089	1.094	0.579
STD DEV	761.7	0.006	0.013	0.013	0.014	0.149

Appendix 2. Continued

Site 7

SPEC. NO.	KM	L	F	P	P'	T
2-1	17281.2	1.031	1.056	1.089	1.090	0.258
2-2	16423.6	1.023	1.061	1.086	1.089	0.426
3-1	17661.2	1.022	1.069	1.093	1.097	0.486
3-2	16460.9	1.015	1.063	1.079	1.084	0.594
4-1	17007.5	1.031	1.069	1.103	1.105	0.349
4-2	16733.5	1.016	1.087	1.104	1.113	0.675
5-1	16766.1	1.013	1.062	1.075	1.081	0.644
5-2	16776.5	1.030	1.053	1.084	1.085	0.261
6-1	17317.9	1.023	1.068	1.093	1.097	0.468
6-2	18453.0	1.026	1.066	1.093	1.096	0.405
1-1	17377.2	1.014	1.072	1.088	1.094	0.650
1-2	16063.0	1.020	1.072	1.094	1.098	0.534
AVERAGE	17026.8	1.022	1.067	1.090	1.094	0.479
STD DEV	642.4	0.007	0.009	0.009	0.009	0.145

Appendix 2. Continued

Site 8

SPEC. NO.	KM	L	F	P	P'	T
2-1	22095.2	1.054	1.069	1.127	1.127	0.089
5-2	24812.8	1.032	1.095	1.130	1.135	0.462
6-1	20955.0	1.036	1.091	1.130	1.134	0.403
6-2	23625.4	1.028	1.077	1.107	1.111	0.433
2-2	23928.8	1.037	1.090	1.130	1.134	0.383
1-1	17620.2	1.048	1.032	1.081	1.082	-0.224
3-1	28022.6	1.019	1.050	1.070	1.072	0.420
3-2	27470.7	1.032	1.080	1.114	1.118	0.402
4-1	26875.4	1.055	1.050	1.108	1.108	-0.067
4-2	19711.4	1.060	1.041	1.103	1.104	-0.203
AVERAGE	23511.7	1.040	1.067	1.110	1.113	0.210
STD DEV	3446.6	0.013	0.023	0.021	0.022	0.281

Appendix 2. Continued

Site 9

SPEC. NO.	KM	L	F	P	P'	T
1-1	32469.5	1.022	1.156	1.182	1.199	0.717
1-2	23726.2	1.027	1.134	1.165	1.177	0.629
2-1	34193.1	1.048	1.148	1.202	1.211	0.461
3-1	30578.0	1.019	1.163	1.184	1.204	0.765
5-1	36862.2	1.058	1.206	1.275	1.290	0.495
6-1	34892.6	1.033	1.211	1.251	1.274	0.678
2-2	35176.5	1.034	1.188	1.229	1.247	0.649
3-2	25889.3	1.044	1.124	1.173	1.180	0.433
4-1	31799.8	1.009	1.191	1.202	1.230	0.895
4-2	29006.3	1.007	1.154	1.162	1.185	0.899
5-2	32302.5	1.048	1.191	1.248	1.264	0.540
6-2	31693.4	1.034	1.196	1.237	1.256	0.653
AVERAGE	31549.1	1.032	1.172	1.209	1.226	0.651
STD DEV	3834.0	0.016	0.029	0.038	0.039	0.154

Appendix 2. Continued

Site TPA05

SPEC. NO.	KM	L	F	P	P'	T
1-1	1139.8	1.068	1.319	1.409	1.439	0.562
1-2	1186.0	1.057	1.318	1.394	1.427	0.617
2-1	1425.0	1.057	1.404	1.484	1.534	0.671
3-1	1028.3	1.063	1.336	1.420	1.455	0.598
3-2	976.8	1.058	1.359	1.437	1.477	0.642
4-1	1445.4	1.061	1.395	1.480	1.526	0.647
4-2	1959.3	1.074	1.432	1.538	1.586	0.605
5-1	1483.8	1.070	1.390	1.488	1.529	0.599
2-2	1517.6	1.073	1.347	1.445	1.478	0.561
5-2	1352.0	1.073	1.349	1.448	1.481	0.561
AVERAGE	1351.4	1.065	1.365	1.454	1.493	0.606
STD DEV	287.9	0.007	0.038	0.044	0.050	0.039

Appendix 2. Continued

Site-mean directions of principal magnetic susceptibility and their long and short axes of 95% confidence ellipses

Site No.	K_1 (°)	K_2 (°)	K_3 (°)	α_{11} (°)	α_{12} (°)	α_{21} (°)	α_{22} (°)	α_{31} (°)	α_{32} (°)
1	004/21	144/63	268/15	8.5	4.6	7.6	3.9	6.5	4.8
2	011/23	134/52	267/28	7.0	4.3	5.4	3.1	6.3	3.2
3	210/36	007/52	112/11	14.4	5.6	14.2	5.7	7.9	2.8
4	011/21	113/29	250/53	24.4	6.3	24.7	7.7	11.6	4.5
5	028/51	201/39	294/04	4.4	2.9	24.2	3.6	24.2	3.7
6	046/67	285/12	191/19	15.0	2.8	15.0	6.8	7.0	2.4
7	034/71	288/06	196/18	12.3	5.0	12.1	4.9	7.3	1.9
8	257/76	019/08	111/12	8.4	4.4	10.3	4.8	8.6	5.7
9	336/50	072/05	166/40	14.5	3.0	14.6	2.8	4.4	2.5
TPA05	110/40	328/43	218/20	4.7	2.2	3.5	2.5	4.0	2.3

Notes: 004/21: trend/plunge of K_i; α_{i1} and α_{i2}: long and short axes of 95% confidence ellipse (Hext, 1964) about K_i, where i = 1 to 3.

Appendix 3. Site-mean directions of principal stress tensors and their 95% confidence limits

		Bingham's statistics					Fisher's statistics		
Site	n	trend/plunge (°)	k_1	k_2	α_{31} (°)	α_{32} (°)	trend/plunge (°)	k	α_{95} (°)
1	681	076.0/03.6	-28.06	-4.79	0.8	2.0	075.9/03.8	11	1.7
		335.3/69.1	-5.58	-4.70	2.0	2.2	335.2/69.1	7	2.3
		167.8/20.4	-29.66	-5.41	0.8	1.9	168.8/20.4	13	1.6
2	510	252.2/00.6	-27.53	-4.90	0.9	2.3	252.4/01.0	12	1.9
		345.7/71.7	-5.88	-3.92	2.2	2.9	346.7/71.3	6	2.8
		160.0/18.7	-26.68	-4.54	0.9	2.4	159.9/18.9	10	2.1
3	576	081.5/07.2	-33.41	-4.04	0.8	2.5	081.3/08.1	10	2.0
		330.7/69.4	-6.39	-4.08	2.0	2.6	328.7/69.0	6	2.5
		173.9/18.8	-31.92	-6.42	0.8	1.8	173.9/19.1	15	1.5
4	2082	091.1/15.5	-11.77	-3.04	0.8	1.7	091.4/15.8	6	1.3
		253.9/73.3	-4.36	-2.05	1.5	2.5	255.1/73.3	4	1.8
		354.9/03.8	-11.94	-3.30	0.8	1.6	354.7/03.3	7	1.3
5	345	075.7/01.9	-27.65	-3.63	1.1	3.5	075.5/02.6	8	2.8
		340.1/71.8	-9.69	-3.42	2.0	3.8	338.9/71.5	6	3.2
		163.8/18.7	-27.65	-8.25	1.1	2.0	163.8/19.1	20	1.7
6	153	255.0/00.7	-67.76	-50.08	1.0	1.2	255.0/00.7	112	1.1
		162.2/74.1	-38.85	-2.71	1.5	6.6	161.6/76.8	6	4.9
		345.6/15.7	-53.92	-2.70	1.3	6.6	345.6/13.1	6	4.9

Notes: n: number of stress tensors; trend/plunge: directions of principal stresses in the order σ_1, σ_2 and σ_3; k_1 and k_2: Bingham's precision coefficients; α_{31} and α_{32}: short and long axes of 95% confidence ellipse (Bingham, 1974); k: Fisher's precision coefficient; α_{95}: radius of 95% confidence circle (Fisher, 1953). The results of Fisher's statistics are obtained by converting bipolar data to unipolar data before applying Fisher's statistics.

Appendix 3. Continued

		Bingham' statistics					Fisher's statistics		
Site	n	trend/plunge (°)	k_1	k_2	α_{31} (°)	α_{32} (°)	trend/plunge (°)	k	α_{95} (°)
7	1974	249.3/06.1	-12.16	-2.73	0.8	1.9	249.3/06.6	6	1.5
		118.8/79.3	-4.17	-2.19	1.6	2.5	117.7/78.8	4	1.9
		336.5/08.3	-12.40	-3.78	0.7	1.4	336.4/08.7	8	1.2
8	438	256.3/07.2	-23.03	-6.30	1.1	2.1	256.5/06.1	15	1.8
		085.1/83.1	-6.58	-4.59	2.2	2.7	079.2/84.0	7	2.8
		347.2/01.1	-23.16	-4.69	1.1	2.6	346.9/00.5	10	2.2
9*	333	073.2/04.0	-20.39	-0.36	1.7	29.0	073.3/06.6	3	5.5
		309.5/86.3	-20.15	-0.39	1.7	27.7	268.3/81.2	3	5.5
		161.9/01.1	-122.41	-115.63	0.5	0.5	161.9/01.2	58	1.0
10	62	068.6/09.6	-77.76	-12.16	1.5	3.8	068.6/09.8	35	3.1
		291.6/77.4	-14.05	-6.06	3.7	5.8	295.8/76.2	12	5.3
		160.9/07.7	-71.18	-6.27	1.6	5.6	161.2/09.3	17	4.5
11	239	246.1/11.1	-34.09	-23.32	1.1	1.4	246.1/11.1	53	1.3
		076.6/78.7	-26.45	-3.42	1.4	4.4	074.5/78.8	7	3.6
		336.6/02.2	-27.10	-3.37	1.4	4.4	336.4/01.7	7	3.6
12	168	065.5/12.1	-22.52	-6.55	1.7	3.3	065.9/13.4	16	2.8
		214.2/74.4	-7.28	-6.04	3.3	3.6	227.0/74.8	9	3.8
		333.1/07.9	-22.81	-6.31	1.7	3.4	332.9/04.8	13	3.1

Note: for the site marked with star (*), the Fisher's 95% confidence limit was used in subsequent analysis.

Appendix 3. Continued

		Bingham's statistics					Fisher's statistics		
Site	n	trend/plunge (°)	k_1	k_2	α_{31} (°)	α_{32} (°)	trend/plunge (°)	k	α_{95} (°)
13	575	244.6/00.2	-24.06	-3.69	1.0	2.7	064.7/00.5	8	2.1
		153.4/80.1	-7.92	-3.22	1.8	3.1	156.4/79.6	6	2.6
		337.9/09.8	-25.19	-6.17	0.9	1.9	337.9/10.3	15	1.6
14	259	057.4/02.8	-36.20	-13.02	1.1	1.8	057.3/03.1	33	1.5
		317.3/72.6	-13.90	-5.51	1.8	3.0	316.0/72.8	11	2.7
		149.0/17.3	-35.34	-5.56	1.1	3.0	149.0/16.9	14	2.5
15	936	062.5/03.0	-22.42	-3.24	0.8	2.3	062.6/03.5	7	1.9
		178.8/83.3	-5.94	-3.22	1.7	2.5	184.9/83.5	5	2.2
		332.2/06.4	-20.94	-6.10	0.8	1.5	332.2/06.0	14	1.3
16	1469	060.7/15.8	-14.50	-3.42	0.8	1.8	060.7/15.3	7	1.5
		207.8/71.3	-5.24	-2.22	1.5	2.7	206.8/72.0	4	2.0
		322.9/07.8	-16.34	-3.48	0.7	1.8	323.0/07.9	8	1.4
17	1374	245.7/00.8	-17.11	-3.68	0.8	1.8	245.8/01.3	8	1.4
		343.9/78.1	-4.75	-2.28	1.7	2.8	345.3/76.4	4	2.1
		151.0/12.4	-17.16	-3.13	0.8	2.0	150.9/13.3	7	1.6
18	1260	235.4/01.4	-15.09	-3.93	0.8	1.7	235.0/00.1	8	1.5
		330.9/77.6	-3.88	-3.64	1.9	2.0	326.7/76.8	5	2.1
		145.4/12.7	-15.28	-3.82	0.8	1.8	145.5/13.3	8	1.5

Appendix 3. Continued

		Bingham's statistics					Fisher's statistics		
Site	n	trend/plunge (°)	k_1	k_2	α_{31} (°)	α_{32} (°)	trend/plunge (°)	k	α_{95} (°)
19	783	053.3/02.7	-19.94	-3.97	0.9	2.2	053.3/02.2	8	1.9
		313.2/76.4	-4.20	-3.11	2.4	2.9	317.8/74.0	4	2.7
		142.2/13.7	-20.94	-3.52	0.9	2.4	142.4/16.0	7	2.0
20	803	045.6/01.1	-20.24	-5.87	0.8	1.6	045.4/02.0	13	1.4
		311.1/77.7	-5.97	-3.87	1.8	2.3	310.0/75.5	6	2.2
		135.1/12.3	-20.38	-3.94	0.9	2.2	135.2/14.4	8	1.8
21	1033	227.1/02.0	-17.39	-3.76	0.8	2.0	227.1/02.2	8	1.7
		327.9/78.0	-3.84	-3.60	2.2	2.3	326.9/76.3	5	2.3
		136.9/11.7	-17.36	-3.94	0.8	1.9	137.0/13.3	8	1.7
22	605	213.0/00.4	-25.54	-7.31	0.9	1.6	213.0/00.4	18	1.4
		306.3/76.1	-7.41	-4.00	1.8	2.6	305.1/75.0	7	2.4
		123.5/13.9	-25.86	-4.01	0.9	2.4	123.5/15.0	9	2.0
23	740	212.6/00.8	-16.32	-3.89	1.0	2.3	212.3/02.3	8	1.9
		121.1/84.4	-10.05	-3.82	1.3	2.4	105.8/84.0	7	2.1
		300.9/05.9	-15.87	-9.15	1.0	1.3	301.0/06.5	19	1.2
24	357	034.4/05.9	-32.50	-5.84	1.0	2.5	034.2/06.2	15	2.0
		230.7/83.6	-5.93	-4.72	2.6	3.0	209.6/83.6	7	3.0
		125.1/02.3	-33.71	-4.72	1.0	2.8	305.2/00.2	12	2.3

Appendix 4. Published stratigraphic and strucutral data

Reprinted from:

The Geological Fieldwork 1990, B.C. Ministry of Energy, Mines and Petroleum Resources, Paper 1991-1, pp. 121-129.

STRUCTURE OF THE TAKLA GROUP EAST OF THE FINLAY-INGENIKA FAULT, McCONNELL CREEK AREA, NORTH-CENTRAL B.C. (94D/8, 9)

By G. Zhang and A. Hynes
McGill University

KEYWORDS: Regional geology, Takla Group, Johanson Lake, stratigraphy, Darb Creek, Goldway Peak, Osilinka Ranges, Kliyul Creek, Dortatelle Creek, Wrede Range, transcurrent faulting, rotational structure.

INTRODUCTION

The study area is located northwest and south of Johanson Lake, bounded to the northeast by the northwest-trending Lay fault and to the west by the north-northwest-trending Finlay-Ingenika fault. The Finlay-Ingenika fault is a dextral transcurrent fault, and is part of the very prominent strike-slip fault system in north-central British Columbia (Gabrielse, 1985). This project was undertaken to examine the structures on the east side of the Finlay-Ingenika fault, to provide geological evidence for the dextral transcurrent displacement and to study local deformation associated with it.

This report summarizes the results of 1:50 000-scale geological mapping in July and August 1990 in parts of map sheets 94D/8 and 94D/9. Fieldwork concentrated on stratigraphic and structural relationships.

GEOLOGICAL SETTING

The study area is in the Intermontane Belt of Monger (1984), and forms part of the Quesnellia tectonostratigraphic terrane. North and south of the study area, rocks of Quesnellia are separated from Stikinia rocks to the west by the Cache Creek Terrane, which is generally regarded as a subduction-related assemblage. These terranes were amalgamated by latest Triassic to earliest Jurassic time, to form a large, composite terrane, Terrane I, that accreted to the ancient margin of North America in Jurassic time (Monger, 1984). There is widespread evidence of dextral transcurrent motion of Terrane I, and possibly part of the Omineca metamorphic belt, during the late Cretaceous (Gabrielse, 1985) and some workers have advocated as much as 2400 kilometres of transport (*e.g.* Umhoefer, 1987). The Finlay-Ingenika fault, the boundary between Quesnellia and Stikinia in the project area, is one of the system of dextral strike-slip faults on which the motion occurred.

The area is underlain predominantly by Upper Triassic Takla Group volcanic, volcaniclastic and sedimentary rocks. West of the Finlay-Ingenika fault the Takla Group was subdivided during 1:250 000 mapping of the McConnell Creek map area (Lord, 1948; Church, 1974, 1975; Richards, 1976a, b; Monger, 1977) into a lower Dewar Formation consisting of volcanic sandstone, siltstone and black argillite, a middle Savage Mountain Formation of dark grey-green basalt, volcanic breccia and siltstone and an upper Moosevale Formation, consisting of red and green or reddish grey marine and nonmarine volcaniclastics together with intermediate alkaline feldspar porphyry (Monger, 1977). Takla Group east of the Finlay-Ingenika fault remains undivided. It is dominated by grey green, dark and pale grey volcanic breccia, sandstone and siltstone, interbedded with minor augite and feldspar-porphyritic lava flows, with minor black argillite and dark grey and purplish grey limestone. No conclusive stratigraphic correlations have been made between the Takla Group rocks on either side of the fault, and Minehan (1989b) has suggested that the rocks east of the fault should be assigned to a different group (Johanson Group) because they are geochemically very different (calcalkaline rather than alkaline) from the western Takla Group, despite their similar appearance.

LOCAL STRATIGRAPHY

The Takla Group east of the Finlay-Ingenika fault is predominantly volcaniclastic, with minor volcanic and sedimentary rocks. Stratigraphic successions and rock assemblages vary greatly from one locality to another. The stratigraphy and petrology are therefore described separately for three different regions of the map area: the northwest, southwest and southeast (Figure 1-12-1).

The stratigraphic succession in the Wrede Range in the northwest has been described by Bellefontaine and Minehan (1988) and Minehan (1989a, b). The typical stratigraphic section occurs within Minehan's (1989a) Block C. It attains thicknesses of up to 1800 metres and can be divided into four units (Figure 1-12-2a).

A lowest Unit 1 has a minimum thickness of about 800 metres but the base is not exposed. The lowest part of this unit is exposed along a small northeast-trending ridge in the south of the region and is dominated by dark green and greenish grey, massive volcanic breccia, sandstone and siltstone, together with minor clinopyroxene or plagioclase-porphyritic lava flows. The dark grey to greenish grey breccia is compositionally heterogeneous. There are crystals of plagioclase and clinopyroxene together with fragments of porphyry, volcanic sandstone and siltstone. The fragments are angular to subrounded, and average less than 10 centimetres in diameter. The breccias are poorly bedded and poorly sorted. The grey-green volcanic sandstone is com-

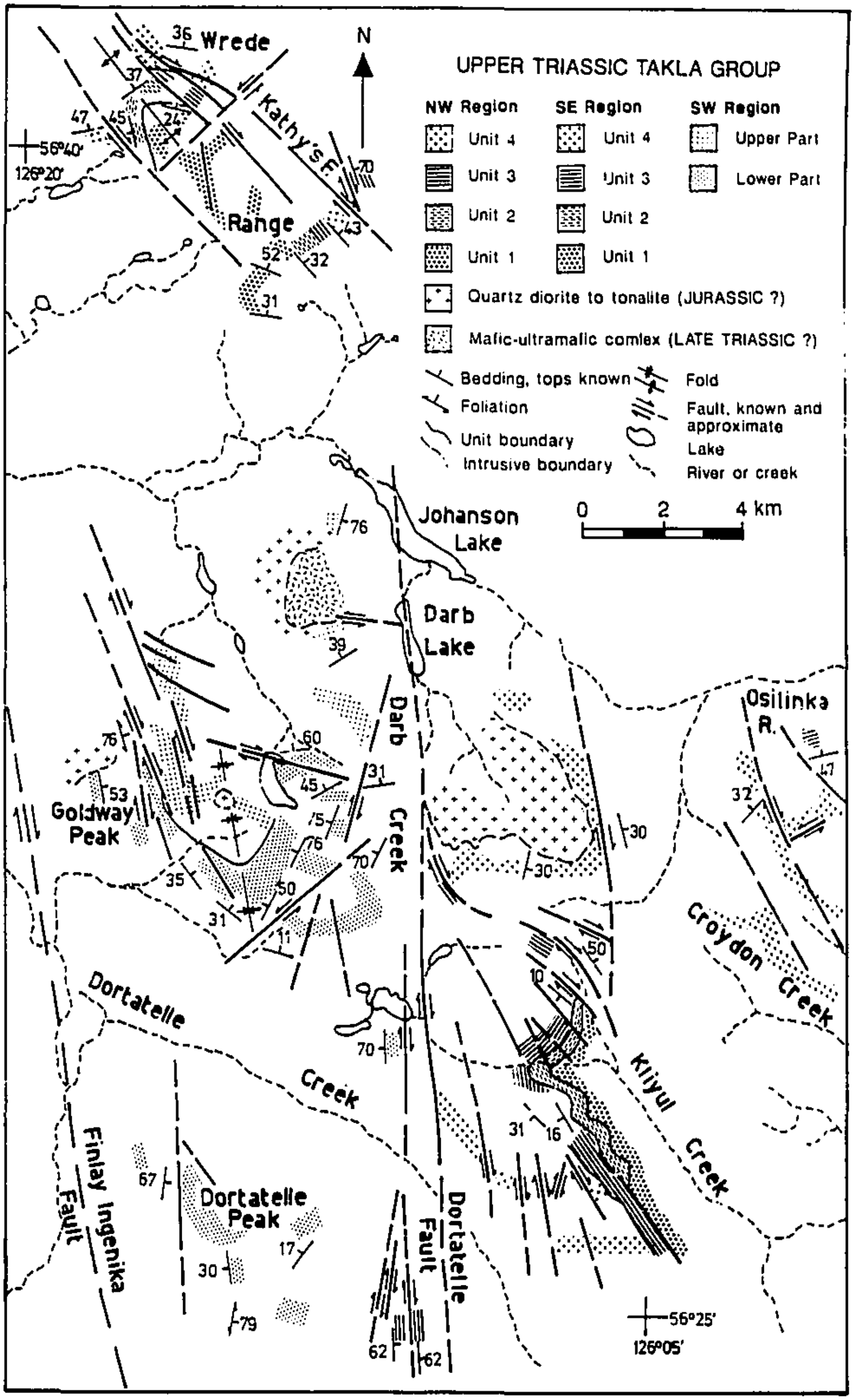

Figure 1-12-1. Generalized geology of the Johanson Lake area.

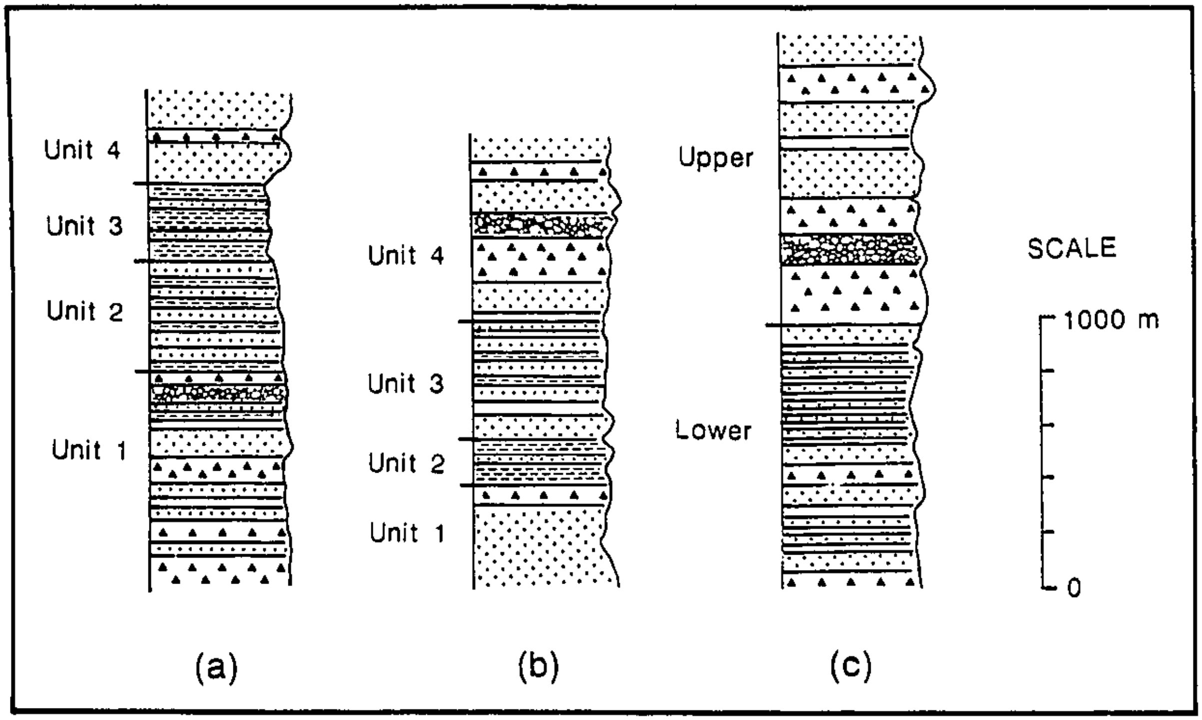

Figure 1-12-2. Generalized stratigraphic columns of Takla Group in the northwest (a) southeast (b) and southwest (c) regions. Triangles: volcanic breccia: dots: volcanic sandstone: horizontal lines: volcanic siltstones: dashed horizontal lines: black argillite and limestone: irregular circles: lava flows.

posed predominantly of plagioclase, amphibole and clinopyroxene crystals, with minor small lithic fragments similar to those in the breccia. It may occur as graded, upward-facing beds, typically 20 centimetres thick, or as massive units up to 300 metres thick. Volcanic siltstone is minor, greenish or pale grey, and commonly shows very fine, alternating dark and pale grey laminations, presumably reflecting alternation of clinopyroxene/amphibole and plagioclase-rich layers. Clinopyroxene and clinopyroxene-plagioclase-porphyritic flows are greenish grey, dark grey or dark purple and are characterized by equant euhedral clinopyroxene and anhedral plagioclase phenocrysts typically up to 5 millimetres long but locally as long as 1 centimetre. Commonly, clinopyroxene is fresh, dark green to pale greenish yellow and displays sector twinning and pseudodimetric shape in cross-section. These lava flows closely resemble the breccia in the field but are distinguished by the complete absence of fragmentation, even on the weathered surfaces.

The middle part of Unit 1, exposed on the col to the northeast, consists of greenish grey and pale grey volcanic sandstone and siltstone interbedded with black, reddish weathering, thin-layered argillite and purplish grey limestone with individual beds up to 30 centimetres thick. The upper part of Unit 1 consists of characteristically greenish grey, massive lava flows of clinopyroxene and clinopyroxene plagioclase porphyry and volcanic sandstone. The flows contain fragments of purple limestone typically 10 to 20 centimetres and locally up to 2 metres in diameter. It is therefore likely that the lava flow disrupted the limestone of the middle part of the unit.

Unit 2, up to 400 metres thick, is well exposed along the northeast-trending ridge northeast of Unit 1. This unit is made up of greenish grey and pale grey, well-bedded volcanic sandstone and siltstone interbedded, with black, thin-layered argillite and marly limestone. The sedimentary rocks account for about 40 per cent of the unit and individual argillite beds are typically 2 centimetres thick. Toward the top of the unit sedimentary rocks become progressively more abundant.

Unit 3, a predominantly sedimentary package about 270 metres thick, consists mainly of black, reddish weathering, thin-layered argillite and dark grey or black, thin-layered, marly limestone. Thirty per cent of the unit is thick-bedded (40 to 50 cm), greenish grey and dark grey volcanic sandstone and siltstone.

Unit 4, the uppermost unit of the succession, is exposed on the highest peak in the southern part of the region. It is dominated by massive, greenish grey volcanic sandstones and has a minimum thickness of 300 metres. To the northeast this unit is cut by the northwest-trending Kathy's fault (Figure 1-12-1).

In the southeastern region, west of Kliyul Creek, four units are recognized and a minimum thickness of 1600 metres is estimated for the whole succession, although the estimate is imprecise because of widespread shearing and fault truncation at its top. Thicknesses of Units 2 and 3 have been well defined and measured (Figure 1-12-2b).

Unit 1, exposed along the west side of Kliyul Creek, is dominated by grey volcanic sandstone. Most of this unit is covered by vegetation and moraine but a minimum thickness of 400 metres can be estimated. The top of the unit contains abundant recessive clasts of carbonate.

Unit 2 is up to 170 metres thick, and consists mainly of black, reddish weathering argillite and dark grey or black, 2 to 10-centimetre layered limestone. The unit also contains minor interbedded, grey or greenish grey volcanic sandstone and siltstone. This unit extends to the south and is truncated by a northwest-trending fault which juxtaposes Unit 3 and Unit 1.

Unit 3, well exposed on the ridge west of the Kliyul Creek, consists of grey or greenish grey volcanic sandstone and siltstone interbedded with dark grey or black limestone and minor black argillite, and is up to 440 metres thick. The lower part is dominated by greenish grey volcanic siltstone which contains abundant fragments of dark grey or purplish, well-bedded limestone, ranging from several centimetres to several metres in diameter. The upper part is greenish grey or pale grey, medium-layered (10 to 20 cm) volcanic sandstone interbedded with dark grey or black, thin-layered limestone or argillite. These limestone beds are very widespread and are useful marker horizons in the region. At the top of the unit there is a thin-layered, fine-grained volcanic sandstone, which is the boundary between Units 3 and 4.

Unit 4 consists mainly of massive, greenish grey volcanic sandstone and breccia with minor siltstone and clinopyroxene porphyry and is well exposed in the western part of the region. Rocks of this unit are very resistant and commonly form high peaks and steep cliffs. In the west, near the Dortatelle fault (Monger, 1977), these rocks are sheared into protomylonite. Lineations defined by stretched mineral crystals and elongated breccia fragments are very common. Because of the intense shearing, the total thickness of the unit cannot be measured, but a minimum thickness of 600 metres is estimated.

The stratigraphic succession in the Osilinka Ranges, east of Johanson Lake (Figure 1-12-1), appears similar to that in the northwest, but exact correlations between them have not proved possible.

The Goldway Peak and Dortatelle Peak area (Figure 1-12-1), in the southwest, has a stratigraphic succession very different from that east of the Dortatelle fault. It is dominated by volcanics and volcaniclastics and can be divided into two parts. The lower part consists of greenish grey, thin-layered volcanic sandstone interbedded with pale grey, thin-layered volcanic sandstone and siltstone, commonly with individual bed thickness less than 2 centimetres. Nonvolcanic sedimentary rocks are rare, but are observed near the glacier southeast of Goldway Peak and on the eastern flank of Dortatelle Peak where there are small amounts of thin-bedded (2 cm) dark grey or black limestone and argillite. The upper part consists of massive or poorly bedded, greenish grey volcanic sandstone and breccia with minor clinopyroxene porphyry. The breccias are polymictic and made up of predominantly subrounded fragments of volcanic sandstone and clinopyroxene porphyry. Thickness of this succession has not been measured but a minimum thickness of 2000 metres can be estimated (Figure 1-12-2c).

INTRUSIVE ROCKS

The upper Triassic Takla Group rocks are intruded by the Johanson Lake mafic-ultramafic complex, an Alaskan-type intrusive complex (Nixon and Hammack, 1990), the Darb Lake dioritic body which is located in the centre of the map area, and many intermediate to felsic dikes and sills, typically less than 3 metres wide. These intermediate to felsic rocks are probably related to the Hogem batholith and Jurassic to Cretaceous in age (Monger, 1977).

DEFORMATION

Rocks in the map area experienced deformation predominantly, and perhaps exclusively, associated with the dextral, transpressive displacement along the Finlay-Ingenika fault. This deformation is characterized by dextral strike-slip faults trending northwest, north-northwest and north-northeast, and sinistral strike-slip faults trending east-northeast. The faults cut the rocks into a number of fault-bounded, weakly deformed blocks, in which cleavages and small-scale shear zones are the only visible structures. These characteristics are typical of continental crustal deformation associated with large-scale transcurrent faulting (*e.g.* Nelson and Jones, 1986; Geissman *et al.*, 1989). There are also some large-scale, open to medium folds with axes trending northwest.

FOLDS

Two large-scale folds, an anticline and a syncline, have been recognized. The Wrede Range anticline, in the northwestern region of the map area, has Unit 1 volcanics and volcaniclastics in its core and Unit 2 volcaniclastic and interbedded sedimentary rocks on the two limbs. Bedding attitudes measured in Unit 2 define a fold axis trending 325° and plunging 30°. Axial-surface cleavage is common on both limbs, especially in the Unit 2 argillitic beds. The anticline is truncated on both northeast and southwest sides by northwest-trending, dextral strike-slip faults.

The Goldway Peak syncline is exposed around Goldway Peak, in the southwestern region. The core of the syncline consists of the upper, massive volcanic breccia and sandstone and the limbs are dominated by the lower, well-bedded, thin-layered volcanic sandstone and siltstone. The fold-axis trends 340° and plunges 40°. On both limbs near the nose, secondary, outcrop-scale folds are well developed. They are either box-type or chevron folds. The east limb of the Goldway Peak syncline is truncated by a northwest-trending, dextral strike-slip fault and the strata have been rotated clockwise through about 30° due to drag on the fault.

In contrast, the west limb was sheared by north-northwest-trending dextral strike-slip faults, which are parallel to the bedding surface, leading to steep dips for the strata.

Small-scale folds are also common in the well-bedded, thin-layered units throughout the map area, especially in the Unit 3 thin-layered limestone interbedded with volcanic siltstone west of Kliyul Creek. Most folds have axial surfaces at small (<45°) angles to the bedding surfaces and are probably due to bedding-parallel slip.

Timing of formation of the folds is uncertain. They predate the faults but may well have formed in the early stages of the dextral transpression (*cf.* Wilcox *et al.*, 1973; Sylvester, 1988).

FAULTS

Steeply dipping or vertical strike-slip faults are the most significant structural features in the map area. The faults may be divided into northwest, north-northwest, north-northeast and east-northeast-trending structures, which show different slip senses.

Northwest-trending faults are predominantly dextral and occur mainly in the Wrede Range and west of Kliyul Creek. In the Wrede Range, two northwest-trending faults cut the northeastern limb of the Wrede Range anticline and bring reddish sedimentary rocks of Unit 3 into contact with volcanic rocks of Units 1 and 4. These faults are well exposed to the northwest, where the volcanic rocks are sheared into protomylonite over a zone 20 metres wide. Drag folds and Riedel shears (Tchalenko, 1970; Sylvester, 1988) in the fault zone indicate dextral slip. By matching the offsets, a dextral displacement of 1 kilometre has been estimated along the faults. Some faults provide evidence of an early stage of dip-slip motion. For example, two sets of slickenlines are observed on the cleaved rock surfaces in a fault zone on Darb Creek near the Dortatelle fault. The earlier is dip-slip with a thrust sense, and the later is horizontal, dextral. These faults may originally have been thrust faults that were associated with the initiation of dextral displacement on the Finlay-Ingenika fault in the Ingenika valley west of the map area (*cf.* Sylvester, 1988).

North-northwest-trending faults are predominant in the southern part of the map area, and all show dextral displacement. The biggest and most obvious one is the Dortatelle fault. It extends 30 kilometres from north of Johanson Lake through Darb Creek to the south and is well exposed near the biggest lake north of Dortatelle Creek. Rocks in a fault zone 40 metres wide were sheared into protomylonite. In the mylonitic rocks kinematic indicators such as mylonitic foliation fish and S-C fabrics (Berthe *et al.*, 1979) are common (Plate 1-12-1c). Centimetre-scale drag folds, plunging steeply north-northwest, with axial planes striking northwest and dipping steeply northeast, are widespread. All the kinematic indicators are consistent with dextral strike-slip on the fault. To the south the fault passes through a col in which the volcanic rocks are mylonitic over a zone 50 metres wide. A fault-parallel, horizontal mineral-stretching lineation is very well developed, especially in the sheared clinopyroxene porphyry. A similar lineation is defined elsewhere by elongated fragments of volcanic breccia (Plate 1-12-1b). In a fault east of the Darb Creek dioritic body, a quartz diorite dike is incorporated in the mylonitic zone, indicating that fault motion occurred after emplacement of the extensive dioritic plutons in the map area, *i.e.* during the Jurassic or later (Monger, 1977). Faults in this group are parallel to, and have the same slip senses as, the Finlay-Ingenika fault west of the map area. They are also better developed and more closely spaced approaching the major fault to the west. It is therefore inferred that they were formed as a result of the dextral transcurrent movement on the Finlay-Ingenika fault.

North-northeast-trending faults are not as common in the map area as those of the other two sets. This may be due to vegetation and moraine cover in north-northeast-trending valleys. Two large-scale, north-northeast trending faults were mapped on the ridges west of Darb Creek. They cut the lower part of the volcanic sandstone and are characterized by protomylonites, with a mineral-stretching lineation parallel to the fault strike. S-C structures in the mylonitic zone, which is up to 20 metres wide, indicate dextral movement. Another shear zone with the same trend was mapped on the ridge behind the glacier west of Kliyul Creek. The Unit 4 greenish clinopyroxene porphyry is sheared into a narrow (10 cm) mylonitic band, in which S-C structures show dextral slip. On the east wall there is a small rotational structure, characterized by a number of curved cleavage planes that project to the south and diverge towards and converge away from the shear zone (Plate 1-12-1d). They are approximately parallel to the mylonitic foliation and die out outside the shear zone. The rotational structure is therefore a local feature and was probably associated with dextral transpression. The attitudes and slip senses on this north-northeast trending fault set are consistent with their formation as Riedel shears (R) related to the main motion on the Finlay-Ingenika fault (*cf.* Tchalenko, 1970; Sylvester, 1988).

East-northeast-trending faults generally display sinistral displacement. Although faults of this group are not well developed, they were found at several places within the map area. One such fault lies in the valley west of Darb Creek and is inferred from stratigraphic relationships. A 750-metre sinistral displacement of the lower part of the thin-layered, greenish grey volcanic sandstone and pale grey volcanic siltstone unit is required to match stratigraphic offsets. Another fault, striking approximately east, was mapped within the Johanson Lake mafic-ultramafic block, west of Darb Creek. It is characterized by a mylonitic zone, about 1 metre wide, and the drag folds of mylonitic foliation show a sinistral strike-slip sense. Approaching the Dortatelle fault, this small fault, together with the fault-bounded block, has been rotated clockwise through 35°. Small east-northeast-trending shear zones are also present in the area. A mylonitic zone 40 centimetres wide, striking 055°, observed on the peak of the Osilinka Ranges in massive, greenish grey volcaniclastics, has S-C fabrics indicative of sinistral displacement. The east-northeast-trending faults may be conjugate to the north-northeast-trending set, reflecting the R′ Riedel set (Tchalenko, 1970; Keller *et al.*, 1982; Sylvester,

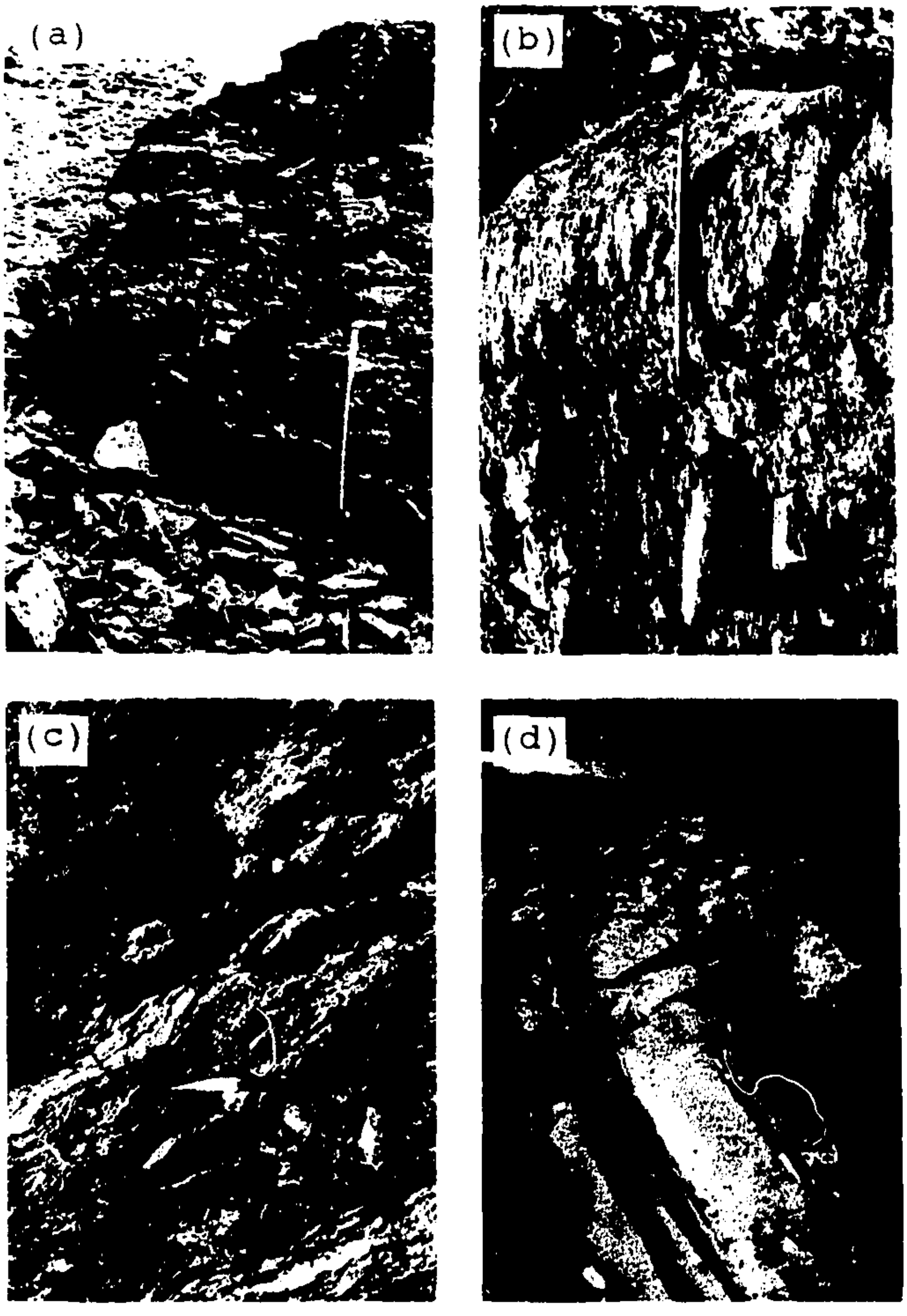

Plate 1-12 (a) Cleavage defined by closely spaced shear planes; (b) Lineation of stretched volcanic breccia in a north-northwest-trending, strike-slip fault; pencil parallel to the lineation, looking at north-northwest down; (c) S-C fabrics of the mylonitic rocks in Dortatelle fault, pencil parallel to the C planes, looking at south down; (d) Transpressive rotational structure consisting of curved cleavage planes; pencil parallel to the cleavage planes, hammer handle parallel to the small shear zone, looking at west down.

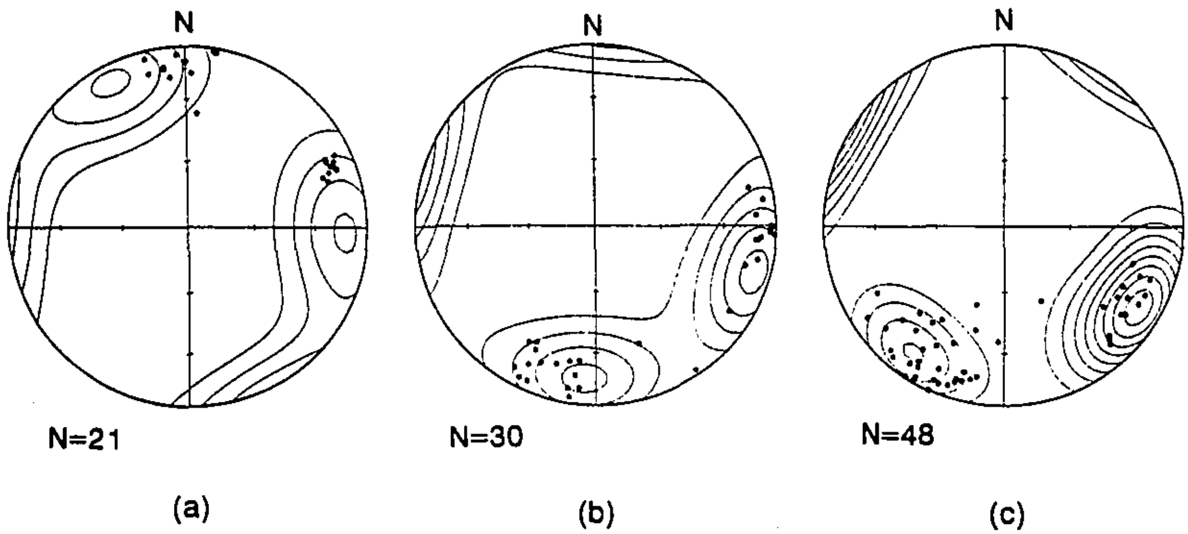

Figure 1-12-3. Stereonet plots of conjugate cleavages from the ridge north of Croydon Creek (a) the southern margin of Darb Creek dioritic body (b) and Goldway Peak (c). Solid circles: slickenlines; lines: contours of poles to the cleavages; N: number of cleavage planes measured.

1988) associated with faulting on the Finlay-Ingenika system.

All the faults, although they trend differently and have different slip senses, may be explained by association with the Finlay-Ingenika faulting. They cut the rocks into fault-bounded, weakly deformed blocks, ranging in size from several square kilometres to tens of square kilometres. With progressive displacement on the Finlay-Ingenika fault, deformation was apparently concentrated in the previously formed faults, while the fault-bounded blocks remained only very weakly deformed. Typically the only visible deformation outside the fault zones themselves is a cleavage and weak shear zones.

CLEAVAGE

Cleavage is extensively developed in the map area. It is characterized by spaced shear planes and in the cleaved rocks no appearent fabrics have been found. The shear planes are usually steeply dipping and closely spaced, at intervals of 2 to 10 centimetres (Plate 1-12-1a). They are commonly slickensides with slickenlines, and many are characterized by crystals of tremolite or patches of chlorite and epidote. Shear senses are evident from the slickenline steps and offset of such features as quartz veins or the conjugate cleavage. Most cleavage is regional but some is local in its distribution. The local cleavage is commonly associated with nearby faults and can be easily distinguished from the regional by tracing away from the fault. Regionally distributed cleavage generally occurs in conjugate sets trending north to north-northeast and east-northeast to east, although there is considerable variation. Assuming the regional cleavage was homogeneously distributed before the widespread faulting in this region, its attitudes may be used to indicate the bulk rotation of fault-bounded blocks.

Several hundred shear planes were measured in the field, and a preliminary analysis (Figure 1-12-3) indicates significant variations between the three major fault blocks. On the ridge north of Croydon Creek two sets of conjugate cleavages trend north and east-northeast, respectively (Figure 1-12-3a), which are consistent with those caused by Finlay-Ingenika faulting. To the west, in the block near the southern margin of the Darb Creek dioritic body, they trend north-northeast and east, respectively (Figure 1-12-3b). Near the Finlay-Ingenika fault at Goldway Peak, they are oriented northeast and east-southeast, respectively (Figure 1-12-3c). Based on the above assumption, this variation of the orientations of the regional, conjugate cleavages indicates that the fault-bounded blocks have been rotated clockwise, and the amount of block rotation varies, reaching a maximum close to the Finlay-Ingenika fault.

CONCLUSIONS

The deformation observed in the Takla Group rocks east of the Finlay-Ingenika fault can therefore all be explained by dextral transcurrent motions on the Finlay-Ingenika fault. There is no compelling evidence for deformation associated with the collision of Quesnellia with Stikinia or of Terrane I with North America. During the early stages of deformation, folds with axes trending northwest, northwest-trending thrust faults and two sets of conjugate strike-slip faults, striking north-northeast and east-northeast, were formed, together with north-northwest-trending, secondary dextral strike-slip faults. These structures cut the Takla Group rocks into a number of fault-bounded, weakly deformed blocks. With progressive displacement on the

Finlay-Ingenika fault, deformation became concentrated in early-formed fault zones. The northwest-trending thrust faults may have been rotated and dextral strike-slip motion appears to have been superimposed on them. The fault-bounded, brittle, upper crustal blocks appear to have been rotated clockwise in response to the large amount of dextral transcurrent displacement, the amount of rotation increasing toward the major faults. This rotation of discrete blocks is a mode of deformation common at shallow crustal levels in many strike-slip zones (Nelson and Jones, 1986; Ron *et al.*, 1986; Hudson and Geissman, 1987; Geissman *et al.*, 1989) and may provide one means of rationalizing the disparities between estimates of the amount of tectonic displacement derived from geological and paleomagnetic studies (Monger and Irving, 1980; Irving *et al.*, 1985; Rees *et al.*, 1985; Gabrielse, 1985).

ACKNOWLEDGMENTS

This research was made possible by grants from the British Columbia Ministry of Energy, Mines and Petroleum Resources, the Geological Survey of Canada and the Natural Sciences and Engineering Research Council. Their support is gratefully acknowledged.

REFERENCES

Bellefontaine, K.A. and Minehan, K. (1988): Summary of Fieldwork in the Ingenika Range, North-central British Columbia (94D/09; 94C/12); *B.C. Ministry of Energy, Mines and Petroleum Resources*, Geological Fieldwork 1987, Paper 1988-1, pages 195-198.

Berthé, D., Choukroune, P. and Jegouzo, P. (1979): Orthogneiss, Mylonite and Non-coaxial Deformation of Granites: the Example of the South Armorican Shear Zone; *Journal of Structural Geology*, Volume 1, pages 31-42.

Church, B.N. (1974): Geology of the Sustut Area; *B.C. Ministry of Energy, Mines and Petroleum Resources*, Geology, Exploration and Mining in British Columbia 1973, pages 411-455.

Church, B.N. (1975): Geology of the Sustut Area; *B.C. Ministry of Energy, Mines and Petroleum Resources*, Geology, Exploration and Mining in British Columbia 1974, pages 305-309.

Gabrielse, H. (1985): Major Dextral Transcurrent Displacements along the Northern Rocky Mountain Trench and Related Lineaments in North-central British Columbia; *Geological Society of America*, Bulletin, Volume 96, pages 1-14.

Geissman, J.W., Harlan, S.S. and Wawrzyniec, T.F. (1989). Strike-slip Faulting and Block Rotation in the Lake Mead Fault System; *Geology*, Volume 17, pages 1057-1058.

Hudson, M.R. and Geissman, J.W. (1987): Paleomagnetic and Structural Evidence for Middle Tertiary Counterclockwise Block Rotation in the Dixie Valley Region, West-central Nevada; *Geology*, Volume 15, pages 638-642.

Irving, E., Woodsworth, G.J., Wynne, P.J. and Morrison, A. (1985): Paleomagnetic Evidence for Displacement from the South of the Coast Plutonic Complex, British Columbia; *Canadian Journal of Earth Sciences*, Volume 22, pages 584-598.

Keller, E.A., Bonkowski, M.S., Korsch, R.J. and Shlemon, R.J. (1982): Tectonic Geomorphology of the San Andreas Fault Zone in the Southern Indio Hills, Coachella Valley, California; *Geological Society of America*, Bulletin, Volume 93, pages 46-56.

Lord, C.S. (1948): McConnell Creek Map-area, Cassiar District, British Columbia; *Geological Survey of Canada*, Memoir 251, 72 pages.

Minehan, K. (1989a): Takla Group Volcano-sedimentary Rocks, North-central British Columbia; *B.C. Ministry of Energy, Mines and Petroleum Resources*, Geological Fieldwork 1988, Paper 1989-1, pages 227-232.

Minehan, K. (1989b): Paleotectonic Setting of Takla Group Volcano-sedimentary Rocks, Quesnellia, North-central Columbia; unpublished M.Sc. thesis, *McGill University*, 102 pages .

Monger, J.W.H. (1977): The Triassic Takla Group in McConnell Creek Map-area, North-central British Columbia; *Geological Survey of Canada*, Paper 76-29, 45 pages.

Monger, J.W.H. (1984): Cordilleran Tectonics: a Canadian Perspective; *Bulletin Société Géologique de France*, Volume 7, pages 255- 278.

Monger, J.W.H. and Irving, E. (1980): Northward Displacement of North-central British Columbia; *Nature*, Volume 285, pages 289-293.

Nelson, M.R. and Jones, C.H. (1986): Paleomagnetism and Crustal Rotations along a Shear Zone, Las Vegas Range, Southern Nevada; *Tectonics*, Volume 6, pages 13-33.

Nixon, G.T. and Hammack, J.L. (1990): Geology and Noble Metal Geochemistry of the Johanson Lake Mafic-Ultramafic Complex, North-central British Columbia; Geological Fieldwork 1989, *B.C. Ministry of Energy, Mines and Petroleum Resources*, Paper 1990-1, pages 417-424.

Rees, C.J., Irving, E. and Brown, R.L. (1985): Secondary Magnetization of Triassic-Jurassic Volcaniclastic Rocks of Quesnel Terrane, Quesnel Lake, B.C.; *Geophysical Research Letters*, Volume 12, pages 498-501.

Richards, T.A. (1976a): McConnell Creek Map Area (94D/E), Geology; *Geological Survey of Canada*, Open File 342.

Richards, T.A. (1976b): Takla Group (Reports 10-16): McConnell Creek Map Area (94D, East Half), British Columbia; *Geological Survey of Canada*, Paper 76-1a, pages 43-50.

Ron, H., Aydin, A. and Nur, A. (1986): Strike-slip Faulting and Block Rotation in the Lake Mead Fault System; *Geology*, Volume 14, pages 1020-1023.

Sylvester, A.G. (1988): Strike-slip Faults; *Geological Society of America*, Bulletin, Volume 100, pages 1666-1703.

Tchalenko, J.S. (1970): Similarities between Shear Zones of Different Magnitudes; *Geological Society of America*, Bulletin, Volume 81, pages 1625-1640.

Umhoefer, P.J. (1987): Northward Translation of "Baja British Columbia" along the Late Cretaceous to Paleocene Margin of Western North America; *Tectonics*, Volume 6, pages 377-394.

Wilcox, R.E., Harding, T.P. and Seely, D.R. (1973): Basic Wrench Tectonics; *American Association of Petroleum Geologists*, Bulletin, Volume 57, pages 74-96.

Appendix 4. Continued

Reprinted from:

The Geological Fieldwork 1991, B.C. Ministry of Energy, Mines and Petroleum Resources, Paper 1992-1, pp. 147-154.

STRUCTURES ALONG FINLAY-INGENIKA FAULT, McCONNELL CREEK AREA, NORTH-CENTRAL BRITISH COLUMBIA (94C/5; 94D/8, 9)

By G. Zhang and A. Hynes
McGill University

KEYWORDS: Regional geology, Takla Group, Johanson Lake, stratigraphy, Goldway Peak, Osilinka Ranges, Kliyul Creek, Dortatelle Creek, Wrede Range, Aiken Lake, Sustut Lake, Hogem Ranges, transcurrent faulting, stretching lineation.

INTRODUCTION

The study area is located in the vicinity of Johanson Lake, some 350 kilometres north-northwest of Prince George, bounded to the northeast by the north-northwest-trending Lay fault and to the southwest by Willow Creek. The north-northwest-trending Finlay-Ingenika fault, one of the very prominent dextral strike-slip fault systems of north-central British Columbia (Gabrielse, 1985), passes through the western half of the study area.

The main aims of the project are to examine the structures on both sides of the Finlay-Ingenika fault, to provide geological evidence for the dextral transcurrent displacement and to study local deformation associated with it. Geological mapping in parts of map sheets 94C/5 and 94D/8, 9 at a scale of 1:5000, was conducted in 1990 and 1991. Preliminary results from the fieldwork of 1990 were reported last year (Zhang and Hynes, 1991). This report provides considerably more data on the nature of the deformation, and extends the mapped region southeast towards Aiken Lake and to the Hogem Ranges west of the Finlay-Ingenika fault.

Throughout the region, exposure on prominent ridges is excellent. Although primary access is possible via the gravel road from either Mackenzie or Fort St. James to Johanson Lake and the Cheni mine, the nature of the terrain necessitates use of a helicopter for camp moves.

REGIONAL GEOLOGY

The map area lies within the Intermontane Belt, one of the five morphogeological belts of the Canadian Cordillera (Wheeler and McFeely, 1987), and straddles the Quesnellia and Stikinia tectonostratigraphic terranes (Monger, 1984). North and south of the study area, Stikinia rocks are separated from those of Quesnellia to the east by the Cache Creek Terrane, a subduction-related assemblage, and bounded to the east by the Slide Mountain Terrane, a deep-water oceanic assemblage. These terranes were amalgamated by latest Triassic to earliest Jurassic time, forming a composite terrane, "Terrane I", which accreted to the ancient margin of North America in Jurassic time (Monger, 1984). Dextral strike-slip faulting took place extensively along the eastern margin of Terrane I, and possibly part of the Omineca metamorphic belt, during the late Cretaceous (Gabrielse, 1985). The Finlay-Ingenika fault, which lies between the Quesnellia and Stikinia terranes in the study area, is one of the dextral strike-slip faults on which the transcurrent motion occurred.

Quesnellia and Stikinia terranes in the study area are characterized by volcanic, volcaniclastic and sedimentary rocks of the Upper Triassic Takla Group. West of the Finlay-Ingenika fault the Takla Group was subdivided into three formations during 1:250 000 mapping of the McConnell Creek map area (Lord, 1948; Church, 1974, 1975; Richards, 1976a, b; Monger, 1977; Monger and Church, 1977). The lower Dewar Formation is dominated by volcanic sandstone, siltstone and argillite, and is overlain by a middle Savage Mountain Formation consisting of submarine, massive volcanic breccia and pillow lava with minor volcanic siltstone at the top. The upper Moose Valley Formation is predominantly reddish marine and nonmarine volcaniclastic rocks (Monger, 1977; Monger and Church, 1977). East of the Finlay-Ingenika fault the Takla Group remains undivided (Monger, 1977). It consists mainly of greenish grey, dark and pale grey volcanic, volcaniclastic and sedimentary rocks. No conclusive stratigraphic correlations have been made between the Takla Group rocks on either side of the fault (Minehan, 1989a, b). The Takla Group rocks east of the fault are extensively intruded by multiphase, early Jurassic to Cretaceous dioritic rocks (Woodsworth, 1976).

STRATIGRAPHY OF THE TAKLA GROUP EAST OF FINLAY-INGENIKA FAULT

Takla Group rocks east of the Finlay-Ingenika fault are predominantly volcaniclastic. They include some porphyritic rocks that are possibly volcanic flows and feeders, and minor sedimentary rocks. Stratigraphic successions and rock assemblages vary greatly from one locality to another. The stratigraphy and petrology have therefore been described separately for three different regions of the study area: the northwest (the Wrede Range), southwest (west of the Dortatelle fault) and southeast (between the Dortatelle fault and Kliyul Creek) (Zhang and Hynes, 1991, Figure 1-12-2).

In the southeastern region, a stratigraphic succession about 1500 metres thick along the east-trending ridges west of Aiken Lake (Figure 1-12-1) is lithologically very similar to that observed on the ridges between the Dortatelle fault (Monger, 1977) and Kliyul Creek (Zhang and Hynes, 1991; Figure 1-12-1). A lowest Unit 1 is dominated by grey volcanic sandstone. Most of this unit is covered by vegeta-

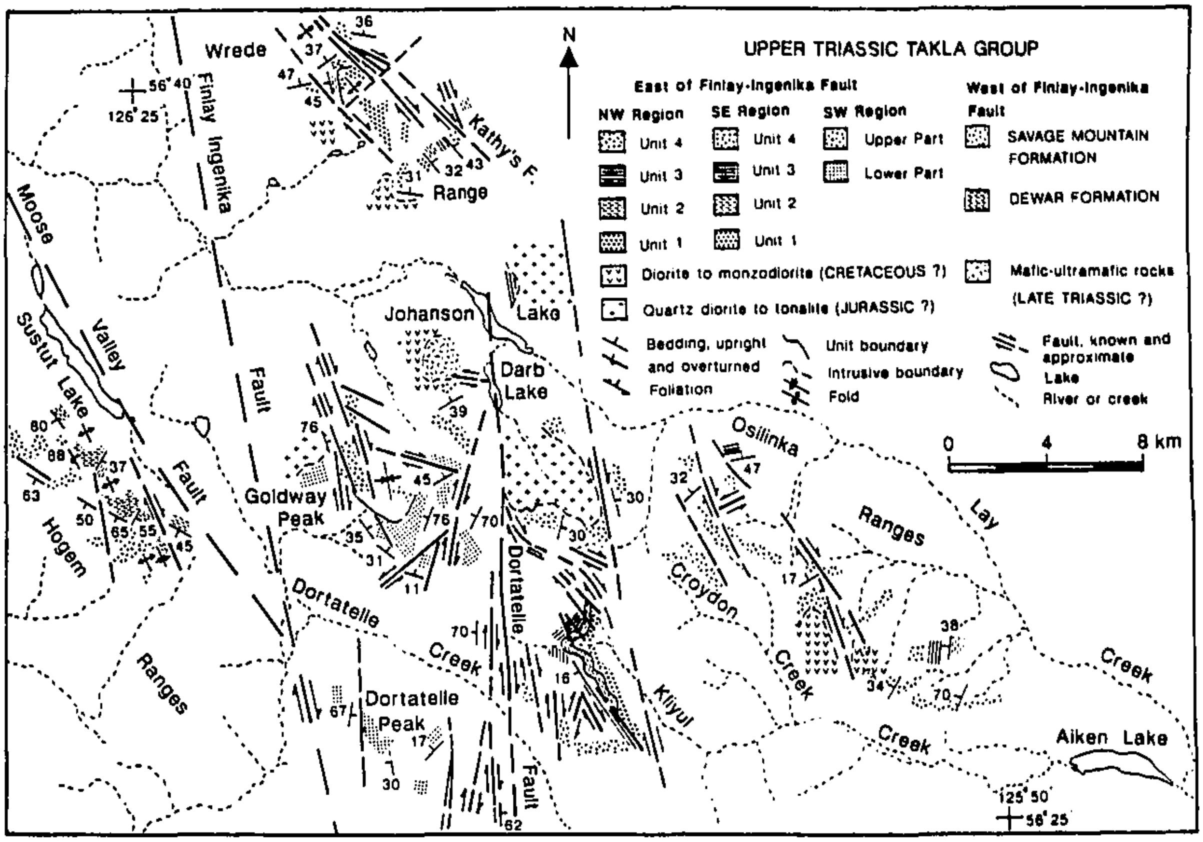

Figure 1-12-1. Generalized geology of the Johanson Lake area.

tion but a minimum thickness of 400 metres can be estimated west of Kliyul Creek. The top of this unit displays abundant recessive patches of carbonate. Unit 2 is up to 170 metres thick west of Kliyul Creek and attains a thickness of about 430 metres west of Aiken Lake. It consists of reddish weathering, black argillite with siltstone laminae and 2 to 10-centimetre layers or lenses of dark grey or black limestone. This unit also contains minor interbedded, grey volcanic sandstone and siltstone, ranging in thickness from 30 centimetres to several metres. Unit 3 is well exposed on the ridges west of both Kliyul Creek and Aiken Lake. The lower part is dominated by greenish grey volcanic siltstone which contains abundant fragments of dark grey or purplish, well-bedded limestone, ranging from several centimetres to several metres in diameter. Small-scale, slumping folds, generally several tens of centimetres in wavelength, are common in the fragments of the well-bedded limestone west of the Kliyul Creek, but not observed in those west of Aiken Lake. Fossils of brachiopods, bivalves and possibly some ammonites were found in the carbonate clasts west of Aiken Lake. The upper part is greenish grey or pale grey, medium-layered (10 to 20 cm) volcanic sandstone interbedded with dark grey or black, thin-layered limestone or black, dark grey to grey argillite (west of Aiken Lake). The thickness of this unit is up to 440 metres west of Kliyul Creek and 400 metres west of Aiken Lake. These limestone-rich beds are very widespread and useful marker horizons in the region. Unit 4 consists mainly of greenish grey, massive volcanic breccia and sandstone with minor clinopyroxene and clinopyroxene-plagioclase porphyries and is well exposed on the ridges east of the Dortatelle fault and northeast of Croydon Creek. The greenish grey breccias are compositionally heterogeneous and dominated by fragments of clinopyroxene and clinopyroxene-plagioclase porphyries. The fragments are angular to subrounded, commonly sitting in a porphyritic matrix with the same composition as the fragments, and average less than 20 centimetres in diameter. The breccias are usually poorly bedded and poorly sorted. The porphyritic rocks contain phenocrysts of either euhedral clinopyroxene or both euhedral clinopyroxene and anhedral plagioclase, commonly less than 5 millimetres in diameter but locally as much as 1 centimetre. The porphyritic rocks are generally several tens of centimetres to several metres thick and interbedded with the volcanic breccias, but sometimes occur as feeders where they cut the laminations of the volcaniclastic rocks, for example, on the ridges west of Aiken Lake. Rocks of this unit are very resistant and commonly cliff forming.

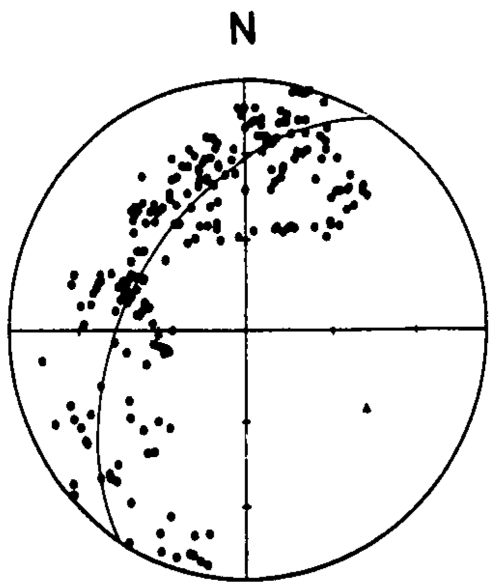

Figure 1-12-2. Stereonet plot of bedding planes from the Hogem Ranges. Solid circles: poles to bedding planes; open triangle: minimum eigenvector; great circle: plane normal to the eigenvector; N: number of measurements. Eigenvectors calculated using methods of Mardia (1972).

TAKLA GROUP WEST OF FINLAY-INGENIKA FAULT

Rocks of the Takla Group west of the Finlay-Ingenika fault are exposed in the Hogem Ranges (Figure 1-12-1) and are divided into two formations in the study area: Dewar and Savage Mountain (Richards, 1976a; Monger, 1977; Monger and Church, 1977).

The Dewar Formation is well exposed along the northern slopes of the Hogem Ranges. The lower part of the formation is dominated by reddish weathering, dark grey to black, locally graphitic and pyritic argillite with lenses of dark grey marly limestone. The upper part is mainly black argillite interbedded with pale grey volcanic sandstone and siltstone, with minor breccia containing fragments of argillite and volcanic sandstone. Beds ranging in thickness from laminae to 70 centimetres are common. The base of this formation is not exposed but a minimum thickness of 500 metres can be estimated.

The Savage Mountain Formation is characterized by massive, dark grey volcanic breccia with minor volcanic sandstone and siltstone. The fragments in the breccias are angular to subrounded and range in diameter from several centimetres to 40 centimetres. They consist of dark grey, reddish grey and dark purple clinopyroxene and clinopyroxene-plagioclase porphyries. The matrix of the breccias is predominantly clinopyroxene or clinopyroxene-plagioclase porphyritic. This unit contains locally conspicuous, coarse-grained, "bladed" feldspar porphyry. At the base of the formation one horizon contains clasts of purplish grey limestone and argillite with brachiopod and bivalve fossils. Rocks of this formation are very resistant and form high peaks in the area.

INTRUSIVE ROCKS

The Takla Group rocks east of the Finlay-Ingenika fault contain abundant intrusions associated with the Alaskan-type Johanson Lake mafic-ultramafic complex (Nixon and Hammack, 1990), and many dioritic to monzodioritic bodies occur north and south of Johanson Lake and north of Kliyul Creek. There are also many intermediate to felsic dikes and sills, typically less than 3 metres thick. These intermediate to felsic rocks are probably related to the Hogem batholith and early Jurassic to Cretaceous in age (Lord, 1948; Richards, 1976a; Woodsworth, 1976).

DEFORMATION

Rocks in the study area experienced deformation associated predominantly with dextral, transpressive displacement along the Finlay-Ingenika fault. Steeply dipping or vertical strike-slip faults (Figure 1-12-1) cut the rocks into a number of fault-bounded, weakly deformed blocks, in which cleavages and small-scale shear zones are the only visible structures. These characteristics are typical of continental crustal deformation associated with large-scale transcurrent faulting (*e.g.*, Nelson and Jones, 1986; Geissman *et al.*, 1989; Ron *et al.*, 1986, 1990). In addition, there are some large-scale, open to medium folds with axes trending northwest to north-northwest (Figure 1-12-1).

FOLDS

Four large-scale folds have been recognized. The Wrede Range anticline and Goldway Peak syncline occur in the Wrede Range and Goldway Peak regions, respectively (Figure 1-12-1) and have been described previously (Zhang and Hynes, 1991). The Sustut Lake anticline and syncline are exposed in the Hogem Ranges area, immediately south of Sustut Lake (Figure 1-12-1).

The Sustut Lake syncline, which lies to the northeast of the anticline, involved only the black argillite and grey volcanic sandstone and siltstone of the Dewar Formation. Its northeastern limb is truncated by a north-northwest-trending, dextral strike-slip fault. The Sustut Lake anticline has the black argillite and grey volcanic sandstone and siltstone of the Dewar Formation in its core and dark grey volcanic breccia of the Savage Mountain Formation on both limbs. The southwestern limb dips steeply southwest and is locally vertical, or even overturned (Figure 1-12-1). Secondary, outcrop-scale folds are also developed. They are either symmetrical or asymmetrical in cross-section and very common in the well-bedded sedimentary rocks of the Dewar Formation (Plate 1-12-1d). Poles to bedding planes in the region fall on a great circle (Figure 1-12-2) and delineate a cylindrical fold axis trending at 122° with a plunge of 41°. The age of formation of the folds is unknown.

They were truncated by the faults and may therefore have developed during the early stages of the dextral transpression (*cf.* Wilcox *et al.*, 1973; Sylvester, 1988).

FAULTS

Subvertical or vertical strike-slip faults are the most widespread structural features in the study area. They are abundant along and near the Finlay-Ingenika fault, and become fewer and shorter away from it. On the ridges immediately west of Aiken Lake, for example (Figure 1-12-1), they are rarely seen. This spatial relationship of the strike-slip faults to the Finlay-Ingenika fault suggests that deformation in the study area was associated closely with the transcurrent motion on the Finlay-Ingenika fault and was largely restricted to a narrow belt, about 30 kilometres wide, adjacent to the major fault (Figure 1-12-1).

Based on the attitudes and slip senses, the faults were divided into four groups: dextral strike-slip faults trending northwest, north-northwest and north-northeast, and sinistral strike-slip faults trending east-northeast. All the faults can be readily interpreted as a resulting from dextral motion on the Finlay-Ingenika fault (Zhang and Hynes, 1991). The attitudes and slip senses of north-northeast and east-northeast-trending fault sets are consistent with their formation as Riedel (R) and conjugate Riedel (R') shears, respectively, related to the main motion on the Finlay-Ingenika fault (*cf.* Tchalenko, 1970; Keller *et al.*, 1982; Sylvester, 1988). The northwest-trending faults generally display two stages of displacement. The earlier is dip-slip with a thrust sense, and the later is horizontal, dextral. The thrusts are thought to have developed in association with the initiation of dextral displacement on the Finlay-Ingenika fault (*cf.* Sylvester, 1988), with the dextral, strike-slip motion superimposed once the fault was fully established. Faults in the north-northwest-trending group are parallel to, and have the same slip senses as, the Finlay-Ingenika fault. They are inferred to have formed as secondary shears of the Finlay-Ingenika fault. At several localities, for example south of Darb Lake and north of Dortatelle Creek, dioritic dikes are incorporated in mylonitic zones associated with the faults, indicating that fault motions occurred after emplacement of the extensive dioritic plutons in the study area.

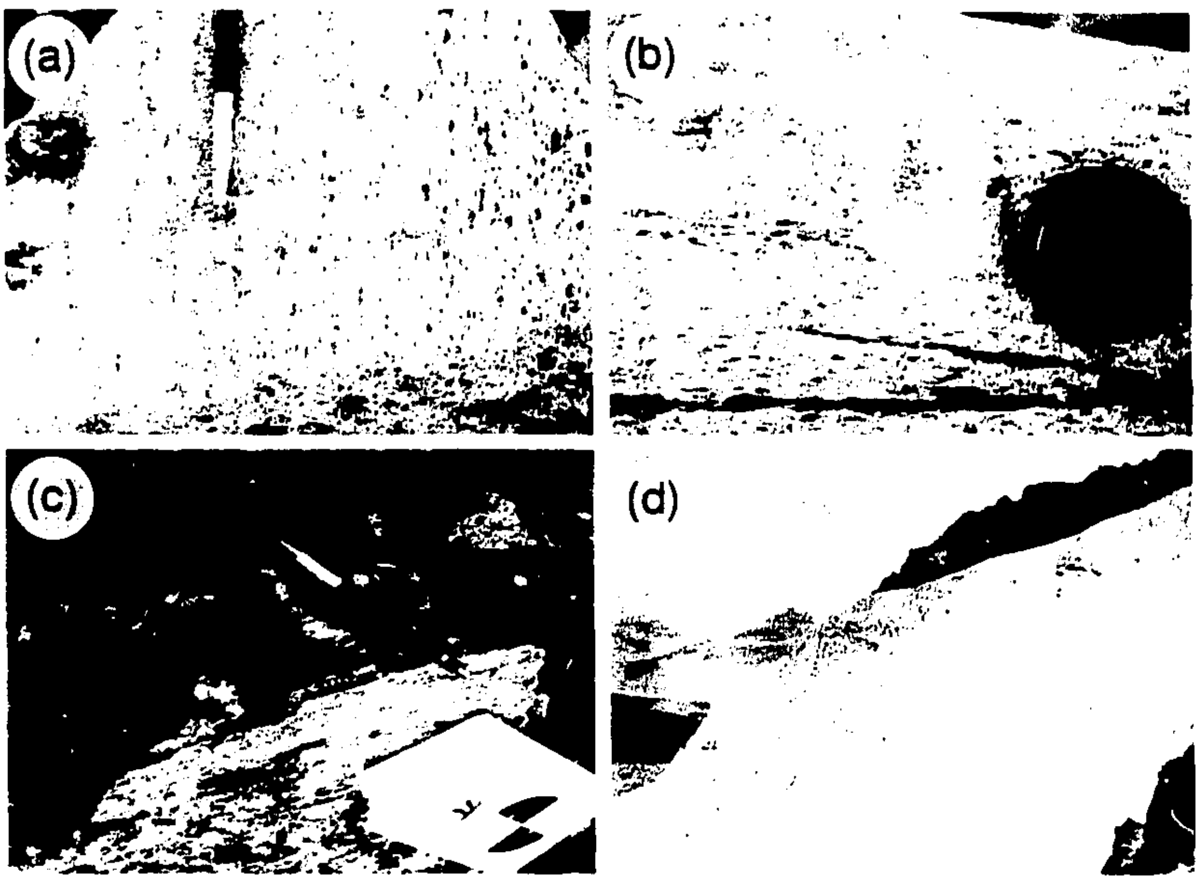

Plate 1-12-1(a). Primary mineral lineation in clinopyroxene porphyry; (b) Mineral stretching lineation in the north-northwest-trending faults east of Dortatelle Creek, looking northeast down. (c) North-northwest-trending fault west of Aiken Lake, pencil parallel to the extensional fissure filled with calcite fibres, book parallel to the fault plane, looking southwest down; (d) Outcrop-scale folds in well-bedded sedimentary rocks of the Dewar Formation in the Hogem Ranges, looking north.

The faults cut the Takla Group into fault-bounded, weakly deformed blocks, ranging in size from several square kilometres to tens of square kilometres (Figure 1-12-1). With progressive displacement on the Finlay-Ingenika fault, deformation was apparently concentrated in the previously formed fault zones, while the fault-bounded blocks remained only very weakly deformed. Cleavage is the only visible deformation outside the fault zones but within the fault zones rocks are strongly deformed and sheared into protomylonite to mylonite with a variety of kinematic indicators and fabrics, by which slip senses on the faults were determined.

Kinematic Indicators and Fabrics

S-C mylonites (Berthé *et al.*, 1979; Lister and Snoke, 1984; Shimamoto, 1989) are present in most of the faults, especially as they pass through the greenish grey clinopyroxene or clinopyroxene-plagioclase porphyries or volcanic breccias. They provide one of the most useful kinematic indicators in the study area. The C surfaces are predominantly closely spaced, displacement discontinuities or zones of relatively high shear strain, while the S surfaces are characterized by alignment of phyllosilicate minerals such as chlorite (Zhang and Hynes, 1991, Plate 1-12-1c). Angles between the C and S surfaces vary from 40°± (in slightly deformed domains) to 0°± (in strongly deformed domains). Hundreds of the C and S surfaces were measured along the Dortatelle fault and the fault east of Goldway Peak, and intersections of them are always subvertical or vertical, suggesting that horizontal displacement was predominant in the study area.

Drag folds, developed in mylonitic foliation, are common features in the strike-slip fault zones, and also provide kinematic indicators. Such folds in the Dortatelle fault zone, for example, are tight and asymmetrical, ranging in wavelength from less than 1 centimetre to several tens of centimetres. Axial planes of the folds are subvertical, striking northwest, with fold axes trending northwest and plunging 70° to 80°, and have an angle of 35°± to the fault plane. This geometry is consistent with that of the S-C fabrics and indicative of dextral strike-slip.

Extensional fissures (Ramsay and Huber, 1983) are common along the strike-slip faults and even between some cleavage planes. They are commonly filled with fibrous tremolite or calcite that grew either perpendicular or subperpendicular to the walls, especially where they cut volcanic breccias or porphyries. Typical relationships are exhibited in the north-northwest-trending fault on the ridge west of Aiken Lake (Plate 1-12-1c). Here, slickenlines marked by fibrous crystals of calcite on the fault plane display a dextral strike-slip sense, and six extensional fissures filled with calcite fibres were measured along the fault. Figure 1-12-3 plots the structural data and local, tectonic principal strains (e_1, e_2, and e_3) which were determined based on the assumption that the motion on the fault is simple shear. It is obvious from the plot that the principal strain e_2, which is determined by the intersection of the fault plane and mean extensional fissure plane (Fisher, 1953), is approximately perpendicular to the slickenline (the angle between them on the fault plane is 88°). The slickenlines and extensional fissures are therefore in excellent agreement with dextral strike-slip on the fault. Furthermore, the Fisher's mean (Fisher, 1953) of poles to the fissures moved away from the maximum principal strain e_1 (Figure 1-12-3), indicative of clockwise rotation of the fissures as a result of progressive incremental straining after their formation.

In addition to the above principal kinematic indicators, other fabrics such as stretching lineations and foliations are well developed in the fault zones. There are two types of mineral lineation in the study area: primary and secondary. The primary mineral lineations occur only in the clinopyroxene or clinopyroxene-plagioclase porphyries, and were observed at two localities on the ridge between Dortatelle and Kliyul creeks. They are due to the alignment of prismatic crystals of clinopyroxene and hornblende(?) (Plate 1-12-1a). No evidence of deformation has been found although some mineral grains are partially or entirely replaced by chlorite or epidote, which may have obscured such evidence. In its absence, these lineations are tentatively attributed to primary processes. The secondary lineations are characterized by stretched mineral grains, now predominantly chlorite (Plate 1-12-1b) and are confined to fault zones, especially in the north-northwest-trending faults on the ridge between the Dortatelle and Kliyul creeks (Figure 1-12-1). The minerals are commonly stretched subhorizontally into ribbons up to several centimetres long, while on the vertical section they have subrounded shapes. The stretching lineations (Plate 1-12-1b) cut the contacts

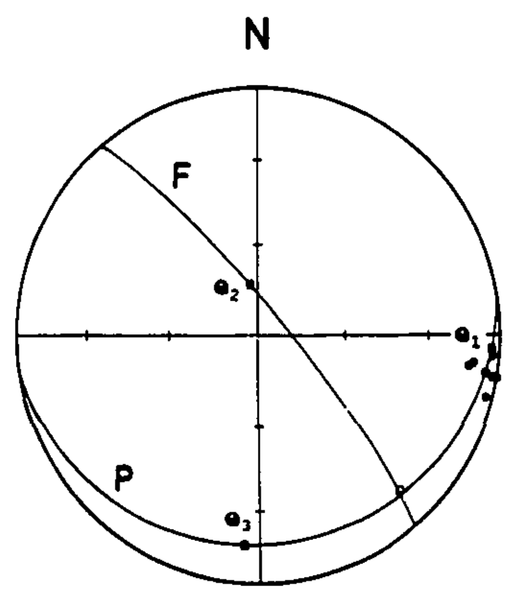

Figure 1-12-3. Stereonet plot of structural data from the north-northwest-trending fault on the ridge west of Aiken Lake. Solid circles: poles to the extensional fissure planes; solid square: principal strains (e_1, e_2 and e_3); open circle: Fisher's mean of poles to the extensional fissure planes; F: the fault plane; P: the principal plane normal to the intermediate principal strain (e_2).

between clinopyroxene-plagioclase porphyry and volcanic breccia, and minerals in different clasts of the breccia are aligned in the same direction, indicative of their deformational origin.

Foliations are the most common fabrics in or along the faults, and are characterized by parallel alignment of either phyllosilicate minerals or flattened fragments of volcanic breccia. Progressive development of cleavage due to flattening of volcanic breccia fragments is well developed in an area of about one square kilometre, bounded to the west by a north-northwest-trending, dextral strike-slip fault immediately north of the Goldway Peak. In the eastern part of this area fragments of clinopyroxene and clinopyroxene-plagioclase porphyries, in which phenocrysts of euhedral clinopyroxene and wispy plagioclase are relatively fresh, undeformed and randomly distributed, are only slightly flattened and may indeed have experienced deformation only during pyroclastic flow (Plate 1-12-2a). Passing westwards, a demonstrably tectonic flattening is superimposed, giving rise to a marked increase in the elongation ratio of fragments (Plate 1-12-2b), the local development of foliation, and deformation of a mafic dike (Plate 1-12-2d), which locally truncates the primary fabrics. In the western part of the area fragments are very strongly deformed, and foliations are extensive and penetrative in the breccia where the phenocrysts of euhedral clinopyroxene were no longer present (Plate 1-12-2c). The mean flattening plane strikes 335° and dips 73° northeast and makes an angle of 10° with the fault plane to the west, indicating that a clockwise rotation of 35° occurred, which is in good agreement with the estimate of rotation of cleavage (see below).

Outside the fault zones, rocks exhibit only a weakly developed spaced (typically at intervals of 2 to 10 cm) cleavage. The cleavage is steeply dipping and generally occurs in conjugate sets. It is interpreted to have formed at an early (pre-faulting) stage of the deformation, and its attitudes are used to constrain motions in the area since formation of the faults.

Statistics of Cleavage

Statistics of regionally distributed cleavage have been made at 24 sites within the fault-bounded blocks. Conjugate cleavages measured from the block northeast of Croydon Creek (Zhang and Hynes, 1991; Figure 1-12-3a in Zhang and Hynes, 1991) show orientations consistent with those to be expected in a stress field due to the initiation of dextral transcurrent motion on the Finlay-Ingenika fault (*cf.* Tchalenko, 1970; Keller *et al.*, 1982; Sylvester, 1988). If the regional cleavage was uniformly distributed before the

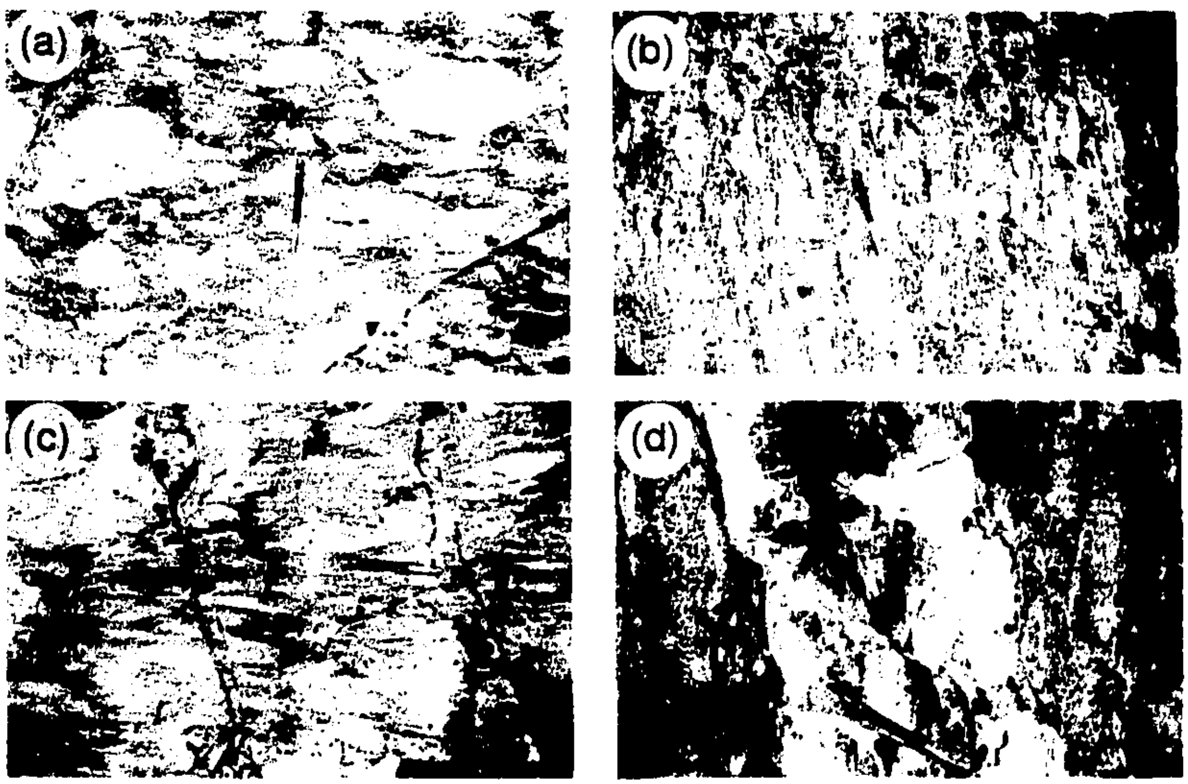

Plate 1-12-2 (a, b and c). Flattened fragments of volcanic breccia moving progressively westwards towards a dextral fault, looking northeast, north-northwest and northeast down, respectively; (d) Deformed mafic dike in the same region as (b), pencil parallel to the shear planes with thrust slip sense, looking north-northwest.

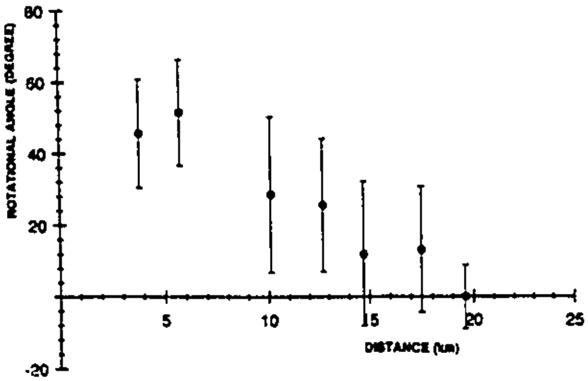

Figure 1-12-4. Variation of block rotational angle with distance away from the Finlay-Ingenika fault. The error bars represent the 95 per cent confidence circles for the rotational angles.

widespread strike-slip faulting in the study area, the variation of orientations of the cleavage can be used to indicate the block rotation. Based on this assumption, the rotational axes and angles for six sites were determined by comparing the mean attitudes for the regional cleavages with those from the block northeast of Croydon Creek. The mean rotational axis is subvertical, and the amount of block rotation varies over the study area, reaching its maximum (51.6±14.9°) close to the Finlay-Ingenika fault and minimum (0.0±9.0°) about 20 kilometres away from the fault (Figure 1-12-4).

CONCLUSIONS

The structures observed along the Finlay-Ingenika fault are dominated by subvertical to vertical, dextral strike-slip faults trending northwest, north-northwest and north-northeast, and sinistral strike-slip faults trending east-northeast. The faults are distributed in a narrow belt, about 30 kilometres wide, adjacent to the Finlay-Ingenika fault. This distribution, together with the attitudes and slip senses of the strike-slip faults, strongly suggests that the deformation developed in association with dextral, transcurrent motions on the Finlay-Ingenika fault. As displacement on the Finlay-Ingenika fault progressed, the deformation was apparently concentrated in the previously formed fault zones, while the fault-bounded, weakly deformed blocks were rotated clockwise about subvertical axes in response to the transcurrent motions. Statistics of regional cleavage indicate that the amount of block rotation varies over the study area, decreasing away from the major fault. This variable rotation of blocks is similar to that described by Nelson and Jones in the Las Vegas Range (1986) and in contrast to the uniform rotation described and modelled elsewhere (*e.g.*, Ron *et al.*, 1986; Hudson and Geissman, 1987; Geissman *et al.*, 1989; Ron *et al.*, 1990). Such rotations may characterize many parts of the Intermontane Belt and could in part explain the apparent disparities between the paleomagnetic declinations observed from the western allochthonous terranes and North America (Monger and Irving, 1980; Irving *et al.*, 1985; Rees *et al.*, 1985; Irving and Wynne, 1990). We are currently conducting paleomagnetic studies to test this assertion.

ACKNOWLEDGMENTS

This research was made possible by grants from the British Columbia Ministry of Energy, Mines and Petroleum Resources and the Natural Sciences and Engineering Research Council. Their support is gratefully acknowledged.

REFERENCES

Berthé, D., Choukroune, P. and Jegouzo, P. (1979): Orthogneiss, Mylonite and Non-coaxial Deformation of Granites: The Example of the South Armorican Shear Zone; *Journal of Structural Geology*, Volume 1, pages 31-42.

Church, B.N. (1974): Geology of the Sustut Area; *in* Geology, Exploration and Mining in British Columbia 1973, *B.C. Ministry of Energy, Mines and Petroleum Resources*, pages 411-455.

Church, B.N. (1975): Geology of the Sustut Area; *in* Geology, Exploration and Mining in British Columbia 1974, *B.C. Ministry of Energy, Mines and Petroleum Resources*, pages 305-309.

Fisher, R.A.S. (1953): Dispersion on a Sphere; *Royal Society of London*, Proceedings, Series A, 217, pages 295-305.

Gabrielse, H. (1985): Major Dextral Transcurrent Displacements Along the Northern Rocky Mountain Trench and Related Lineaments in North-central British Columbia: *Geological Society of America*, Bulletin, Volume 96, pages 1-14.

Geissman, J.W., Harlan, S.S. and Wawrzyniec, T.F. (1989): Strike-slip Faulting and Block Rotation in the Lake Mead Fault System; *Geology*, Volume 17, pages 1057-1058.

Hudson, M.R. and Geissman, J.W. (1987): Paleomagnetic and Structural Evidence for Middle Tertiary Counterclockwise Block Rotation in the Dixie Valley Region, West-central Nevada; *Geology*, Volume 15, pages 638-642.

Irving, E. and Wynne, P.J. (1990): Paleomagnetic Evidence Bearing on the Evolution of the Canadian Cordillera; *Royal Society of London*, Philosophical Transactions, A 331, pages 487-509.

Irving, E., Woodsworth, G.J., Wynne, P.J. and Morrison, A. (1985): Paleomagnetic Evidence for Displacement from the South of the Coast Plutonic Complex, British Columbia; *Canadian Journal of Earth Sciences*, Volume 22, pages 584-598.

Keller, E.A., Bonkowski, M.S., Korsch, R.J. and Shlemon, R.J. (1982): Tectonic Geomorphology of the San Andreas Fault Zone in the Southern Indio Hills, Coachella Valley, California; *Geological Society of America*, Bulletin, Volume 93, pages 46-56.

Lister, G.S. and Snoke, A.W. (1984): S-C Mylonite: *Journal of Structural Geology*, Volume 6, pages 617-638.

Lord, C.S. (1948): McConnell Creek Map-area, Cassiar District, British Columbia; *Geological Survey of Canada*, Memoir 251, 72 pages.

Mardia, K.V. (1972): Statistics of Directional Data; *Academic Press*, London and New York, pages 212-339.

Minehan, K. (1989a): Takla Group Volcano-sedimentary Rocks, North-central British Columbia; *in* Geological Fieldwork 1988, *B.C. Ministry of Energy, Mines and Petroleum Resources*, Paper 1989-1, pages 227-232.

Minehan, K. (1989b): Paleotectonic Setting of Takla Group Volcano-sedimentary Rocks, Quesnellia, North-central British Columbia; unpublished M.Sc. thesis, *McGill University*, 102 pages.

Monger, J.W.H. (1977): The Triassic Takla Group in McConnell Creek Map-area, North-central British Columbia; *Geological Survey of Canada*, Paper 76-29, 45 pages.

Monger, J.W.H. (1984): Cordilleran Tectonics: A Canadian Perspective; *Bulletin Societé Géologique de France*, Volume 7, pages 255-278.

Monger, J.W.H. and Church, B.N. (1977): Revised Stratigraphy of the Takla Group, North-central British Columbia; *Canadian Journal of Earth Sciences*, Volume 14, pages 318-326.

Monger, J.W.H. and Irving, E. (1980): Northward Displacement of North-central British Columbia; *Nature*, Volume 285, pages 289-293.

Nelson, M.R. and Jones, C.H. (1986): Paleomagnetism and Crustal Rotations along a Shear Zone, Las Vegas Range, Southern Nevada; *Tectonics*, Volume 6, pages 13-33.

Nixon, G.T. and Hammack, J.L. (1990): Geology and Noble Metal Geochemistry of the Johanson Lake Mafic-Ultramafic Complex, North-central British Columbia; *in* Geological Fieldwork 1989, *B.C. Ministry of Energy, Mines and Petroleum Resources*, Paper 1990-1, pages 417-424.

Ramsay, J.G. and Huber, M.I. (1983): The Techniques of Modern Structural Geology; *Academic Press*, London and New York, Volume 1, 307 pages.

Rees, C.J., Irving, E. and Brown, R.L. (1985): Secondary Magnetization of Triassic-Jurassic Volcaniclastic Rocks of Quesnel Terrane, Quesnel Lake, B.C.; *Geophysical Research Letters*, Volume 12, pages 498-501.

Richards, T.A. (1976a): McConnell Creek Map Area (94D/E), Geology; *Geological Survey of Canada*, Open File 342.

Richards, T.A. (1976b): Takla Group (Reports 10-16): McConnell Creek Map Area (94D, East Half), British Columbia; *Geological Survey of Canada*, Paper 76-1a, pages 43-50.

Ron, H., Aydin, A. and Nur, A. (1986): Strike-slip Faulting and Block Rotation in the Lake Mead Fault System; *Geology*, Volume 14, pages 1020-1023.

Ron, H., Nur, A. and Eyal, Y. (1990): Multiple Strike-slip Fault Sets: A Case Study From the Dead Sea Transform; *Tectonics*, Volume 9, pages 1421-1431.

Shimamoto, T. (1989): The Origin of S-C Mylonites and a New Fault-zone Model; *Journal of Structural Geology*, Volume 11, pages 51-64.

Sylvester, A.G. (1988): Strike-slip Faults; *Geological Society of America*, Bulletin, Volume 100, pages 1666-1703.

Tchalenko, J.S. (1970): Similarities Between Shear Zones of Different Magnitudes; *Geological Society of America*, Bulletin, Volume 81, pages 1625-1640.

Wheeler, J.O. and McFeely, P. (1987): Tectonic Assemblage Map of the Canadian Cordillera; *Geological Survey of Canada*, Open File 1565.

Wilcox, R.E., Harding, T.P. and Seely, D.R. (1973): Basic Wrench Tectonics; *American Association of Petroleum Geologists*, Bulletin, Volume 57, pages 74-96.

Woodsworth, G.J. (1976): Plutonic Rocks of McConnell Creek (94 D West Half) and Aiken Lake (94 C East Half) Map-area, British Columbia; *Geological Survey of Canada*, Paper 76-1A, pages 26-30.

Zhang, G. and Hynes, A. (1991): Structure of the Takla Group East of the Finlay-Ingenika Fault, McConnell Creek Area, North-central B.C. (94D/8, 9); *in* Geological Fieldwork 1990, *B.C. Ministry of Energy, Mines and Petroleum Resources*, Paper 1991-1, pages 121-129.